A multicomponent multiphase flow simulation of the Raikoke eruption plume

Zur Erlangung des akademischen Grades eines
DOKTORS DER NATURWISSENSCHAFTEN (Dr. rer. nat.)
von der KIT-Fakultät für Physik des
Karlsruher Institut für Technologie (KIT)

genehmigte

DISSERTATION

von

M.Sc. Sascha Bierbauer
aus Neuenstein

Tag der mündlichen Prüfung:	19.04.2024
Referentin:	Prof. Dr. Corinna Hoose
Korreferent:	Prof. Dr. Christian von Savigny

Abstract

This study provides one of the first explicit simulations of an explosive volcanic eruption with a numerical weather prediction model, considering the dynamical effects as well as the detailed interaction between the plume and the atmosphere, including microphysical processes. It is an important step, which lays the foundations for future research with advanced simulations that resolve both the atmospheric state and multicomponent multiphase features of the plume (mixture consisting of more than one component and thermodynamic phase). Previous approaches usually lacked in either a detailed representation of both atmospheric conditions and processes or they neglected multicomponent multiphase features of the plume and the dynamical effects caused by an eruption.

This thesis investigates the dynamical and microphysical plume development in its early stage by focusing on the interaction between the eruption, the plume, and the surrounding atmosphere, and the accompanied dynamical and microphysical processes (especially cloud formation). For that purpose the equation system of the ICOsahedral Nonhydrostatic - Aerosol and Reactive Trace Gases (ICON-ART) model system is modified to consider ash as a considerable part of the total air density. This enables considering the volcanic plume as a multicomponent multiphase flow.

The new implementations are tested in two quasi-2D simulations and in a high resolution simulation of real case scenario of the Raikoke eruption 2019. The falling mixed-bubble case (mixture of cold dry air and ash) shows the effect of ash on the dynamics, increasing the bubble's velocity by up to 16 % compared to a simple cold-bubble. The idealized volcanic eruption depicts the contribution of exit velocity and exit temperature at the source in causing momentum and thereby, development of the plume.

Simulation results for the real case scenario show good agreement with observations in terms of the vertical and horizontal ash dispersion. However, the agreement with simulated plume height strongly depends on the prescribed exit temperature at the source, and the modeled ash burden is overestimated compared to satellite retrievals.

Both the exit velocity and exit temperature lead to a strong updraft, which triggers the formation of clouds and precipitation. Additional emission of water vapor by the volcano slightly supports the formation of clouds and the consequent latent heat release, thereby, enhancing the amount of ash in the upper parts of the volcanic plume. However, it does not affect the total plume height. Simulated water contents of both liquid and frozen hydrometeors have a range of values with maximum values comparable with the water contents typical of strong cumulonimbus, and the mass of ice particles are in the range of observations of ice masses in historic volcanic plumes. Out of all eruption phases, only the strongest ones inject a small amount of water vapor of up to 16.5 kilotons into the lower stratosphere.

Atmospheric waves occur during each eruption phase in the simulation. Pressure perturbations show a good agreement with measurements during eruptions of the Soufrière Hills Volcano on the Caribbean island of Montserrat.

The results show that the modified ICON-ART is ready to be used for further new applications concerning multicomponent multiphase flows.

Zusammenfassung

Diese Arbeit liefert eine der ersten expliziten Simulationen eines explosiven Vulkanausbruchs mit einem numerischen Wettervorhersagemodell und betrachtet dabei dynamische Effekte sowie die detaillierte Wechselwirkung zwischen der Vulkanfahne und der Atmosphäre unter Berücksichtigung mikrophysikalischer Prozesse. Dies ist ein wichtiger Schritt, der den Grundstein für künftige erweiterte Simulationen legt, die sowohl den atmosphärischen Zustand als auch die Strömungseigenschaften der Vulkanfahne als Mehrphasenströmung (Strömung eines Gemischs, bestehend aus mehreren Komponenten und Aggregatzuständen) auflösen. Bei früheren Ansätzen fehlte es in der Regel entweder an einer detaillierten Darstellung der atmosphärischen Bedingungen und Prozesse, oder sie vernachlässigten die Eigenschaften der Vulkanfahne als Mehrphasenströmung und die durch einen Ausbruch verursachten dynamischen Effekte.

Die vorliegende Arbeit untersucht die dynamische und mikrophysikalische Entwicklung einer Vulkanfahne in ihrem Anfangsstadium. Dafür konzentriert sie sich auf die Wechselwirkung zwischen der Eruption, der Vulkanfahne und der umgebenden Atmosphäre sowie damit verbundene dynamische und mikrophysikalische Prozesse (insbesondere Wolkenbildung). Zu diesem Zweck wird das Gleichungssystem des ICON-ART (ICOsahedral Non-hydrostatic model - Aerosols and Reactive Trace gases) Modellsystems in einer Weise modifiziert, dass Asche als ein wesentlicher Teil der Gesamtluftdichte berücksichtigt wird. Dies ermöglicht die Betrachtung der Vulkanfahne als eine Mehrphasenströmung.

Die neuen Implementierungen werden in zwei quasi-2-dimensionalen Simulationen und in einer hochaufgelösten Simulation des realen Szenarios des Raikoke-Ausbruchs im Jahr 2019 getestet. Die Simulation einer fallenden mixed-bubble (Blase aus kalter trockener Luft und Asche) zeigt den Einfluss von Asche auf die Dynamik, indem sie die Geschwindigkeit der Blase im Vergleich zu einer einfachen cold-bubble (Blase aus kalter trockener Luft) um bis zu 16 % erhöht. Der idealisierte Vulkanausbruch veranschaulicht den Beitrag der Austrittsgeschwindigkeit und der Austrittstemperatur an der Quelle, die einen Impuls bewirken, und zeigt dabei die Entwicklung einer Vulkanfahne.

Die Simulationsergebnisse des Raikoke-Ausbruchs zeigen eine gute Übereinstimmung mit den Beobachtungen in Bezug auf die vertikale und horizontale Ausbreitung der Asche. Die Übereinstimmung mit der simulierten Fahnenhöhe hängt jedoch stark von der vorgeschriebenen Austrittstemperatur an der Quelle ab, und die simulierte Aschemasse in einer Luftsäule wird gegenüber Satellitenmessungen überschätzt. Die Austrittsgeschwindigkeit und die Austrittstemperatur führen zu einem starken Auftrieb, der die Bildung von Wolken und Niederschlag auslöst. Die zusätzliche Emission von Wasserdampf durch den Vulkan begünstigt die Wolkenbildung und die daraus resultierende Freisetzung latenter Wärme ge-

ringfügig. Dies führt zu einem erhöhten Anteil an Asche in den obersten Bereichen der Vulkanfahne, beeinflusst aber nicht ihre Gesamthöhe. Die simulierten Wassergehalte von flüssigen und gefrorenen Hydrometeoren liegen in einem Bereich mit Maximalwerten, die mit den Wassergehalten von starken Cumulonimbus vergleichbar sind. Zudem liegt die simulierte Gesamtmasse von Eispartikeln in der Vulkanfahne in einem Bereich von Eismassen, die in historischen Vulkanfahnen beobachtet wurden. Von allen Eruptionsphasen führen nur die stärksten zu einer leichten Erhöhung der Wasserdampfmasse von bis zu 16,5 Kilotonnen in der unteren Stratosphäre. In der Simulation treten atmosphärische Wellen während jeder Eruptionsphase auf. Die simulierten Druckschwankungen stimmen mit Messungen während Eruptionen des Soufrière Hills Vulkans, auf der karibischen Insel Montserrat, überein.
Die Ergebnisse zeigen, dass die modifizierte Version von ICON-ART für weitere neue Simulationen bezüglich Mehrphasenströmungen eingesetzt werden kann.

Contents

1 Introduction **1**

1.1 Processes and impacts occurring due to volcanic eruptions . . . 3

1.2 Models to simulate volcanic eruption plumes . . . 5

1.2.1 Empirical scaling relationships (0th order) . . . 5

1.2.2 1-D integral models . . . 6

1.2.3 3-D plume models . . . 6

1.2.4 Modeling volcanic plume dispersion with atmospheric models . . . 7

1.3 Objectives of this work . . . 8

2 Generation of volcanic eruption plumes **11**

2.1 The mechanisms of volcanic eruptions . . . 11

2.2 Dynamics and development of a volcanic plume . . . 12

2.3 Volcanic aerosols in the atmosphere . . . 14

2.4 Natural multicomponent multiphase flows . . . 15

3 The multicomponent multiphase model ICON-ART **19**

3.1 Multicomponent multiphase flows in atmospheric models . . . 19

3.1.1 The atmosphere in a barycentric framework . . . 19

3.1.2 The mass budget treatment in a barycentric framework . . . 21

3.2 Multicomponent multiphase flows in the ICON model . . . 21

3.2.1 The atmosphere in the barycentric framework in ICON . . . 22

3.2.2 The mass budget treatment in ICON . . . 24

3.3 The ART module . . . 25

3.3.1 Sedimentation of aerosols . . . 27

3.3.2 Coagulation of aerosols . . . 28

4 Simulations of volcanic eruption plumes with ICON-ART **31**

4.1 Earlier approaches for simulating volcanic plumes with ICON-ART . . . 31

4.2 New implementations to enable explicit simulations of volcanic plumes with ICON-ART . . . 32

4.2.1 Mass source for the total air mixture . . . 32

4.2.2 Mass sink for the total air mixture . . . 33

4.2.3 Momentum and heat source during volcanic eruptions 34

5 Idealized quasi 2D-simulations 37
5.1 Simulation of density currents and mass sink 37
5.1.1 Model setup 37
5.1.2 Results for the density current simulations 38
5.2 Simulation of an idealized volcanic eruption and mass source 42
5.2.1 Model setup 42
5.2.2 Results for the idealized volcanic eruption simulations 42

6 Real case scenario - simulation of the Raikoke eruption in June 2019 47
6.1 Model setup 47
6.1.1 Filtering the ash from the background 49
6.1.2 Observational data from GOES-17 and Himawari-8 satellite 49
6.2 Development of the ash plume 50
6.2.1 Horizontal and vertical distribution of ash in simulation and observation . . 50
6.2.2 Quantitative comparison of the ash mass loading 55
6.2.3 Sensitivity to $\hat{\theta}_{v,e}$ at the source 57
6.2.4 Sensitivity to volcanogenic water vapor emission 59
6.3 Impact of the eruption on hydrometeors and water vapor 62
6.3.1 Development of clouds and precipitation 62
6.3.2 Impact of volcanogenic water vapor emission on cloud formation 71
6.3.3 Vertical distribution of water vapor in the atmosphere affected by the eruption 79
6.4 Generation of atmospheric waves during the eruptions 82

7 Conclusions and Outlook 89
7.1 Concluding remarks 89
7.2 Outlook 93

A Additional figures 95
A.1 Figures for section 6.2.1 95
A.2 Figures for section 6.2.2 100
A.3 Figures for section 6.3.1 102
A.4 Figures for section 6.3.2 109
A.5 Figures for section 6.3.3 116

B Acronyms 117

C Bibliography **121**

D List of Figures **135**

E List of Tables **139**

1. Introduction

Explosive volcanic eruptions have various effects either on their surrounding area on a short timescale or globally over several years. The eruptions of Krakatau in 1883 or Tambora in 1815 are counted among the strongest eruptions in recent history and had a widespread climatic effect (Schaller et al., 2009; Stothers, 1984). The 1815 Tambora eruption led to reduced temperature and increased precipitation, like snowfall, and frost, resulting in the famous 'Year without summer' in Europe and North America. This subsequently led to crop failure, famines, diseases and social distress in many regions of the northern hemisphere (Stommel and Stommel, 1979; Stothers, 1984; Luterbacher and Pfister, 2015; Brönnimann and Krämer, 2016).

Recently, a highly explosive, shallow-submarine eruption of the Hunga Tonga-Hunga Ha'apai (HTHH) volcano took place in January 2022. The generated plume even reached the mesosphere with an estimated observed top height of approximately 55 km, creating a new record in the satellite era (Carr et al., 2022). Due to its submarine nature, this eruption released a huge amount of water (H_2O) from the ocean. Thus, it is hypothesised that the large amount of H_2O led to cloud formation, latent heat release and therefore, strong convection which uplifted the plume to higher altitudes. As a consequence, large amounts of water vapor reached the stratosphere (Schoeberl et al., 2022; Xu et al., 2022; Vömel et al., 2022). Furthermore, it generated atmospheric Lamb waves (Lamb, 1881) which travelled multiple times around the globe (Otsuka, 2022; Amores et al., 2022; Adam, 2022). The climatic effect of this eruption, particularly, the injected water vapor in the stratosphere, is currently an important research question for the scientific community.

In contrast, the eruption of Eyjafjallajökull in Iceland in 2010 had no impact on the large scale climate. However, northwesterly winds transported the emitted ash to central Europe (Muser, 2022). Jet engines are susceptible to damage from even short encounters with volcanic ash (Casadevall, 1994; Grindle, 2002). Thus, in order to prevent catastrophic accidents, many areas of the European airspace were closed for 8 days, that led to cancellations of 100.000 flights (Schumann et al., 2011). This resulted in an economic loss of approximately US$1.7 billion for the aviation sector during the period of the 15-21 April 2010 (Mazzocchi et al., 2010; Ragona et al., 2011) and further global economic loss (Mazzocchi et al., 2010; Budd et al., 2011).

Another phenomenon during volcanic eruptions are pyroclastic density currents (PDCs). They occur due to collapsing eruption plumes upon exhaustion of the initial momentum (Textor et al., 2005). They have a hazardous, destructive and unpredictable nature, causing massive damage to the surrounding area or even death tolls (Jacobs et al., 2014). In addition, they may also cause giant volcanic clouds (Sparks

et al., 1997; Gilbert and Sparks, 1998; Dartevelle et al., 2002).

This short selection of volcanic eruptions shows how diverse their impacts can be. Both ash and sulfate particles can travel thousands of kilometers from the volcano, when they reach the stratosphere. Ash particles can stay in the atmosphere for up to a few months until they fall out by sedimentation (Robock, 2000; Niemeier et al., 2009; Jensen et al., 2018). Sulfuric particles can even remain up to two years in the atmosphere, until the residual stratospheric meridional circulation causes their removal (Robock, 2000). In the stratosphere, volcanic aerosols serve as a surface for stratospheric heterogeneous chemistry, which destroys ozone (O_3) in the stratosphere (Solomon et al., 1996; Solomon, 1999). Furthermore, volcanic aerosols modify the Earth's radiation budget by scattering and absorbing longwave (LW) and shortwave (SW) radiation, which influences surface temperatures and atmospheric dynamics (Robock, 2000; Marshall et al., 2022). On the other hand, volcanic plumes affect the local environment (Spence et al., 2005; Stewart et al., 2006; Wardman et al., 2012) and ash particles and volcanic gases can be hazardous for public health (Horwell and Baxter, 2006).

Despite their diverse impacts, all explosive volcanic eruption plumes have one property in common. They are prominent examples of geophysical multicomponent multiphase flows (Jacobs et al., 2014). However, the impacts of volcanic eruption plumes vary in many respects and depend on many conditions and processes, particularly during the initial phase of the plume development. In order to forecast and predict these impacts using numerical models, a holistic understanding of the physical system is crucial which thereby, makes this task more challenging. Weather and climate models are intended to represent the earth's atmosphere in detail and resolve small or large scale atmospheric processes, depending on their application. But in case of volcanic eruptions, they usually neglect the coupling between the dispersion of the erupted mixture or the physical and chemical evolution of a plume. This leads to a gap when it comes to the forecast of short-term dispersion, effects on clouds, and the impact of volcanic eruptions on the climate (Timmreck, 2012; von Savigny et al., 2020). On the other hand, volcanic plume models have been developed to examine the dynamics of eruption columns (Costa et al., 2013; Suzuki et al., 2016). Depending on their complexity, they characterize the multiphase flow features of the eruptive mixture in detail (Suzuki et al., 2016). However, they do not simulate the atmospheric state on their own. They either use a predefined one or use meteorological data from external atmospheric models to consider atmospheric conditions. Therefore, they are strongly dependent on weather models. Hence, the atmospheric profile is not updated and thus, not well represented in volcanic plume models at each simulation time step. Moreover, they often neglect important aerosol-dynamical processes, like coagulation of aerosols that results in larger aerosol sizes, or their removal from the atmosphere due to sedimentation. In addition, many plume models neglect cloud microphysical processes including phase changes of water, leading to latent heat release.

This study aims to combine benefits of both model types in one single model for the first time. Therefore, dynamical effects, microphysical processes and plume dispersion depending on both eruptive and atmospheric conditions, are considered at each time step of the simulation. The desired result of this study

is the improvement of plume dispersion forecast for the benefit of the wider community. The following sections introduce the existing research done in the field of modeling volcanic eruptions using different plume and atmospheric models. Note that the term 'plume' in this thesis describes the material emitted by the volcano, to distinguish it from meteorological clouds.

1.1. Processes and impacts occurring due to volcanic eruptions

There are various processes which affect the volcanic plume development, that in turn impacts the environment. Some of these processes which are most relevant for the scope of this study are illustrated in figure 1.1.

An explosive volcanic eruption emits a mixture of hot gases (like water vapor, sulfuric gases, and halogens) and tephra (solid ash particles with diameter > 2mm (Rose and Durant, 2009)) into the atmosphere, whereas, only ash particles < 32 μm (very fine ash) are relevant for long-range transport in the atmosphere (Rose and Durant, 2009). The source conditions at the vent control the amount of erupted material as well as the initial momentum and heat. Momentum, heat, and entrainment of surrounding air can lead to a strong updraft in the atmosphere close to the volcano. However, the emitted mixture increases the total air density, leading to a much higher air density in the plume area compared to the surrounding air. Thus, if the plume is negatively buoyant, it overbalances the updraft and collapses, consequently, leading to development of PDCs (Druitt, 1998; Sulpizio et al., 2014). If the plume remains in the atmosphere, the interaction between the plume and the atmosphere is crucial for its further development. Especially mi-

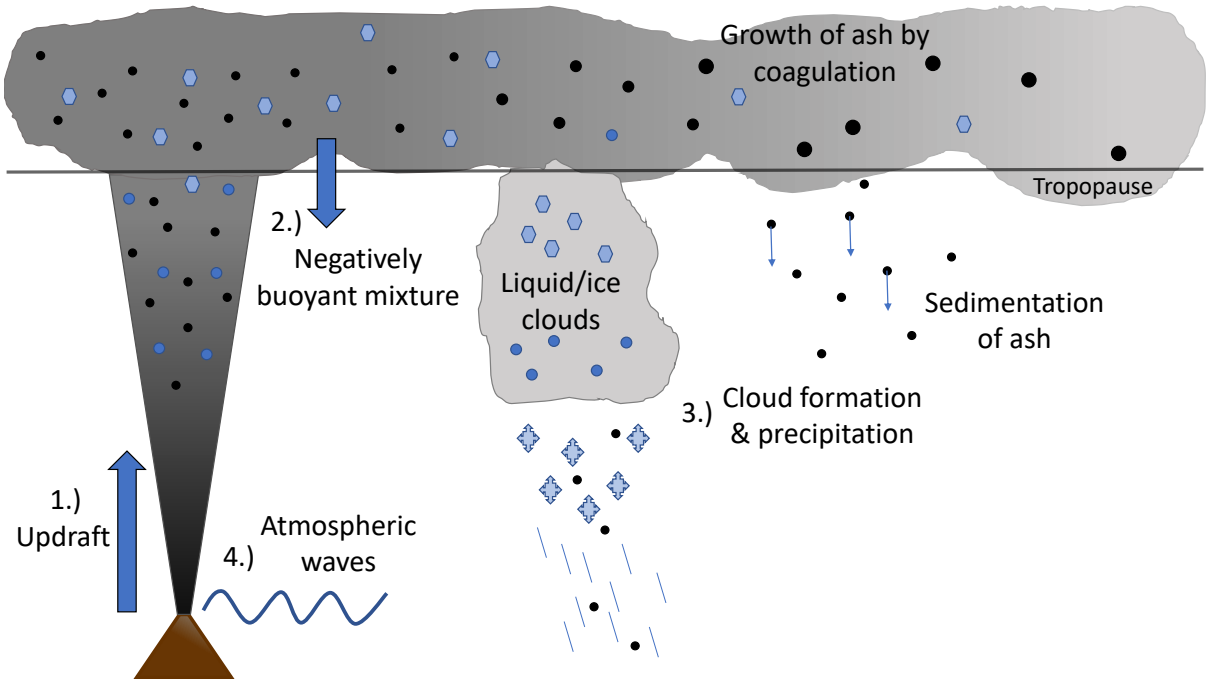

Figure 1.1.: Schematic illustration of a volcanic eruption plume as an example of a multicomponent multiphase flow, along with the processes and impacts that affect the plume and the atmosphere. The lengths are not to scale.

crophysical processes during the first minutes and hours are relevant for the further development, which include the formation of clouds. The updraft lifts moist air and emitted volcanogenic water vapor to higher altitudes. In addition, volcanic aerosols can serve as cloud condensation nuclei (CCN)s or ice nuclei (IN)s (Twomey, 1974; Malavelle et al., 2017; Haghighatnasab et al., 2022). As a consequence, phase changes occur, forming liquid and frozen particles in form of clouds and precipitation. This can support the removal of ash by wet deposition (Kawaratani and Fujita, 1990; Dare et al., 2016) or by washout, similar to when reduction of air pollution happens during rain events (Yoo et al., 2014; Hu et al., 2021). Ice is present in all volcanic plumes that cool down below freezing temperature, owing to plume lofting to high altitudes (Rose et al., 2004), and potentially reduces the residence time of ash and sulfur dioxide (SO_2) in the plume (Pinto et al., 1989). The Rabaul eruption in 1994 in Papua New Guinea generated a plume that contained > 2 megatons of ice (Rose et al., 2004). Wet ash and mud falls occurred near the volcano and additionally, no ash could be detected by satellites and only low levels of SO_2 were revealed by remote sensing (80 ± 50 kilotons) (Rose et al., 1995). Hence, ice was probably responsible for the removal of ash and SO_2 due to precipitation. The Hekla eruption in 2000 in Iceland created a plume which consisted of >1 megatons of ice and snow, documented by meteorological radar (Lacasse et al., 2004; Rose et al., 2004). The large eruption of Pinatubo in 1991 in the Philippines produced a huge plume containing about 80 megatons of ice, 50 megatons of fine ash (<15 μm radius), and 18-19 megatons SO_2 (Guo et al., 2004a,b). Said ice had a significant effect on the plume, as it apparently sequestered a large amount of SO_2 of the atmosphere during the first day (Guo et al., 2004a). Moreover, about 90 % of ice and ash fell out of the plume in 3 days, suggested that they fell out as ice/ash aggregates (Guo et al., 2004b). In contrast, condensation or sublimation of water vapor, and freezing of liquid droplets lead to latent heat release. This heats the surrounding air and can result in convection, which subsequently lifts ash and gases to higher altitudes. This could be shown by simulations of volcanic plumes which rose 2-3 km due to latent heat release by formation of hydrometeors (Woods, 1993). Herzog et al. (1998) performed simplified 2D simulations of volcanic plumes and focused on the effect of the formation of hydrometeors and subsequent latent heat release on the plume development. Release of latent heat added 13 % to the thermal energy released by the volcano, resulting in further plume lofting of 1500 m.

Of great interest is the role of water vapor that reaches the stratosphere, especially since the HTHH eruption. It plays an important role in stratospheric chemistry, as it can contribute to ozone loss (Vogel et al., 2011; Robrecht et al., 2019) or impedes polar stratospheric ozone recovery (Shindell, 2001). Moreover, increased water vapor in the stratosphere has the potential to affect the global climate by enhancing the rate of surface warming (Solomon et al., 2010). As the stratosphere contains a small amount of water vapor, small changes in the stratospheric water budget can influence the stratospheric chemistry and climate (Forster and Shine, 2002; Solomon et al., 2010; Vömel et al., 2022). However, only a few volcanic eruptions were large enough to emit detectable amounts of water vapor in the stratosphere (Murcray et al., 1981; Schwartz et al., 2013; Sioris et al., 2016). Hence, volcanic eruptions are not considered to be a major source for stratospheric water vapor (Vömel et al., 2022). Aerosol dynamical processes have

an effect on plume conditions, including coagulation between ash particles or sedimentation of ash, as these processes influence e.g. radiative properties or hygroscopicity of ash particles. Furthermore, the energy released by an explosive volcanic eruption is expected to generate various types of atmospheric waves (Amores et al., 2022). These include inertia gravity waves, infrasound waves, Rossby waves, shock waves, and Lamb waves, as for the case of HTHH (Otsuka, 2022; Amores et al., 2022). The Soufrière Hills eruption on the Caribbean island of Montserrat in 2003 and 2009 caused internal gravity waves (Baines and Sacks, 2017). Shock waves travel faster than the speed of sound and occur when the released energy is large enough (Medici et al., 2014). They have been reported only for a small number of volcanic eruptions (Morrisey and Mastin, 2000).
In order to investigate and forecast these impacts using numerical models, it is fundamental to account for these processes in the early stages of a volcanic plume. Different applications to simulate the development of volcanic plumes and their impacts with numerical models, sorted according to increasing complexity, are presented in the following sections.

1.2. Models to simulate volcanic eruption plumes

Numerical models for investigating volcanic plumes have been developed with increasing complexity during the last decades. They all aim to describe the dynamics of volcanic plumes and to provide estimations of source conditions (Costa et al., 2016). Thus, these models have a key application in supporting sectors to reduce hazards, for instance, the aviation sector. However, the accuracy of the dispersion forecast is critically dependent on the choice of eruption source conditions. To determine these conditions, there are empirical scaling relationships based on 0th order. Beyond that, two categories of more complex eruption column models exist: First, one-dimensional (1-D) integral models which depend on mathematical description of turbulent buoyant plumes theory by Morton et al. (1956). Second, three-dimensional (3-D) models that resolve turbulent structures of volcanic plumes in detail. The following shows a brief overview of some models.

1.2.1. Empirical scaling relationships (0th order)

Observations of eruption plumes provide a relationship between the plume height and the mass eruption rate (MER). Some empirical scaling relationships include a simplified description of the atmosphere (Mastin et al., 2009; Degruyter and Bonadonna, 2012; Woodhouse et al., 2013; Carazzo et al., 2014). Mastin et al. (2009) used a dataset of observed historical eruptions to compile a relationship, that neglects explicit atmospheric conditions. Since it is based on observational data, the relationship contains averaged wind effects, though. Degruyter and Bonadonna (2012), Woodhouse et al. (2013), and Carazzo et al. (2014) used 1-D models to take atmospheric conditions into account. Degruyter and Bonadonna (2012) considered the atmospheric temperature, wind profiles, thermodynamic properties and values of the entrainment coefficients to provide their relationship. Furthermore, Woodhouse et al. (2013) ac-

counted for measured atmospheric buoyancy frequency and source thermodynamic properties. Based on this, Woodhouse et al. (2016) devised the source mass flux as a function of the plume height. Carazzo et al. (2014) compared strong and weak eruption plumes to give a relationship between the plume height and the MER, that considers wind velocity.

1.2.2. 1-D integral models

Morton et al. (1956) developed a mathematical description of the Buoyant Plume Theory (BPT), which is a mathematical description of turbulent buoyant plumes. Among other things, the BPT considers turbulent mixing as a horizontal inflow of ambient air into the plume (entrainment) and a closure of the equations for mass, momentum, and buoyancy fluxes. Moreover, it assumes self-similarity of the radial profile of the time-averaged plume properties like axial velocity and bulk density (Costa et al., 2016). A detailed description can be found in Morton et al. (1956). Wilson et al. (1978) applied this theory for the first time and subsequently, initiated the origin of all other 1-D models. Those models describe the steady state of a volcanic plume and calculate e.g. the MER and an emission profile according to the plume top height. Within the last decades, these models have been further developed to increase the accuracy of their numerical calculations. Woods (1988) and Woods and Bower (1995) assessed the effect of vent conditions and magma types. Woods (1993) and Sparks et al. (1997) added atmospheric conditions. Moreover, Koyaguchi and Woods (1996) accounted for external surface water and Woods and Bursik (1991) considered thermal equilibrium and particle fallout. Some examples of 1-D models include *PlumeRise*, *Plumeria*, and *FPlume*. *PlumeRise* considers thermodynamics of phase changes of water and plume bending by wind effects (Woodhouse et al., 2013, 2016). *Plumeria* accounts for the effect of condensation of water and ice formation on the plume dynamics (Mastin, 2007; Mastin, Larry G, 2014). Furthermore, *FPlume* applies phase changes of water, particle fallout, entrainment of moist environmental air and particle re-entrainment (Folch et al., 2016; Macedonio et al., 2016).

1.2.3. 3-D plume models

3-D plume models are much more complex, as they make use of the time-dependent solution of the Navier-stokes equations, to account for mass, energy/enthalpy and momentum conservation. For the initialization, they need information about the atmospheric state and of the flux of ash and gases during an eruption. Thereby, they solve the equations for each grid cell on a 3D grid domain. 3-D models differ in the consideration of physical and chemical processes, like subgrid-turbulence or cloud microphysics. One example of 3-D plume models is the Active Tracer High Resolution Atmospheric Model (ATHAM) (Oberhuber et al., 1998; Herzog et al., 1998; Herzog and Graf, 2010). It is designed to simulate explosive eruption plumes and can be used for simulations with spatial resolutions typical for large-eddy simulations (LES). It considers the composition of the emitted mixture, the exit velocity and temperature, as well as the vent size in the lower boundary conditions. Furthermore, it accounts for entrainment

of ambient air into the plume by a prognostic turbulence closure scheme and phase changes of water. Another model is ASH Equilibrium Eulerian (ASHEE) (Cerminara, 2015; Cerminara et al., 2016). It is a compressible, multiphase flow model, which is based on the turbulent, dispersed multiphase flow theory (Balachandar and Eaton, 2010). By using an LES formalism, it is able to simulate the effect of sub-grid turbulence on large-scale dynamics. The model Pyroclastic Dispersal Analysis Code (PDAC) describes the multiphase flow dynamics of a mixture consisting of gas and solid pyroclasts, which are ejected from the volcano vent (Neri et al., 2003; Ongaro et al., 2007; Carcano et al., 2013). The subgrid scale turbulence scheme is based on an LES approach.

1.2.4. Modeling volcanic plume dispersion with atmospheric models

The approach to forecast the dispersion of volcanic plumes with atmospheric models is different compared to plume models. In contrast to the latter, atmospheric models can represent the highly variable atmospheric state in detail. However, information of the source conditions are mandatory for forecasting the plume dispersion. Knowing parameters like the MER, initial plume rise height, emission profile, i.e. the vertical distribution of mass, and the eruption duration can notably improve the quality of the forecast of the emitted gases and particles (Scollo et al., 2008; Harvey et al., 2018). Empirical scaling relationships (section 1.2.1) or 1-D models (section 1.2.2) provide the MER and the emission profile for the mixture. Depending on the choice of the emission profile, further uncertainties occur (de Leeuw et al., 2021). Various approaches for estimating the emission profile exist. Stuefer et al. (2013) provided idealized profiles and Rieger (2017) applied backward trajectory modeling to derive a Gaussian-shaped profile. Furthermore, various other profiles exist including plume-theory-based profiles (Marti et al., 2017), uniform profiles (Beckett et al., 2020; Muser et al., 2020), as well as estimated profiles by observations (de Leeuw et al., 2021). Nevertheless, there are limitations of dispersion forecast with atmospheric models. The plume dispersion is decoupled from unresolved plume dynamics and the influence of atmospheric conditions on the emission height is neglected (Bruckert, 2023). This results in uncertainties for investigating the effects of volcanic eruptions on regional and global scales (Textor et al., 2005; Timmreck, 2012; von Savigny et al., 2020). Approaches to overcome these limitations exist from Collini et al. (2013), who coupled Weather Research and Forecasting Model / Advanced Research WRF (WRF/ARW) meteorological model with the FALL3D dispersal model to simulate the Cordon Caulle eruption 2011. They achieved good agreement in ash transport simulations with satellite observations. Marti et al. (2017) combined the Nonhydrostatic Multiscale Model on the B-grid – Multiscale Online Nonhydrostatic AtmospheRe CHemistry model – ASH (NMMB-MONARCH-ASH) meteorological and transport model with FPlume. Bruckert et al. (2022) coupled the ICON-ART model with FPlume to simulate the Raikoke eruption of 2019. They calculated the source conditions online and highlighted, that they significantly improved the ash burden and dispersion of the plume, when resolving the different eruption phases.
Although, these studies improved the accuracy of plume dispersion modeling and its effects, by combining the benefits of atmospheric and plume models, many processes still remain unresolved and neglected.

Plume models only provide an emission profile for the atmospheric models. There is a lack of information of the high plume density compared to the surrounding air. Moreover, atmospheric models neglect both the high momentum and high temperature of the mixture. This further leads to neglecting any dynamical effects due to the eruption and the high plume density. These effects can have a wide influence ranging from large scale atmospheric conditions to microphysical processes like cloud formation. Even though cloud formation takes place on scales typical for LES approaches, it can largely impact both the plume development and the atmospheric state. The previous studies and the highlighted gaps in this field of research provide the motivation for this study to device a new approach.

1.3. Objectives of this work

The purpose of this study is to address and overcome the limitations of simulating volcanic eruption plumes and plume dispersion. This is essential to reduce uncertainties and to enhance the understanding of plume development and dispersion, that has an impact on weather and climate. For one of the first times, an numerical weather prediction model (NWP) model (ICON-ART) is hereby used to explicitly simulate volcanic eruption plumes without using an additional external plume model or emission profile. ICON-ART describes the atmosphere as a multicomponent multiphase system, which accounts for dry air and water in different phases (e.g. cloud water, cloud ice, water vapor) as parts of the total air mixture. As part of this study, the model has been modified such that it considers ash as part of the total air mixture. Therefore, ash is added to the density of the total air. Furthermore, the implementations take into account a source and sink for the mass of total air. Both are mandatory to account for the high plume density compared to the surrounding air and the multicomponent multiphase features of a volcanic plume. Moreover, the momentum input is accounted for via the incorporation of exit velocity and exit temperature. The latter also accounts for the high temperature of the mixture and thus, the heat transfer between the plume and the surrounding air. By applying these implementations, high-resolution simulations are performed to investigate small-scale processes which take place during the plume development, and to use a resolved turbulence scheme. This application allows describing the atmospheric state, the plume dynamics, aerosol dynamics and microphysical processes at each simulation time step. The following research questions are examined in this study:

1. What has to be modified in an NWP model like ICON-ART to realise the explicit simulation of a volcanic eruption plume as multicomponent multiphase flow?
2. Can the modified ICON-ART provide reliable results regarding the plume height, dispersion, and ash mass loading?
3. How sensitive is the plume development to different exit temperatures at the source?
4. Does the emission of volcanogenic water vapor affect the plume development?

5. How does the volcanic eruption affect the formation of clouds and precipitation in the vicinity of the volcano?

6. How does the eruption alter the vertical distribution of water vapor in the atmosphere?

7. Is the modified ICON-ART able to simulate atmospheric waves caused by volcanic eruptions?

To answer the research questions, this thesis highlights the following chapters. Chapter 2 discusses the relevant processes to understand the topic. After that, chapter 3 introduces the ICON-ART modeling framework together with the new implementations, which are important to enable the simulation of volcanic multicomponent multiphase flows. Chapter 5 describes the model setup and results of the idealized simulations to preliminary test the new implementations. Afterwards, the model setup of a real case scenario and a description of observational data to validate the model results, and the corresponding results are shown in chapter 6. It focuses on three main parts: the first one is about ash dispersion, a sensitivity study regarding different temperatures for the heat source and the impact of volcanogenic water vapor emission on the plume development. The second part discusses the cloud formation and the vertical distribution of water vapor in the lower atmosphere, particularly in the lower stratosphere, affected by the eruption. The last part deals with the generation of atmospheric waves due to the eruption. Finally, chapter 7 concludes the results and provides an outlook.

2. Generation of volcanic eruption plumes

A large variety of eruption types exist but overall, they are distinguished between effusive and explosive eruptions. Effusive eruptions release mainly lava and affect only their nearby environment. Explosive eruptions may have a global impact on a temporal scale of months or even years. This section starts by briefly explaining the mechanisms of volcanic eruptions, followed by describing development of plume dynamics during explosive eruptions. Later, it gives a short overview about ash in the atmosphere and aerosol-dynamical processes which are relevant for this study. Finally, it introduces multicomponent multiphase flows with a focus on volcanic plumes.

2.1. The mechanisms of volcanic eruptions

Volcanoes emit lava, tephra and gas during an eruption. Lava is molten rock that reached the Earth's surface and is called magma below the surface. Magma is formed by partial melting of rocks in the Earth's mantle or lower crust, typically at depths between 10 and 200 km (Jain, 2014). It consists of minerals (e.g. silicon (Si), iron, magnesium (Mg)) and small amounts of dissolved gases (e.g. water vapor, carbon dioxide (CO_2)). The amount of silicon dioxide (SiO_2) and dissolved gases differ among different types of magma. Four main types of magma exist, each of which can be distinguished by the content of dissolved SiO_2: basaltic (48% - 52% SiO_2), andesitic (52% - 63% SiO_2), dacite (63% - 68% SiO_2), and ryholitic (68% - 77% SiO_2). With larger amount of SiO_2, the exit temperature decreases and so does the magma's viscosity, which impacts the plume dynamics due to increase of the exit velocity (Bruckert, 2023). The term tephra includes all solid materials, which are ejected into the atmosphere, ranging from very fine ash particles up to larger rocks, like volcanic bombs. As for the released gases, the most abundant ones are water vapor, CO_2 and sulfuric gases like SO_2. Schmincke (2004) described three types of volcanic eruptions with different mechanisms: magmatic, phreatomagmatic and phreatic eruptions, which are briefly explained in the following. In a magma chamber, volatile constituents are dissolved in magma under high pressure and the latter is undersaturated. Magmatic eruptions are characterised by rising magma and thus, decreasing pressure. In contrast, the partial pressure of the dissolved gases increases until supersaturation is reached and the magma's temperature decreases while ascending. This leads to a crystallization of the melt and to a higher gas concentration. Hence, gas bubbles start growing, depending on magma viscosity, temperature, diffusivity, lithostatic pressure, volatile concentration and separation of bubbles in the melt. The bubbles lower the density of the mixture. As a consequence, the buoyancy increases and accelerates the rising melt. Simultaneously, the loss of volatiles increases

the viscosity of the melt, which counteracts the acceleration due to the higher buoyancy. An explosive eruption finally releases lava, tephra and gas by strong decompression. Phreatomagmatic eruptions occur when the magma comes in contact with water, and consequently, the rapid heat exchange leads to steam explosions and magma fragmentation. A famous example for this eruption type is the initial phase of the Eyjafjallajökull eruption in 2011, as magma melted the ice of the overlying glacier.
The third type of eruptions are phreatic eruptions, which take place when magma heats ground water or surface water that results in a steam explosion. In contrast to phreatomagmatic eruptions, phreatic eruptions eject no magmatic material, but fragments from surrounding rocks.
During the Eyjafjallajökull eruption in 2011, two eruption types took place. In the initial phase, a phreatomagmatic was triggerd, as magma melted the ice of the overlying glacier. Over time, it changed to a magmatic eruption, since no more water reached the vent (Dellino et al., 2012; Gudmundsson et al., 2012).
The viscosity of the magma determines whether an eruption is effusive or explosive. For a low-viscous magma, the eruption tends to be effusive. Some of the examples include the volcanoes on Hawaii or Stromboli. Volcanoes which have more viscous magma usually erupt more explosively. Large amounts of very fine ash is emitted by these eruptions to very high altitudes of several kilometers. These volcanic eruptions are capable of having global effects. Newhall and Self (1982) devised the so-called Volcanic Explosivity Index (VEI), in order to compare the explosiveness of different volcanic eruptions. The classification ranges between the weakest eruptions with VEI = 0 and the strongest with VEI = 8. It depends on the amount of erupted material, the height of the plume and duration of the eruption. For VEI ≥ 2, the scale is logarithmic, i.e. an increase of VEI by one equals an increase of the strength by 10.
This study focuses on the Raikoke eruption in 2019, which was a magmatic eruption with a VEI of 4 and a basaltic magma composition (McKee et al., 2021).

2.2. Dynamics and development of a volcanic plume

The total flux of tephra through the vent, which is generated by a volcanic eruption, is called mass eruption rate (MER). It is an important quantity to consider to investigate the plume development and determine the ash dispersion. Several approaches exist to calculate the MER, E_{tot} in kg/s. A simple empirical relationship (0th order) is given by Mastin et al. (2009):

$$E_{tot} = \left(\frac{1}{0.3535} H\right)^{\frac{1}{0.241}} \tag{2.1}$$

with the maximum plume height H in m. However, Mastin et al. (2009) neglects vent conditions (e.g. exit velocity, vent diameter) and atmospheric conditions. One-dimensional plume models such as Plumeria

(Mastin, 2007) or FPlume (Folch et al., 2016) consider these conditions and therefore, provide more detailed approaches. The MER by Folch et al. (2016) is calculated as

$$E_{tot} = \pi r_v^2 \overline{\rho} v_e \tag{2.2}$$

where r_v is the vent diameter in m, $\overline{\rho}$ is the density of the mixture at the vent in kg/m^3 and v_e denotes the exit velocity in m/s. With larger r_v and higher v_e, the MER increases.

More complex 3D plume models consider the whole plume volume and describe the fluid dynamics of the plume mixture. Therefore, they allow a more detailed investigation of the plume. Examples of 3D plume models are ATHAM (Oberhuber et al., 1998; Herzog et al., 2003) or ASHEE (Cerminara et al., 2016).

A volcanic eruption plume consists of three regions (Sparks et al., 1997), as shown in the schematic in figure 2.1.

During an eruption, a hot mixture of tephra and gases exits the vent at high velocities, thus, gaining high momentum. The lowest region is the jet region or gas thrust region. Here, the upward motion is driven by the remaining momentum of the mixture.

At higher altitudes, turbulent mixing entrains ambient air into the plume. The entrained air heats and expands and thereby, decreases the plume density. When the plume density becomes lower than that of the surrounding air, the plume becomes buoyant and rises due to convection. This forms the convective region. The level up to which the mixture ascends and cools until the plume density equals the density

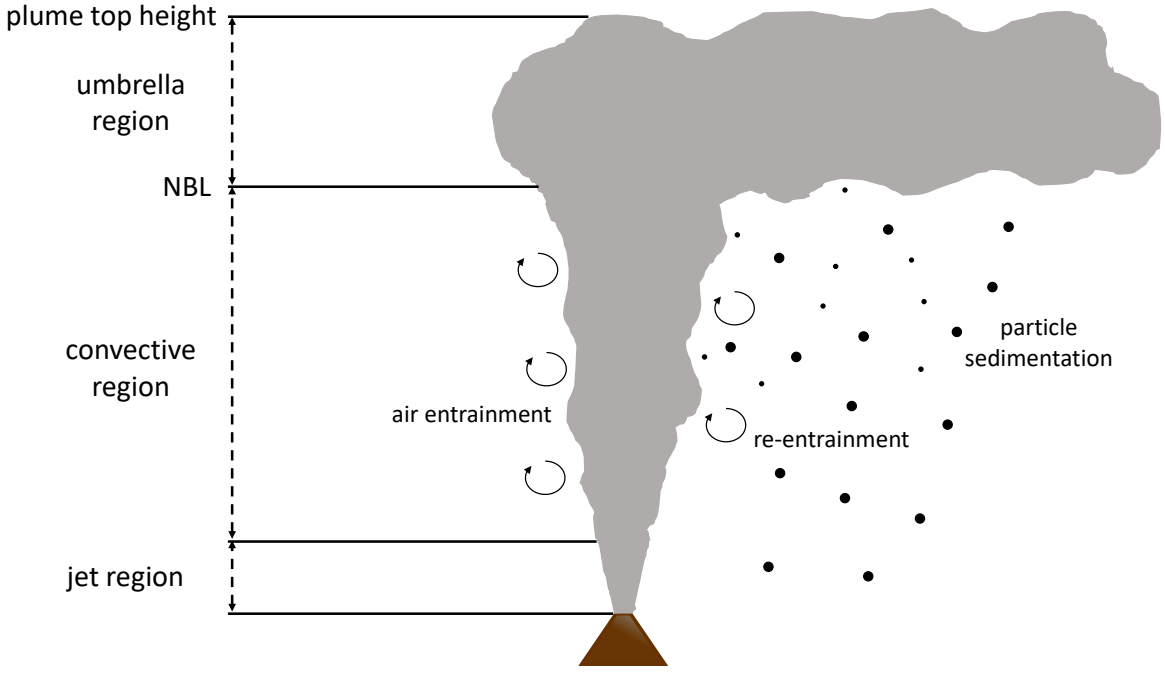

Figure 2.1.: Volcanic eruption plume with its plume regions. The lengths are not to scale.

of the ambient air is called the neutral buoyancy level (NBL). Above the NBL, the umbrella region or umbrella cloud develops. Here, the mixture rises to the plume top height due to overshooting (Sparks et al., 1997) and the plume spreads horizontally by wind and gravity waves (Costa et al., 2013).
Atmospheric conditions have a large impact on the plume development, in terms of influence by wind (Bursik, 2001) and air entrainment from the surrounding (Tate and Middleton, 2000; Carazzo et al., 2006; Carazzo et al., 2008). Strong horizontal winds lead to plume bending and a lower plume height. In contrast, high wind velocities enhance the vertical wind shear. Hence, the entrainment increases and therefore, the buoyancy. Moreover, warm or moist entrained air is less dense, which results in a lower plume density and in increased convection. Furthermore, during cloud development, latent heat is released due to water-phase changes, which heats the mixture and assists the plume to reach to higher altitudes (Woods, 1993).
If both the initial momentum and entrainment of ambient air near the vent are sufficient, they overcome the negative buoyancy of the mixture. However, if either one is insufficient, the negative buoyancy remains and the plume collapses either partially or completely. This results in a hazardous PDC (Degruyter, Wim and Bonadonna, Costanza, 2013).

2.3. Volcanic aerosols in the atmosphere

Aerosols of many different species occur in the atmosphere. Primary aerosols are emitted directly into the atmosphere. Some of these include sea salt from the ocean, mineral dust from deserts, pollen from plants or soot as a biomass burning aerosol. Secondary aerosols are not directly emitted, instead, precursor gases form the origin from which secondary aerosols are formed. Volcanoes emit ash as a primary aerosol during eruptions. In addition, they emit SO_2, that is oxidized to H_2SO_4. H_2SO_4 is a precursor gas for the production of sulfate aerosols, hence, these are secondary aerosols. For this work, very fine ash is the relevant aerosol species, as they remain airborne for several hours to days. The formation of secondary aerosols is neglected as chemical processes are not considered.
The size distributions of aerosols have a wide range from several nanometers to tens of microns (Whitby, 1978; Boucher, 2015). Depending on their diameter, the aerosol size distribution is divided into different modes. The Aitken mode comprises diameters from 0.01 μm to 0.1 μm, the accumulation mode from 0.1 μm to 1 μm, and the coarse mode from 1 μm to 10 μm. Boucher (2015) calls larger particles as supercoarse or Muser et al. (2020) defines them as giant mode particles. Freshly formed secondary aerosols are contained in the Aitken mode. In case of volcanic eruptions, the directly emitted volcanic ash is categorized into the accumulation, coarse and giant mode due to its larger diameter. Aerosol dynamical processes like nucleation, condensation, coagulation and sedimentation, modify the aerosol diameters and change the size distribution. Nucleation describes the transformation of matter from one phase to a new thermodynamically stable phase, which hasn't been there before. It forms particles in the Aitken mode. Due to coagulation and condensation, the particles grow and reach larger modes (Seinfeld

and Pandis, 2016). Condensation takes place when gaseous compounds like H_2SO_4 or H_2O condense onto surfaces of already existing aerosols. As the current work neglects the aerosol dynamical processes of nucleation and condensation, a more detailed description of the two can be found in Bruckert (2023). The following part explains coagulation and sedimentation in more detail.

The process when aerosol particles collide, stick together and form larger particles is called coagulation. The main driver for this process is the Brownian motion. It can also be caused by hydrodynamic, electrical, gravitational or other forces. Coagulation occurs especially when aerosol concentrations are large such as within volcanic plumes (Boucher, 2015). The number concentration of an aerosol mode decreases during coagulation as two particles form one larger particle. Hence, the median diameter in the corresponding mode is higher. In contrast, the mass concentration is constant, as the sum of mass of two coagulating particles is the same as that of the resulting large particle.

Sedimentation is a downward motion of aerosol particles. It depends on their size, shape and density, and it is larger for bigger particles (Seinfeld and Pandis, 2016). Abdelkader et al. (2017) and Muser et al. (2020) show that aerosol aging increases the sedimentation of aerosols, as it increases their size and/or changes their shape and density. Aerosol particles in the accumulation mode with a diameter of around 0.5 μm have the smallest sedimentation velocity. Thus, they stay in the atmosphere the longest (Boucher, 2015). As a consequence, particles in the accumulation mode tend to accumulate. Thereby, sedimentation acts as a sink for the number concentration, mass concentration and median diameter of a size distribution. This can have further effects in a volcanic plume. Coagulation of volcanic ash aerosols increases their size, thereby, increasing their sedimentation velocity. Enhanced sedimentation leads to enhanced removal of volcanic ash from the plume. Volcanic ash can act as CCN or IN, thus, modified amount of ash could alter their interaction with the surrounding air. Hence, sedimentation can have implications for the plume dispersion as well as the plume development.

2.4. Natural multicomponent multiphase flows

The atmosphere can be considered as a multicomponent multiphase system, consisting of dry air and water as the dominant components, which form the air mixture. Water occurs in all three phases like water vapor, liquid cloud droplets, rain drops and ice crystals. In case of volcanic eruptions, an additional dominant component of the air in the plume area is ash. The additional ash makes the total air mixture denser and affects the atmospheric dynamics, as described in the following part. Figure 2.2 shows a schematic about the dynamics of a mixture without ash and with ash. The temperature in the environment is assumed to be uniform in the whole region for both cases. Without ash, the density in the cloud ρ_1 is the sum of the partial density of dry air ρ_d and of water ρ_{H_2O}. The latter accounts for water in different phases. The surrounding only consists of dry air with $\rho_3 = \rho_d$. This results in a downward dynamical mass flux $\boldsymbol{F}_1^{dyn}$, as ρ_1 in the cloud is larger than ρ_3 in the surrounding. The mixture moves towards the ground. When reaching the ground, it moves horizontally. The cloud on the right side additionally con-

tains ash and thus, has a higher density ρ_2, compared to the cloud on the left side. Consequently, it leads to a higher dynamical mass flux $\boldsymbol{F}_2^{dyn}$, compared to $\boldsymbol{F}_1^{dyn}$, resulting in a higher vertical velocity. This generates a density current that moves horizontally when it reaches the ground. In nature, such density currents can be observed from time to time as PDCs during volcanic eruptions, which is explained in section 2.2. Figure 2.3 shows an example of a PDC during an eruption of Mount St. Helens. Considering ash in the total air mixture is mandatory for the correct simulation of a multicomponent multiphase flow like a volcanic eruption plume, as it can have an impact on the atmosphere and the plume development. This requires a source and sink of the total air mixture, when ash is emitted or deposits at the surface, respectively. However, this process has been neglected in previous simulations with numerical weather prediction models, as both source and sink of the total air mixture have been missing. This implies the missing contribution of the partial density of ash in the total density of the air mixture, which results in a lack of considering the dynamical effects due to ash. In the following chapters, this study addresses the gaps leading to the missing contribution of ash in the total air mixture and presents the implementations done to overcome this limitation.

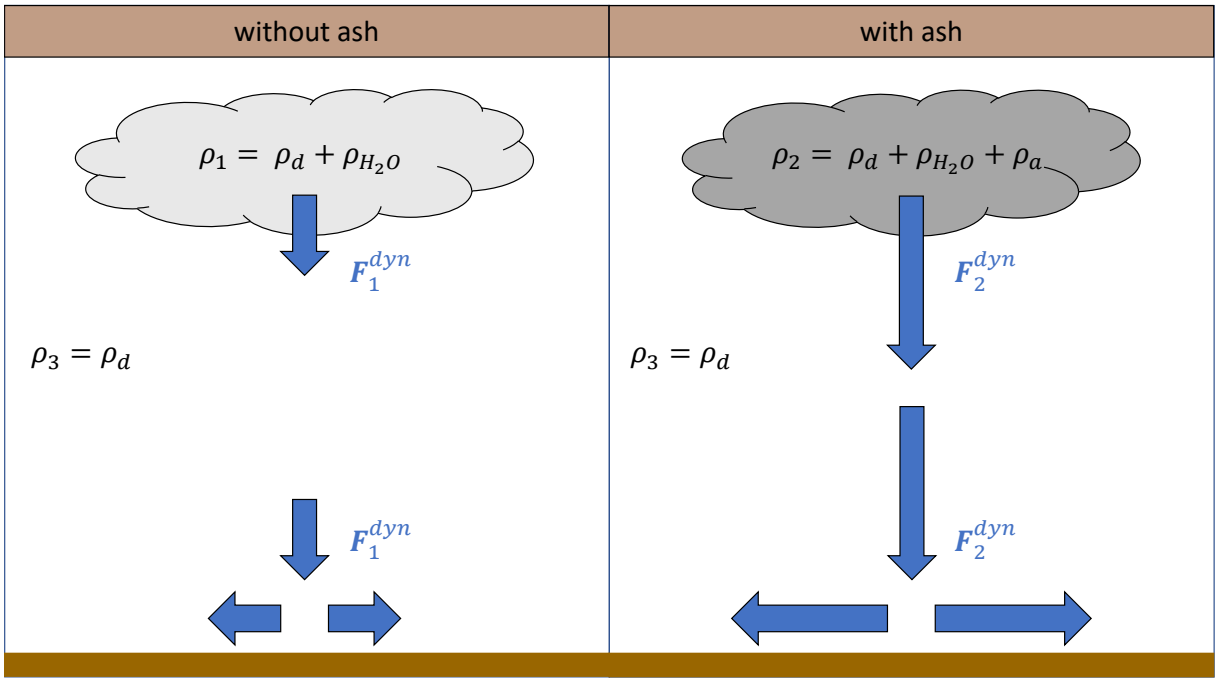

Figure 2.2.: Schematic showing the impact on atmospheric dynamics by ash being part of the total air mixture.

Figure 2.3.: Pyroclastic density current occurring during an eruption of Mount St. Helens. Source: United States Geological Survey (USGS, 1980).

3. The multicomponent multiphase model ICON-ART

When simulating a multicomponent multiphase flow with a numerical weather prediction model it is mandatory to consider the dominant components in the equation system of the model, as they form the total air mixture. This chapter starts with an introduction of how to mathematically handle multicomponent multiphase flows in numerical weather prediction models. It continues with an explanation of ICON with a focus on its dynamical core, followed by an introduction to the ART module. Lastly, it shortly presents how volcanic plumes were simulated in past approaches.

3.1. Multicomponent multiphase flows in atmospheric models

When simulating the atmosphere with a numerical atmospheric model, the formulation of an adequate equation set which takes into account the total mixture is essential.

3.1.1. The atmosphere in a barycentric framework

Each component of the total air mixture moves with its own specific velocity $\mathbf{v}_k$. An equation set for each component is computationally too expensive. For this purpose, a key point is the choice of a reference velocity. The reference velocity does not change the physical background, so it is arbitrary in general. However, the form of the resulting equation set depends on the reference velocity. An appropriate choice of a reference velocity for geophysical fluid systems like the atmosphere, is the barycentric velocity (mean mass weighted) which accounts for all contributing constituents (Wacker and Herbert, 2003; Wacker et al., 2006). The following equations are based on Wacker and Herbert (2003). The total density ρ of the mixture is the sum of the partial densities of all components k:

$$\rho = \sum_k \rho_k \tag{3.1}$$

ρ_k is solved by the continuity equation of constituent k:

$$\frac{\partial \rho_k}{\partial t} = -\nabla \cdot \mathbf{F}_k + \sigma_k \tag{3.2}$$

σ_k denotes the internal production rate and $\mathbf{F}_k$ is the specific mass flux of component k. The latter is defined as

$$\boldsymbol{F}_k = \rho_k \mathbf{v_k} \tag{3.3}$$

where $\mathbf{v}_k$ is the specific velocity of each component. The barycentric velocity $\mathbf{v}_b$ is the reference velocity of the whole system and defined as

$$\mathbf{v}_b = \frac{\sum_k \rho_k \mathbf{v_k}}{\rho}. \tag{3.4}$$

Each fraction $\frac{\rho_k}{\rho}$ denotes a weighting factor. In general, all specific velocities $\mathbf{v}_k$ and $\mathbf{v}_b$ are different. Hence, each component has an additional diffusion velocity $\mathbf{v}'_k$, which is relative to $\mathbf{v}_b$:

$$\mathbf{v}'_k = \mathbf{v}_k - \mathbf{v}_b \tag{3.5}$$

A corresponding diffusion flux for component k, relative to the barycentric motion, follows from the above:

$$\boldsymbol{J}_k = \boldsymbol{F}_k - \rho_k \mathbf{v}_b = \rho_k (\mathbf{v}_k - \mathbf{v}_b) = \rho_k \mathbf{v}'_k \tag{3.6}$$

Rearranging equation (3.5) and inserting it into equation (3.3) results in

$$\boldsymbol{F}_k = \rho_k \mathbf{v}_b + \rho_k \mathbf{v}'_k. \tag{3.7}$$

When inserting equation (3.6) into equation (3.7), equation (3.2) transforms to the continuity equation of constituent k in the barycentric framework:

$$\frac{\partial \rho_k}{\partial t} = -\nabla \cdot (\rho_k \mathbf{v}_b + \boldsymbol{J}_k) + \sigma_k \tag{3.8}$$

The continuity equation for the total air mixture is derived by summing up equation (3.8) over all constituents k. For this purpose, two conditions have to be satisfied. First, chemical reactions and transitions among the constituents have no impact on the total mass (Wacker and Herbert, 2003). Thus, summing up all σ_k gives

$$\sum_k \sigma_k = 0. \tag{3.9}$$

Secondly, independent of the dynamical situation, the total mixture has no diffusion fluxes as it represents all constituents as a whole. Therefore, equation (3.6) together with equation (3.4) show the validity of the condition

$$\sum_k \boldsymbol{J}_k = 0. \tag{3.10}$$

Finally, the resulting continuity equation for the total mixture is as follows:

$$\frac{\partial \rho}{\partial t} = -\nabla \cdot \rho \mathbf{v}_b \tag{3.11}$$

3.1.2. The mass budget treatment in a barycentric framework

An important part for the simulation of a multicomponent multiphase system is the correct treatment of the mass budget of the mixture. Thus, it is necessary to define suitable conditions for the upper and lower boundary of the system. The first corresponds to the top of the atmosphere and, the latter to the earth's surface. The upper boundary condition (UBC) is that no mass leaves the atmosphere to space. Corresponding to that, the atmosphere is a materially closed system. As for the earth's surface, the atmosphere is not a materially closed system. This means that during a volcanic eruption, the erupted mixture (especially ash) enters the atmospheric system. Moreover, evaporation transports water from the surface into the atmosphere. Ash and water condensates leave the atmospheric system through sedimentation and precipitation, respectively. These assumptions are handled in the lower boundary condition (LBC). The LBC is defined by a vertical velocity at the surface $w|_s$. For a physically reasonable LBC, the vertical velocity of a relevant component has to vanish (Wacker and Herbert, 2003):

$$w|_s = 0 \tag{3.12}$$

If $w|_s$ is the barycentric velocity of the total mixture, its net mass flux through the surface is zero. The form of equation (3.12) used as LBC neglects sources and sinks in the total mass budget. As water and ash are part of the mixture, a non-vanishing barycentric velocity at the surface is more appropriate, in order to account for sources and sinks in the total mass budget during emission, evaporation and sedimentation. Trace gases like CO_2 contribute to the mass of dry air. However, the contribution of external sources of dry air, e.g. volcanic eruptions or anthropogenic sources, are very small compared to the mass of dry air in the atmosphere. Thus, their contribution is negligible and the assumption is that the mass of dry air is constant. Hence, the surface is considered to be impermeable for dry air and its specific vertical velocity at the surface $w_d|_s$ is zero.

3.2. Multicomponent multiphase flows in the ICON model

For the investigation of volcanic eruptions, this study uses the ICON-ART model. ICON-ART is the combination of the ICOsahedral Non-hydrostatic (ICON) modeling framework (Zängl et al., 2015) and the Aerosols and Reactive Trace gases (ART) module (Rieger et al., 2015). It is jointly developed by the German Weather Service (DWD), the Max Planck Institute for Meteorology (MPI-M), the Institute of Meteorology and Cimate Research (IMK) at the Karlsruhe Institute of Technology (KIT) and the German Climate Computing Center (DKRZ). DWD uses ICON operationally as an NWP model. Moreover, it

can be applied for various scales ranging from local high-resolution large-eddy simulations (LES) to global climate simulations (Zängl et al., 2015; Heinze et al., 2017; Giorgetta et al., 2018).

3.2.1. The atmosphere in the barycentric framework in ICON

ICON solves the three-dimensional, non-hydrostatic and compressible Navier-Stokes equations on a global model domain. It uses an unstructured triangular grid with the base as an icosahedron which gives ICON its name. This icosahedron is divided into 20 equally sized triangles projected onto a sphere. Further refinements provide higher horizontal resolution resulting from two steps. The first step is Root Division (R) that divides the edges of the triangles into n equally sized parts. This is labeled by Rn. Thus, n^2 new triangles are created in each original one. The second step accomplishes k bisection (B) steps, denoted by Bk. It divides all newly formed triangles into 4 smaller equilateral triangles. This results in an RnBk grid (Zängl et al., 2015). The number of grid cells n_c, edges n_e, and vertices n_v are defined as

$$n_c = 20n^2k^4 \quad ; \quad n_e = 30n^2k^4 \quad ; \quad n_v = 10n^24^k + 2. \tag{3.13}$$

The effective grid size $\overline{\Delta x}$ is calculated as follows

$$\overline{\Delta x} = \sqrt{\overline{a_c}} = \sqrt{\frac{\pi}{5}}\frac{r_E}{n2^k} \tag{3.14}$$

with $\overline{a_c}$ as the mean grid cell area and r_E as the earth's radius (Zängl et al., 2015).
Among other things, this study focuses on ICON's dynamical core, a detailed description of which can be found in Zängl et al. (2015). The equation system in the model describes a multicomponent multiphase system which is mentioned in more detail in section 3.1. In ICON, the reference velocity is the barycentric velocity, which is introduced by equation (3.4). In the following, $\mathbf{v}_b$ is denoted as $\mathbf{v}$. Moreover, the Hesselberg-averaging (Hesselberg, 1926) is applied to solve the basic non-hydrostatic equations. It decomposes a variable ϕ into a density-weighted mean (barycentric mean) $\hat{\phi}$ and a deviation ϕ'':

$$\phi = \hat{\phi} + \phi'' \tag{3.15}$$

Finally, the Hesselberg-averaged equation system is based on the suggested prognostic variables by Gassmann and Herzog (2008) and has the following form:

$$\frac{\partial \hat{v}_n}{\partial t} + \frac{\partial \hat{K}_n}{\partial n} + \left(\hat{\zeta} + f\right)\hat{v}_t + \hat{w}\frac{\partial \hat{v}_n}{\partial z} = -c_{pd}\hat{\theta}_v\frac{\partial \overline{\pi}}{\partial n} - D_{\hat{v}_n} \tag{3.16}$$

$$\frac{\partial \hat{w}}{\partial t} + \hat{v}_h \cdot \nabla\hat{w} + \hat{w}\frac{\partial \hat{w}}{\partial t} = -c_{pd}\hat{\theta}_v\frac{\partial \overline{\pi}}{\partial z} - g - D_{\hat{w}} \tag{3.17}$$

$$\frac{\partial \overline{\rho}\hat{\theta}_v}{\partial t} + \nabla \cdot \left(\overline{\rho}\hat{\mathbf{v}}\hat{\theta}_v\right) = \overline{Q} - D_{\hat{\theta}_v} \tag{3.18}$$

$$\frac{\partial \overline{\rho}}{\partial t} + \nabla \cdot (\overline{\rho}\hat{\mathbf{v}}) = 0 \tag{3.19}$$

$$\frac{\partial \overline{\rho}\hat{q}_k}{\partial t} + \nabla \cdot (\overline{\rho}\hat{q}_k\hat{\mathbf{v}}) = -\nabla \cdot \left(\overline{J}_k^z \boldsymbol{k} + \overline{\rho q_k'' \mathbf{v}''}\right) + \overline{\sigma}_k \tag{3.20}$$

with $\overline{\pi}$ as the Exner function:

$$\overline{\pi} = \left(\frac{R_d \overline{\rho}\hat{\theta}_v}{p_{00}}\right)^{\frac{R_d}{c_{vd}}} \tag{3.21}$$

Equation (3.16) and (3.17) are the momentum equations in horizontal and vertical direction, respectively. In addition, equation (3.18) is the first law of thermodynamics, equation (3.19) is the continuity equation for the total air mixture and equation (3.20) is the continuity equation for constituent k. The prognostic variables solved by the equation system include the horizontal wind velocity normal to the triangle edges $\hat{v}_n$, the wind velocity in vertical direction $\hat{w}$, the virtual potential temperature $\hat{\theta}_v$, the density of the total air mixture $\overline{\rho}$, and the mass fraction for the included constituents in the total air mixture $\hat{q}_k$ via the tracer equation. Furthermore, the wind velocity tangential to the edges is v_t, so that (v_n, v_t, w) form a right-handed trihedron. Moreover, $\frac{\partial}{\partial n}$ is the horizontal derivative in edge-normal direction, $\hat{K}_h = \frac{1}{2}\left(v_n^2 + v_t^2\right)$ is the horizontal component of the kinetic energy, $\hat{\zeta}$ is the vertical component of the relative vorticity, and f is the Coriolis parameter. Furthermore, g is the gravitational constant, c_{pd}/c_{vd} is the specific heat capacity for dry air at constant pressure/volume, R_d the specific gas constant of dry air, and $\overline{Q}$ is the diabatic heat source. As for equations (3.16) and (3.17), $D_{\hat{v}_n}$ and $D_{\hat{w}}$ denote the turbulent diffusion fluxes of the momentum in horizontal and vertical direction, respectively, and $D_{\hat{\theta}_v}$ in equation (3.18) are turbulent diffusion fluxes of $\hat{\theta}_v$. The variable $\overline{J}_k^z$ is the vertical diffusion flux for constituent k, which is a flux relative to the advective flux $\overline{\rho}\hat{q}_k\hat{\mathbf{v}}$, and $\overline{\rho q_k'' \mathbf{v}''}$ is the turbulent diffusion flux of the k-th partial mass fraction. Internal conversion among different phases or particles is denoted by $\overline{\sigma}_k$. Table 3.1 shows the specific constituents of the air mixture in ICON.

Similar to equation (3.1), the density of the total air mixture $\overline{\rho}$ is the sum of the partial density of all constituents:

$$\overline{\rho} = \sum_k \overline{\rho}_k \tag{3.22}$$

Table 3.1.: Constituents of the air mixture in ICON

$k = d$	dry air
$k = v$	water vapor
$k = c$	cloud water
$k = i$	cloud ice
$k = r$	rain
$k = s$	snow
$k = g$	graupel

The mass fraction of constituent k is defined as

$$\hat{q}_k = \frac{\hat{\rho}_k}{\overline{\rho}}. \tag{3.23}$$

Note that there is no prognostic equation for the mass fraction of dry air $\hat{q}_d$ as it is a diagnostic variable. Given that the prognostic equation for $\overline{\rho}$ and all mass fractions except for dry air are solved, $\hat{q}_d$ can be diagnosed. Using equations (3.22) and (3.23) it follows that:

$$\hat{q}_d = 1 - \sum_{k \neq d} \hat{q}_k \tag{3.24}$$

The continuity equation in equation 3.19 is the sum of equation (3.20) over all constituents k. Consequently, it follows that

$$\sum_k \overline{J}_k^z = 0 \quad ; \quad \sum_k \overline{\rho q_k'' \mathbf{v}''} = 0. \tag{3.25}$$

3.2.2. The mass budget treatment in ICON

This part describes how the mass budget in ICON is currently handled. The recent form of equation (3.19) neither accounts for mass loss due to sedimentation/precipitation, nor mass gain due to evaporation. In addition, the LBC in equation (3.12) is the barycentric velocity of the total mixture with $\hat{w}|_s = 0$. Consequently, the atmosphere is a closed system with relation to the mass of the total air mixture m_{total}. Furthermore, the diffusion flux from equation (3.20) at the surface $\overline{J}_k^z|_s$ is separated into water vapor, non-precipitating and precipitating constituents as

$$\overline{J}_k^z|_s = \begin{cases} \overline{E}_v - (\overline{\rho}_k \hat{w})\,|_s & k \equiv v \\ -(\overline{\rho}\hat{q}_k \hat{w})\,|_s & \text{non-precipitating} \\ -\overline{S}_k|_s & \text{precipitating/depositing} \end{cases} \tag{3.26}$$

with the evaporation flux $\overline{E}_v = \left(\overline{\rho q_v'' \mathbf{v}''}\right)|_s$ and sedimentation flux $\overline{S}_k|_s$. These are a source term for water vapor and a sink term for rain, snow, and graupel, respectively. To hold equation (3.19) true, it

is assumed that a fictitious flux of dry air through the surface compensates the mass gain and loss due to evaporation/emission and sedimentation, respectively. That results in a constant m_{total} and a variable mass of dry air m_d and hence, in neglected impacts on the dynamics.

3.3. The ART module

The ART module simulates the interaction between aerosols, trace gases, and the atmosphere (Rieger et al., 2015). It was already used for ICON-ART's predecessor COnsortium for Small-scale MOdeling (COSMO)-ART (Bangert et al., 2011) and extends ICON by inclusion of emission and transport of aerosols and trace gases, aerosol dynamics and gas-phase chemistry for the troposphere and stratosphere (Rieger et al., 2015; Weimer et al., 2017; Schröter et al., 2018). A transport equation needs to be solved for each aerosol or chemical tracer. By applying the Hesselberg averaging, the basic equations are

$$\frac{\hat{d}}{dt} = \frac{\partial}{\partial t} + \hat{\mathbf{v}} \cdot \nabla \tag{3.27}$$

and

$$\frac{\hat{d}\overline{\rho}}{dt} = -\overline{\rho}\nabla \cdot \hat{\mathbf{v}} \tag{3.28}$$

with the barycentric velocity $\hat{\mathbf{v}}$. Equation (3.27) is the total time derivative and equation (3.28) is the continuity equation.

For a gaseous species l, the Hesselberg-averaged mass mixing ratio $\hat{\Psi}_{g,l}$ is the ratio of its partial density $\overline{\rho_l}$ and the total air density $\overline{\rho}$:

$$\hat{\Psi}_{g,l} = \frac{\overline{\rho \frac{\rho_l}{\rho}}}{\overline{\rho}} = \frac{\overline{\rho_l}}{\overline{\rho}} \tag{3.29}$$

The temporal and spatial evolution of gas l is formulated in flux-form as follows:

$$\frac{\partial \overline{\rho}\hat{\Psi}_{g,l}}{\partial t} = -\nabla \cdot \left(\hat{\mathbf{v}}\overline{\rho}\hat{\Psi}_{g,l}\right) - \nabla \left(\overline{\rho \mathbf{v}'' \Psi''_{g,l}}\right) + P_l - L_l + E_l \tag{3.30}$$

The first term on the right hand side of equation (3.30) describes the flux divergence in horizontal and vertical direction and the second term describes changes due to turbulent fluxes. P_l is the chemical production rate, L_l is the loss and E_l is the emission rate of gas l.
For aerosols, multiple size modes represent the size distribution, while the latter follows a log-normal distribution. A two-moment scheme is applied for all modes. That implies that two prognostic variables, the number concentration and the mass mixing ratio, are transported for each mode.

An aerosol of mode l is represented by the Hesselberg-averaged number concentration $\hat{\Psi}_{0,l}$ as zeroth moment and mass mixing ratio $\hat{\Psi}_{3,l}$ as third moment

$$\hat{\Psi}_{0,l} = \frac{\overline{\rho \frac{N_l}{\rho}}}{\overline{\rho}} = \frac{\overline{N_l}}{\overline{\rho}} \tag{3.31}$$

$$\hat{\Psi}_{3,l} = \frac{\overline{\rho \frac{M_l}{\rho}}}{\overline{\rho}} = \frac{\overline{M_l}}{\overline{\rho}} \tag{3.32}$$

where N_l denotes the number concentration and M_l is the mass concentration. The log-normal distribution for the mass specific number distribution $\hat{\psi}_{0,l}$ and mass mixing ratio $\hat{\psi}_{3,l}$ are functions of the aerosol diameter d_p and are calculated as

$$\hat{\psi}_{0,l}(d_p) = \frac{\hat{\Psi}_{0,l}}{\sqrt{2\pi}\ln\sigma_l} \cdot \exp\left(-\frac{(\ln d_p - \ln d_{0,l})^2}{2\ln^2\sigma_l}\right) \tag{3.33}$$

and

$$\hat{\psi}_{3,l}(d_p) = \frac{\hat{\Psi}_{3,l}}{\sqrt{2\pi}\ln\sigma_l} \cdot \exp\left(-\frac{(\ln d_p - \ln d_{3,l})^2}{2\ln^2\sigma_l}\right) \tag{3.34}$$

where $d_{0,l}$ and $d_{3,l}$ are the median diameters for $\hat{\psi}_{0,l}$ and $\hat{\psi}_{3,l}$, respectively and σ_l is the standard deviation. These are the size parameters of the log-normal distribution. During a simulation, σ_l remains constant. Thereby, $d_{0,l}$ is given as follows:

$$d_{0,l} = \sqrt[3]{\frac{\hat{\Psi}_{3,l}}{\frac{\pi}{6}\rho_p \cdot \exp\left(\frac{9}{2}\ln^2\sigma_l\right) \cdot \hat{\Psi}_{0,l}}} \tag{3.35}$$

With the aerosol density ρ_p. The median diameter of $\hat{\psi}_{3,l}$ is calculated using

$$\ln d_{3,l} = \ln d_{0,l} + 3\ln^2\sigma_l. \tag{3.36}$$

Finally, the transport equations in flux-form for $\hat{\psi}_{0,l}$ and $\hat{\psi}_{3,l}$ are defined as

$$\begin{aligned}\frac{\partial \overline{\rho}\hat{\Psi}_{0,l}}{\partial t} =& -\nabla\cdot\left(\hat{\mathbf{v}}\overline{\rho}\hat{\Psi}_{0,l}\right) - \nabla\cdot\left(\overline{\mathbf{v}''\rho\hat{\Psi}''_{0,l}}\right) - \frac{\partial}{\partial z}\left(v_{sed,0,l}\overline{\rho}\hat{\Psi}_{0,l}\right) \\ & - W_{0,l} - Ca_{0,l} + Nu_{0,l} + E_{0,l}\end{aligned} \tag{3.37}$$

and

$$\begin{aligned}\frac{\partial \overline{\rho}\hat{\Psi}_{3,l}}{\partial t} = &-\nabla\cdot\left(\hat{\mathbf{v}}\overline{\rho}\hat{\Psi}_{3,l}\right)-\nabla\cdot\left(\overline{\mathbf{v}''\rho\hat{\Psi}''_{3,l}}\right)-\frac{\partial}{\partial z}\left(v_{sed,3,l}\overline{\rho}\hat{\Psi}_{3,l}\right)\\ &-W_{3,l}-Ca_{3,l}+Nu_{3,l}+Co_{3,l}+E_{3,l}.\end{aligned} \tag{3.38}$$

Advective and turbulent fluxes for the k-th moment are described by $\hat{\mathbf{v}}\overline{\rho}\hat{\Psi}_{k,l}$ and $\overline{\mathbf{v}''\rho\hat{\Psi}''_{k,l}}$, respectively. Furthermore, $v_{sed,k,l}\overline{\rho}\hat{\Psi}_{k,l}$ is the sedimentation flux with sedimentation velocity $v_{sed,k,l}$. The former is denoted as $\overline{S}_{k,l}$ in the following and both $\overline{S}_{k,l}$ and $v_{sed,k,l}$ only have a vertical component. $W_{k,l}$ represents the aerosol removal due to wet deposition and $Ca_{k,l}$ is the coagulation. The latter is a particle growth process and leads to new formed particles. Nucleation $Nu_{k,l}$ describes the formation of new particles and is only considered for the *Aitken* mode. Condensation of gaseous compounds onto particles $Co_{3,l}$ is a source term only accounted for the third moment. At last, $E_{k,l}$ denotes the emission.
As this study neglects $Nu_{k,l}$ and $Co_{3,l}$, a detailed description can be found in Kerminen and Wexler (1995) for the former and, in Whitby (1978) and Riemer (2002) for the latter. More details about the advective flux and the turbulent flux are explained in Rieger et al. (2015) and Rieger (2017), respectively. The following describes the parameterization of $v_{sed,k,l}$ and $Ca_{k,l}$ in more detail.

3.3.1. Sedimentation of aerosols

The parameterization of $v_{sed,k,l}$ follows the definition from the works provided by e.g. Binkowski and Shankar (1995), Riemer (2002), and references therein. $v_{sed,k,l}$ depends on the aerosol size and is given by Stokes Law with Cunningham slip correction C_c (Seinfeld and Pandis, 2016):

$$v_{sed,k,l}\left(d_{0,l}\right) = \frac{gC_c\rho_p}{18\nu_{air}\overline{\rho}}d_{0,l}^2 \tag{3.39}$$

The gravitational constant is denoted by g and ν_{air} is the kinematic viscosity of air. For C_c the linearized form is used:

$$C_c = 1.0 + 1.246\frac{2\lambda_{air}}{d_{0,l}} \tag{3.40}$$

The mean free path of air is denoted by λ_{air}. By integrating over the log-normal distribution of the particles the sedimentation velocities $v_{sed,0,l}$ and $v_{sed,3,l}$ are defined as (Kramm et al., 1992):

$$v_{sed,0,l} = \frac{g\rho_p}{18\nu_{air}\overline{\rho}}d_{0,l}^2\left[\exp\left(2\ln^2\sigma_l\right)+1.246\cdot\frac{2\lambda_{air}}{d_{0,l}}\cdot\exp\left(\frac{1}{2}\ln^2\sigma_l\right)\right] \tag{3.41}$$

$$v_{sed,3,l} = \frac{g\rho_p}{18\nu_{air}\overline{\rho}}d_{0,l}^2\left[\exp\left(8\ln^2\sigma_l\right)+1.246\cdot\frac{2\lambda_{air}}{d_{0,l}}\cdot\exp\left(\frac{7}{2}\ln^2\sigma_l\right)\right] \tag{3.42}$$

Larger particles have larger $v_{sed,k,l}$, which leads to a shift of the size distribution to smaller diameters (Rieger, 2017).

3.3.2. Coagulation of aerosols

Particles grow due to coagulation with particles of their own species. At the same time the number concentration decreases. Riemer (2002) and references therein described the parameterization of the terms $Ca_{0,l}$ and $Ca_{3,l}$ in equation (3.37) and equation (3.38). Muser (2022) applied the parameterization in ICON-ART. Coagulation is distinguished between intra- and inter-modal. The former considers particles of the same mode i and the resulting particles remain in i. Inter-modal coagulation takes into account particles of different modes i and j. Here, both particles are assigned to the mode with the larger particle diameter (Muser, 2022). ICON-ART allows the coagulation of insoluble, soluble and mixed particles. As the current work only considers insoluble particles, the following part neglects soluble and mixed particles. The coagulation rate for the zeroth and third moment are given by

$$Ca_{0,i} = Ca_{0,ii} + Ca_{0,ij}, \tag{3.43}$$

$$Ca_{3,i} = Ca_{3,ij}. \tag{3.44}$$

The terms $Ca_{0,ii}$ and $Ca_{0,ij}$ describe the intra-modal and inter-modal coagulation rate of the k-th moment, respectively. For intra-modal coagulation, the zeroth moment of the size distribution decreases, while the third moment stays the same. Depending on the sizes of mode i and j, inter-modal coagulation either reduces, increases or does not change both the zeroth and third moment. When a large mode coagulates with a small mode, the zeroth moment of the large mode remains the same, whereas the third moment increases. Both moments of the smaller mode decrease. In a system with two modes, i and j, the equation for the coagulation rate consists of (Whitby, 1978)

$$\tilde{C}a_{0,ii} = \frac{1}{2}\int_0^\infty \int_0^\infty \beta\left(d_1, d_2\right) \psi_{0,i}\left(d_1\right) \psi_{0,i}\left(d_2\right) \mathrm{d}d_1 \mathrm{d}d_2, \tag{3.45}$$

$$\tilde{C}a_{0,ij} = \int_0^\infty \int_0^\infty \beta\left(d_1, d_2\right) \psi_{0,i}\left(d_1\right) \psi_{0,i}\left(d_2\right) \mathrm{d}d_1 \mathrm{d}d_2, \tag{3.46}$$

$$\tilde{C}a_{3,ij} = \int_0^\infty \int_0^\infty d_1^3 \beta\left(d_1, d_2\right) \psi_{0,i}\left(d_1\right) \psi_{0,i}\left(d_2\right) \mathrm{d}d_1 \mathrm{d}d_2. \tag{3.47}$$

The coagulation coefficient β depends on the sizes of the included particles. Usually only numerical solutions exist for all sizes of β. Whitby (1978) however, solves the integrals in equation (3.45) to (3.47) analytically for the near-continuum and free-molecular regime. They apply a harmonic mean, that gives

an expression for the full size range. Whitby (1978), Riemer (2002) and Muser (2022) present a detailed derivation of the solutions. The harmonic means for the inter-modal coagulation are defined as

$$\tilde{C}a_{0,ij} = \frac{\tilde{C}a^{nc}_{0,ij}\tilde{C}a^{fm}_{0,ij}}{\tilde{C}a^{nc}_{0,ij} + \tilde{C}a^{fm}_{0,ij}}, \tag{3.48}$$

$$\tilde{C}a_{3,ij} = \frac{\tilde{C}a^{nc}_{3,ij}\tilde{C}a^{fm}_{3,ij}}{\tilde{C}a^{nc}_{3,ij} + \tilde{C}a^{fm}_{3,ij}}. \tag{3.49}$$

The coagulation rates of the k-th moment for the near continuum and free molecular regime are depicted by $\tilde{C}a^{nc}_{k,ij}$ and $\tilde{C}a^{fm}_{k,ij}$, respectively. For intra-modal coagulation, the derivation of the solution of $\tilde{C}a_{0,ii}$ follows in an analogous manner. To determine the coagulation rates $Ca_{0,i}$ and $Ca_{3,i}$, the harmonic means are inserted into equations (3.45) to (3.47).

In ICON-ART, the coagulation rate of the k-th moment $\tilde{C}a_{k,l}$ is converted to the coagulation rate for the mass mixing ratio $Ca_{0,l}$ and for the number mixing ratio $Ca_{3,l}$, respectively, with

$$Ca_{0,l} = \frac{\tilde{C}a_{0,l}}{\rho} \tag{3.50}$$

and

$$Ca_{3,l} = \frac{\rho_{p,l}\tilde{C}a_{3,l}}{\rho}. \tag{3.51}$$

4. Simulations of volcanic eruption plumes with ICON-ART

This chapter first introduces how volcanic eruption plumes were simulated in past approaches with their corresponding limitations in ICON-ART. Afterwards, it presents the implementations to enable the explicit simulation of a volcanic eruption plume.

4.1. Earlier approaches for simulating volcanic plumes with ICON-ART

After the eruption of Eyjafjallajökull in 2010, the simulation of volcanic eruptions attracted huge attention, as it led to many problems especially for aviation. Therefore, Rieger et al. (2015) developed an approach for simulating the volcanic plume with ICON-ART for that specific case. Since then, the approach has been used for previous simulations. It is based on the simple empirical relationship by Mastin et al. (2009), shown by equation (2.1) in section 2.2, to calculate the total MER E_{tot}. Afterwards, E_{tot} is multiplied by a factor, only considering very fine ash. The mass is then distributed to the three modes, accumulation, coarse and giant and emitted using a Gaussian profile, which is given by

$$f_e(z^*) = 0.0076 + 0.9724 \cdot \exp\left(-\left(\frac{z^* - 0.4481}{0.3078}\right)^2\right) \tag{4.1}$$

where $z^* = \frac{z}{H}$ is the normalized plume height. Finally, the vertical emission profile is calculated. This is achieved by integrating equation (4.1), which is normalized afterwards. Hence, discrete point sources along each model layer between the bottom and top height of the plume are defined by the use of:

$$E(z^*) = E_{tot} \frac{f_e(z^*)}{\int_0^1 f_e(z^*)\, dz} \tag{4.2}$$

Moreover, Muser et al. (2020) simulated the Raikoke eruption in 2019 by applying a predefined vertical emission profile. Bruckert et al. (2022) coupled FPlume with ICON-ART to simulate the Raikoke eruption, which provided a more accurate emission profile and improved the results.
However, these approaches neglect the effect of the exit velocity and exit temperature on the dynamics. Moreover, ash is neglected in the total air mixture due to the limitations mentioned in section 3.2.2 that also exist for emission of ash (source) and the sedimentation of ash at the surface (sink). Hence, the plume is not considered as a multicomponent multiphase flow and both dynamical effects and microphysical processes like cloud development triggered by the eruption are not taken into account. The plume development depends on these processes in the initial state. Therefore, an investigation of the

plume development from the source to the maximum plume height is required, considering microphysical processes due to the eruption and ash as part of the total air mixture. This is achieved by explicit simulations of volcanic eruption plumes.

4.2. New implementations to enable explicit simulations of volcanic plumes with ICON-ART

The following part focuses on the implementations applied for this study, which are necessary to enable explicit simulations of volcanic plumes.

The mass conservation of the total air mixture explained in section 3.2.2 is decent to be considered for the case of NWP, as evaporation or precipitation usually affect the total air mass m_{total} to a minor extent within few days. However, explosive volcanic eruptions emit very large amounts of ash and other constituents into the atmosphere. This additional mass coming from the emitted mixture affects the atmospheric dynamics in the plume region and nearby and needs to be accounted for in numerical simulations of the plume development and its dispersion. Therefore, the conservation of m_{total} is not accurate, whereas, m_d should be conserved as it only consists of gases like nitrogen (N_2) and oxygen (O_2). To address this, a modified LBC is implemented to account for a sink for m_{total} upon deposition of ash. Besides, a source for m_{total} is implemented to account for the mass input for the total air mixture during the emission of ash. These implementations allow the consideration of the mass of ash m_a in m_{total}, which results in ash affecting the atmospheric dynamics.

Moreover, a single point source in the lowest model layer at the vent location emits the mixture, instead of using a vertical emission profile like in previous simulations, e.g. of Rieger (2017) or Muser et al. (2020) (see section 4.1). The source conditions include exit velocity and exit temperature which during an explosive eruption lead to a strong updraft which lifts the total air mixture (emitted constituents and surrounding air) to higher altitudes.

4.2.1. Mass source for the total air mixture

For the simulation of a volcanic eruption, a single point source in the lowest model layer emits ash of mode l via $E_{3,l}$ (in the following $l \equiv a$) from equation (3.38) and volcanogenic water vapor via E_l (in the following $l \equiv v$) from equation (3.30) (Rieger et al., 2015):

$$E_{3,a} = \frac{E_{tot} \cdot f_a}{V} \cdot f_{lrt} \tag{4.3}$$

$$E_v = \frac{E_{tot} \cdot f_v}{V} \tag{4.4}$$

The grid cell volume in m^3 is denoted by V. The factor f_a and f_v are the distribution factors, i.e. the fraction of emitted ash mode l and water vapor, respectively, and f_{lrt} is the factor of emitted ash, which

is available for long-range transport. $E_{3,a}$ is added to the already existing mass mixing ratio of ash mode a $\hat{q}_a$ and accordingly E_v to already present water vapor $\hat{q}_v$ in the grid cell, where the emission takes place via

$$\hat{q}_a(t+dt) = \hat{q}_a(t) + E_{3,a} \cdot \frac{dt}{\overline{\rho}} \tag{4.5}$$

$$\hat{q}_v(t+dt) = \hat{q}_v(t) + E_v \cdot \frac{dt}{\overline{\rho}} \tag{4.6}$$

with t as current model time step in seconds. Moreover, equation (4.5) and equation (4.6) are used for the mass source of m_{total}. This is achieved by multiplying dt by the sum of all emitted species and adding it to $\overline{\rho}$ afterwards:

$$\overline{\rho}(t+dt) = \overline{\rho}(t) + \overline{\rho}(t) \cdot dt \left(\sum_a E_{3,a} + E_v \right) \tag{4.7}$$

This results in a source for m_{total} due to the emission of volcanic ash.

4.2.2. Mass sink for the total air mixture

For simplicity, this part only focuses on dry air and ash. In equations (3.37) and (3.38), the sedimentation flux $\overline{S}_{k,l}$ at the surface is a sink term for when ash deposits. To consider this sink for the total air mixture as well, the LBC from equation (3.12) is modified. Note that the additional $|_s$ stands for surface. Using the vertical component of the Hesselberg-averaged form of $\boldsymbol{v}$ in equation (3.4), the equation is defined as

$$\hat{w}|_s = \frac{\overline{\rho}\hat{q}_d\hat{w}_d + \overline{\rho}\hat{q}_a\hat{w}_a}{\overline{\rho}}|_s \tag{4.8}$$

with the mass mixing ratio of dry air $\hat{q}_d|_s$ and of ash in mode a $\hat{q}_a|_s$. Furthermore, $\hat{w}_d|_s$ and $\hat{w}_a|_s$ denote the specific velocity of dry air and ash in mode a, respectively. For the modification of equation (3.4) the following assumptions are made. First, the surface is impermeable for dry air, which leads to $\hat{w}_d|_s = 0$. Secondly, ash deposits at the surface and leaves the atmospheric system, resulting in $\hat{w}_a|_s < 0$. The latter can be written as the sum of $\hat{w}|_s$ and its deviation $\hat{w}'_a|_s$, which is the sedimentation velocity that is introduced in equation (3.38) as $v_{sed,3,a}$. Moreover, $v_{sed,3,a}$ only has a vertical component, so it can be written as $w_{sed,3,a}$. Consequently, $\hat{w}_a|_s$ is calculated as

$$\hat{w}_a|_s = \hat{w}|_s + \hat{w}'_a|_s = \hat{w}|_s + \hat{w}_{sed,3,a}|_s. \tag{4.9}$$

The sedimentation flux of ash $\overline{S}_{3,a}|_s$ is given by

$$\overline{S}_{3,a}|_s = \left(\overline{\rho}\hat{q}_a\hat{w}'_a\right)|_s. \tag{4.10}$$

This can be rearranged to

$$\hat{w}'_a|_s = \frac{\overline{S}_a}{\overline{\rho}\hat{q}_a}|_s \tag{4.11}$$

which can be inserted into equation (4.9) and into equation (4.8) afterwards. Finally, by summing up over all ash modes a the derived modified lower boundary condition is defined as

$$\hat{w}|_s = \frac{-\sum_a \overline{S}_a}{\overline{\rho} - \overline{\rho}\sum_a \hat{q}_a}|_s = \frac{-\sum_a \overline{S}_a}{\overline{\rho}\hat{q}_d}|_s. \tag{4.12}$$

This lower boundary condition serves as a sink for m_{total} as soon as ash deposits at the surface.
The scope of this work only focuses on the impact of emission of ash and volcanogenic water vapor, as well as on the impact of deposition of ash on the mass budget of the total mixture. When accounting for a source of the total air mixture by evaporation or a sink by precipitation, the system becomes more complex. As both water vapor and water condensates are part of the total mixture, evaporation and precipitation should act as a source and sink for the total mixture, respectively. For further information, Wacker and Herbert (2003) and Wacker et al. (2006) provide a more detailed description of the challenges encountered during these considerations. However, the contribution of evaporation and precipitation on the mass budget of the total mixture is small in the current application. Therefore, considering their impact on the mass budget of the total mixture is beyond the scope of this study.

4.2.3. Momentum and heat source during volcanic eruptions

Instead of using a vertical emission profile, in this work, the emitted mixture is transported from a point source located at the lowermost model layer to higher altitudes by a strong updraft due to a momentum and heat source. The vertical velocity $\hat{w}$ and the virtual potential temperature $\hat{\theta}_v$ have fixed values during an eruption. They are used to modulate the momentum and heat source. In the following, when referring to the exit velocity and exit temperature at the source, they are denoted as $\hat{w}_e$ and $\hat{\theta}_{v,e}$, respectively. Note that $\hat{\theta}_{v,e}$ does not directly represent the magma temperature, which is used for an exit temperature at the vent in plume models like FPlume or ATHAM. The magma temperature is indirectly accounted for in $\hat{\theta}_{v,e}$. Besides, the heat capacity c_p in ICON-ART only accounts for that of dry air. Ash and other constituents are not included. Moreover, the lowest model layer is not at the surface but an intermediate level above, which depends on the vertical resolution. That is why $\hat{\theta}_{v,e}$ is a rough estimation for the heat source to consider the hot mixture. Because of the high momentum and temperature which are typical of volcanic eruptions, the values used for $\hat{w}_e$ and $\hat{\theta}_{v,e}$ are much higher compared to usual values occurring in numerical weather prediction. For NWP models like ICON-ART, sudden changes of $\hat{w}$ or $\hat{\theta}_v$ to very high values lead to high instabilities or model crashes, as high discrepancies develop between neighbouring grid cells resulting in strong gradients. To overcome this problem, a spin-up phase is implemented. It starts at an arbitrary time before the actual eruption and $\hat{w}_e$ and $\hat{\theta}_{v,e}$ increase linearly by a factor f_{sp} from

their background value at the beginning of the spin-up to their maximum value, when the spin-up phase ends and the actual eruption starts. The increase depends on the model time step dt and the duration of the spin-up phase t_{sp} in seconds. Thereby, the gradients can adjust slowly and the model runs stably. Factor f_{sp} is calculated as

$$f_{sp} = \frac{T_{now} - T_{sp,start}}{t_{sp}} \tag{4.13}$$

with both the current time T_{now}, which implies dt, and the start of the spin-up phase $T_{sp,start}$ in seconds relative to 00:00 UTC. The linear increase of $\hat{w}_e$ and $\hat{\theta}_{v,e}$ is attained by multiplying both by f_{sp}:

$$\hat{w}_e\,(t+dt) = \hat{w}_e\,(t) \cdot f_{sp} \tag{4.14}$$

$$\hat{\theta}_{v,e}\,(t+dt) = \hat{\theta}_{v,e}\,(t) \cdot f_{sp} \tag{4.15}$$

In order to preliminarily test these new implementations, some idealized simulations are performed which are presented in chapter 5. Afterwards, chapter 6 discusses their application in a simulation of a volcanic eruption of a real case scenario.

5. Idealized quasi 2D-simulations

The previous chapters explained the governing equations of the ICON-ART modeling system, its limitations regarding the explicit simulation of volcanic eruptions, and the code modifications performed in this work to enable such explicit simulations. To test these implementations, four idealized, quasi-2D simulations are performed with ICON-ART, which are presented in this chapter.
The first simulation is a falling cold-bubble and serves as a reference. For the second simulation, an ash-bubble is added to the cold-bubble, in order to focus on two aspects: first, the effect of ash on the total density and thereby, the model dynamics and second, it is a test for modified LBC. A comparison between the two simulations explores the impact of both aspects. Two additional simulations are performed to test an idealized volcanic eruption. The first one focuses on the mass source and applying $\hat{w}_e$ and $\hat{\theta}_{v,e}$ to investigate the development of the volcanic plume. The second one neglects $\hat{\theta}_{v,e}$ to point out its role for the plume development.

5.1. Simulation of density currents and mass sink

Two different simulations are performed to investigate the effect of ash on the density and thereby, on the dynamics and to test the sink for m_{total}. This section describes the model setup for both simulations, followed by the discussion of the results.

5.1.1. Model setup

The first simulation is the non-linear density current test case by Straka et al. (1993), which is used for evaluating and comparing dynamical cores of models. The model domain is a quasi-2D torus grid, that has a width of 40 km in zonal direction and 4 cell rows are arranged for the meridional direction. For each row the dynamical core gives identical results. Furthermore, it has doubly-periodic boundary conditions. Both the horizontal and vertical resolution is $\Delta x = \Delta z = 100$ m and the top height $H = 6.4$ km. The atmosphere is neutrally stratified with a virtual potential temperature of $\hat{\theta}_v = 300$ K in the whole domain and only consists of dry air, whereas, water in different phases is neglected. Furthermore, the convection scheme is explicitly computed because of the high horizontal resolution and the model time step is $dt = 0.72$ s.
For the Straka test case, a bubble of cold air (cold-bubble) is initialized in midair. The second simulation

is modified in a way, that an additional bubble of ash is mixed with the cold-bubble (mixed-bubble). The temperature perturbation in K for the cold-bubble is given by

$$\Delta T = \begin{cases} 0.0 & \text{if } L > 1.0 \\ -15.0\left(\cos \pi L + 1.0\right)/2 & \text{if } L \leq 1.0 \end{cases} \tag{5.1}$$

with

$$L = \sqrt{\left[\left(x - x_c\right)\frac{1}{x_r}\right]^2 + \left[\left(z - z_c\right)\frac{1}{z_r}\right]^2}. \tag{5.2}$$

The centre in horizontal direction is $x_c = 0.0$ km and $x_r = 4.0$ km is the maximum horizontal radius of the bubble. The centre in vertical direction is denoted by z_c and located at 3.0 km and $z_r = 2.0$ km is the maximum vertical radius. $\Delta\theta$ can be derived from ΔT by converting $T = \pi\theta$.
The initial mass mixing ratio of ash $\hat{q}_a$ in g/kg for the mixed-bubble is

$$\hat{q}_a = \begin{cases} 0.0 & \text{if } L > 1.0 \\ 25.0\left(\cos \pi L + 1.0\right)/2 & \text{if } L \leq 1.0 \end{cases} \tag{5.3}$$

with the same size and location as the cold-bubble. To investigate the resulting density perturbation $\Delta\overline{\rho}$ compared to an undisturbed atmosphere, an additional reference simulation is performed. This simulation considers an atmosphere at rest, as it does not include any perturbations.

5.1.2. Results for the density current simulations

The following presents the results of the Straka density current test case. Figure 5.1 shows $\hat{\theta}_v$ (a,c,e) for $t = 0$, $t = 5$, and $t = 10$ min after the start of the simulation and the resulting $\Delta\overline{\rho}$ (b,d,f) compared to reference simulation. Note that the figures show the cross section of only the right side of the model domain, as the setup is symmetric. At $t = 0$ min, $\hat{\theta}_v$ in the bubble decreases towards its center with a minimum of $\hat{\theta}_v = 283.4$ K, consequently, $\Delta\overline{\rho}$ in increases to $\Delta\overline{\rho} = 59.2$ g/m^3, which leads to an intensifying negative buoyancy towards the bubble center. Five minutes later (figure 5.1 (c) and (d)), the cold air has reached the ground, moves horizontally and forms a density current. At that time the cold air reaches a distance of 4 km and a Kelvin-Helmholtz (K-H) instability starts developing. K-H instabilities occur, e.g. when a velocity shear in a fluid is present or when two fluids with different densities move with different velocities (Drazin, 2015). These instabilities are sometimes visible in the atmosphere by clouds or can be observed by weather radars (Baumgarten and Fritts, 2014; Luce et al., 2010). Ten minutes after the start of the simulation, the cold air reaches a distance of $x \approx 11$ km, additionally, a vortex is clearly visible and more K-H instabilities develop on the right end of the density current.

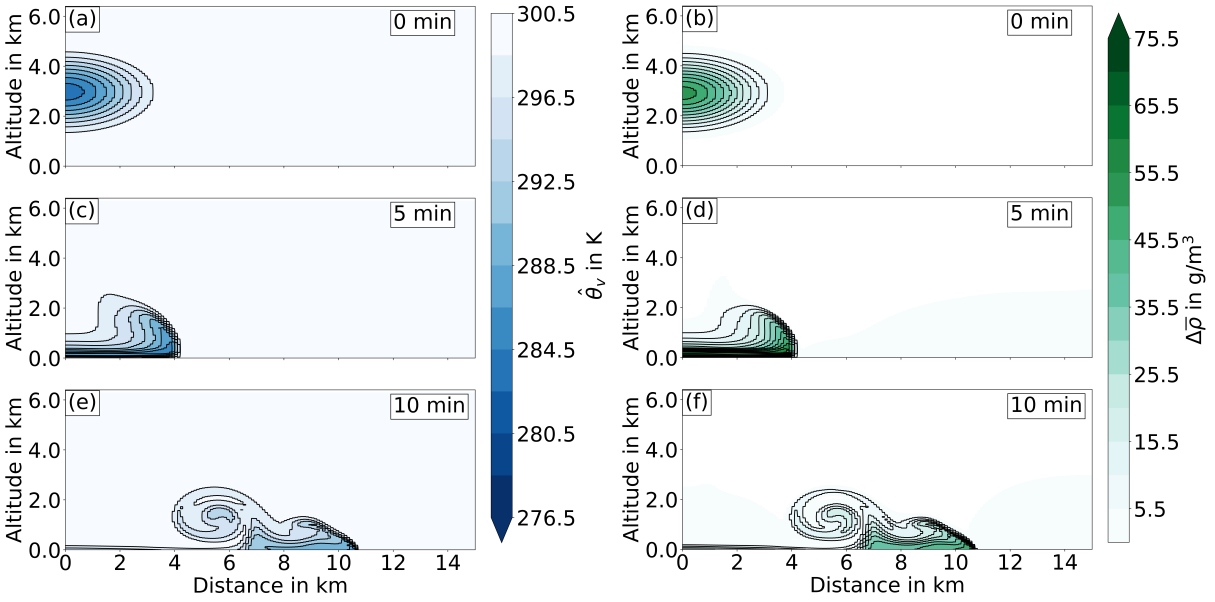

Figure 5.1.: Virtual potential temperature $\hat{\theta}_v$ in K (a,c,e) and the resulting density difference $\Delta\overline{\rho}$ in g/m^3 (b,d,f), compared to the reference simulation, is shown for the Straka density current test case (cold-bubble) simulation at $t = 0,5$, and 10 min after the start of the simulation. As the setup is symmetric, only the right side of the domain is shown. (Straka et al., 1993).

The following part presents the simulation of the modified Straka density current test case. The cold-bubble is complemented by an ash-bubble, which is shown in figure 5.2 by the mass mixing ratio of ash $\hat{q}_a$. The ash-bubble is initialized with $\hat{q}_a$ increasing towards its center with a maximum of 49.90 g/kg. Within 5 min, the ash falls to the ground and travels almost 6 km horizontally, besides, a vortex develops due to K-H instability. At $t = 10$ min, the ash reaches a distance of almost $x = 13$ km and two distinct vortices occur, while $\hat{q}_a$ clearly decreases. Similar pattern is also depicted for both $\hat{\theta}_v$ and $\Delta\overline{\rho}$ in figure 5.3. Compared to the cold-bubble, $\hat{\theta}_v$ is further reduced to minimum 276.5 K in the mixed-bubble center and $\Delta\overline{\rho}$ is increased up to 88.4 g/m^3.

The temporal evolution of the total air mass m_{total} (blue curve), mass of dry air m_d (red curve), and mass of ash m_a (black curve) compared to their initial mass $m(t) - m(0)$ are shown in figure 5.4 for the case of (a) and (b) the modified LBC and for (c) and (d) the non-modified version. In the first case, m_d remains constant during the entire time of the simulation, whereas, m_{total} and m_a decrease by the same ratio, from $t \approx 5$ min (when the bubble reaches the ground) until the end of the simulation. In contrast, m_{total} is constant for the case of the non-modified LBC, whereas, m_d increases by the same ratio as m_a decreases, when the ash reaches the ground.

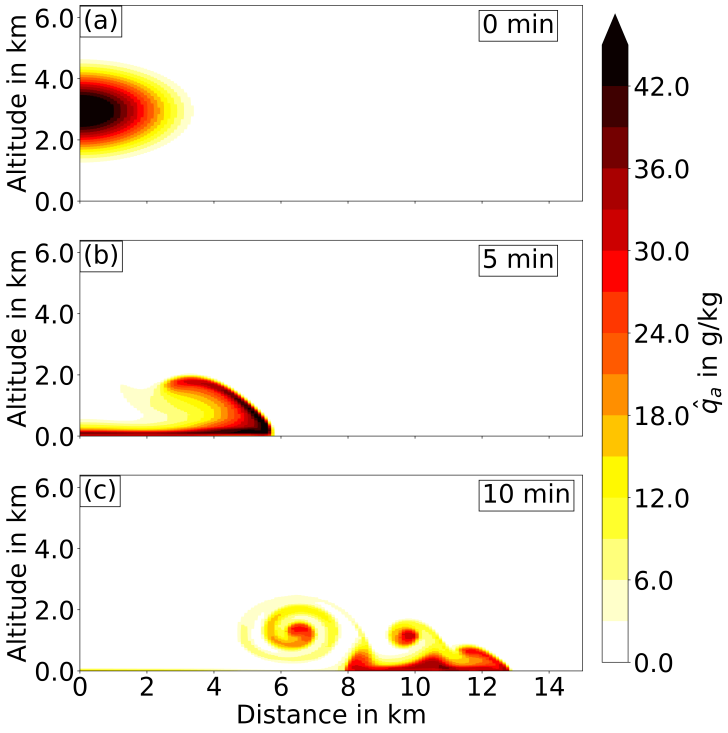

Figure 5.2.: Mass mixing ratio of ash $\hat{q}_a$ in g/kg of the mixed-bubble at $t = 0,5$ and 10 min after the start of the simulation. As the setup is symmetric, only the right side of the domain is shown.

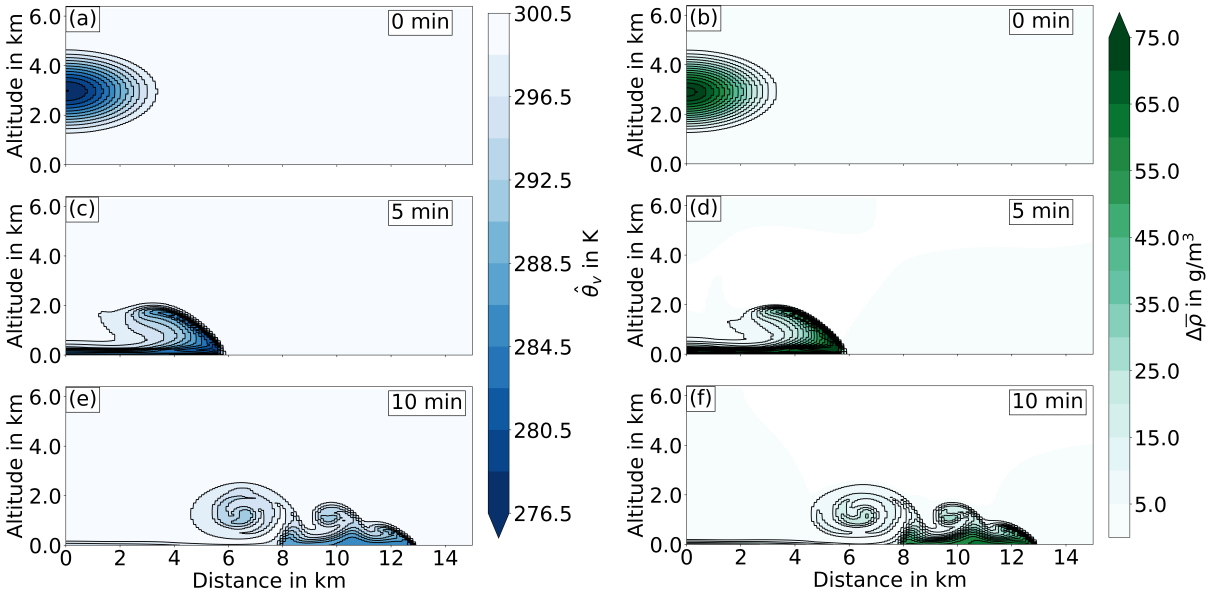

Figure 5.3.: $\hat{\theta}_v$ in K (a,c,e) and $\Delta\overline{\rho}$ in g/m^3 (b,d,f) of the mixed-bubble compared to the reference simulation at $t = 0,5$, and 10 min after the start of the simulation. As the setup is symmetric, only the right side of the domain is shown.

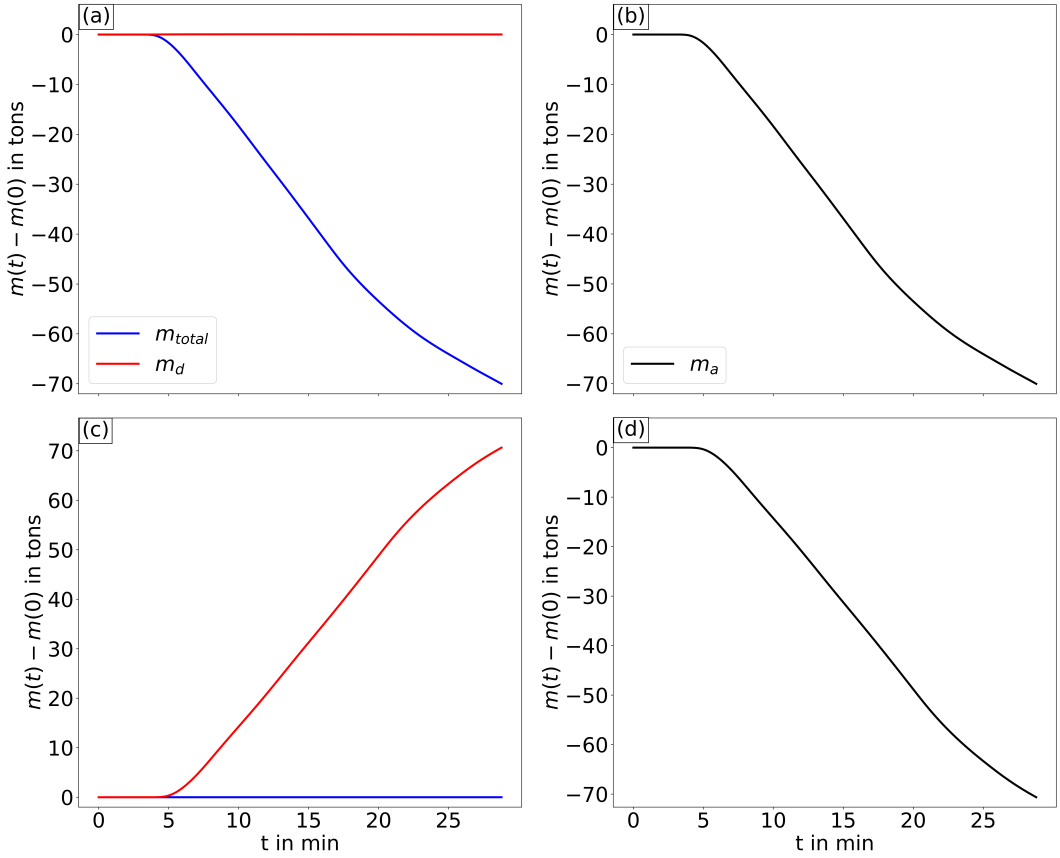

Figure 5.4.: Temporal evolution of masses compared to their initial mass ($m(t) - m(0)$) in tons of the total air mixture (m_{total}, blue curve), dry air (m_d, red curve), and of ash (m_a, black curve) for (a) and (b) the modified LBC and, (c) and (d) the non-modified LBC.

Discussion

The comparison between the simulated cold-bubble and mixed-bubble shows that the inclusion of ash in the total air mixture further decreases $\hat{\theta}_v$ and increases $\Delta\overline{\rho}$, which results in negative buoyancy that intensifies towards the bubble center. Consequently, the mixed-bubble falls faster towards the ground and covers up to 16% larger distance (vertical and horizontal) in the same amount of time, compared to the cold-bubble. Moreover, the larger gradients of $\Delta\overline{\rho}$ lead to more K-H instabilities and two distinct vortices, instead of only one when simulating the cold-bubble. The visible motion is mainly due to the modified dynamics, caused by ash being part of the total air mixture. The simulation of mixed-bubble also considers sedimentation of ash that is much slower, thus, it is not noticeable. Nevertheless, the sedimentation of ash at the surface leads to the reduction of m_a and m_{total} via the modified LBC. Therefore, this simulation demonstrates the effect of ash on the dynamics and the resulting multicomponent multiphase flow, which is explained in section 3.1. Furthermore, the temporal evolution of masses reveal the successful implementation of the modified LBC.

5.2. Simulation of an idealized volcanic eruption and mass source

This section focuses on the simulation of an idealized volcanic eruption, by applying the source for m_{total} as well as $\hat{w}_e$ and $\hat{\theta}_{v,e}$. The following explains the model setup and subsequently, the results.

5.2.1. Model setup

The idealized simulation of a volcanic eruption focuses on the source of mass as well as $\hat{w}_e$ and $\hat{\theta}_{v,e}$. It uses the same model domain as the previous simulations with a different top height of $H = 15$ km, $\Delta z = 150$ m and, the model time step is reduced to 0.5 s to retain model stability. A vertical temperature gradient $\Gamma = -0.65$ K / 100 m is also introduced, starting from 298.15 K at z = 0 m to 220.0 K at a height z = 12000 m, beyond which the atmosphere is neutrally stratified. The heat source $\hat{\theta}_{v,e}$ in a fully neutrally stratified atmosphere would lead to a strong and long-lasting updraft and a dispersion of ash in the entire domain. This would make an investigation of the plume development very challenging. Thereby, the inclusion of temperature gradient helps to overcome this challenge and enable the development of the plume. A single point source is located at $x = 0.0$ m in the lowest model layer. The emission takes place from $t = 3$ min until $t = 23$ min with a constant $MER = 10^4$ kg/s, accompanied by the further source conditions $\hat{w}_e = 150$ m/s and $\hat{\theta}_{v,e} = 450$ K. The sink for m_{total} is neglected, in order to focus on the source. An additional simulation without using the heat source is performed and compared to the first simulation, to highlight the role of the heat source. Besides, a reference simulation without emission is performed to investigate $\Delta\overline{\rho}$.

5.2.2. Results for the idealized volcanic eruption simulations

The left column in figure 5.5 shows $\hat{q}_a$ in g/kg for (a) $t = 5$, (c) $t = 15$, (e) $t = 25$, and (g) $t = 35$ min after the start of the eruption. At $t = 5$ min, a symmetric plume has developed and reaches a height of about 6.5 km. This plume consists of a thin but distinct jet and an umbrella region, that covers a height between 4 and 6.5 km, and approximately 4 km in horizontal direction. Ten minutes later, the plume ascends to a height of ~ 8 km and the umbrella region has considerably expanded, while it loses its former symmetry and eddies occur, particularly on the right side of the plume. At $t = 23$ min, the eruption stops and at $t = 25$ min, the plume drops to a height of 7 km, whereas, it extents further horizontally and develops a wavy shape. Moreover, the former straight jet has lost its shape and develops a wavy pattern as well. After 35 min, the plume covers an even larger horizontal distance but has descended further and the former jet is barely noticeable. Furthermore, an overshooting top occurs at the upper plume center.
The right column of figure 5.5 depicts the corresponding $\Delta\overline{\rho}$ in g/m^3 compared to the reference simulation. At $t = 5$ min after the start of the eruption, the jet is indicated by the explicitly negative $\Delta\overline{\rho}$ in the center with negative values also occurring towards east and west. The jet transitions to the umbrella region at a height of about 5 km, where $\Delta\overline{\rho}$ becomes positive. Ten minutes later in figure 5.5 (d), the umbrella region has developed two distinct areas, located between a height of 3 and 4 km ($\Delta\overline{\rho} < 0$ g/m^3)

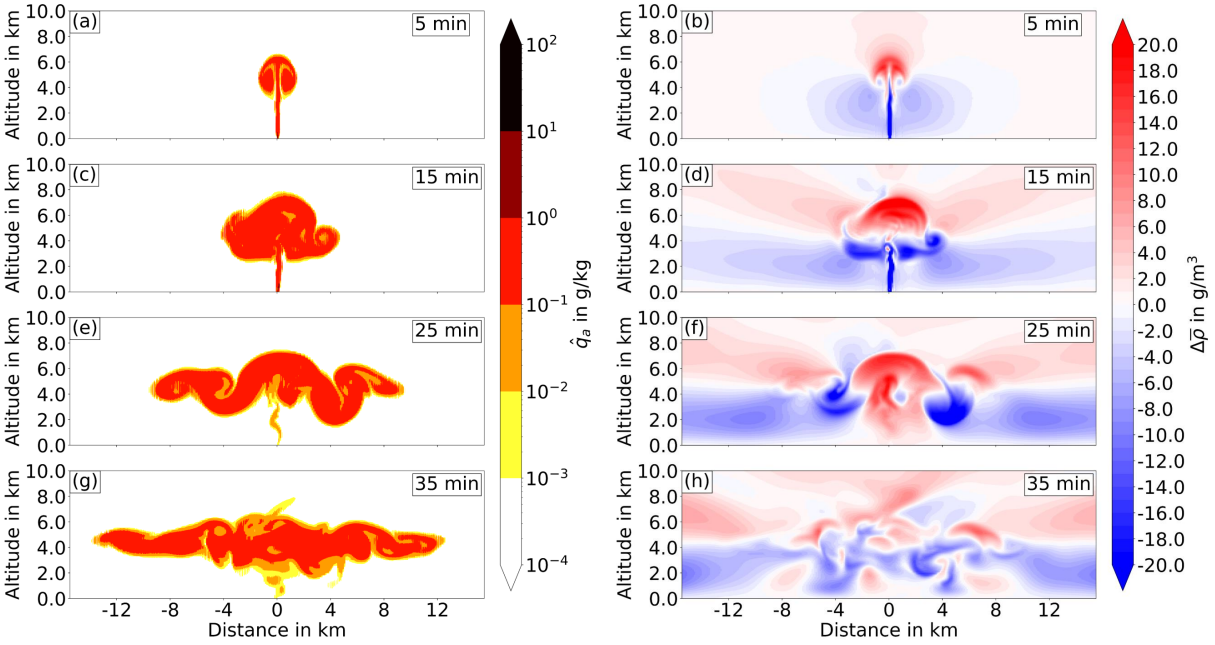

Figure 5.5.: Mass mixing ratio of ash $\hat{q}_a$ in g/kg (a,c,e,g) and density difference $\Delta\overline{\rho}$ in g/m^3 (b,d,f,h) of an idealized volcanic eruption compared to the reference simulation at $t = 5, 15, 25$, and 35 min after the start of the eruption.

and between 5 and 6 km ($\Delta\overline{\rho} > 0$ g/m^3), which are divided by a rather thin region with $\Delta\overline{\rho} \approx 0$ g/m^3. Moreover, the jet is still visible but has dropped over time. At $t = 25$ min, a distinctive area with $\Delta\overline{\rho} > 0$ g/m^3 occurs in the plot center from the surface up to a height of approximately 7 km, that is accompanied by pronounced regions with $\Delta\overline{\rho} < 0$ g/m^3 on both sides, which seem to descend to lower levels. 35 min after the start of the eruption, $\Delta\overline{\rho}$ dissipates and there is no distinct shape recognizable.

The temporal evolution of the total air mass m_{total}, mass of dry air m_d, and mass of ash m_a compared to their initial mass $m(t) - m(0)$ in kilotons are shown in figure 5.6 for the case of taking into account the mass source of m_{total} (a) and (b) and the case of neglecting it (c) and (d). The consideration of the mass source leads to an increase of m_{total} by the same ratio as m_a when the eruption takes place, whereas, m_d remains constant over the whole time. Neglecting the mass source results in a conserved m_{total} and a reduction of m_d by the same amount as m_a increases during the eruption.

Figure 5.7 shows the result of the idealized volcanic eruption for the case without specific heat source. In (a), five min after the start of the eruption, a rather short and indistinct jet region is visible and a narrow umbrella has developed, reaching a top height of 3 km. Even 10 min later in 5.7 (c) the plume does not rise further and large parts of the plume seem to collapse, while the horizontal extent is much smaller compared to the one in figure 5.5. At $t = 25$ min, when the eruption has stopped, the plume seems to collapse at its right end, which is also noticeable at $t = 35$ min. The plume spreads about 7 km from the center to both sides and develops an overshooting top that reaches a height of 4 km.

The right column in figure 5.7 depicts the corresponding $\Delta\overline{\rho}$. In (b), a minor jet occurs directly at the

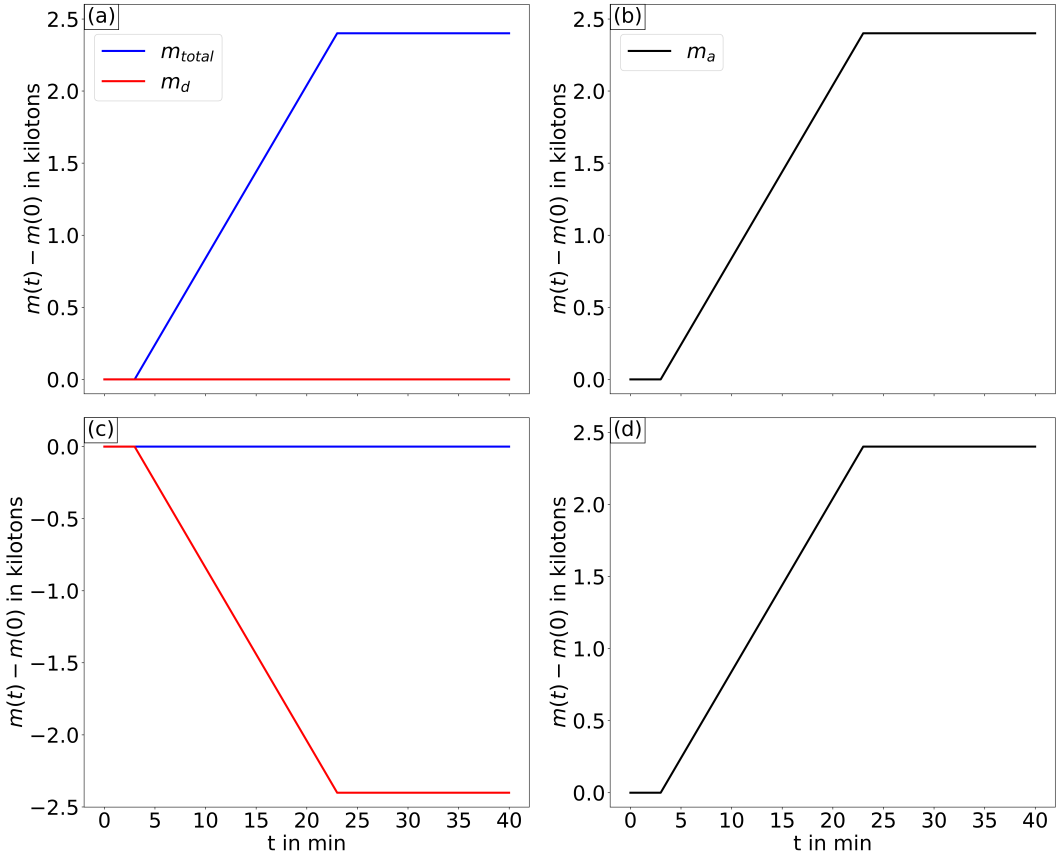

Figure 5.6.: Temporal evolution of masses compared to their initial mass ($m(t) - m(0)$) in tons of the total air mixture (m_{total}, blue curve), dry air (m_d, red curve), and of ash (m_a, black curve) for (a) and (b) considering the mass source for m_{total} and (c) and (d) neglecting it.

source ($\Delta\overline{\rho} < 0$ g/m^3), whereas, $\Delta\overline{\rho}$ becomes positive right above it and indicates the narrow umbrella region. Ten minutes later, a boundary at a height of 1 km develops and divides distinct areas with negative values of $\Delta\overline{\rho}$ below the boundary and positive values of $\Delta\overline{\rho}$ above it. After the end of the eruption at $t = 25$ min, the denser part of the total mixture ($\Delta\overline{\rho} > 0$ g/m^3) seems to sink towards the ground, whereas, on its left and right side, two less dense regions ($\Delta\overline{\rho} < 0$ g/m^3) seem to fall towards the ground (comparable to figure 5.5 (f)). At $t = 35$ min, a distinct shape does not occur anymore and $\Delta\overline{\rho}$ dissipates.

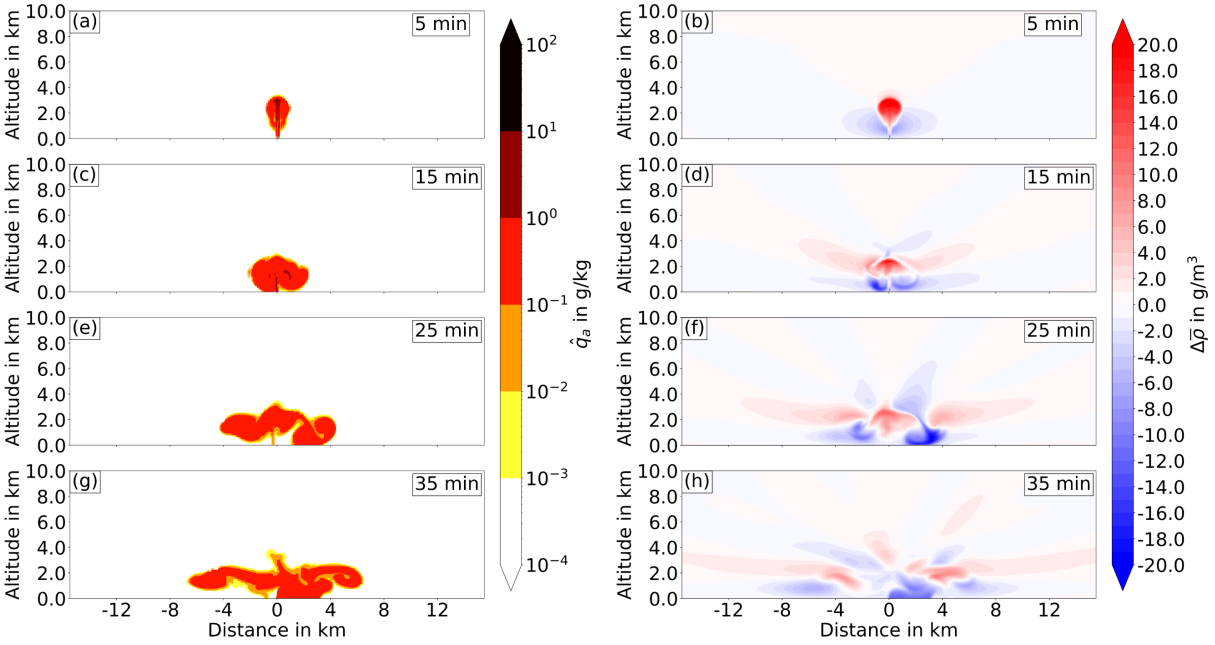

Figure 5.7.: Mass mixing ratio of ash $\hat{q}_a$ in g/kg (a,c,e,g) and density difference $\Delta\overline{\rho}$ in g/m^3 (b,d,f,h) of an idealized volcanic eruption compared to the reference simulation at $t = 5, 15, 25$, and 35 min after the start of the eruption. $\hat{\theta}_{v,e}$ is neglected.

Discussion

The simulation of an idealized volcanic eruption demonstrates the development of a volcanic plume, by lifting ash from the source to higher altitudes in the jet and convective region, and subsequent horizontal spreading that indicates the umbrella region. $\hat{w}_e$ and $\hat{\theta}_{v,e}$ at the source lead to a distinctive jet and convective region, which have a smooth transition, and are indicated by the clearly negative $\Delta\overline{\rho}$ (figure 5.5 (b) and (d)). This results in a positive buoyancy and thereby, to a strong updraft that lifts ash from the source to higher altitudes. Moreover, the area next to the jet/convective region with $\Delta\overline{\rho} < 0$ g/m^3 in figure 5.5 (b) probably indicates ambient air converging towards the jet/convective region, which has a much lower $\overline{\rho}$ than the surrounding air. This develops a strong $\overline{\rho}$-gradient and subsequently eddies, which cause entrainment of the ambient air into the convective region. This results in enhancing the buoyancy and thus, the updraft. The boundary within the umbrella region between the distinct areas with $\Delta\overline{\rho} > 0$ g/m^3 and $\Delta\overline{\rho} < 0$ g/m^3 (figure 5.5 (d) and 5.7 (d)) shows the NBL. At the NBL, $\Delta\overline{\rho} = 0$ g/m^3 but the plume does not immediately stop rising, as the plume still has momentum left. Instead, it ascends further until the momentum is exhausted and the plume reaches its top height. As $\Delta\overline{\rho} > 0$ g/m^3 above the NBL, it leads to negative buoyancy that results in a downdraft and simultaneously, it spreads horizontally. Hence, the umbrella region develops and can get a wavy shape (gravity wave-driven) (see figure 5.5 (c)). Areas with distinct negative and positive $\Delta\overline{\rho}$ next to each other lead to large gradients, which cause the formation of eddies. When the eruption stops so does the momentum input, thus, the

plume center becomes negatively buoyant due to $\Delta\overline{\rho} > 0$ g/m^3 (see figure 5.5 (f)) and starts sinking. In addition, the entire ash plume descends due to sedimentation. Over time, density gradients and eddies dissipate due to dissipation of $\Delta\overline{\rho}$ (see figure 5.5 (h)). The overall slightly asymmetrical shape of the plume might be caused by the very turbulent flow due to high momentum and heat as well as input of mass.

In the case of an eruption without the heat source, the plume is neither able to reach altitudes of more than 3-4 km nor does it spread horizontally to a great extent. The missing heat source leads to much smaller $\Delta\overline{\rho}$-gradients between the plume area and the surrounding air, thus, less eddies develop and there is less entrainment of ambient air into the plume. This results in a low positive or even negative buoyancy and consequently, in a weak updraft and very weak or even completely missing convective region, whereupon, the plume (partly) collapses, instead of rising to high altitudes.

Furthermore, these simulations demonstrate the successful implementation of the source of m_{total}, that leads to an increasing m_{total} and m_a by the same ratio, whereas, m_d remains constant during the eruption.

6. Real case scenario - simulation of the Raikoke eruption in June 2019

The implementations tested beforehand for idealized simulations are finally applied to a real case experiment, through the simulation of the Raikoke eruption in June 2019. Through this simulation, this study focuses on the plume dynamics as well as the development of hydrometeors due to the eruption, near the volcano. The regional and global aspects like chemistry, aerosol dynamics, and the aerosol-radiation interaction have already been explored in previous studies (Muser et al., 2020; Muser, 2022; Bruckert et al., 2022; Bruckert, 2023). Therefore, this study focuses on the microphysical plume development during the initial phase of the eruption. The current chapter first gives an overview about the model setup and the observational data to validate the model results. The second part presents the newly gained results, containing the vertical and horizontal plume development as well as the formation of clouds and precipitation, which is triggered by the eruption and may have an effect on the plume development. Furthermore, it investigates how the eruption affects the vertical distribution of water vapor and whether water vapor reaches the stratosphere due to the eruption. Finally, this chapter ends with a discussion of the generation of atmospheric waves. These aspects were neglected in previous studies of the Raikoke eruption.

6.1. Model setup

The Raikoke volcano is located on a Kuril island in the northeast Pacific at 48.29°N and 153.24°E. Ten individual eruption phases characterized the recent eruption, which took place from the 21st to the 22nd of June in 2019. They lasted between 5 min and 3 h and the plumes reached heights between 5 and 13 km (Horváth et al., 2021b). For this real case scenario, a so-called Limited Area Mode (LAM) is applied, in which ICON-ART restricts the computed data to a limited area. Like a global simulation, a LAM-simulation needs initial conditions as well as meteorological information at the domain's lateral boundaries. The generation of the initial and boundary conditions is done from a preparatory global simulation. During the LAM-simulation, the boundary conditions are updated every hour. Figure 6.1 shows the simulated model domain with a horizontal resolution of $\Delta x = 300$ m. The high horizontal resolution allows to explicitly resolve the convection, as also seen in section 5.1 and 5.2 for idealized simulations. The simulation starts on the 21st of June at 12 UTC and ends on the 22nd at 9 UTC, thereby, all 10 eruption phases are covered in a single simulation. The model time step is $dt = 0.5$ s. For each eruption phase, the MER, the exit velocity $\hat{w}_e$, and the exit volatile fraction, i.e. the fraction of emitted

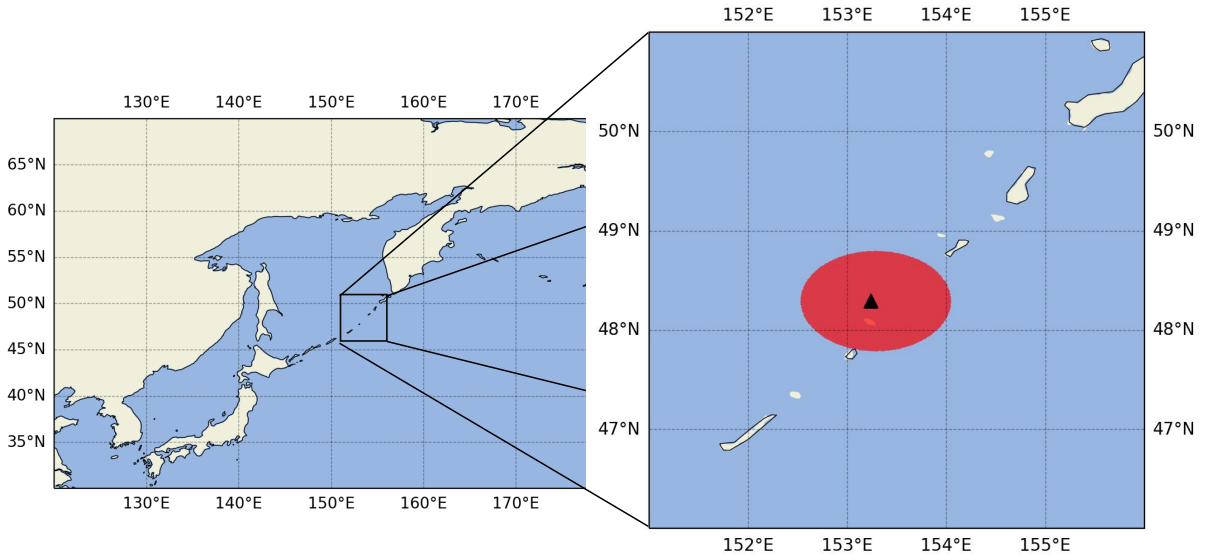

Figure 6.1.: The red circle shows the simulated model domain for the LAM-simulation of the Raikoke eruption. The black triangle marks the location of Raikoke.

volcanogenic water vapour, are taken from Bruckert et al. (2022). They used estimated plume heights based on Horváth et al. (2021b) as input data for FPlume and calculated the MER. The source conditions MER, $\hat{w}_e$, and the duration of each eruption phase are shown in table 6.1 (Bruckert et al., 2022). Moreover, $\hat{\theta}_{v,e}$ is set to 650 K if not stated differently and additionally, the vent size is not considered. In the current study, the MER is distributed such that 97% of it is for very fine ash, which is equally divided into the three aerosol modes - accumulation, coarse and giant, and, 3% is for volcanogenic water vapour. Gases like SO_2 are not emitted, as aerosol dynamical processes like condensation of gaseous compounds onto ash, causing aerosol aging, become more important after several hours (Bruckert et al., 2022), thus, further away from the volcano. Since the simulated model domain only covers an area near Raikoke, chemical processes are neglected as well. Owing to the same reason, investigating the interaction between radiation and ash is not within the focus of this work, as a self-lofting of the plume due to

Table 6.1.: Eruption source conditions for all phases of the Raikoke eruption (Bruckert et al., 2022)

Phase	Date & Time (UTC)	MER (kg/s)	Exit velocity (m/s)
01	21 June 17:55 - 18:20	377.842	106
02	21 June 18:50 - 19:05	704.135	118
03	21 June 19:40 - 20:05	982.171	124
04	21 June 20:40 - 20:50	655.248	118
05	21 June 21:20 - 21:25	977.764	124
06	21 June 22:00 - 22:05	1.876.884	133
07	21/22 June 22:40 - 01:55	5.473.703	145
08	22 June 03:40 - 04:05	2.072.078	133
09	22 June 05:40 - 05:55	3.586.637	142
10	22 June 07:00 - 07:10	237.137	91

heating by solar radiation becomes important after several hours to days (Muser, 2022; Bruckert et al., 2022; Bruckert, 2023).

For the formation of hydrometeors, a one-moment microphysics scheme is used. It considers 5 species of water (water vapor, cloud water, rain, cloud ice, and snow) and both homogeneous and heterogeneous freezing. In this scheme, homogeneous freezing of pure cloud water to cloud ice takes place for temperatures $T < -38°C$. In general, heterogeneous freezing requires aerosols acting as INs (Hoose and Möhler, 2012). However, as the interaction between aerosols and clouds is neglected, the one-moment scheme uses an averaged number of INs, based on measurements, to have a realistic amount of ice. A detailed description of the scheme can be found in Doms et al. (2011).

6.1.1. Filtering the ash from the background

In ICON-ART, all aerosol modes are initialized with 100 particles per kg to avoid a division by zero in the calculation routines. Because of this, it is necessary to use a threshold for the mass mixing ratio, in order to separate it from the background and consider a grid cell as part of the ash plume. Muser et al. (2020) introduced the threshold values which are also used in this study: 0.01 μg/kg, 1.0 μg/kg and 100.0 μg/kg for the accumulation, coarse and giant mode, respectively.

6.1.2. Observational data from GOES-17 and Himawari-8 satellite

To validate the simulated plume heights of the Raikoke eruption, the estimated plume heights from Horváth et al. (2021b) are used, that are based on the geometric side view height estimation method (Horváth et al., 2021a). For this method, observations at daytime by geostationary satellites with a near-limb view are exploited. Near-limb views have a view zenith angle (VZA) larger than 80° and see vertical eruption columns protruding from the Earth's ellipsoid from a close-to-orthogonal direction. Using these near-limb views, a height-by-angle method derives point estimations of the eruption column heights in the vicinity of the vent, with an uncertainty of $\pm$500 m. For the Raikoke eruption in 2019, Horváth et al. (2021b) used Geostationary Operational Environmental Satellite (GOES)-17 observations and applied this method for all eruption phases, as the eruption took place at daytime.

The model results for the horizontal ash plume dispersion are validated through a comparison with observations from Himawari-8 satellite images. Himawari-8 is a geostationary satellite operated by the Japan Aerospace Exploration Agency (JAXA) and the Japan Meteorological Agency (JMA) and uses a 16-band visible and infrared infrared Advanced Himawari Imager (AHI), that allow to estimate both the ash and SO_2 mass loadings. Muser et al. (2020) and references therein provide more detailed description of the data products and the methodology. The current work shows both a qualitative and quantitative comparison for the ash plume dispersion. For the qualitative comparison, the ash column loading (vertically integrated mass of ash per m^2) is calculated for the high-resolution datasets from ICON-ART and is compared to Himawari-8 satellite images. To validate the model results quantitatively, VOLcanic Cloud

Analysis Toolkit (VOLCAT) retrievals from Mike Pavolonis from National Oceanic and Atmospheric Administration (NOAA) are used. "VOLCAT is a collection of software developed by NOAA, in partnership with the University of Wisconsin-Madison" (Pavolonis et al., 2018). It utilizes a pixel-by-pixel based algorithm to retrieve parameters such as temperature and emissivity, by using infrared measurements from satellites (Pavolonis et al., 2013). Thereby, it detects volcanic plumes and plume properties such as ash mass loading can be derived (Pavolonis et al., 2015; Pavolonis et al., 2015; Pavolonis et al., 2018). The retrievals are calculated by considering the AHI infrared bands and have a resolution of 5x5 km^2 near Raikoke. To match the resolution of the VOLCAT retrievals, the model results for ash column loading are averaged (from $\Delta x = 300$ m) to a 5x5 km^2 resolution as well.

6.2. Development of the ash plume

This section focuses on the plume development, particularly the vertical and horizontal dispersion.
For this purpose, the eruption phases 2, 7 and 10 are chosen, which represent a medium, large, and small eruption, respectively. First, they are compared with satellite images from GOES-17, which provides the observed plume height, and Himawari-8. Subsequently, the simulated ash mass loading is compared with the VOLCAT retrievals. This is followed by the sensitivity study about the effect of different $\hat{\theta}_{v,e}$-values for the heat source on the plume height. Finally, this section explores the impact of emitted volcanogenic water vapor on the plume development.

6.2.1. Horizontal and vertical distribution of ash in simulation and observation

The following figures consecutively present the simulated vertical plume shape and height, and the horizontal plume dispersion of the three eruption phases, by showing (a) the latitudinally averaged $\hat{q}_a$ and, (c) the ash column loading as sum of all ash modes. In addition, the GOES-17 (G17) and Himawari-8 (Hi8) satellite images are shown in (b) and (d), respectively. For orientation, the right side in both the G17 and the Hi8 images is east/northeast. A more detailed explanation can be found in Horváth et al. (2021b).

Eruption phase 2:

Figure 6.2 shows the plume during the second phase at 19:00 UTC. In (a), the jet region smoothly transitions to the convective region, while the umbrella region is not clearly distinguishable. Above a height of 3 km, the plume drifts to the east, whereas, some ash from the current and the earlier phase is transported to the west below 3 km. Furthermore, the first plume is still visible and indicated by ash that is transported to the eastern domain boundary. The G17 observation shows a similar plume shape and moreover, the plume of phase 1, dispersed towards eastern direction, is still visible as well indicated by the dark contrast. The simulated plume height of 9.5 km is in good agreement with the observation, which reports a slightly higher height of 9.7 km. Both the simulated horizontal plume dispersion and the Hi8 observation are comparable, as ash is mainly dispersed to the east in both figure 6.2 (c) and (d).

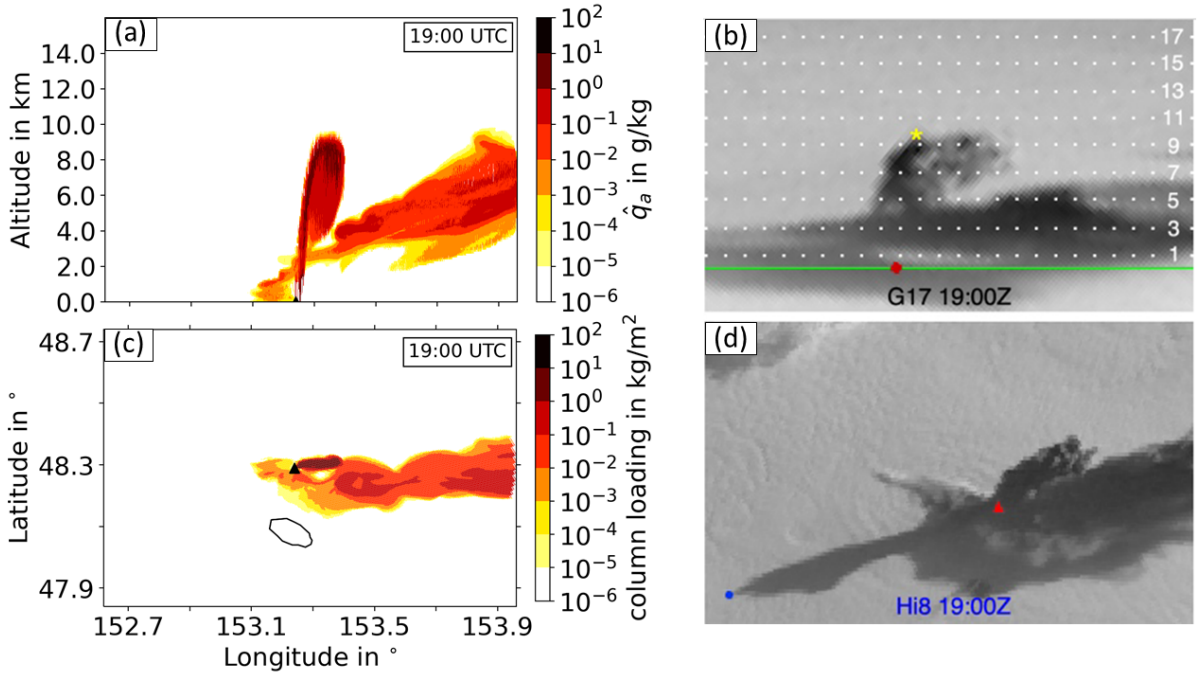

Figure 6.2.: Eruption phase 2 at 19:00 UTC. (a) Mean mass mixing ratio of all ash modes $\hat{q}_a$ in g/kg in the model. (b) GOES-17 (G17) satellite image of eruption plume, with dotted lines depicting the estimated altitude in km and the green line shows the volcano baseline. (c) Ash column loading in kg/m^2 as sum of all ash modes. (d) Himawari-8 (Hi8) satellite image of eruption plume. The black triangles in (a) and (c) and the red dot/triangle in (b) and (d) mark the location of Raikoke. When present, the yellow/blue asterisks indicate the same plume top feature in both satellite images. The blue dot is the shadow terminus on the marine stratocumulus cloud layer in the Hi8 image (Horváth et al., 2021b).

In (c), the plume of the second phase is indicated by the large column loading of 1-10 kg/m^2 (dark red color) near Raikoke, whereas, values between 10^{-1} and 10 kg/m^2 towards the east correspond to the first plume. Moreover, some ash appears in the south and west of Raikoke as well. In the Hi8 image, ash can be distinguished from meteorological clouds through a contrast of dark (in the east) and bright, respectively.

Eruption phase 7:

Eruption phase 7 was the strongest and longest phase with a duration of 3 h 15 min from 22:40 to 01:55 UTC, while figure 6.3 shows its stage at 01:20 UTC. In (a), both the jet and convective region have a smooth transition and, the plume develops an overshooting top indicated by the dark colored peak ($\hat{q}_a = 1 - 10$ g/kg) at the vicinity of Raikoke that reaches a height of approximately 12.3 km. Following this dark peak to the east, ash sinks to a height of $\sim$11.7 km, where it is further transported towards the domain boundary. However, the highest plume height is at 14 km, which is indicated by the lighter red and orange colors ($\hat{q}_a = 10^{-4} - 10^{-1}$ g/kg) but is still 2 km lower than the observed plume top height of 16.5 km, depicted by the yellow asterisk in the G17 image. Furthermore, ash covers the full vertical extent between the surface and a height of 14 km, while the largest amount of ash is predominantly

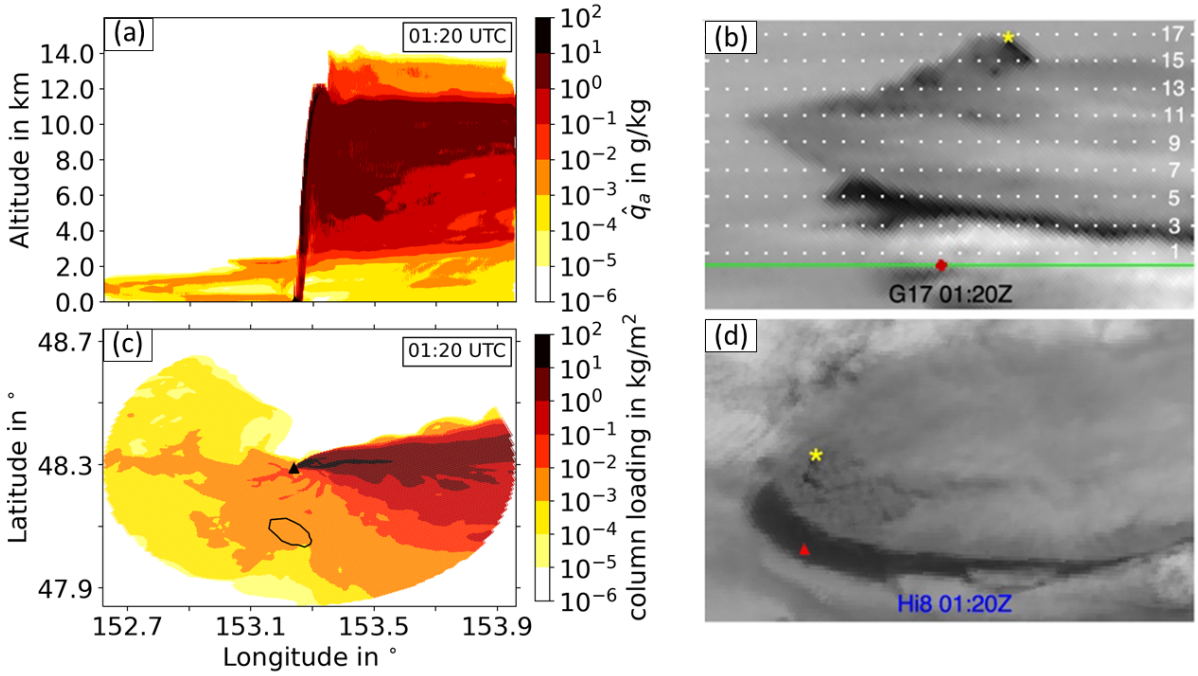

Figure 6.3.: Raikoke eruption phase 7. See figure 6.2 for description.

located at the upper part of the plume, indicated by the dark red color. Moreover, the entire area from Raikoke towards the west contains ash at a height of 1.5-2 km.

Figure 6.3 (c) depicts a large area covered by ash from the east towards the south and to the northwest, while the plume generated by the seventh eruption phase is distinguishable by the dark colors towards the east with a maximum ash mass loading of 30 kg/m^2. The ash coverage agrees with the Hi8 image, that shows a large and thick plume which is transported to the east/northeast and furthermore, Himawari-8 captured ash covering a large area in the south and west as well (not shown). However, in the Hi8 image the spread of the plume presumably has a larger north-south extent than in the model (figure 6.3 (c)).

Eruption phase 10:

The last and weakest eruption phase started at 07:00 UTC and lasted for 10 min. The only model output that clearly captures the plume of the tenth phase is at 07:10 UTC, however, the observation is only provided for 07:00 UTC. Hence, figure 6.4 shows the model results at 07:10 UTC and the observations at 07:00 UTC. Both the plume shape and top height (9 km) are comparable to that of the second phase, whereas, this tenth phase contains less ash as indicated by the lower $\hat{q}_a$. Furthermore, ash from previous phases is still visible in the east and the west. However, the G17 image reveals an indistinct plume with a much lower plume height of 5 km, while ash is visible in the surrounding as well.

In contrast, the simulated horizontal plume dispersion agrees well with the Hi8 observation, as both show a much less pronounced plume. Moreover, a second plume presumably from the previous phase travels

to the southeast and in addition, the surrounding area is still covered by ash in the model and presumably in the observation as well.

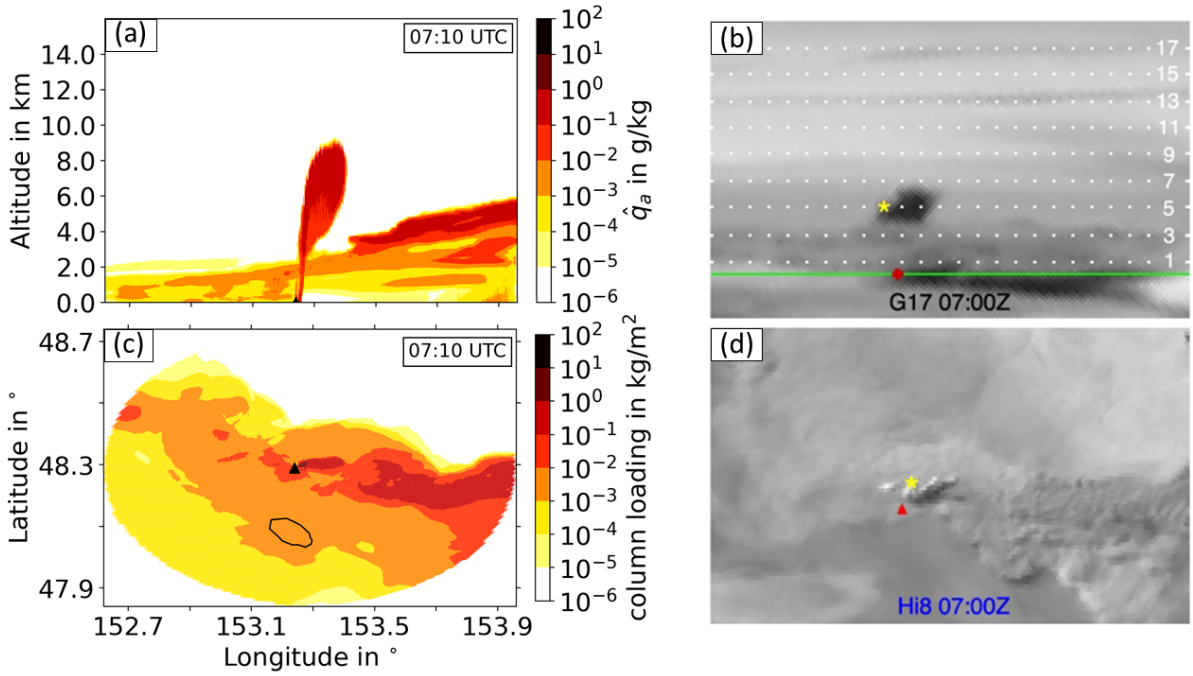

Figure 6.4.: Raikoke eruption phase 10. See figure 6.2 for description.

Discussion

The comparison shows that the vertical and horizontal plume shape could be reproduced to a great extent (refer to section A.1 for remaining phases). However, the simulated plume heights do not differ much among many eruption phases. While the plume heights in both model and G17-observation agree almost perfectly for phases 2 and 4, the model underestimates and clearly overestimates it for the seventh (15% discrepancy compared to observation) and tenth phase (80% discrepancy compared to observation), respectively. As $\hat{\theta}_{v,e}$ is kept constant and only $\hat{w}_e$ and the MER vary among the eruption phases, this prompts the speculation that $\hat{w}_e$ and the MER affect the plume height only to a minor extent in most of the phases, while $\hat{\theta}_{v,e}$ has a much larger impact on it. This would confirm the importance of the heat source also highlighted in section 5.2.

The individual plume regions (jet, convective, umbrella) can not clearly be distinguished as the jet smoothly transitions to the convective region, which agrees with the result of the idealized volcanic eruption in section 5.2. Moreover, the plumes are strongly dispersed by winds which makes it challenging to identify the umbrella region. However, during phase 7 (figure 6.3 (a)) an overshooting top develops between a height of 11.5 and 12.3 km at the vicinity of Raikoke, thus, it is assumed that the NBL is located at a height of $\sim$ 11.5 km. Overshooting tops are also identifiable for other eruption phases (see section A.1).

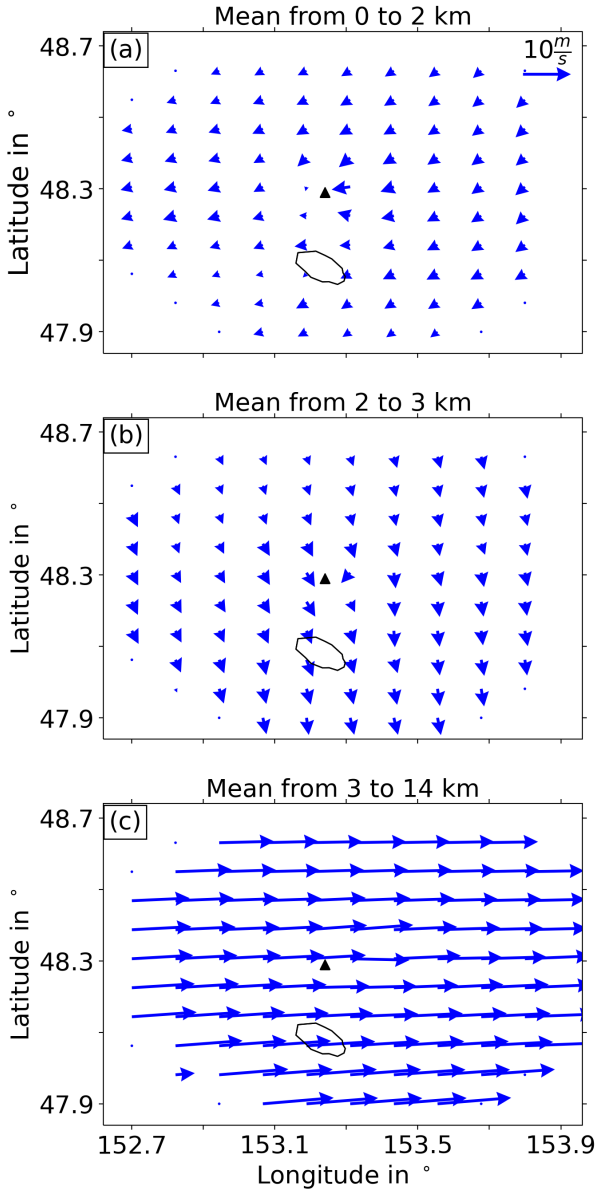

Figure 6.5.: Vertically averaged horizontal wind in m/s between a height of (a) the lowest model layer and 2 km, (b) 2 and 3 km, and (c) 3 and 14 km, at 19:00 UTC.

The wind conditions at different heights are jointly responsible for the vertical plume shape and the horizontal dispersion of ash in different directions. In order to explain this, figure 6.5 shows the mean horizontal wind vectors for three vertical layers, which are chosen between a height of (a) the lowest model layer and 2 km, (b) 2 and 3 km, and (c) 3 and 14 km. As the wind conditions do not change much over time, only the conditions at 19:00 UTC are shown. The vectors are normalized relative to a wind velocity of 10 m/s. Northeasterly winds are predominant between the lowermost model layer and 2 km height, which are rather weak ($\approx$ 4 m/s) and transport ash slowly to the southwest. Slightly faster winds convey ash towards the south between a height of 2 and 3 km. In contrast, westerly winds prevail between the heights 3 and 14 km, with high wind speeds reaching about 30 m/s. Hence, majority of ash

is quickly drifted to the east where it leaves the model domain after a short time. Over time, the winds change to southeasterlies and northwesterlies for the heights 2-3 km and 3-14 km, respectively. This agrees with the observation from Horváth et al. (2021b), who mentioned that an anti-cyclonic circulation led to weak southeasterly winds in the boundary layer near Raikoke, subsequently, resulting in the observed northeastern drift of the ash. In contrast, strong westerly winds of about 25-30 m/s at 11 km altitude transported the plume rapidly to eastern direction. This consequently results in a good agreement of the horizontal dispersion of ash between model and observation. Some ash from upper levels settles due to sedimentation and dynamics (higher $\overline{\rho} \rightarrow$ negative buoyancy) and gets influenced by either northwesterly and southeasterly winds. Thus, ash covers an increasing area with proceeding time, which is most obvious during phase 7.

6.2.2. Quantitative comparison of the ash mass loading

The previous section shows a rather qualitative comparison of the plume dispersion. This section shows the quantitative comparison between the model results and the VOLCAT retrievals, with regard to the ash mass loading in figure 6.6, corresponding to the times in section 6.2.1 at 19:00 UTC (phase 2), 01:20 UTC (phase 7), and 07:10 UTC (phase 10).

In figure 6.6 (a) and (b) at 19:00 UTC, the direction of ash dispersion is comparable between model and retrieval, mostly towards east and northeast, respectively. However, the simulated north-south spread indicates a narrower plume compared to the retrieval and, the ash column loading is 1-2 order of magnitudes larger in the model. Moreover, the model simulates ash in the west of Raikoke which is not captured by the retrieval.

The discrepancy is larger for the seventh phase in figure 6.6 (c) and (d), as the simulated plume seems to have a smaller extent towards north and south and the ash column loading is again 1-2 order of magnitudes larger in the model. Furthermore, the retrieval does not capture ash in the south, whereas, the entire region is covered by ash in the model. However, both model and retrieval show slightly better agreement regarding the area in the west.

In figure 6.6 (f), the plume of the tenth phase is not visible in the retrieval and ash in the south is not captured as well, although, in figure 6.6 (e), it is clearly shown by the model result. In contrast, the retrieval only depicts ash towards the west of Raikoke and a small amount in the southeast.

The comparisons for the remaining phases can be found in section A.2 and reveal comparable discrepancies between model and observation, as the retrieval seems not to be able to capture ash in many areas. In contrast, the visible channel presumably shows ash during most phases in the region around Raikoke. Furthermore, the model always simulates a smaller north-south spread of the plumes compared to the retrieval.

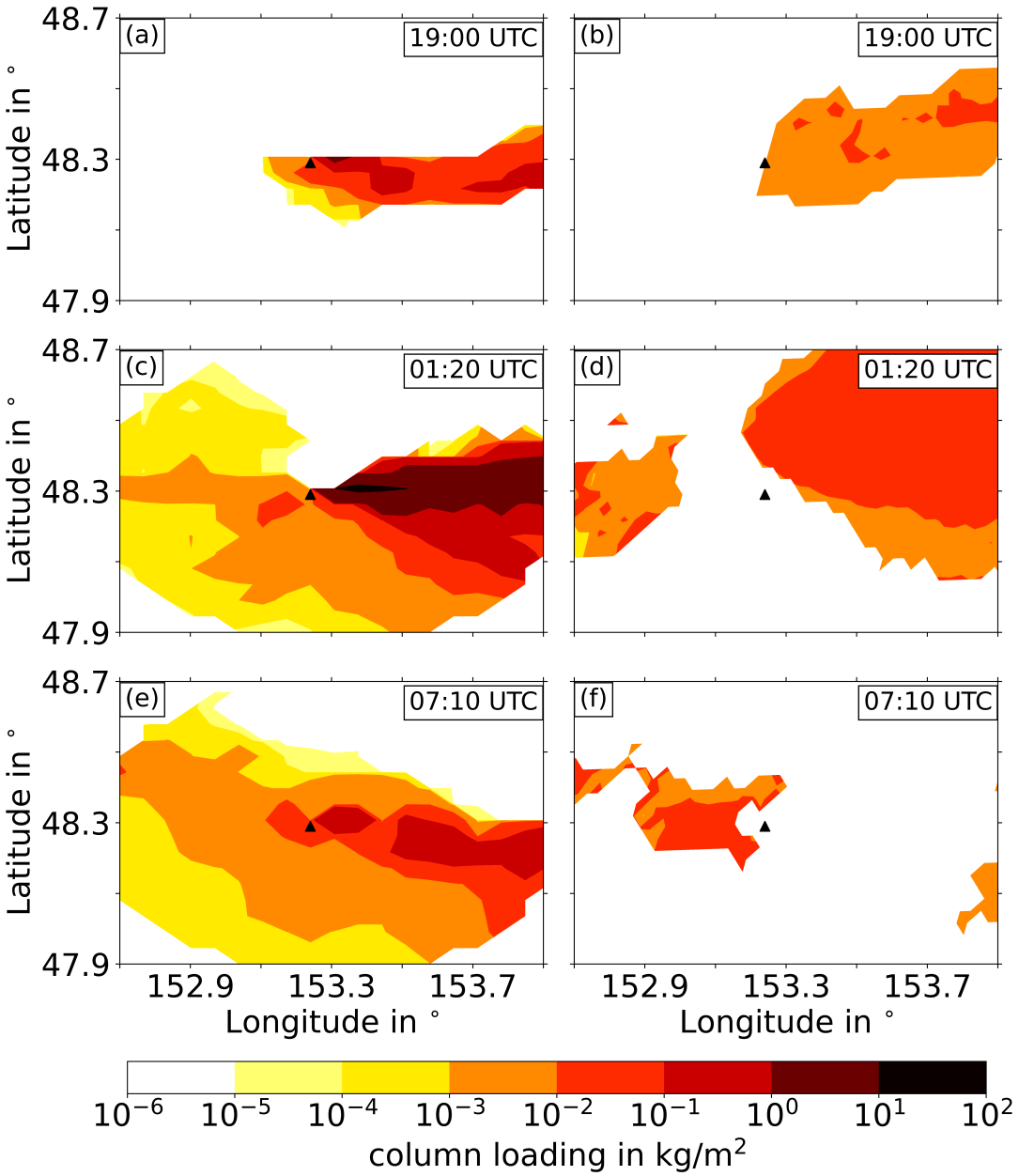

Figure 6.6.: Comparison of ash column loading in kg/m^2 between model (a,c,e) and VOLCAT retrieval (b,d,f) for phases 2, 7, and 10.

Discussion

The plume dispersion is often comparable between the model and retrieval as for each phase both model and retrieval capture majority of the ash that drifts to northeast-southeast. The discrepancies in the plume shape, occurrence of areas covered by ash, and the ash column loading may be due to multiple reasons. As the model simulates a narrower plume, a large amount of ash is concentrated in a small area which leads to large ash mass loading. Regarding the Hi8-observation, saturation could occur for really thick plumes, such that larger values of the ash mass loading are cut off in the retrieval. Moreover, it is possibly

challenging in the Hi8-observations to distinguish ash and meteorological clouds, if they occur in similar areas and heights. This could hamper the consideration of ash in the retrieval and leads to a larger difference in the ash mass loading. Thus, the model is particularly advantageous for cases with distinct cloud coverage.

6.2.3. Sensitivity to $\hat{\theta}_{v,e}$ at the source

As section 5.2 reveals the importance of considering the heat source and the results in section 6.2.1 prompt the speculation of a strong impact of $\hat{\theta}_{v,e}$ on the plume height, this section investigates the sensitivity of the plume height to the heat source. Therefore, multiple simulations are performed with different values of $\hat{\theta}_{v,e}$ from 550 K to 750 K in increments of 50 K, whereas, the remaining source conditions are the same for all simulations. Moreover, the aim is to find suitable values of $\hat{\theta}_{v,e}$ to decrease the discrepancy between the simulated and the observed plume heights. Figure 6.7 (a) presents the results of this sensitivity study and shows the simulated plume heights for each eruption phase and for each value of $\hat{\theta}_{v,e}$. In addition, the observed plume heights from Horváth et al. (2021b) and the ones used in Bruckert et al. (2022) are included. The results reveal that when $\hat{\theta}_{v,e}$ is fixed, the simulated plume height changes to a small extent among the first six phases as well as between phases 8 and 9. Contrastingly, the plume of phase 7 always reaches a markedly higher altitude, and the plume of phase 10 always achieves the lowest height. To match the simulated plume height with the observation from Horváth et al. (2021b),

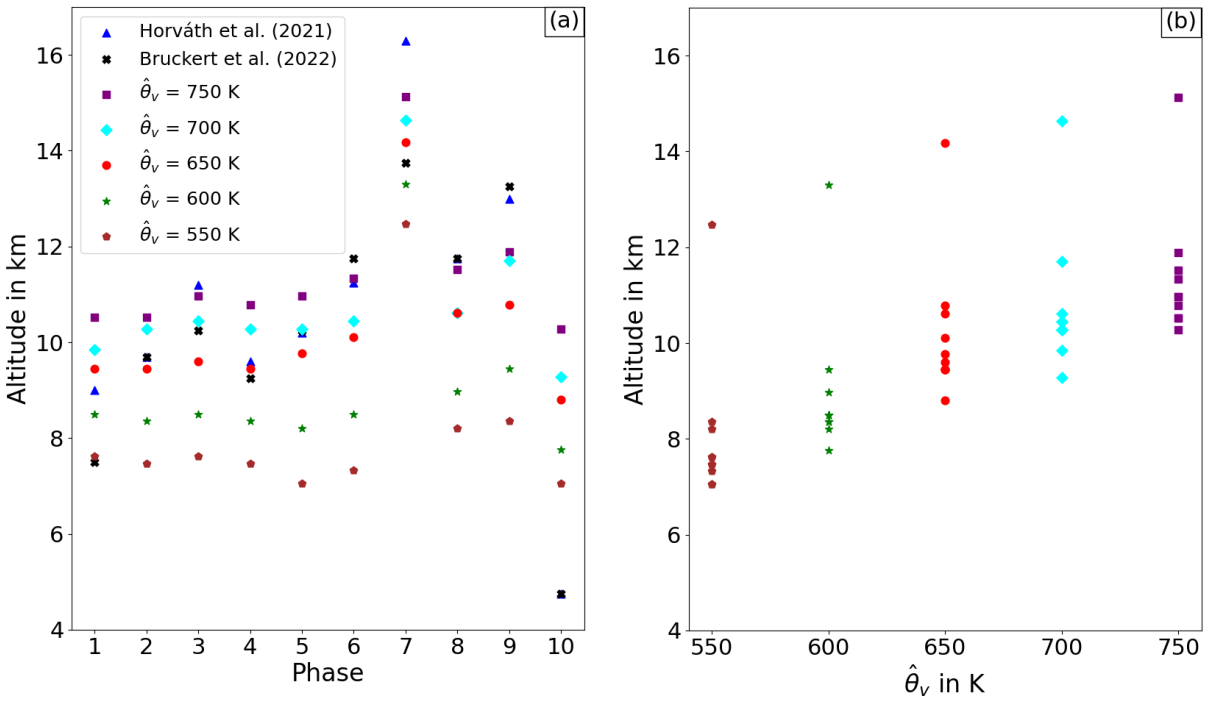

Figure 6.7.: (a) Estimated plume heights by Horváth et al. (2021b) (blue triangles) and Bruckert et al. (2022) (black crosses) and simulated plume heights for each phase with different values of $\hat{\theta}_{v,e}$, ranging from 550 K to 750 K in increments of 50 K. (b) Simulated plume top heights as a function of $\hat{\theta}_{v,e}$ for all phases.

the heat source has to be adjusted by individually choosing $\hat{\theta}_{v,e}$ for each eruption phase. The model agrees well with the observation with $\hat{\theta}_{v,e} = 650$ K for phases 1, 2, 4, and 5, whereas, $\hat{\theta}_{v,e} = 750$ K leads to the best agreement for phases 3, 6, 8, and 9. However, the model still underestimates plume height for phase 7 even with the highest $\hat{\theta}_{v,e}$ of 750 K and overestimates it for phase 10 even with the lowest value of $\hat{\theta}_{v,e} = 550$ K.

The comparison between the model and the plume heights used in Bruckert et al. (2022) shows slightly different results for phase 1, 3, and 7, as $\hat{\theta}_{v,e} = 550$ K, $\hat{\theta}_{v,e} = 700$ K, and $\hat{\theta}_{v,e} = 650$ K result in the best agreement, respectively. To get comparable plume heights for all remaining phases, it requires the same $\hat{\theta}_{v,e}$ as used for the comparison with Horváth et al. (2021b).

Figure 6.7 (b) depicts the simulated plume height as a function of $\hat{\theta}_{v,e}$ as the heat source for all eruption phases. For a fixed value of $\hat{\theta}_{v,e}$, the plume heights differ slightly among all phases except the seventh phase, which shows a much higher plume height for all values of $\hat{\theta}_{v,e}$. Increasing $\hat{\theta}_{v,e}$ in steps of 50 K causes a plume lofting of $\sim$1000 m, while increasing $\hat{\theta}_{v,e}$ is more effective for generally lower plume heights, whereas, the impact seems to be less for higher plume heights.

Discussion

According to Horváth et al. (2021b) and Bruckert et al. (2022), the plume heights noticeably differ among the eruption phases. When using a fixed $\hat{\theta}_{v,e}$ for all phases in the simulation, the plume heights do not differ much among the phases. The results obtained for all simulations with different fixed values of $\hat{\theta}_{v,e}$ (figure 6.7 (a)) reveal the discrepancies in the plume height between the model and observations for each eruption phase. To address these disagreements, individual $\hat{\theta}_{v,e}$-values best suited for each eruption phase are chosen from these results. Individually adjusting $\hat{\theta}_{v,e}$ nearly halves the underestimation of the plume height for phase 7 from 15% ($\hat{\theta}_{v,e} = 650$ K) to 8% ($\hat{\theta}_{v,e} = 750$ K) and decreases the overestimation for phase 10 from 80% ($\hat{\theta}_{v,e} = 650$ K) to 29% ($\hat{\theta}_{v,e} = 550$ K). The small changes in the plume height for fixed $\hat{\theta}_{v,e}$-values support the hypothesis that $\hat{w}_e$ and the MER have a rather small impact on the plume height, whereas, $\hat{\theta}_{v,e}$ is the main driver. Nevertheless, the fact that the plume during phase 7 always reaches a much higher height compared to the plumes of the other phases, can be due to the considerably larger $\hat{w}_e$ as well as the much longer duration. This eventually leads to a strong updraft sustained for about 3 h that causes a rise of the plume height with proceeding time. A stronger eruption characterized by larger $\hat{w}_e$ and MER emits a larger amount of the hot mixture and it is hypothesized, that it increases the $\hat{\theta}_{v,e}$-gradient between the jet/convective region and the surrounding area (and consequently, $\overline{\rho}$-gradient), which leads to more eddies. This intensifies the convective region to a larger extent which subsequently, causes a stronger updraft.

To conclude the results, a larger value of $\hat{\theta}_{v,e}$ is required to simulate a plume height that matches with the observation, whereas, $\hat{\theta}_{v,e}$ has to be smaller for weaker eruptions. The plume height has a somewhat linear dependence on $\hat{\theta}_{v,e}$, however, this dependence slightly decreases towards larger $\hat{\theta}_{v,e}$-values, which may be owed to the damping effect of the tropopause, that may require an substantially higher $\hat{\theta}_{v,e}$.

6.2.4. Sensitivity to volcanogenic water vapor emission

This part discusses the effect of the additional emission of volcanogenic water vapor on the plume development. A higher amount of water vapor may lead to a faster supersaturation, which results in cloud development and thereby, latent heat release. The latter serves as an additional heat source which has

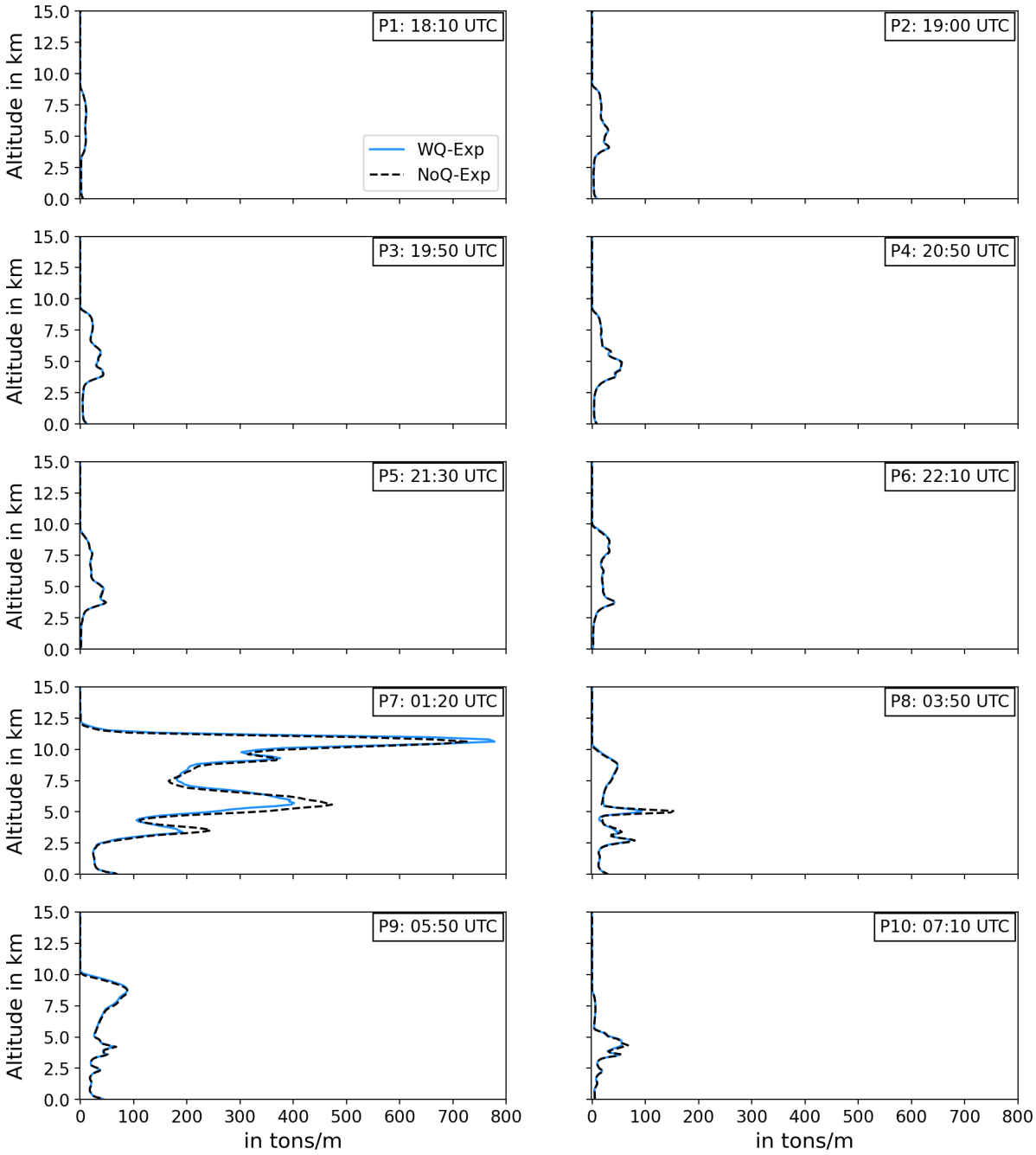

Figure 6.8.: Vertical ash mass distribution in tons/m as sum of all ash modes and for all phases. The solid blue curve represents the simulation with emission of volcanogenic water vapor (WQ-Exp) and the dashed black curve shows the simulation that neglects volcanogenic water vapor emission (NoQ-Exp).

the potential to lift the plume to higher altitudes. Hence, this postulates if volcanogenic water vapor causes additional plume lofting. The comparison between a simulation with volcanogenic water vapor emission (WQ-Exp) and a simulation without volcanogenic water vapor emission (NoQ-Exp) explores this impact. For this purpose, the following part focuses on the vertical ash mass distribution of WQ-Exp and NoQ-Exp and their difference at a specific time among all phases. Figure 6.8 shows the vertical mass distribution of ash in tons/m for WQ-Exp (blue curve) and NoQ-Exp (dashed black curve) for all phases (P1-P10). As for phases 1-6 in both simulations, the ash mass is mainly distributed between heights of about 2.5 km and 9 km, and up to 10 km for phase 6, with a maximum of 70 tons/m during P4 and P5. Phase 7 stands out by the occurrence of ash at higher heights and a markedly larger ash mass of up to 780 tons/m and 730 tons/m for WQ-Exp and NoQ-Exp, respectively. Hence, the difference between both simulations is clearly visible, whereas, the total plume height is identical. In contrast, at lower heights of about 3 and 6 km the ash mass in NoQ-Exp reaches 250 tons/m and 480 tons/m, respectively, which is explicitly larger than in WQ-Exp with 190 tons/m at 3 km and 400 tons/m at 6 km. At 03:50 UTC during phase 8, the ash mass in NoQ-Exp reaches a maximum of about 160 tons/m at a height of 5 km, which is much larger than in WQ-Exp with 100 tons/m. The last major eruption phase P9 shows a maximum ash mass of about 100 tons/m at a height of 9 km, which is the same for both simulations. As for phase 10, the decreased mass above a height of 6 km is noticeable in both simulations, as it is the weakest eruption. These results reveal that the emission of volcanogenic water vapor does not influence the total plume height. However, the difference between WQ-Exp and NoQ-Exp regarding the ash mass is evident particularly during phase 7 and 8.

To verify if this effect is visible during the other phases as well, figure 6.9 shows the difference of ash mass between WQ-Exp and NoQ-Exp in Δ tons/m, corresponding to the phases shown in figure 6.8. The results for WQ-Exp and NoQ-Exp barely differ in phase 1, whereas, the difference becomes more prominent during phases 2-6. More ash reaches the highest parts of the plume in WQ-Exp than in NoQ-Exp, as the difference is always positive with up to 3 tons/m, although, the lower parts of plume in WQ-Exp contain less ash than in NoQ-Exp. A considerably larger amount of ash reaches the highest parts of the plume during the seventh phase in WQ-Exp than in NoQ-Exp, resulting in an increased mass of about 120 tons/m. In contrast, the ash mass at lower levels is approximately 100 tons/m smaller compared to NoQ-Exp. It is also visible during phase 8 with 50 tons/m less ash mass in WQ-Exp than in NoQ-Exp at a height of 5 km. The pattern during phase 9 is comparable to the previous phases, whereas, for phase 10, the mass in WQ-Exp is mostly less compared to NoQ-Exp.

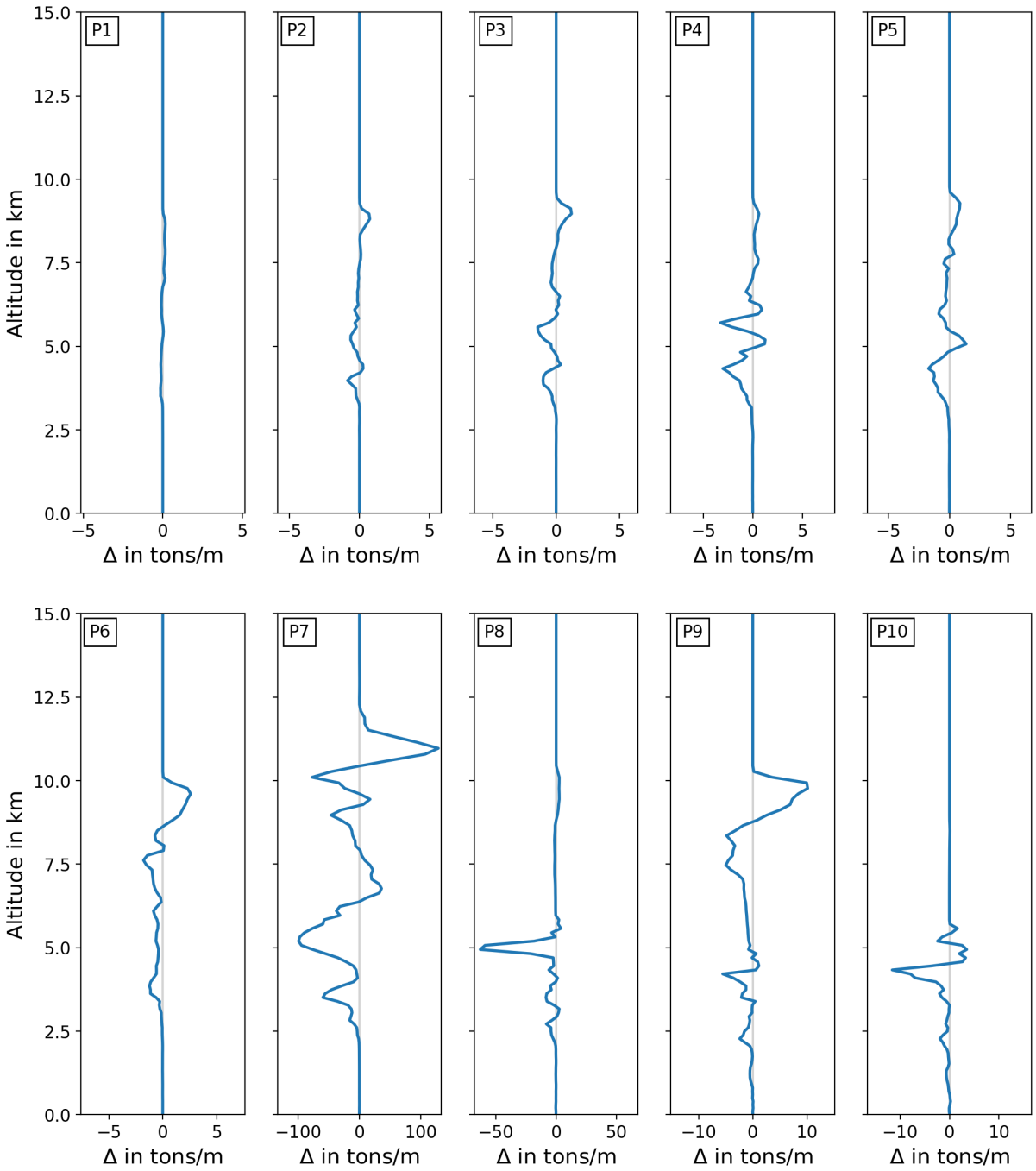

Figure 6.9.: Difference of vertical ash mass distribution Δ in tons/m between WQ-Exp and NoQ-Exp from figure 6.8 for the corresponding times and phases P. Note the different ranges of the x-axis.

Discussion

The results show that emitting volcanogenic water vapor does not cause an additional lofting of the plume, as it reaches the same height in both WQ-Exp and NoQ-Exp for each phase. This might be due to the major effect of $\hat{\theta}_{v,e}$ as the heat source, that outbalances the impact of latent heat release by cloud formation due to the additional water vapor. However, a higher amount of ash reaches the highest parts of the plume for each phase in WQ-Exp. This is especially distinct during phase 7, as the volcano continuously emits a large amount of water vapor for more than 3 h, leading to a high latent heat release that supports lifting of ash. Even though this effect is much smaller for the other phases (weaker eruption and short duration), ash tends to reach higher altitudes when the volcano emits water vapor. In contrast, neglecting volcanogenic water vapor emission leads to accumulation of ash in lower heights, due to less cloud formation, consequently, less latent heat release and less convection. Moreover, the wind speed increases with height and transports ash out of the domain faster, whereas, ash remains in the model domain at lower heights for a longer time due to weaker winds. The higher amount of ash in the highest parts of the plume can lead to implications for the plume development, as it takes more time until ash deposits at the surface, hence, it remains airborne for a longer time and is transported longer distances. This draws the conclusion that even though emitting volcanogenic water vapor does not lead to plume lofting, it can influence the plume development.

6.3. Impact of the eruption on hydrometeors and water vapor

The second part of this chapter shows the development of cloud water, cloud ice, rain, and snow due to the eruption. Therefore, it analyses the vertical and horizontal distribution of each hydrometeor type by showing their water contents and water paths, respectively, for the eruption phases 2, 7, and 10. The results of the remaining eruption phases can be found in section A.3. As for the water contents, its mean is calculated for the area between latitudes 48.3°N and 48.33°N, as this is the most affected area by the eruption regarding cloud formation. Afterwards, this section presents the difference between WQ-Exp and NoQ-Exp, to show the effect of the water vapor emission on cloud formation. This helps to understand whether the dynamics influenced by the eruption, or the emission of water vapor has a larger impact on cloud formation. Finally, this section explores the impact of the eruption on the vertical distribution of water vapor and evaluates if water vapor reaches the stratosphere due to the eruption.

6.3.1. Development of clouds and precipitation

The following figures show the mean water content which is averaged in latitudinal direction from 48.3°N to 48.33°N, as it is the most affected area by the eruption regarding cloud formation. In addition, the calculation of the mean temperature provides the $T = 0$°C-boundary (black line) and $T = -38$°C-boundary (red line) in vertical direction. The first indicates the altitude below which ice crystals melt and the second shows the height where frozen particles form by homogeneous freezing. Between them, both

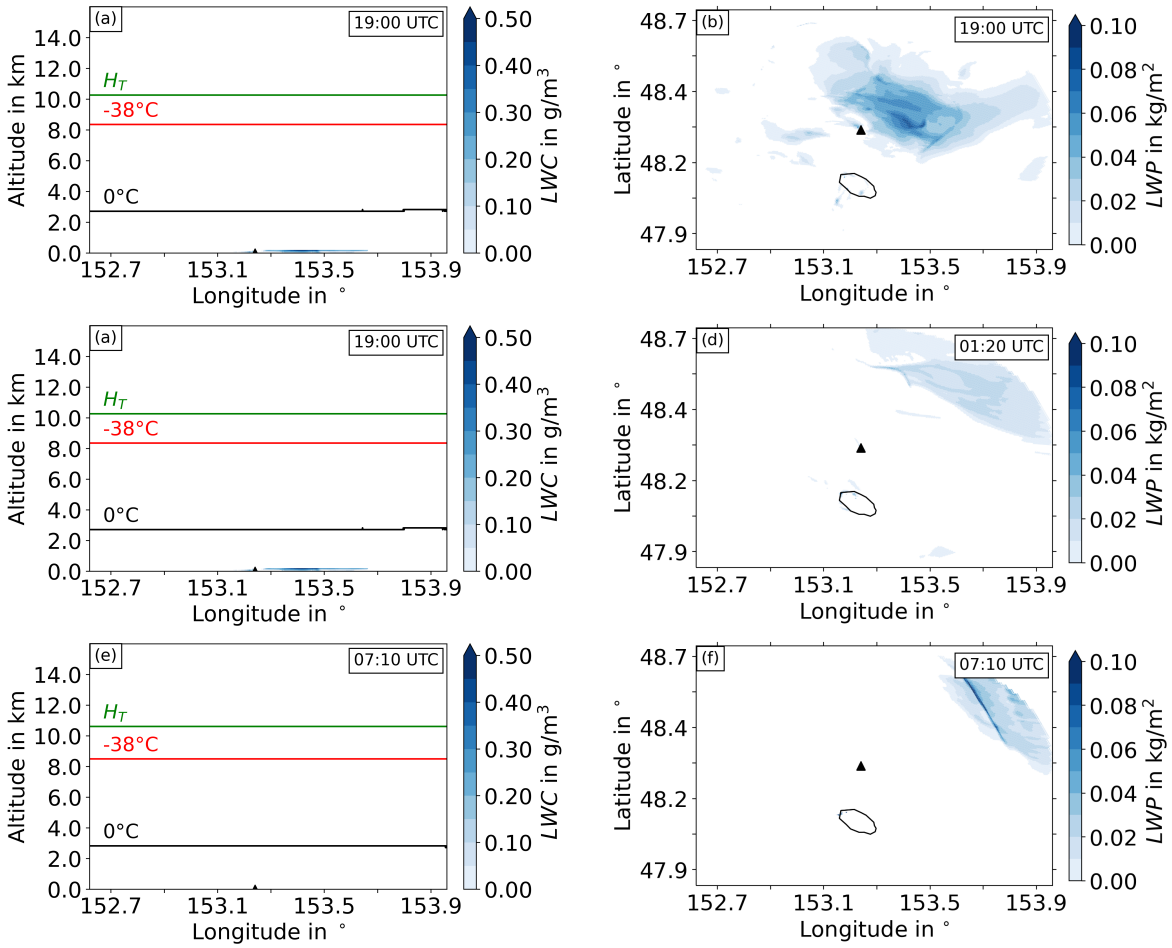

Figure 6.10.: Cloud water in the Ref simulation. Left column: Mean liquid water content (*LWC*) in g/m^3 latitudinally averaged from 48.3°N to 48.33°N at (a) 19:00, (c) 01:20, and (e) 07:10 UTC. The black line shows the $T = 0$°C-boundary, red line $T = -38$°C and the green line the tropopause height H_T. Right column: liquid water path (*LWP*) in kg/m^2 at (b) 19:00, (d) 01:20, and (f) 07:10 UTC.

liquid droplets and frozen particles can occur and form mixed-phase clouds (Pruppacher et al., 1998). Note that the simulation neglects interaction between ash and clouds, hence, cloud ice does not form heterogeneously by means of ash as INs. However, the one-moment microphysics scheme used in these simulations considers heterogeneous freezing through use of an averaged number of INs (see section 6.1). The tropopause H_T is shown by the green line and the water paths are shown for the whole model domain.

First, figure 6.10 (a,c,e) show the mean liquid water content (*LWC*) and figure 6.10 (b,d,f) show the liquid water path (*LWP*) at 19:00, 01:20, and 07:10 UTC in the Ref simulation. These times correspond to the eruption phases 2, 7, and 10, respectively, and hence, it provides a comparison with the cloud formation in the WQ-EXP simulation during the phases. As rain, cloud ice, and snow do not form in the Ref simulation, they are neglected in figure 6.10. In figure 6.10 (a), cloud water only occurs in the lowest model layer eastward from Raikoke with *LWC* up to 0.53 g/m^3, whereas, no clouds appear at 01:20 UTC and 07:10 UTC. The $T = 0$°C-, $T = -38$°C-boundary, and H_T are located at a constant height of about

2.8 km, 8.7 km, and 10.5 km, respectively. According to figure 6.10 (b), clouds cover a region from northwest to the east of Raikoke with a maximum value of $LWP \sim 0.1$ kg/m^2. Furthermore, small clouds appear in the west, south, and in southeastern direction. At 01:20 and 07:10 UTC, clouds only cover the northeastern area.

Eruption phase 2:

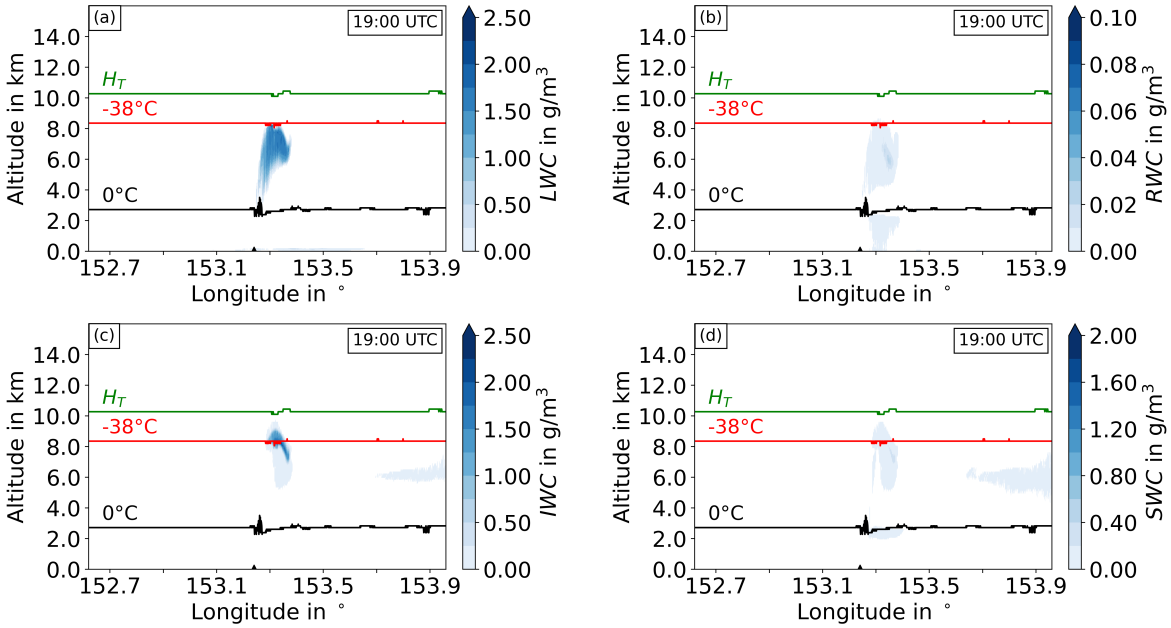

Figure 6.11.: Mean water contents in g/m^3 latitudinally averaged from 48.3°N to 48.33°N for phase 2 at 19:00 UTC of (a) liquid clouds (*LWC*), (b) rain (*RWC*), (c) ice clouds (*IWC*) and (d) snow (*SWC*). See figure 6.10 for description of the black, red, and green lines.

Figure 6.11 shows (a) the *LWC*, (b) rain water content (*RWC*), (c) ice water content (*IWC*), and (d) snow water content (*SWC*) at 19:00 UTC. As for figure 6.11 (a), note the higher maximum value of the colorbar compared to figure 6.10 (a,c,e). A liquid cloud forms above Raikoke between 3 and 8 km height and drifts towards east, with *LWC* of up to 2.5 g/m^3. Rain either forms due to collision-coalescence of cloud droplets or due to melting snow. Therefore, rain appears in two regions, first between altitudes of 5 and 8 km and the second to the east of Raikoke from the surface to an altitude of 2 km, with maximum values of $RWC \approx 0.05$ g/m^3. Cloud ice forms above the liquid cloud mostly where cloud water reaches the $T < -38$°C-boundary. However, cloud ice covers a rather small area and has maximum *IWC* of about 2.5 g/m^3. After cloud ice formation, it is transported to the east and seems to sink to a height of approximately 6 km. Another region of cloud ice occurring in the further east is the contribution by the first eruption phase. Snow forms due to the aggregation of cloud ice and appears in the similar areas as the latter and has a maximum $SWC = 0.8$ g/m^3. A third area containing snow is at the $T < 0$°C-boundary, which might have formed during the first eruption phase. Due to the eruption, the $T = 0$°C-boundary

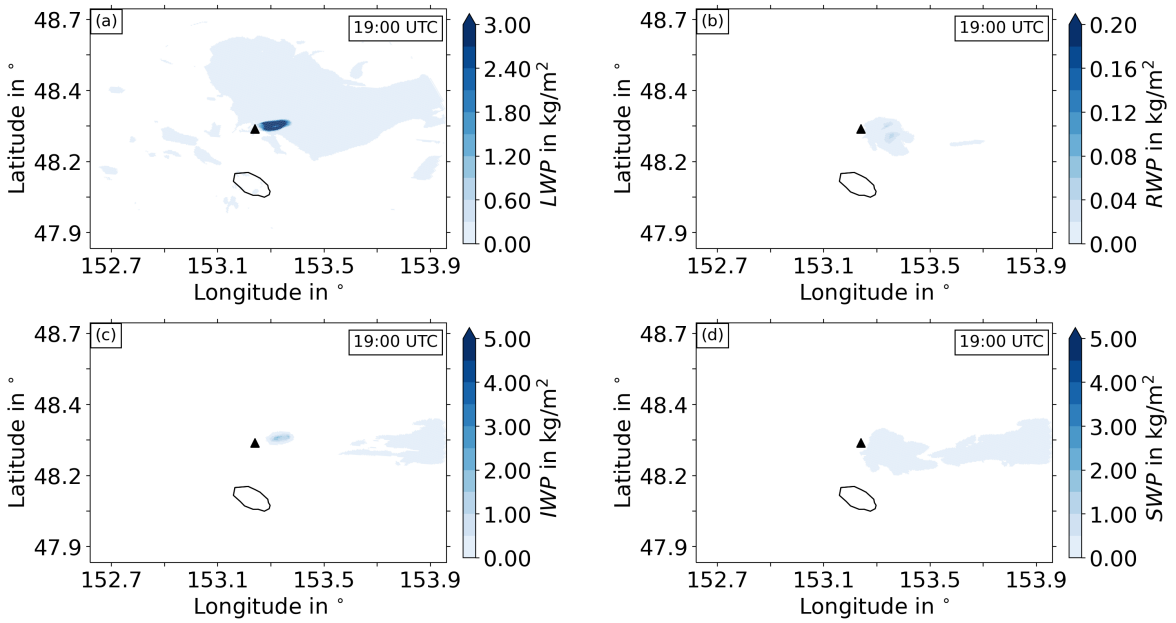

Figure 6.12.: Water paths in kg/m^2 for phase 2 at 19:00 UTC of (a) liquid clouds (*LWP*), (b) rain (*RWP*), (c) ice clouds (*IWP*), and (d) snow (*SWP*).

is lifted above Raikoke and develops a slightly wavy structure eastwards, but this influence is minor on both the $T = -38°$C-boundary and H_T. Figure 6.12 displays the *LWP*, rain water path (*RWP*), ice water path (*IWP*), and snow water path (*SWP*). Again note the adapted colorbar in (a) compared to figure 6.10 (b,d,f) for better visualization. The *LWP* shows a very distinct cloud next to Raikoke with up to $LWP = 3$ kg/m^2, which points out compared to the surrounding clouds. Rain spreads from Raikoke to the southeast and the *RWP* reaches about 0.05 kg/m^2. The region near Raikoke that contains cloud ice is very similar to the one containing cloud water and, the cloud ice in the eastern area formed due to the first eruption, coincides with the one in figure 6.11 (c). Snow is located in the area where rain occurs as well, as the latter forms due to melting snow, and the *SWP* goes up to 0.28 kg/m^2. Aside from that, snow spreads over another region towards the eastern boundary of the domain, that again formed during the first eruption.

Eruption phase 7:

Figure 6.13 shows (a) *LWC*, (b) *RWC*, (c) *IWC*, and (d) *SWC* during the seventh phase at 01:20 UTC. Phase 7 has a significant impact on the formation of clouds and precipitation. The liquid cloud above Raikoke is narrow, but contains a high amount of cloud water as the maximum *LWC* reaches 2.8 g/m^3. Rain appears in the same area as cloud water and in addition, much rain reaches the surface with *RWC* up to 0.1 g/m^3 eastward from Raikoke. Cloud ice forms right above the liquid cloud and gains more height by the updraft due to the eruption until it reaches a top height of about 12 km. This region shows the highest values of $IWC = 1.8$ g/m^3. After that it sinks again and adopts a wavy structure towards the east,

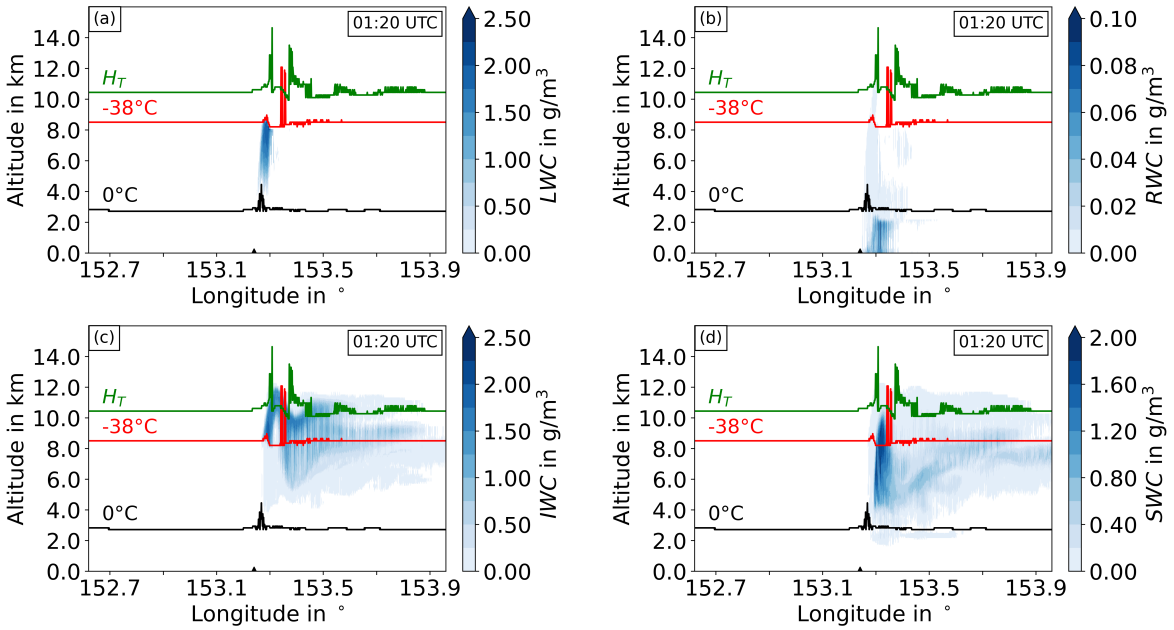

Figure 6.13.: Mean water contents in g/m^3 for phase 7 at 01:20 UTC. See figure 6.11 for description.

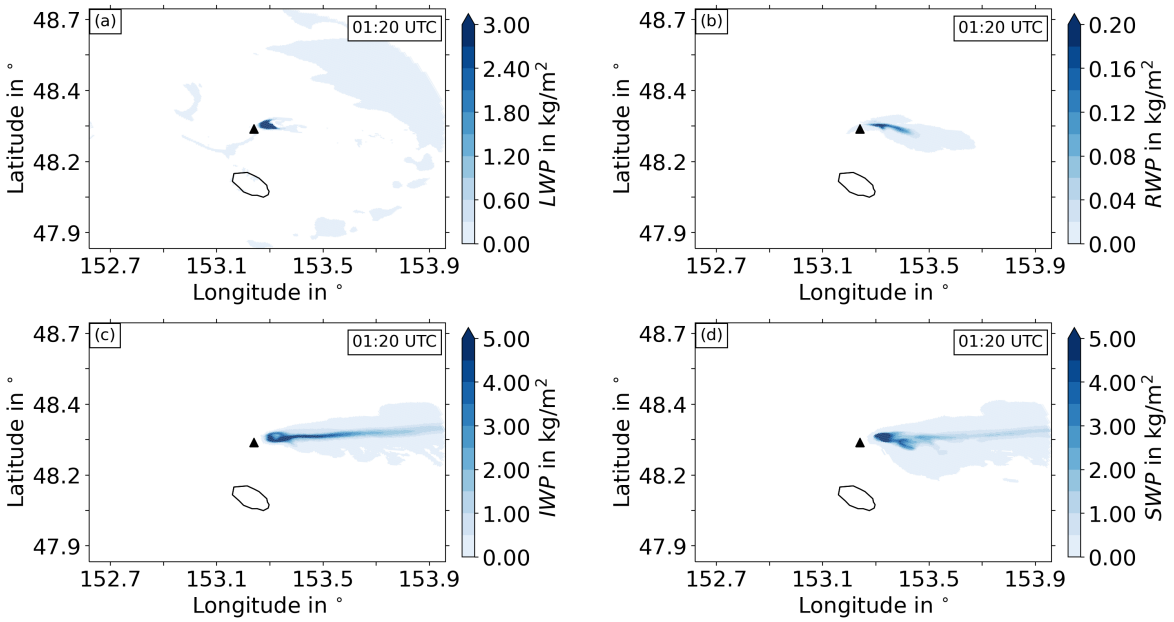

Figure 6.14.: Water paths in kg/m^2 for phase 7 at 01:20 UTC. See fig 6.12 for description.

indicated by the dark blue color. Again snow appears in a very similar region as cloud ice but reaches its lowest height at the $T = 0°$C-boundary, however, some snow even seems to transcend this boundary. This eruption phase affects the $T = 0°$C-boundary, $T = -38°$C-boundary, and H_T to a great extent. The first one is lifted to 1.5 km above Raikoke in the updraft region, and develops a wavy structure eastwards. On the other hand, the $T = -38°$C-boundary shows two peaks, where the first peak experiences a small deformation. The second peak further to the east is lifted by 3.7 km. Furthermore, H_T also features two

distinct peaks, reaching a height of 14.5 km and 13 km, respectively, and the tropopause has a wavy structure as well towards the east.

Regarding the horizontal dispersion in figure 6.14, a clearly visible liquid cloud in (a) develops next to Raikoke but dissipates after a short distance, which coincides with figure 6.13 (a). The maximum LWP reaches almost 5 kg/m^2 and moreover, further clouds occur in the southeast and in the west, which probably formed due to previous eruptions, as they do not occur in the Ref simulation. Rain is drifted from Raikoke to southeastern direction with a RWP of up to 0.18 kg/m^2. Cloud ice and snow are transported to the east of Raikoke, however, the snow spreads over a larger area compared to cloud ice. Their maximum IWP and SWP are 5 kg/m^2 and 4.6 kg/m^2, respectively.

Eruption phase 10:

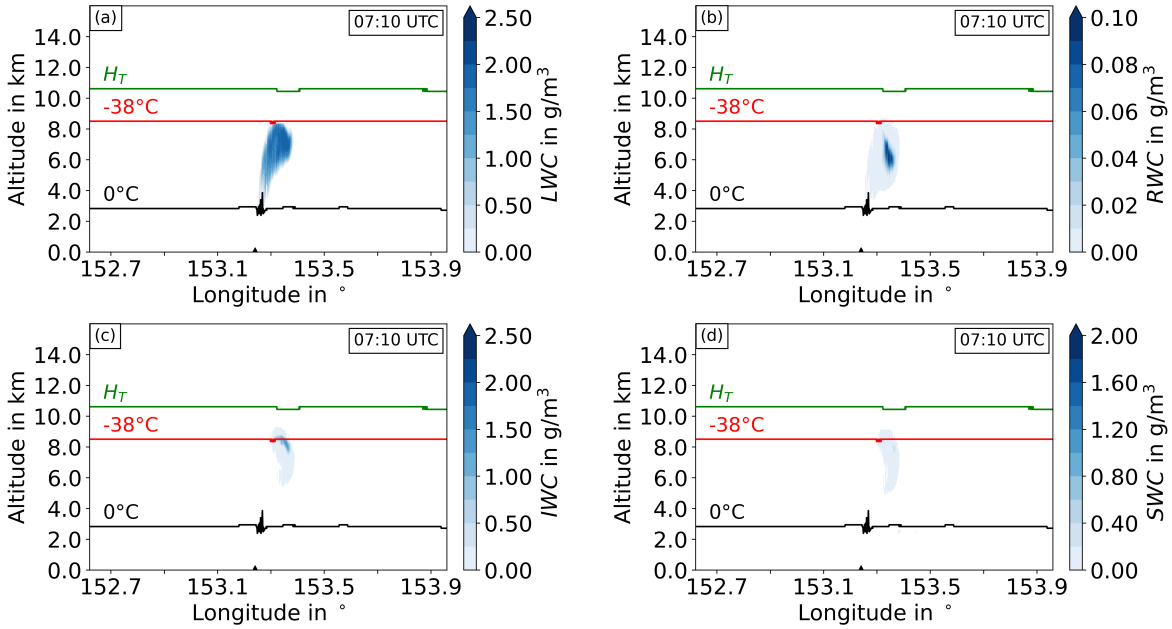

Figure 6.15.: Mean water contents in g/m^3 for phase 10 at 07:10 UTC. See figure 6.11 for description.

The vertical distribution of clouds and precipitation triggered by the tenth eruption, the corresponding water contents, and the deformation of the $T = 0°$C-boundary, $T = -38°$C-boundary, and H_T are comparable to those in phase 2. Again, a distinctive region that contains a large amount of cloud water occurs near Raikoke, and rain also forms in this region but does not reach the surface. Cloud ice and snow cover a small area in both vertical and horizontal direction.

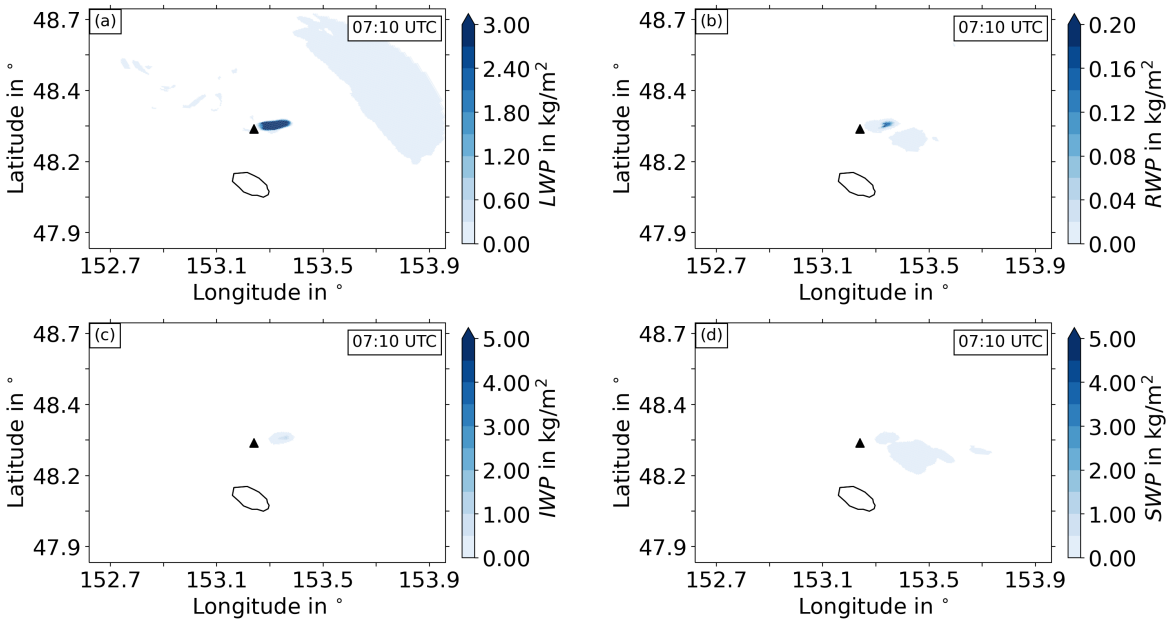

Figure 6.16.: Water paths in kg/m^2 for phase 10 at 07:10 UTC. See fig 6.12 for description.

In order to give further insight into the formation of clouds and precipitation, figure 6.17 shows the temporal evolution of the vertical mass distribution for cloud water, rain, cloud ice, and snow. The mass of cloud water up to a height of 300 m that remains during the entire time mainly corresponds to clouds which are not formed by the eruptions. However, the eruption phases are clearly distinguishable, as the cloud water mass considerably increases during each eruption between a height of 3 and 8 km, whereas, after the end of each eruption, the mass abruptly decreases. Phase 7 is especially pronounced by the continuous occurrence of clouds from 23:00 UTC to 02:00 UTC. A similar pattern indicates rain from 3 to 8 km, however, the largest amount of rain is located below a sharp boundary at a height of 2 km where it persists even after the end of each eruption for some time. According to figure 6.17 (c), cloud ice appears between a height of 4 and 10 km during all phases except for phase 7, during which ice is lifted up to a height of 12 km with mass of ice up to 110 tons/m. As opposed to cloud water and rain, cloud ice remains in the atmosphere after each eruption, although, its mass decreases rapidly as well. Compared to cloud ice, snow often reaches lower heights to almost 2 km, and abruptly disappears at the sharp boundary, where occurrence of large amount of rain coincides (figure 6.17 (b)), particularly during phase 7.

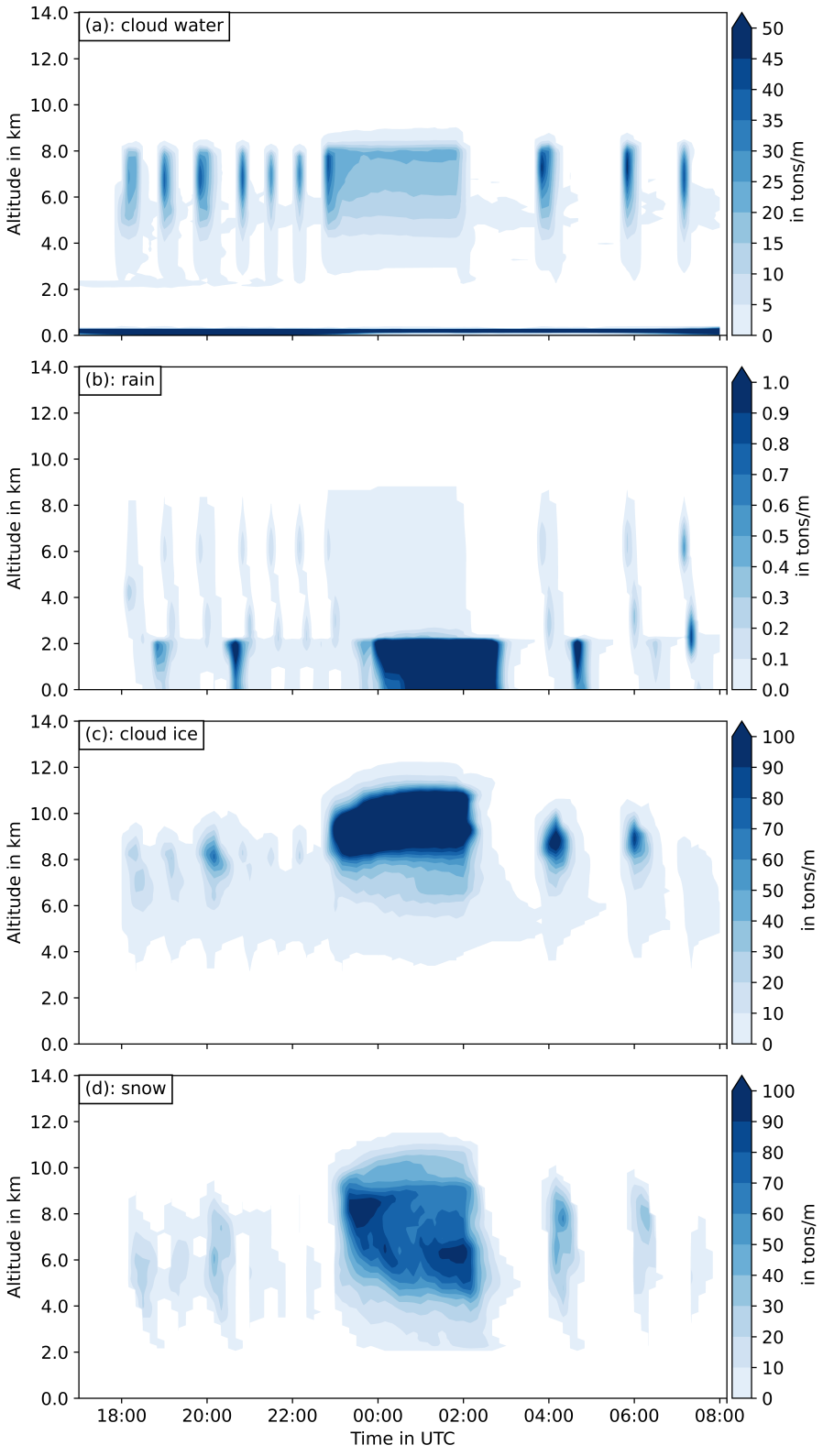

Figure 6.17.: Temporal evolution of vertical mass distribution in tons/m of (a) cloud droplets, (b) rain, (c) cloud ice, and (d) snow for all eruption phases.

Discussion

The comparison between WQ-Exp and Ref simulations regarding the water contents and water paths of the hydrometeors shows that each eruption phase triggers the formation of clouds and precipitation. In general, the generated updraft transports the mixture containing moist ambient air and the emitted volcanogenic water vapor to higher heights. The temperature decreases with increasing height and hence, relative humidity increases until saturation regarding liquid water is reached and formation of cloud water sets in. However, liquid clouds which form due to the eruption, occur only near Raikoke and dissipate eastwards through winds. Upon transport they may reach regions with undersaturated conditions, hence, the liquid droplets evaporate again. Moreover, these clouds form solely above the $T = 0°$C-boundary as below it, the air is probably not saturated with respect to liquid water. A reason could be the heat released by the volcano that heats the surrounding area, lowers the relative humidity, and hampers the formation of clouds. Over time, cloud droplets grow by collision-coalescence until they exceed a certain size and convert into rain drops. Hence, rain often occurs in regions that coincide with the ones where cloud water occurs. However, rain has a sedimentation flux that leads to settling hence, rain reaches lower heights more often compared to cloud water. Between the $T = 0°$C-boundary and $T = -38°$C-boundary, some cloud ice forms due to heterogeneous freezing of cloud water. Remaining cloud water rises further and reaches the $T = -38°$C-boundary, where homogeneous freezing sets in and forms more cloud ice. Homogeneous freezing is assumed to be the major process for cloud ice formation, as the largest amount of cloud ice occurs above the $T = -38°$C-boundary. Formed cloud ice is dispersed eastwards by strong winds, where it then sinks to a height of 4 km due to sedimentation and dynamical effects. The wavy structure seen in *IWC* is probably due to gravity wave driven dynamics (see figure 6.13 (c)). When the plume (ash, dry air, and water) reaches the NBL, it continues to rise up to its top height until the remaining momentum is exhausted. Due to the higher density of the plume compared to the surrounding air, it sinks and transcends the NBL again. Below the NBL, the plume has a lower density than the surrounding air, leading to positive buoyancy and the motion reverses. This alternating motion results in the wavy pattern. Aggregation of cloud ice beyond a certain size results in snow, which has a larger sedimentation flux owing to the larger size, and thus, sinks faster and further than cloud ice. Other processes which cause snow formation is freezing rain either due to heterogeneous nucleation or due to collection of cloud ice. When snow reaches the $T = 0°$C-boundary, it rapidly melts and converts into rain. Hence, rain is frequently abundant below snow and the horizontal dispersion of both rain and snow often have a similar pattern. Moreover, this process leads to markedly higher *RWC*, *RWP*, and larger mass of rain, than the collision-coalescence of cloud water. In figure 6.17 (b), rain persists even after the end of an eruption due to melting snow, and the sharp boundary, which is also visible in figure 6.17 (d), indicates the area where snow starts melting. Among all eruption phases, stronger eruptions and longer duration intensify formation of hydrometeors, thereby, enhancing the water contents, water paths and vertical distribution of masses, as well as the spatial spread of the clouds. However, strong eruptions

(like phase 7) lead to narrow liquid clouds, as the strong updraft quickly carries the cloud water to high altitudes, where it freezes (see figure 6.13). The simulated maximum values of water contents and water paths are comparable with results of other studies using varied methods. Simulated maximum *LWC* agree with observations by Kabanov et al. (2015), that calculated the *LWC* in cumulonimbus (Cb) clouds in the range of 1.0 to 6.0 g/m^3, through radiometer and radar signals. The simulated *IWC* is comparable with *IWC* measurements of up to 3 g/m^3 by Nguyen et al. (2019), using a side-looking X-band airborne radar in tropical mesoscale convective systems (MCSs). The simulated mass mixing ratio of liquid and frozen hydrometeors and their vertical mass disribution, match well with the results from the investigation of hydrometeor formation during volcanic eruptions using the ATHAM model (Herzog et al., 1998; Textor et al., 2006b,a). These results show that volcanic eruptions trigger the formation of clouds and precipitation to a large extent, which facilitate two processes: condensation and freezing release latent heat and lift the plume to higher altitudes, whereas, rain and snow can remove ash from the atmosphere through washout of ash and hence, has a counteracting effect.

6.3.2. Impact of volcanogenic water vapor emission on cloud formation

This section investigates the effects of volcanogenic water vapor on the cloud formation by comparing the WQ-Exp simulation with the NoQ-Exp simulation. To achieve that, the difference of the water contents and water paths for the eruption phases (2, 7, and 10), the vertical mass distribution for all hydrometeor types, and their total masses in the model domain are calculated and presented in section 6.3.1. The results of the remaining phases are shown in section A.4.

Eruption phase 2:

Figure 6.18 shows the differences of mean water contents ΔLWC, ΔRWC, ΔIWC, and ΔSWC at 19:00 UTC. The emission of volcanogenic water vapor leads to a larger water content for all hydrometeor types, whereas, the differences are rather small for this eruption and are mostly < 0.02 g/m^3 for ΔLWC, ΔIWC, and ΔSWC, and < 0.002 g/m^3 for ΔRWC. However, in figure 6.11 (a) and (c), the uppermost parts of both the liquid and ice cloud have a maximum of $\Delta LWC = 0.47$ g/m^3 and $\Delta IWC = 0.69$ g/m^3, respectively. Some small areas within the clouds show negative differences, but they are rather minor (up to $\Delta LWC/\Delta IWC$ = -0.02 g/m^3). The locations of the clouds and precipitation are similar in WQ-Exp and NoQ-Exp, and the shapes are the same as in figure 6.11 (in WQ-Exp).
The differences of the water paths in figure 6.19 also depict rather small differences between WQ-Exp and NoQ-Exp, whereas, ΔLWP shows a somewhat clearer increase of up to 0.24 kg/m^2 in the cloud next to Raikoke. Moreover, in the northeastern area containing the liquid clouds, the ΔLWP-values alternate between positive and negative. Also parts of the ice cloud depict a larger positive difference values up to $\Delta IWP = 0.24$ kg/m^2 but the horizontal spread of the cloud is still narrow. Both ΔRWP and ΔSWP show mostly positive values but they indicate that the results of WQ-Exp and NoQ-Exp do not differ much.

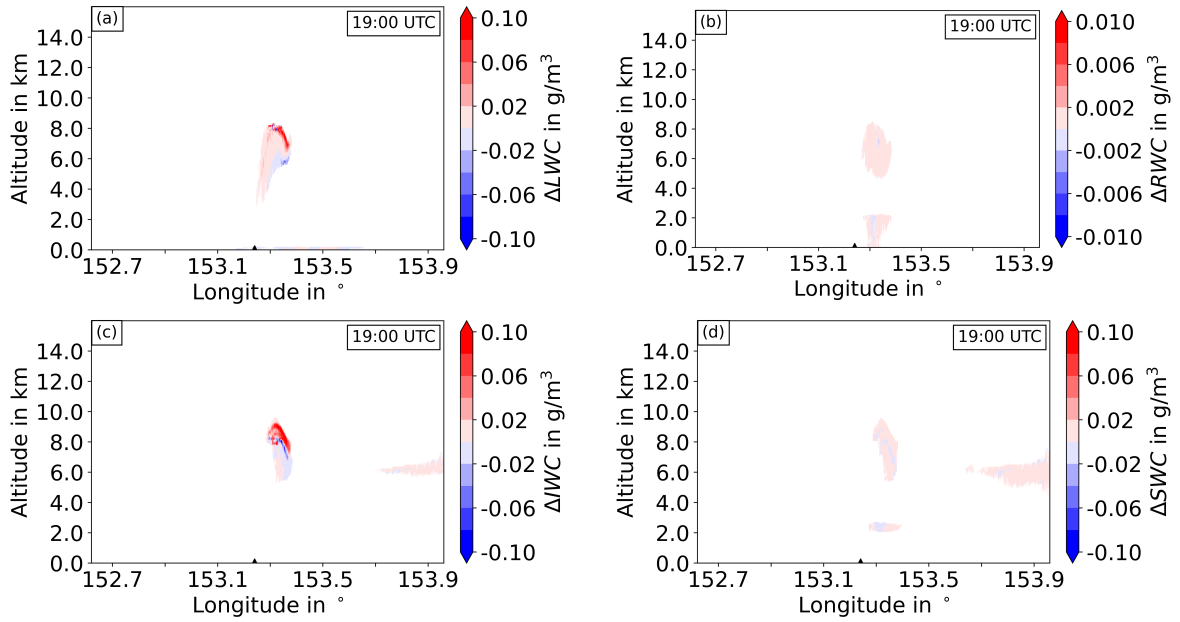

Figure 6.18.: Difference of latitudinally averaged (mean) water contents (a) ΔLWC, (b) ΔRWC, (c) ΔIWC, and (d) ΔSWC in g/m^3 between WQ-Exp and NoQ-Exp at 19:00 UTC during phase 2 in the region from 48.3°N to 48.33°N.

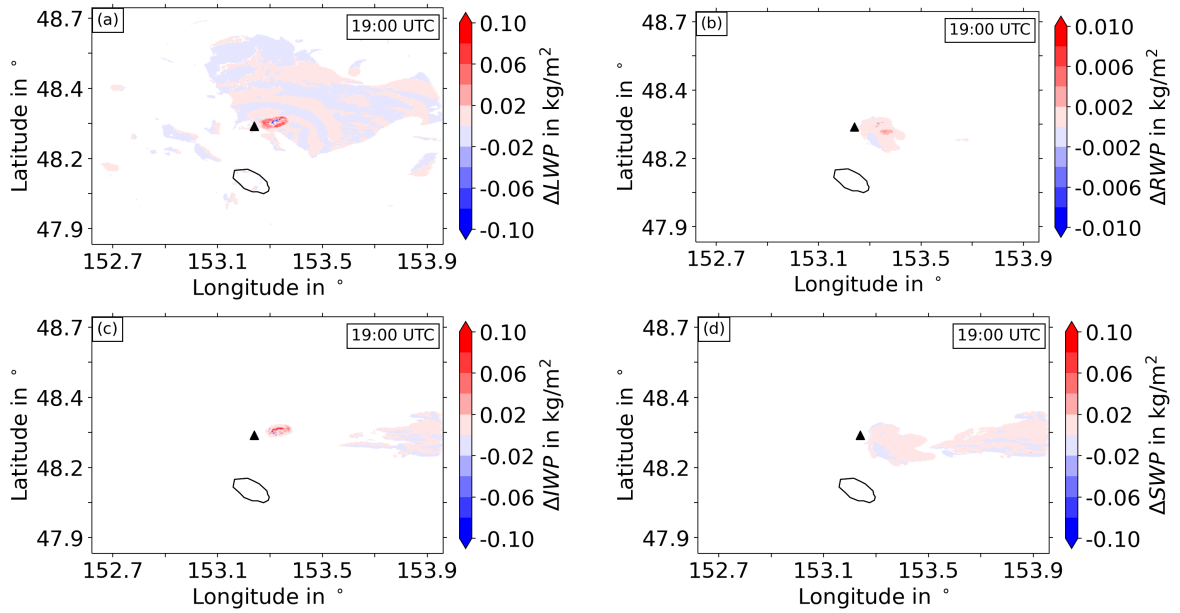

Figure 6.19.: Difference of water paths (a) ΔLWP, (b) ΔRWP, (c) ΔIWP, and (d) ΔSWP in kg/m^2 between WQ-Exp and NoQ-Exp at 19:00 UTC during phase 2.

Eruption phase 7:

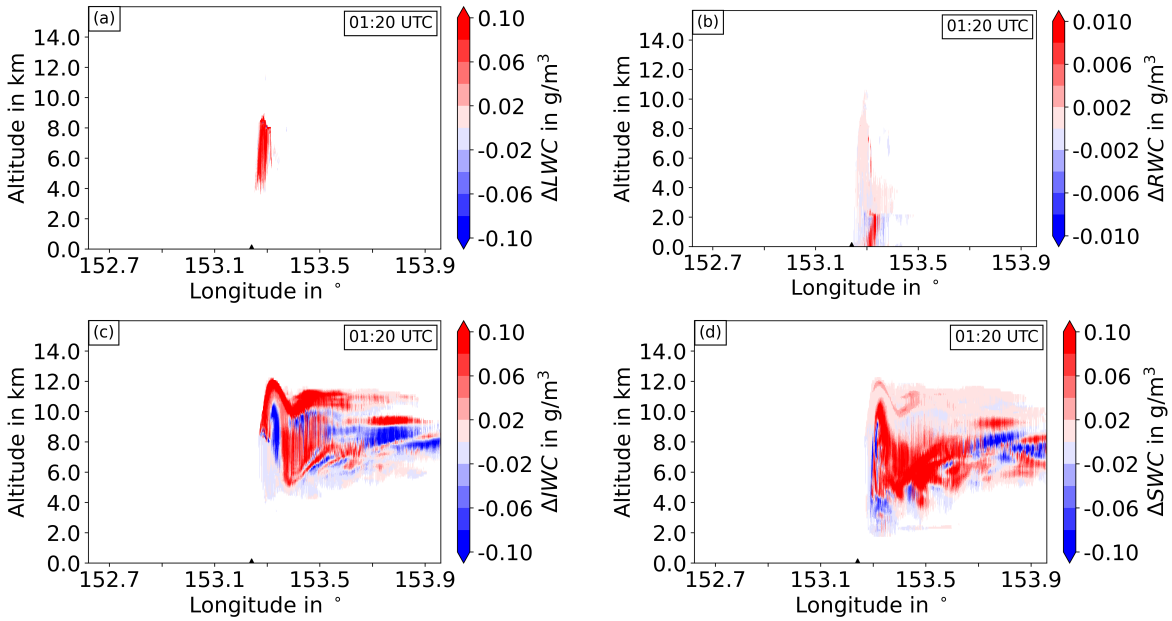

Figure 6.20.: Difference of mean water contents between WQ-Exp and NoQ-Exp at 01:20 UTC during phase 7. See figure 6.18 for description.

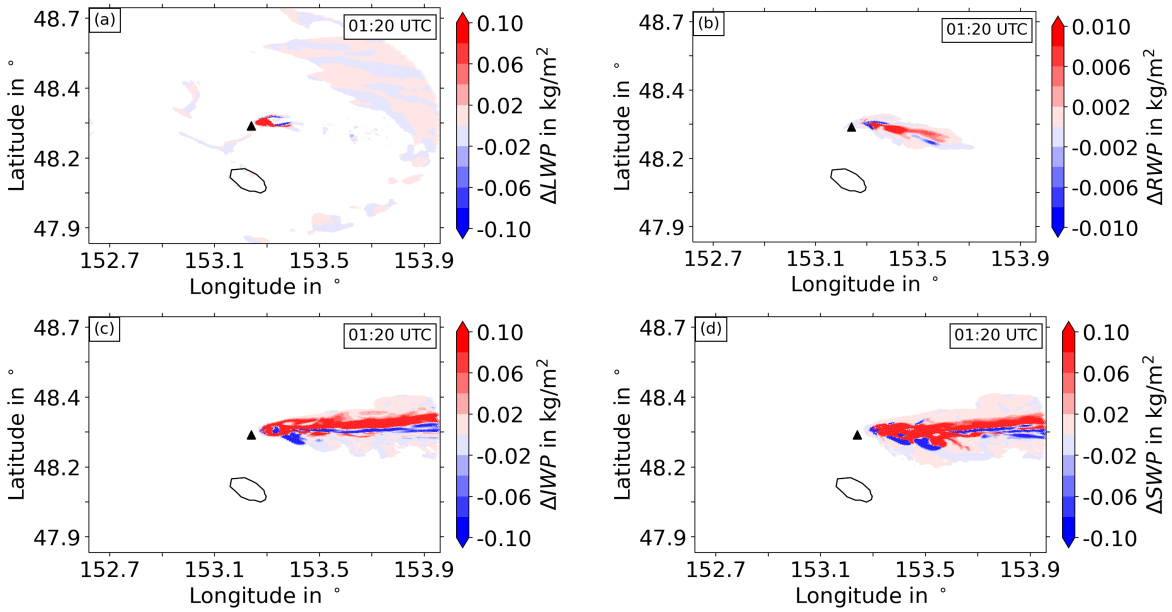

Figure 6.21.: Difference of water paths between WQ-Exp and NoQ-Exp at 01:20 UTC during phase 7. See figure 6.19 for description.

The differences for phase 7 are more distinct in both the water contents and paths. As for ΔLWC in figure 6.20 (a), the values are predominantly positive with maximum $\Delta LWC = 1.07$ g/m^3. Moreover, the formation of rain is more effective in the WQ-Exp simulation, as ΔRWC in the upper area is mostly > 0

g/m^3 whilst, the most pronounced differences occur between the surface and 2 km above it. The values of ΔIWC show an explicit increase and decrease ranging from -1 to +1 g/m^3 (figure 6.20 (c)). However, positive values are seen in more areas, especially in the highest parts of the plume. Moreover, the wavy structure is noticeable here as well like in figure 6.13. The ΔSWC in figure 6.20 (d) indicates a larger amount of snow in WQ-Exp as well, as areas with $\Delta SWC > 0$ g/m^3 clearly dominate. Furthermore, the larger amount of snow leads to an enhanced amount of rain in WQ-Exp.

The more effective formation of clouds and precipitation in WQ-Exp is reflected in figure 6.21 as well, as values > 0 kg/m^2 of each water path mostly spread over a large area, particularly in the case of rain, cloud ice, and snow. Some areas with larger negative values are recognizable as well, which however, appear rarely. The most distinct changes of cloud water are still most notable in the vicinity of Raikoke ($\Delta LWP < 0.24$ kg/m^2), whereas, the clouds in the rest of the domain indicate minor changes in ΔLWP.

Eruption phase 10:

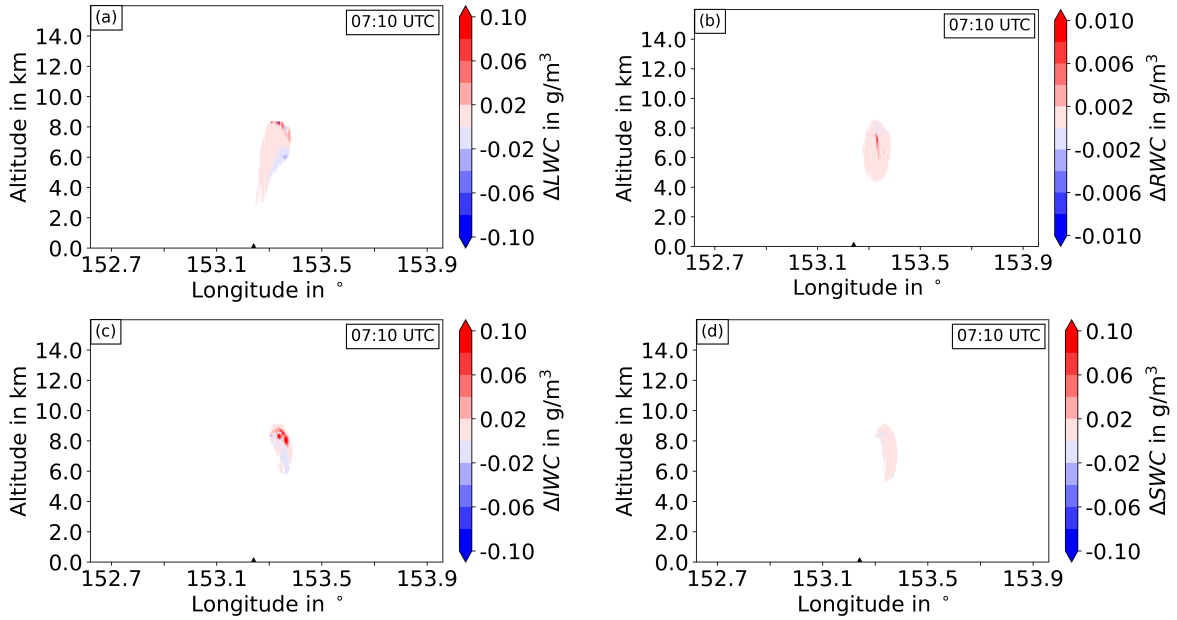

Figure 6.22.: Difference of mean water contents between WQ-Exp and NoQ-Exp at 07:10 UTC during phase 10. See figure 6.18 for description.

As for phase 10, the differences of both the mean water contents (figure 6.22) and water paths (figure 6.23) are much less pronounced and comparable with phase 2. However, it is still visible that volcanogenic water vapor modifies the formation of both clouds and precipitation even for the weakest eruption.

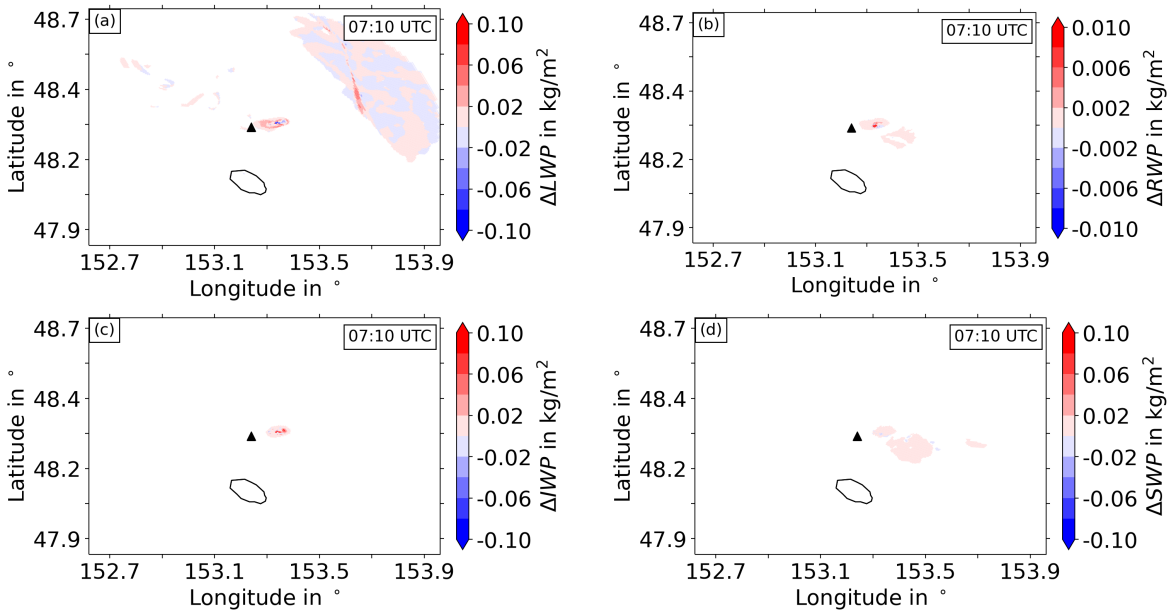

Figure 6.23.: Difference of water paths between WQ-Exp and NoQ-Exp at 07:10 UTC during phase 10. See figure 6.19 for description.

The difference is also calculated for temporal evolution of the vertical mass distribution and displayed for cloud water, rain, cloud ice, and snow in figure 6.24. During most eruption phases, the mass is enhanced in WQ-Exp. Phase 7 stands out with the largest differences, whereas, phases 4, 5, and 6 barely show any differences. Moreover, figure 6.24 (a) reveals predominantly positive values in the lowest levels from 01:00 UTC until the end of the simulation. As for rain in figure 6.24 (b), it reflects a similar pattern that the difference is largest during phase 7 and is lower during phase 4, 5, and 6. Especially the pronounced mass increase from 00:30 UTC to 03:00 UTC is noticeable, whereas, the rain mass in WQ-Exp is considerably less compared to NoQ-Exp at 00:00 UTC. The pattern in the difference plot for ice mass (figure 6.24 (c)) indicates a distinct increase of mass in WQ-Exp in the highest parts of the clouds. This is most identifiable for phases 3, 7, 8, and 9 with an enhancement of up to 60 tons/m compared to NoQ-Exp. However, these phases also show comparatively more mass of ice in NoQ-Exp at lower altitude, thus, showing somewhat a dipole structure. The seventh phase even depicts a second dipole structure further below. A notable increase is also visible in the snow mass in figure 6.24 (d), with the largest differences for phase 3, 7, 8, and 9 with a maximum difference of 22 tons/m during phase 7. Moreover, the WQ-Exp simulation enhances the amount of snow compared to NoQ-Exp for almost the whole area wherever there is occurrence of snow. However, for a short time at 00:00 UTC a lower mass distribution is recognizable in WQ-Exp than in NoQ-Exp.

Finally, figure 6.25 shows the total mass in the model domain for (a) liquid droplets (m_c), (b) rain (m_r), (c) cloud ice (m_i), and (d) snow (m_s). The blue curve refers to the WQ-Exp, the red one to NoQ-Exp, and the green curve to the Ref simulation. In addition, the dashed orange curve represents the difference between WQ-Exp and NoQ-Exp in kilotons. The eruption phases are distinguishable in m_c by the strong

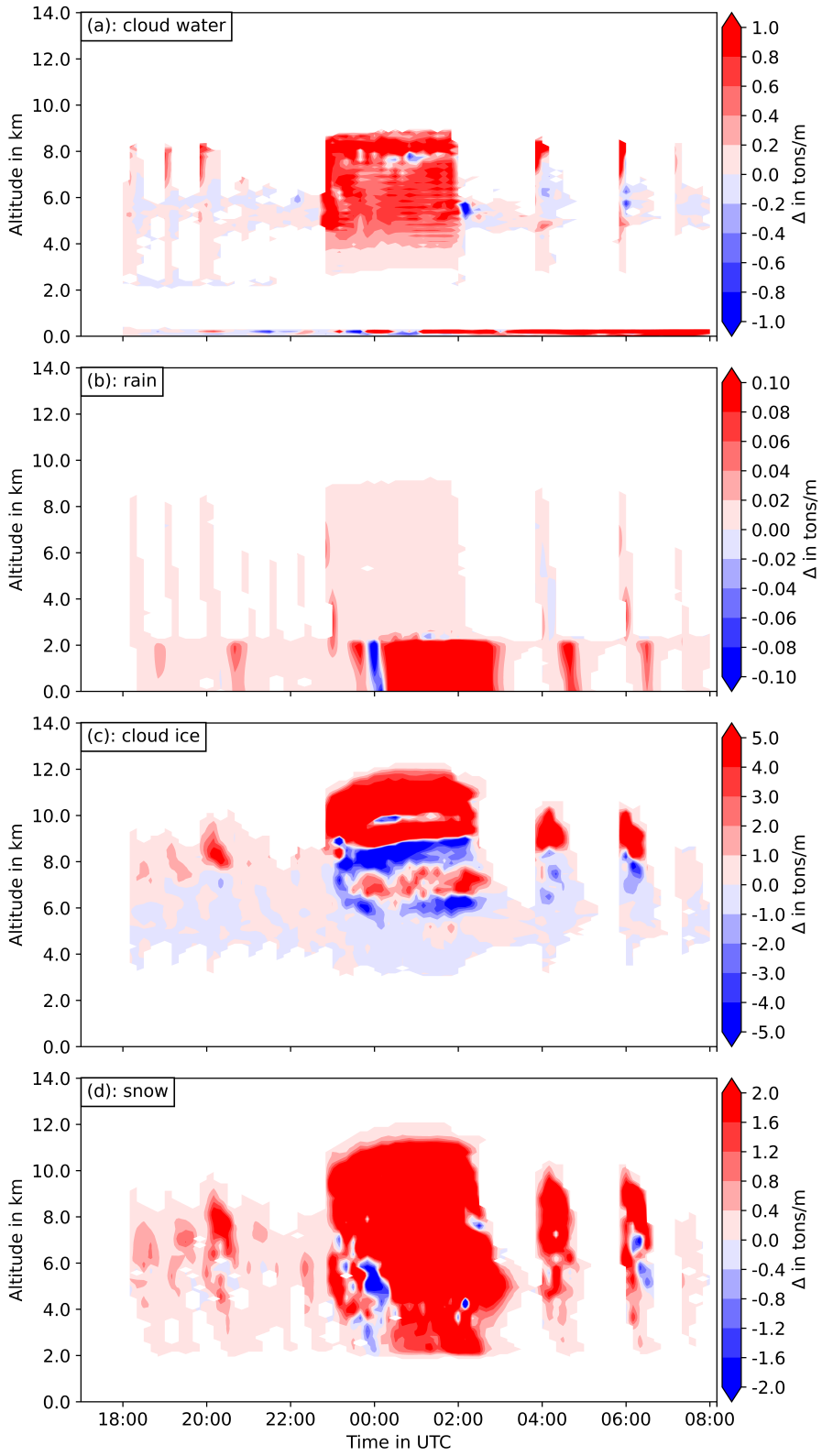

Figure 6.24.: Temporal evolution of the difference of vertical mass distribution Δ in tons/m between WQ-Exp and NoQ-Exp for (a) cloud droplets, (b) rain, (c) cloud ice, and (d) snow for all eruption phases.

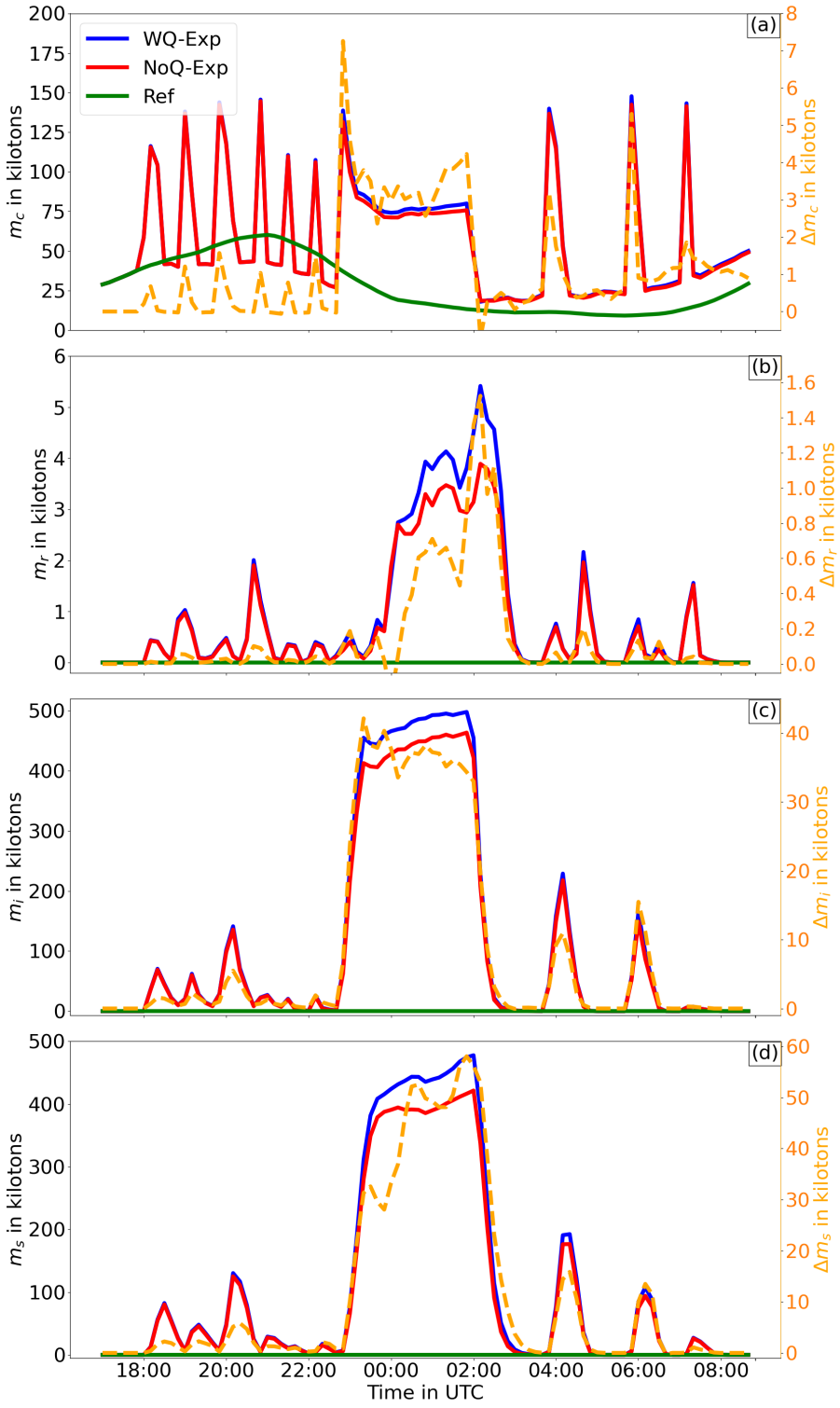

Figure 6.25.: Temporal evolution of mass of (a) cloud water m_c, (b) rain m_r, (c) cloud ice m_i, and (d) snow m_s in kilotons in the model domain. For each the results of WQ-Exp (blue curve), NoQ-Exp (red curve), and Ref (green curve) are shown. The difference between WQ-Exp and NoQ-Exp, Δm_x (dashed orange curve) in kilotons is shown by the secondary y-axis.

increase at the onset of each eruption and a rapid decrease when the eruptions stop. After the first six phases, m_c in WQ-Exp and NoQ-Exp even goes below the one in Ref. The seventh phase is characterized through a first peak and a subsequent mass reduction as seen from the plateau in the curve, until it drops again after the end of the eruption. Except for phase 5 and 6, m_c is comparable among the phases and reaches a maximum of about 137 kilotons in phase 4. Moreover, Δm_c is positive for nearly the entire time, but the values are small with a maximum of 7 kilotons (5%) discrepancy between WQ-Exp and NoQ-Exp. The mass of rain in figure 6.25 (b) is very similar in both WQ-Exp and NoQ-Exp for all phases but the seventh. At the end of the seventh the maximum m_r occurs with 5.5 kilotons in WQ-Exp and 1.5 kilotons (27%) less in NoQ-Ref. In case of no eruptions there is no rain in the model domain during the entire simulation. This is the same for cloud ice and snow and furthermore, m_i and m_s depict a comparable development in both WQ-Exp and NoQ-Exp (figure 6.25 (c) and (d)). A considerably large m_i and m_s build up during phase 7 in WQ-Exp and reach 500 kilotons and 470 kilotons, respectively. The largest differences between WQ-Exp and NoQ-Exp are $\Delta m_i = 42$ kilotons (8%) and $\Delta m_s = 67$ kilotons (14%). Besides, phases 3, 8, and 9 indicate pronounced peaks of m_i and m_s as well but are much lower than those during the seventh phase.

Discussion

The comparison between WQ-Exp and NoQ-Exp reveals that emission of volcanogenic water vapor enhances the water contents and water paths for each hydrometeor type in most areas for all eruption phases. This is also reflected in the vertical mass distribution of the hydrometeors and in their total mass in the model domain. The emission of volcanogenic water vapor increases the relative humidity, thus, the air is saturated faster regarding liquid water and subsequently, cloud water forms earlier and to a larger extent in order to prevent supersaturation. This leads to a more effective formation of rain and cloud ice and thereby, of more snow. A larger amount of rain and snow may lead to faster washout of ash from the atmosphere, thus, depleting the plume of more ash which can consequently affect the plume development. Furthermore, figure 6.24 (c) depicts that compared to NoQ-Exp, there is enhancement of cloud ice in the higher parts of the clouds in WQ-Exp, particularly during phase 3, 7, 8, and 9. This is due to the stronger latent heat release in WQ-Exp, that results in further lofting of cloud ice compared to NoQ-Exp, that explains the dipole structure noticed in the figure. This effect is particularly strong in phase 7, and in this case, the lofted cloud ice can potentially hamper the incoming solar radiation to an extent that it leads to cooling at lower levels in WQ-Exp. Compared to NoQ-Exp, these levels are probably cold enough to initiate formation of more cloud ice, subsequently, shown by the second dipole structure in the results. In general, the seventh eruption phase stands out the most due to its strength and duration, which lead to a long-lasting strong emission of volcanogenic water vapor, causing a modified development of hydrometeors.

After the phases 1-6, the drop of m_c below the values in Ref in figure 6.25 (a) may be due to the heat released by the volcano affecting the surrounding area in different ways. The pre-existing cloud water

in the surrounding area is maybe evaporated due to the heat, or transported to higher heights due to the updraft caused by $\hat{w}_e$ and $\hat{\theta}_{v,e}$. This transported mass, for instance, could possibly transform into precipitation or cloud ice, which later on, may be filtered out by deposition or exit the model domain through strong winds. On comparison with mass of cloud ice observed in historic eruption plumes, both WQ-Exp and NoQ-Exp simulated values in a reasonable range. The Rabaul eruption plume in 1994 in Papua New Guinea contained 2 megatons of ice, likely due to the evaporation of sea water (Rose et al., 1995). About 1 megatons of ice formed in the plume of the Hekla eruption in 2000 in Iceland, which was due to ground water coming into contact with the hot mixture, and led to further water (vapor) supply (Lacasse et al., 2004; Yu and Rose, 2000). The volcanic plume of the large Pinatubo eruption in 1991 in the Philippines contained about 80 megatons of ice (Guo et al., 2004a,b), caused by its strength and its location in the tropics, providing large amounts of water vapor for entrainment. Thus, plumes developed by volcanic eruptions at low latitudes usually consist of a larger amount of ice compared to those at higher latitudes (Rose et al., 2004; Textor et al., 2006b,a), like Raikoke, as also seen from the simulated values in this study.

In general, in all eruption phases, the differences between WQ-Exp and NoQ-Exp are rather small in most areas, for the values of water content, water path, vertical mass distribution, and total mass. In the NoQ-Exp simulation, the formation of clouds and precipitation is due to the dynamical effects of the eruption, whereas, in WQ-Exp, emission of volcanogenic water vapor is also considered, but these simulated minor differences show that this only has a minor effect. This comparison thereby, reveals that the formation of clouds and precipitation is dominantly caused by the dynamical effect due to the $\hat{w}_e$ and $\hat{\theta}_{v,e}$ at the source, instead of volcanogenic water vapor.

6.3.3. Vertical distribution of water vapor in the atmosphere affected by the eruption

This section explores the impact of the eruption on the vertical distribution of water vapor and whether water vapor is injected into the stratosphere. To investigate this, figure 6.26 displays how the difference of the vertical mass distribution between WQ-Exp and Ref develops over time. Again, the eruption phases are distinguishable, as ten distinct individual regions show values > 0 tons/m between a height of 4 km and maximum 9 km (phase 7). From the surface to a height of about 4 km, the values alternate between positive and negative, while three distinct levels occur, where WQ-Exp contains less water vapor than Ref. These levels are located at a height of 2.5 km and 3 km and appear during the entire simulation and, a third one starts forming at 23:00 UTC, which then remains until the end of the simulation. At the remaining heights and times, WQ-Exp clearly contains more water vapor and thereby, these alternating positive and negative values lead to a dipole structure. The largest differences occur below an altitude of about 9 km (below the tropopause), however, low positive values even reach a height of up to 13 km, particularly during phase 7. This may suggest a possibility of water vapor reaching the lower stratosphere. However, the results in section 6.3.1 reveal that the eruption phases cause a pronounced lofting of the tropopause, thus, the enhanced amount of water vapor up to 13 km may still remain below the tropopause.

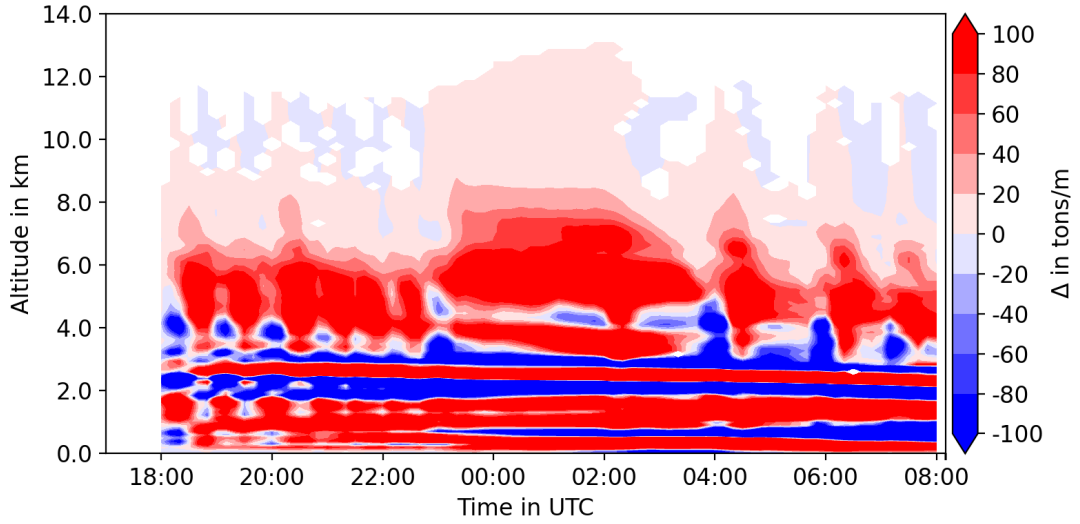

Figure 6.26.: Temporal evolution of the difference of the vertical distribution of the water vapor mass Δ in tons/m between WQ-Exp and Ref.

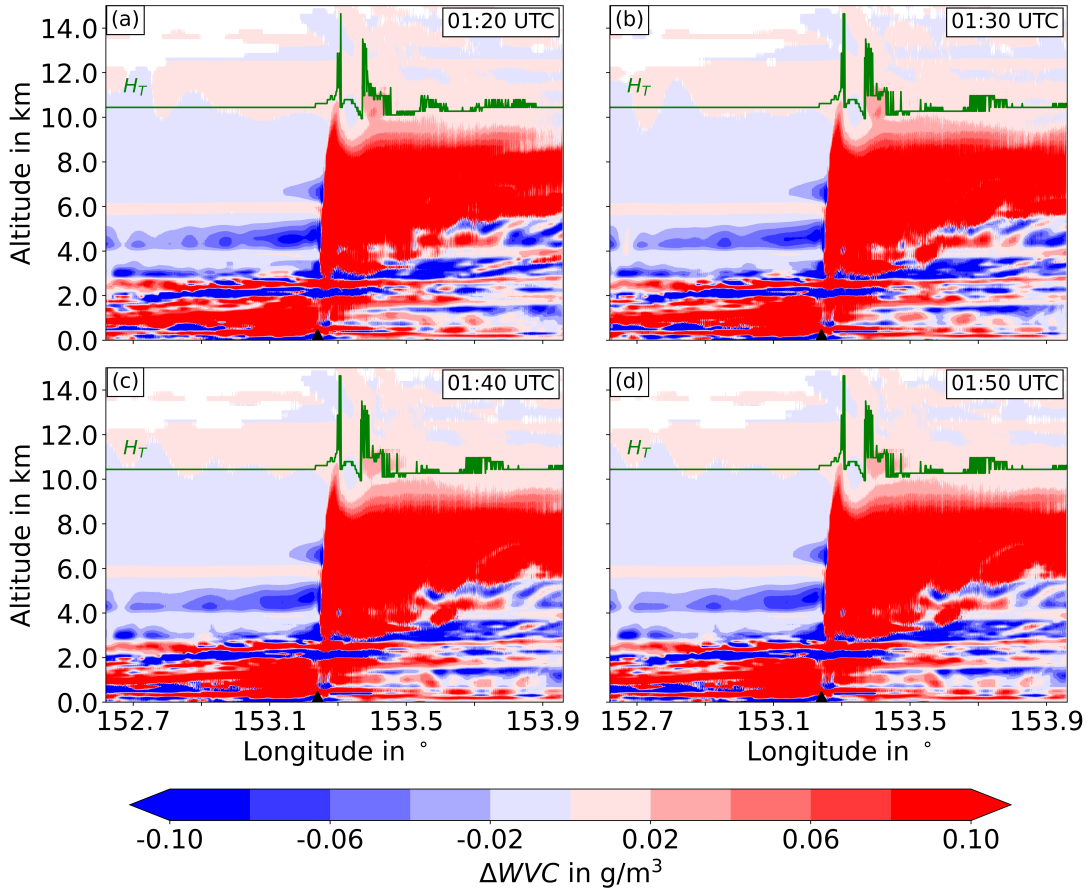

Figure 6.27.: Difference of latitudinally averaged (mean) water vapor content ΔWVC in g/m^3 between WQ-Exp and Ref at (a), 01:20 UTC (b) 01:30 UTC, (c) 01:40 UTC, and (d) 01:50 UTC during phase 7 in the region from 48.3°N to 48.33°N. The green curve shows the height of the tropopause H_T.

Therefore, figure 6.27 depicts the difference of the mean water vapor content ΔWVC between WQ-Exp and Ref during phase 7 from 01:20 UTC until 01:50 UTC, including the mean H_T in WQ-Exp. Both ΔWVC and H_T are calculated for the region from 48.3°N to 48.33°N. The comparison between WQ-Exp and Ref indicates an alternation of positive and negative values in altitudes below approximately 5 km, whereas, the water vapor content from the vicinity of Raikoke to the east at heights between ∼5-10 km is clearly enhanced in WQ-Exp. However, H_T is obviously lifted during the eruption and ΔWVC mainly follows the shape of H_T without transcending it, although, a small amount presumably reaches the lower stratosphere ($\Delta WVC < 0.02$ g/m^3). To find the amount of water vapor that is injected into the lower stratosphere, figure 6.28 (a) shows the water vapor mass m_v above the tropopause as a function of time in UTC. The results are presented for WQ-Exp with $\hat{\theta}_{v,e} = 650$ K (red curve), $\hat{\theta}_{v,e} = 700$ K (black curve), and $\hat{\theta}_{v,e} = 750$ K (magenta curve), as well as for Ref (green curve) and in addition, 6.28b displays the difference Δm_v between each of the three WQ-Exp simulations and Ref. The different simulations of WQ-Exp are chosen, as a larger $\hat{\theta}_{v,e}$ strengthens the updraft that lifts water vapor higher up. Both plots reveal slight increases of m_v during all phases in all WQ-Exp simulations compared to Ref, however, they are very small in majority of the cases. Although, m_v is about 7.5 kilotons, 11 kilotons, and up to

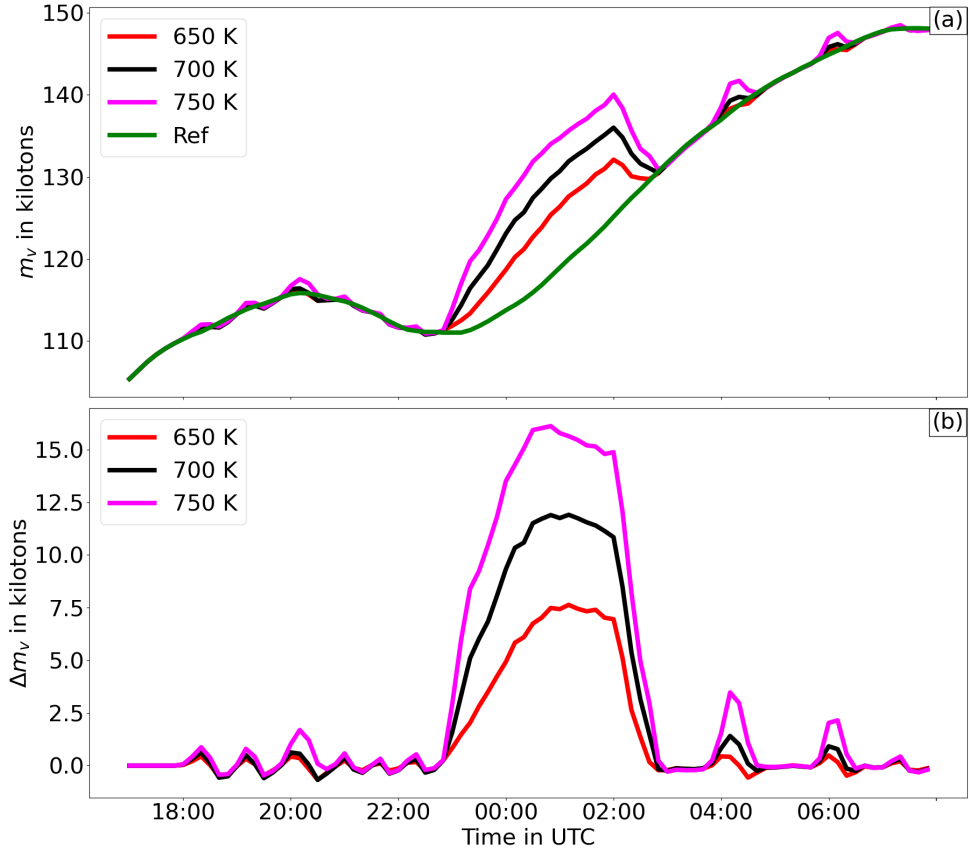

Figure 6.28.: (a) Temporal evolution of the water vapor mass m_v in kilotons above the tropopause for WQ-Exp with $\hat{\theta}_{v,e} = 650$ K (red curve), 700 K (black curve), and 750 K (magenta curve), and Ref (green line). (b) Differences of water vapor mass Δm_v between WQ-Exp and Ref in kilotons.

16.5 kilotons larger in WQ-Exp for $\hat{\theta}_{v,e} = 650$ K (6%), $\hat{\theta}_{v,e} = 700$ K (9%), and $\hat{\theta}_{v,e} = 750$ K (14%), respectively, compared to Ref. Hence, some water vapor seems to transcend the tropopause and reach the lower stratosphere.

Discussion

The comparison between WQ-Exp and Ref reveals a considerable enhancement of water vapor in all eruption phases up to a height of about 8 km, depending on the eruption strength. This enhancement is caused by the emission of volcanogenic water vapor and in addition, due to lofting of ambient water vapor by the strong updrafts associated with the eruptions. Moreover, $\hat{\theta}_{v,e}$ causes a heating of the surrounding area, which may lead to evaporation of preexisting cloud water and hence, a higher amount of water vapor in WQ-Exp. The three pronounced areas in figure 6.26, where WQ-Exp contains less water vapor compared to Ref may occur due to different reasons. With respect to the region of a height between 2 and 3 km, the values alternate from negative to positive and to negative again. The negative values probably occur due to the formation of cloud water in WQ-Exp, as cloud water starts forming at these heights, resulting in a reduction of water vapor. However, some water vapor could be dispersed to areas, which are undersaturated with respect to liquid water and therefore, the water vapor does not condensate and remains in this thin layer. The region that reveals negative values from 23:00 UTC until the end at a height of 1 km may occur due to the long-lasting eruption phase 7, that lifts a large amount of water vapor from this height to higher altitudes. The comparison also shows that some water vapor even reaches heights up to 13 km (phase 7). However, the eruptions not only lift the water vapor but the tropopause as well, hence, water vapor follows the shape of the tropopause and mostly stays below it. Thus, the majority of eruption phases only inject a negligible amount of water vapor into the lower stratosphere, whereas, the seventh phase leads to a somewhat larger increase of the water vapor mass, depending on $\hat{\theta}_{v,e}$ in the heat source. As winds rapidly transport the water vapor out of the model domain, its impact on the radiation budget or on stratospheric chemistry can not be investigated, though, it is assumed to have either no or only minor effects due to the rather small amount.

6.4. Generation of atmospheric waves during the eruptions

Himawari-8 satellite presumably captured atmospheric waves propagating away from Raikoke that are visible in form of somewhat concentric circular shapes in the cloud cover. These waves are most distinct during eruption phase 7 and therefore, this phase is chosen for further investigation of the generation of atmospheric waves triggered by volcanic eruptions. Figure 6.29 shows the Hi8 satellite images from 22:50 UTC to 23:20 UTC. The red rectangles mark the areas in the west and northwest where the waves are most obvious. However, they are generally indistinct and seem to dissipate not far away from Raikoke (figure 6.29 (d)). The satellite images do not provide latitude and longitude, thus, it is challenging to estimate both their phase velocity and wavelength. Nevertheless, they seem to travel only a short

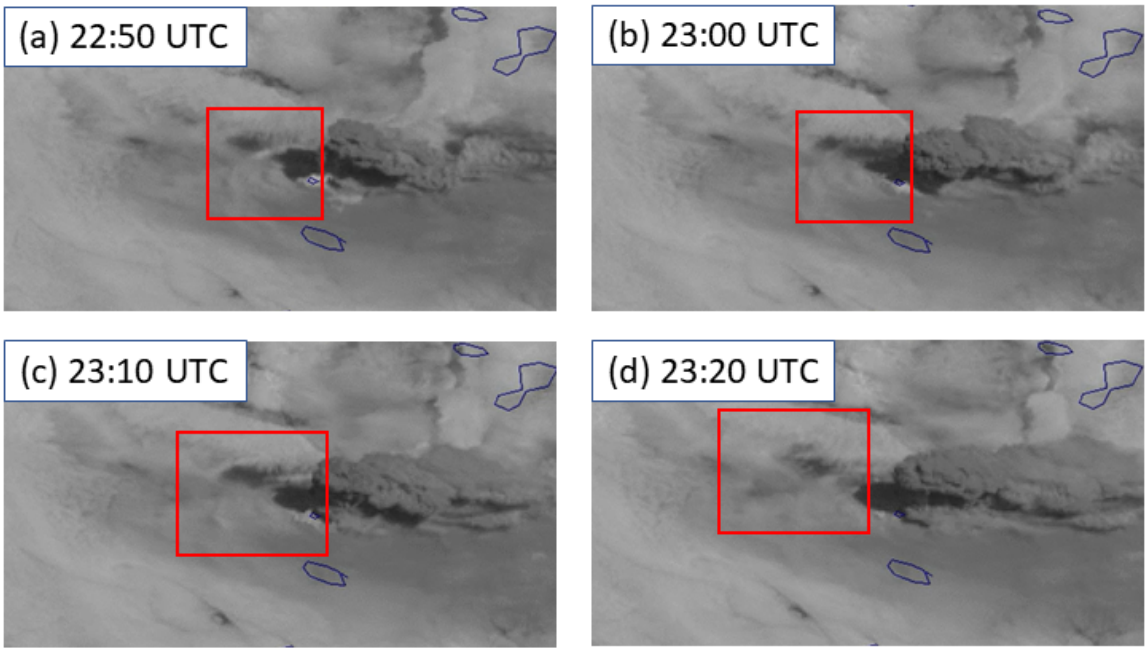

Figure 6.29.: Atmospheric waves captured by the Himawari-8 satellite at (a) 22:50 UTC, (b) 23:00 UTC, (c), 23:10 UTC, and (d) 23:20 UTC.

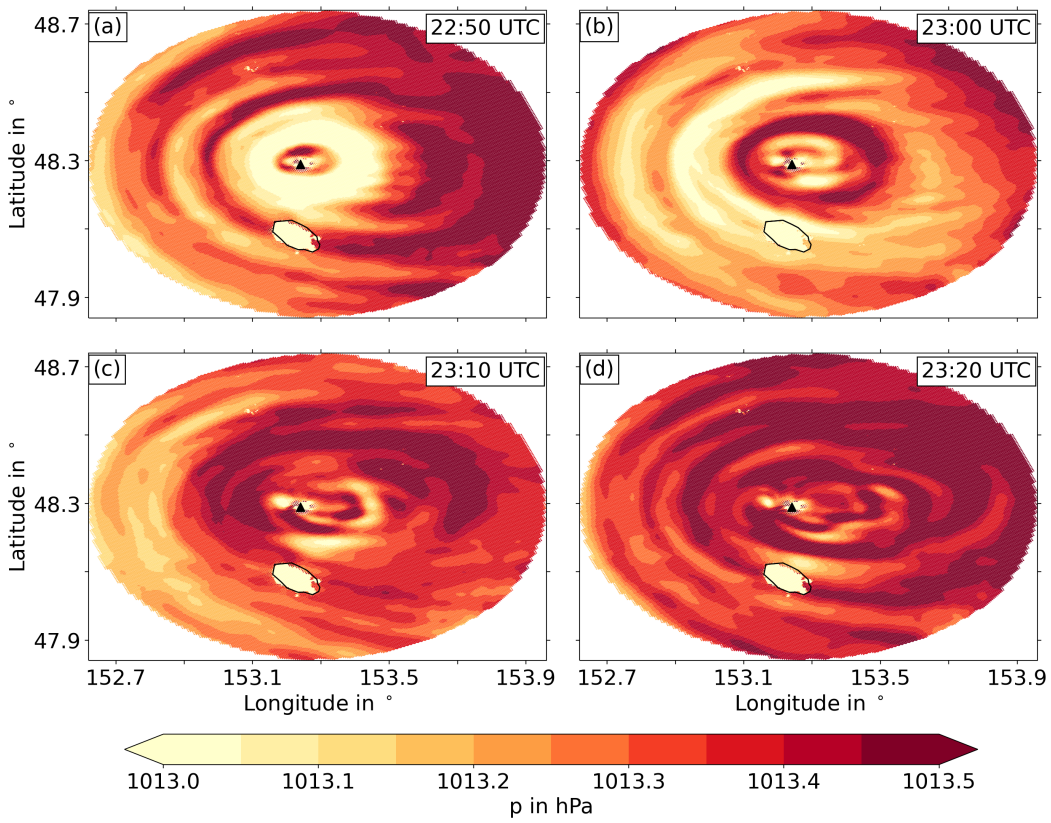

Figure 6.30.: Pressure p in hPa at a height of 100 m at (a) 22:50 UTC, (b) 23:00 UTC, (c), 23:10 UTC, and (d) 23:20 UTC. The black triangle depicts the location of Raikoke.

distance within 10 minutes, hence, they are assumed not to be sound waves. The observations of these waves prompts the motivation to investigate the model's ability to simulate atmospheric waves during the eruption as well. Atmospheric waves can be indicated by perturbations in the air pressure, therefore, figure 6.30 shows the horizontal air pressure p at a height of 100 m from 22:50 to 23:20 UTC. Circles of high p (red color) and comparatively low p (yellow color) indicate the wave's amplitude, which are clearly noticeable at 22:50 UTC and 23:00 UTC. However, they seem to dissipate fast, as they are barely visible at 23:10 UTC and 23:20 UTC. The wave in figure 6.30 (a) and (b) propagates with a slower phase velocity v_p to the east than to the west and, the high p-circle is used to estimate the wavelength λ and v_p at lat = 48.3°, as it is the most distinguishable one. From 22:50 UTC to 23:00 UTC the wave covers a distance of about 0.1° to the west and approximately 0.16° to the east, which corresponds to a wavelength of $\lambda_1 \approx 7$ km and $\lambda_2 \approx 12$ km, respectively. Supposing a period $T = 10$ minutes $= 600$ s, $v_{p,1}$ (to the west) and $v_{p,2}$ (to the east) result in

$$v_{p,1} = \frac{\lambda_1}{T} \approx 11.67 \,\frac{\text{m}}{\text{s}}, \quad v_{p,2} = \frac{\lambda_2}{T} \approx 20 \,\frac{\text{m}}{\text{s}}. \tag{6.1}$$

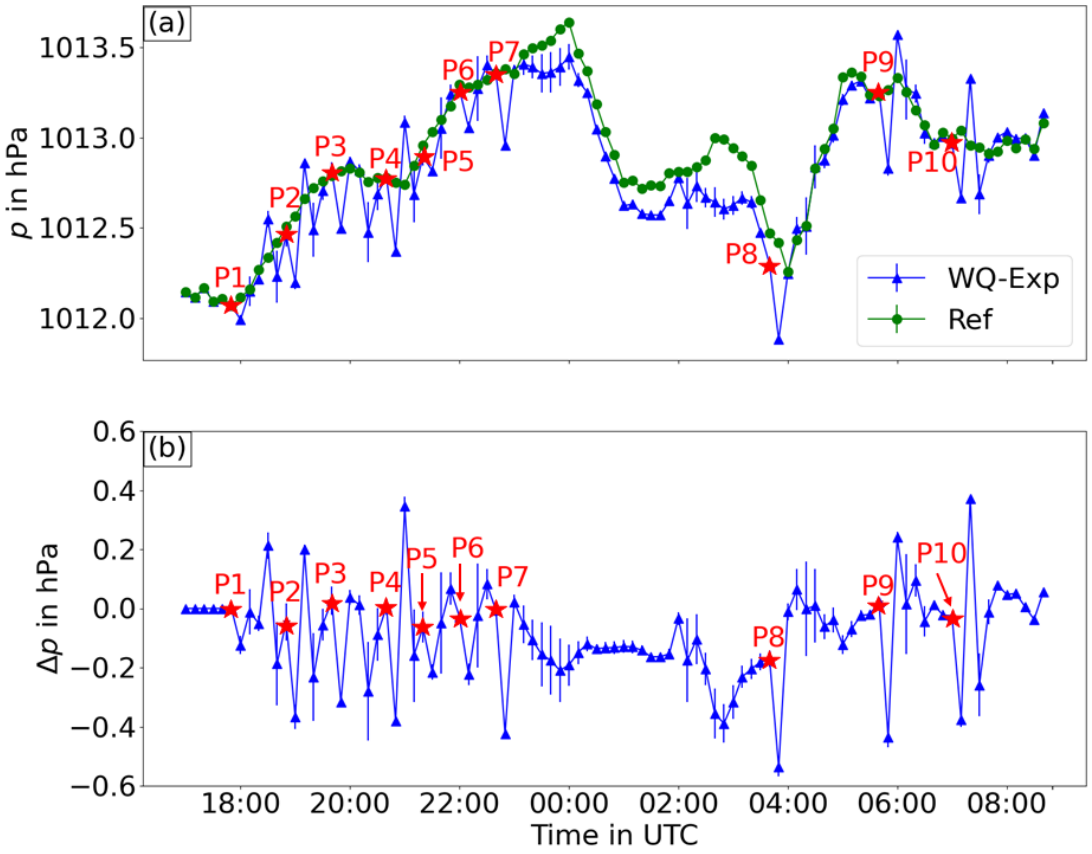

Figure 6.31.: (a) Temporal evolution of the mean pressure p in hPa at 100 m altitude for an area between 48.28°N to 48.32°N and 153.11°E to 153.15°E and, (b) its difference to Ref Δp in hPa. The vertical lines depict the standard deviation and red asterisks show the start of each eruption phase P.

It is challenging to estimate λ and v_p for the times at 23:10 UTC and 23:20 UTC, as the pattern in p strongly dissipates, therefore, these times are neglected.

To analyze the effect of each eruption phase P on p, the temporal evolution of the mean p and its standard deviation are calculated for an area between 48.28°N to 48.32°N and 153.11°E to 153.15°E for WQ-Exp (blue curve) and shown in figure 6.31. In addition, it includes the result of Ref (green curve) and the difference Δp between WQ-Exp and Ref. After the start of each eruption phase, p first decreases and immediately increases one time step later, which leads to an alternating Δp from negative values (minimum -0.58 hPa) to positive values (maximum 0.38 hPa). A permanent negative Δp develops during phase 7, as it is $\Delta p < 0$ hPa over the entire eruption duration. However, p in WQ-Exp follows the shape of p in Ref from 23:10 UTC onwards, which indicates the dissipation of the generated waves shortly after the start of phase 7. For further investigation of the generated waves in the onset of an eruption, figure 6.32 depicts the horizontal p at a height of 100 m for the onset of phase 7 from 22:40:10 UTC to 22:40:40 UTC. It reveals that multiple fine waves appear at frequent intervals in the vicinity of Raikoke, indicated by the dark red color, and travel in circles away from the volcano. They cover a distance of about $\Delta lon \approx 0.05°$ to both eastern and western direction from 22:40:10 UTC to 22:40:20 UTC and, continue travelling with the same v_p for the later time steps. This corresponds to a wavelength λ of

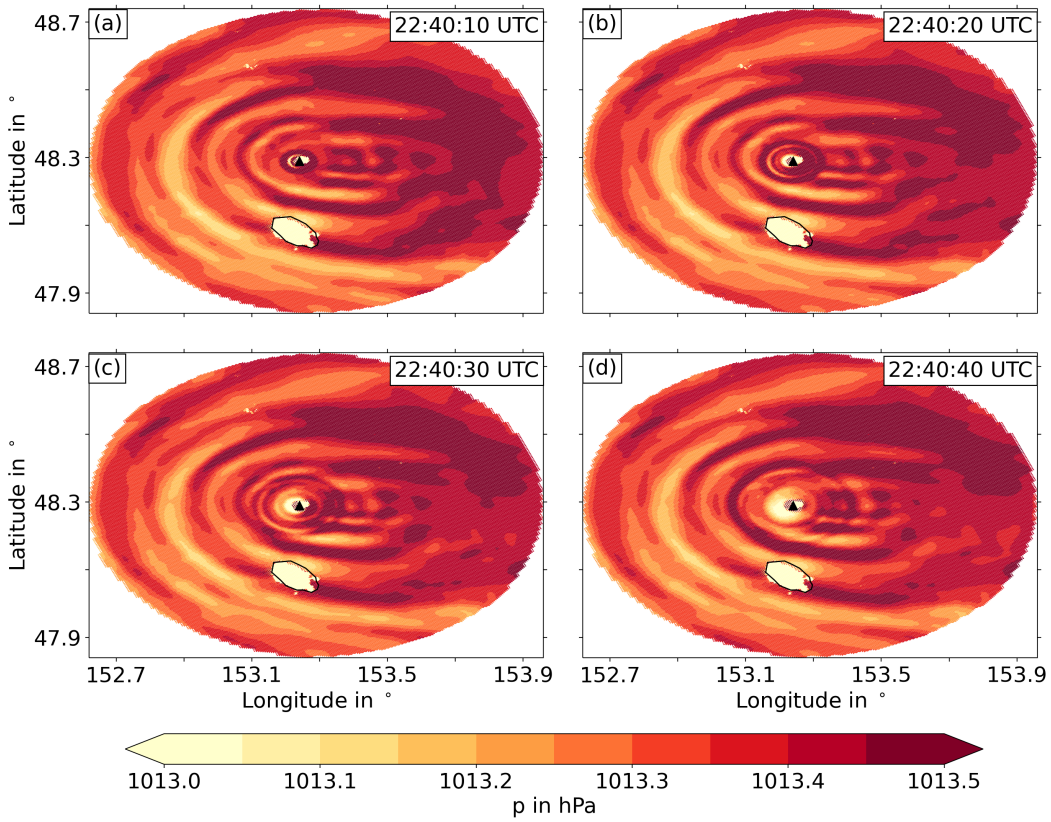

Figure 6.32.: Same description as for figure 6.30 for (a) 22:40:10 UTC, (b) 22:40:20 UTC, (c), 22:40:30 UTC, and (d) 22:40:40 UTC.

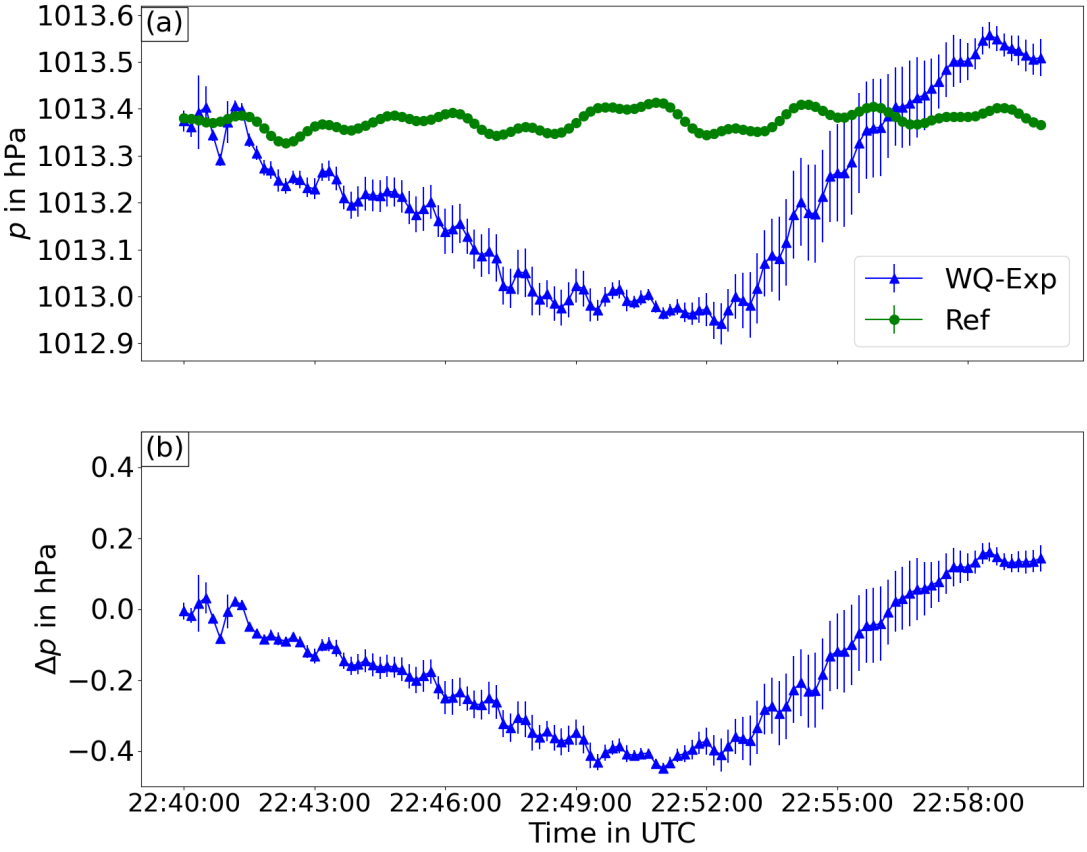

Figure 6.33.: Same description as for figure 6.31 for 22:40:00 UTC to 23:00:00 UTC.

approximately 3.2 km within a period $T = 10$ s, that results in a v_p of approximately 320 m/s, which is nearly the speed of sound $c = 331.29$ m/s in dry air for $T = 0°C$ (Wong, 1986). However, the waves again dissipate after a short distance, as they become indistinct after 30 s.

Finally, figure 6.33 shows the temporal evolution of p for WQ-Exp (blue curve) and Ref (green curve) and in addition, Δp between both simulations, from 22:40 UTC to 23:00 UTC for the same region as for figure 6.31. The comparison between WQ-Exp and Ref in this area reveals a pressure drop in WQ-Exp, starting from the onset of eruption phase 7 at 22:40 UTC until 22:51 UTC, when the minimum of Δp (-0.42 hPa) is reached. Afterwards, p in WQ-Exp increases and exceeds p in Ref of up to $\Delta p \approx 0.18$ hPa shortly after 22:58 UTC.

Discussion

Two main factors are assumed to generate atmospheric waves in the modified ICON-ART during the eruptions, including the high $\hat{w}_e$ and $\hat{\theta}_{v,e}$, and the input of mass due to the ejected material. The first factor causes a strong updraft that leads to a pressure decrease near the surface in the vicinity of Raikoke. Moreover, this could be the reason that the pressure first drops after the start of each eruption (figure 6.31) and specifically during the beginning of phase 7 (figure 6.33). The mass input is the second factor

and counteracts the first one, as it increases $\overline{\rho}$, reduces the positive buoyancy from the updraft until it is counterbalanced and hence, it increases p again.

The investigation of atmospheric waves in the model that are generated during the eruption phases (particularly phase 7) depicts a good agreement with those observed in Himawari-8 satellite images. As they seem to travel rather slowly in both model and observation ($v_p \approx 11.7 - 20$ m/s), they are assumed to be atmospheric gravity waves. However, at the beginning of phase 7, the waves indicated by the simulated p (figure 6.32) have a phase velocity of up to 320 m/s. Although, they are still somewhat slower than c, this may agree with Medici et al. (2014), who stated that weak shock waves ($v_p > c$) are frequently generated by explosive volcanic eruptions and transition to sonic waves shortly after generation.

There are no measurements of the atmospheric pressure nearby Raikoke during the eruptions, however, the simulated pressure perturbations of up to -0.42 hPa are comparable with microbarograph measurements during eruptions of the Soufrière Hills volcano in Montserrat in 2003 and 2009 of -10 to -40 Pa (Baines and Sacks, 2017).

Note that this study is one of the first ones to investigate the generation of atmospheric waves with ICON-ART, as this model has not been developed to focus on atmospheric waves. However, as the pressure perturbations simulated by the model are in a reasonable range, it prompts the motivation to further investigate the generation of atmospheric waves with ICON-ART. To understand the most relevant processes that trigger atmospheric waves, as well as what kind of waves are generated under which conditions, a more detailed investigation is necessary.

7. Conclusions and Outlook

The aim of this study is to enable high resolution, explicit simulations of volcanic eruption plumes, for one of the very first times with a numerical weather prediction (NWP) model. Explicit simulations consider (a) the volcanic plume as a multicomponent multiphase flow, (b) exit velocity at the source during the eruption, and (c) an exit temperature representing the high temperature of the emitted mixture. Additionally, the use of an NWP model allows the atmospheric state to be simulated in detail at each time step. The central focus of this study is to investigate the effects of dynamical and microphysical processes (particularly, cloud formation) in the plume, on the plume development during its initial stage and, the influence of an eruption on the surrounding atmosphere. Within the scope of this study, three different types of simulations were performed. The first two types are idealized quasi 2-D simulations of (a) a falling mixed-bubble comprising of ash and cold air and, (b) a volcanic eruption. These types of simulations serve the purpose of preliminarily testing the new implementations. The mixed-bubble test shows the dynamical effects of added ash on the flow density in the atmosphere and, in addition, it presents the sink of mass of total air. The simulation of an idealized volcanic eruption intends to explicitly simulate the plume development by incorporating the mass source of total air as well as the exit velocity and exit temperature during an eruption. This allows to simulate the plume consisting of the three regions: jet region, with a smooth transition to the convective region, and the umbrella region. Following the successful preliminary tests in case of idealized simulations, the new implementations are then applied for a real case scenario of the Raikoke eruption in June 2019. This eruption was characterized by ten different eruption phases, and all these phases were simulated in a single simulation considering emission of ash and volcanogenic water vapor. These explicit simulations consider detailed source conditions and all other aspects which were neglected in previous works on the dispersion of the Raikoke eruption plume.

7.1. Concluding remarks

Based on the simulations performed as part of this study, and the detailed analysis of the results enable to address the following research questions:

1. **What has to be modified in an NWP model like ICON-ART to realise the explicit simulation of a volcanic eruption plume as multicomponent multiphase flow?**
   To explicitly simulate volcanic eruption plumes with ICON-ART, the additional ash emission and a sink of the mass needs to be accounted for in the total mass budget of air. To fulfill these two ne-

cessities, a mass source for the total air mixture is implemented and the lower boundary condition for $\hat{w}$ is modified in ICON-ART. This results in a conserved mass of dry air, however, varying mass of total air which subsequently enables the interaction between ash and the dynamics. Instead of using vertical emission profiles, as was the case in previous studies, the emitted mixture is transported to higher altitudes due to the updraft caused by the exit velocity $\hat{w}_e$ and exit temperature $\hat{\theta}_{v,e}$ implemented at the source.

The results of the idealized quasi-2D simulations confirmed the importance of the implementations to realize explicit simulations of volcanic eruption plumes, following which, these were applied in the simulation of the Raikoke eruption. For validation of the results, the vertical and horizontal plume shape reproduced by ICON-ART and the ash mass loading were compared with observations. Further sensitivity tests were performed, results of which are addressed below.

2. **Can the modified ICON-ART provide reliable results regarding the plume height, dispersion, and ash mass loading?**
   Simulations with ICON-ART could reproduce to a great extent, the vertical and horizontal plume dispersion as detected from GOES-17 and Himawari-8 satellite observations. However, compared to observations, the plume height given by the model is overestimated for the weakest eruption phase ($> 29\%$, depending on $\hat{\theta}_{v,e}$) and, underestimated for the strongest phases ($> 8\%$). The ash mass loading computed by the model is about 10-100 times greater than that obtained from AHI observations from the Himawari-8 satellite. However, in cloudy regions, it is challenging for AHI observations to distinguish between ash and meteorological clouds, thus, using model results can be advantageous. Whilst there are discrepancies between model results and observations, it is worth noting that both have some associated uncertainties within which, ICON-ART provides reliable plume characteristics.

3. **How sensitive is the plume development to different exit temperatures at the source?**
   The sensitivity study to investigate the dependency of plume development on exit temperature shows that the plume height is more sensitive to differing values of $\hat{\theta}_{v,e}$ than of $\hat{w}_e$ and MER. When comparing different phases (each characterized by specific $\hat{w}_e$ and MER), for a fixed value of $\hat{\theta}_{v,e}$, there are no major differences in the plume height, thus, confirming its low sensitivity to $\hat{w}_e$ and MER. However, this is not the case for the seventh phase, as for a fixed value of $\hat{\theta}_{v,e}$ the plume height is higher compared to that of other phases. This implies that for phase 7, $\hat{w}_e$/MER dominantly affect the plume height due to their considerably higher values and the long duration of the eruption. Changes in $\hat{\theta}_{v,e}$ from 550 K to 750 K in increments of 50 K results in almost linear increase in plume height in the range of 900-1200 m. However, this impact of $\hat{\theta}_{v,e}$ is more pronounced for lower plume heights than for higher. This may be owed to the damping effect of the tropopause, which may require a substantially higher $\hat{\theta}_{v,e}$ to transcend.

Many previous studies have neglected the formation of clouds due to volcanic eruptions and the associated impacts on the plume itself. Cloud formation results in latent heat release, which subsequently acts as an additional heat source, which is hypothesized to affect the plume. To investigate these effects, a comparison between the simulation that considers water vapor emission by the volcano (WQ-Exp) and the simulation that neglects it (NoQ-Exp) is presented.

4. **Does the emission of volcanogenic water vapor affect the plume development?**
   On comparing WQ-Exp and NoQ-Exp, it is shown that the plume height does not change when the volcano emits water vapor, however, in case of WQ-Exp, more ash is present in higher parts of the plume. This is most distinctive during phase 7, as up to 120 tons/m more ash (12%) reaches a height of 11 km in WQ-Exp than in NoQ-Exp. Thus, volcanogenic water vapor leads to more cloud formation and consequently, higher latent heat release, which transports more ash to higher altitudes. More ash present higher up in the plume implies that it may stay longer in the atmosphere before depositing on the surface. Formation of clouds and precipitation is investigated further by analyzing the development of various hydrometeors (cloud water, rain, cloud ice, and snow) triggered by the eruption.

5. **How does the volcanic eruption affect the formation of clouds and precipitation in the vicinity of the volcano?**
   Volcanic eruptions can trigger and significantly modify the formation of clouds (cloud water, cloud ice) and precipitation (rain, snow) through modified dynamics due to $\hat{w}_e$ and $\hat{\theta}_{v,e}$, or due to volcanogenic water vapor emission during the eruption. In case of Raikoke, the maximum water contents and water paths near the volcano are comparable with those usually seen in strong cumulonimbus clouds. In order to find out which of the two processes modifying the dynamics has a more dominant effect on the formation of clouds and precipitation, the results of WQ-Exp and NoQ-Exp are compared. The water contents, water paths and masses do not show large differences between the two cases. The largest differences occur during phase 7 with a difference of the cloud ice mass Δm_i = 44 kilotons (10%) and difference of snow mass Δm_s = 57 kilotons (12%) between WQ-Exp and NoQ-Exp.

These results reveal that to trigger formation of clouds during an eruption, the dynamics modified due to $\hat{w}_e$ and $\hat{\theta}_{v,e}$ has a stronger effect compared to that due to water vapor emission. Furthermore, while latent heat release during cloud formation can lift more ash to higher altitudes, precipitation can lead to washout of ash, thereby, counteracting the ash lofting. Both of these processes can have implications for the plume development.

A topic of research interest is the role of water vapor injected into the stratosphere by volcanic eruptions. However, investigation of the effects of amount of water vapor is also limited by the model domain. For this study, a comparison between the WQ-Exp simulation and the Ref simulation (without volcanic

eruption) is done to find the amount of water vapor added in the atmosphere, and amount that reached the stratosphere, during the Raikoke eruption.

6. **How does the eruption alter the vertical distribution of water vapor in the atmosphere?**
   Compared to the Ref, in WQ-Exp the eruption leads to a large increase of the water vapor mass of more than 100 tons/m especially between a height of 4 and 8 km. Some regions below a height of 4 km show less water vapor in WQ-Exp than in Ref, due to water vapor lofting and cloud formation. Majority of the amount stays below the tropopause, whereas, only during the strongest eruption phases, some water vapor reaches the lower stratosphere. Depending on $\hat{\theta}_{v,e}$ that is used as the heat source, the water vapor mass increases between 5 kilotons ($\hat{\theta}_{v,e}$ = 650 K) and 17 kilotons ($\hat{\theta}_{v,e}$ = 750 K) in the stratosphere during phase 7, which is the maximum amount among all phases. Some water vapor reaches the stratosphere during phase 3, 8, and 9 as well, however, the amount is mostly very small.

Investigation of the impact of water vapor above the tropopause is beyond the scope of this study, as it leaves the model domain after a short time. Nevertheless, the amount is not enough to cause any significant impacts.
Finally, this study investigates the generation of atmospheric waves caused by volcanic eruptions. Atmospheric waves can be indicated through pressure perturbations, which can provide early information about volcanic eruptions when their direct detection is not possible.

7. **Is the modified ICON-ART able to simulate atmospheric waves caused by volcanic eruptions?**
   The simulation of the Raikoke eruption with ICON-ART could also generate atmospheric waves, which can be seen through pressure perturbations. They are mostly assumed to be gravity waves and not sound waves or shock waves, as they travel rather slowly with a phase velocity of $v_p \approx 17$ m/s. Though the waves were generated in simulation of all eruption phases, this effect is most prominent during phase 7, where the velocity is about 320 m/s, almost close to the speed of sound. The waves are also distinguishable in the Himawari-8 satellite images, and as they travel slower, it can be inferred they are not sound waves. The pressure perturbations also occur in the temporal evolution of pressure in a small region near Raikoke, where, after the start of each eruption phase, the pressure drops by up to 0.58 hPa. This is comparable with pressure measurements during eruptions of the Soufrière Hills volcano in 2003 and 2009 (Baines and Sacks, 2017).

The results of this study show the manifold impacts of explosive volcanic eruptions, as they influence the atmosphere, which in turn affects the plume development. The first explicit simulations of a volcanic eruption plume with an NWP model allowed the consideration of the ash-dynamics interaction and the effect of the exit velocity and exit temperature at the source on the surrounding atmosphere. This enabled

the investigation of microphysical processes like formation of clouds and precipitation, as well as the injection of water vapor into the stratosphere and the generation of atmospheric waves due to the eruption. This study provides various novel and valuable insights, however, some uncertainties and limitations still exist.

For sensitivity analysis of the heat source and the simulated plume height, despite different temperature choices for the eruption phases, there is no parameterization yet to establish a relation. In addition, the heat capacities of ash and other constituents were neglected, which may affect the thermal conditions in the plume. Furthermore, these kinds of simulations require a very small integration time step to retain model stability, consequently, resulting in a high computational effort. In this study, a one-moment microphysics scheme is used for cloud formation, and this scheme only considers a climatological number of aerosols, based on measurements, to take into account heterogeneous freezing. Hence, the interaction between aerosols and clouds is neglected. However, emitted ash could serve as both cloud condensation nuclei (CCN)s and ice nucleating particles (IN)s, and thus, occurrence of clouds and precipitation can be modified, which is not accounted for in the one-moment scheme. The following outlook discusses the scope for improvement with regards to some of these aspects.

7.2. Outlook

A main part for the further improvement of explicit simulations of volcanic plumes with ICON-ART is to find a physical relation between the simulated plume height and the heat source. This could be achieved by modifying the thermodynamical equation (equation (3.18)), by adding a term that considers the thermal energy released by the volcano. The results in section 6.2.1 and section 6.2.3 show that a stronger eruption requires a higher $\hat{\theta}_{v,e}$ to match the simulated plume height with the observed one, whereas, a reduced $\hat{\theta}_{v,e}$ is necessary for weaker eruptions. The additional term in equation (3.18) may be related to the MER in order to consider the emitted hot mixture (ash and water vapor) as a larger amount of the emitted mixture would have more associated heat. For this purpose, the heat capacity of ash and water vapor should be considered as well, but so far, only the heat capacity of dry air has been taken into account. Simulations of other volcanic eruptions with strengths different compared to that of the Raikoke eruption may help to find a reliable relation between the plume height and $\hat{\theta}_{v,e}$.

Within the scope of this study, the role of ash as CCNs and INs is neglected for cloud formation in section 6.3, as the interaction of aerosols and clouds is not accounted for. It is possible that its consideration modifies the formation of the hydrometeors when ash acts as CCNs and INs, which might also result in wet deposition of ash and modification of the plume development. Moreover, the current work neglected the emission of SO_2 and corresponding aerosol dynamical and chemical processes. These processes can cause aerosol aging, which modifies the aerosols' properties such as their size and composition (Bruckert et al., 2022) and thereby, might impact the role of ash acting as CCNs and INs. Aerosol aging further influences the sedimentation of ash and thus, its residence time in the atmosphere. In addition, gas-phase

chemistry can lead to formation of secondary sulfuric aerosols which may serve as CCNs or INs as well. Investigating the aerosol-cloud interaction is the topic of ongoing work.

The current study uses a LAM setup with a small model domain and short simulation time which limit the investigation of various processes. To analyze the effect of the investigated processes on the plume development on larger timescales as well as in larger areas, nested model domains can be used, which interact with each other. This also allows to compare the ash mass loading shown in section 6.2.2 with results from Muser et al. (2020), Bruckert et al. (2022), and with observations, which display larger areas and have coarser resolution. Furthermore, nesting helps to explore the impact of water vapor injected into the lower stratosphere presented in section 6.3.3. The small model domain and short simulation time make this challenging as most water vapor rapidly leaves the model domain due to strong winds. A current development on seamless predictions with ICON-ART allows to simulate a volcanic plume as multicomponent multiphase flow, including dynamical and microphysical processes as well as aerosol dynamics and chemical processes, in the early stage of the plume in simulations covering days to months. The modified version of ICON-ART presented in this work can be used for further simulations of volcanic eruption plumes as multicomponent multiphase flow, with different source conditions and/or atmospheric state. A volcanic plume in tropical regions could be affected differently in a way that a larger amount of hydrometeors develop due to abundance of atmospheric water vapor, which can be entrained into the plume. Additionally, the results in section 6.2.4 and 6.3.2 revealed that emitted volcanogenic water vapor has no impact on the plume top height and a rather small effect on cloud formation, respectively. However, considering another eruption characterized by a larger injection of water (vapor) into the atmosphere could have significant influence on both plume development and cloud formation (e.g. eruption of Hunga Tonga-Hunga Ha'pai in 2022).

Strong atmospheric waves were detected during the Hunga Tonga eruption in 2022, and this version of ICON-ART allows to do further investigation of such waves generated by volcanic eruptions. Those investigations can give further insights on how different eruption conditions control the waves' properties and what kind of atmospheric waves these conditions trigger. Furthermore, atmospheric waves can affect the development of clouds and precipitation, as e.g. internal gravity waves transport moist air to sub- or supersaturated regions due to the alternating upward and downward motion. Said motion can also have significant impacts for aviation. According to NOAA, about 40% of all aviation accidents happen due to clear sky turbulence caused by internal gravity waves. Hence, further investigation of atmospheric waves generated by volcanic eruptions may help to understand their effects on atmospheric conditions.

As the presented results are one of the first of its kind with an NWP model it creates opportunities for further model development in resolving both the atmospheric state and the multicomponent multiphase features of the plume. It might be possible to simulate and investigate the characteristics of small scaled pyroclastic density currents or avalanches in future, which are popular examples of hazardous multicomponent multiphase flows.

A. Additional figures

A.1. Figures for section 6.2.1

Phase 1:

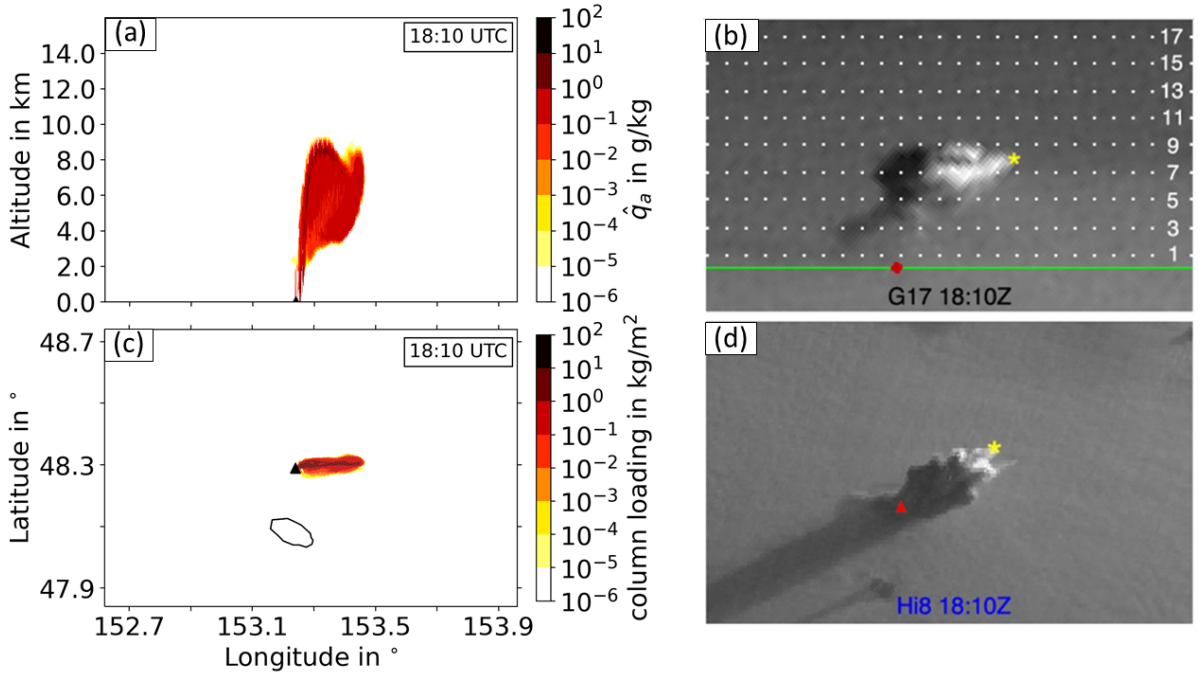

Figure A.1.: Eruption phase 1 at 18:10 UTC. (a) Mean mass mixing ratio of all ash modes $\hat{q}_a$ in g/kg in the model. (b) GOES-17 (G17) satellite image of eruption plume, with dotted lines depicting the estimated altitude in km and the green line shows the volcano baseline. (c) Ash column loading in kg/m^2 as sum of all ash modes. (d) Himawari-8 (Hi8) satellite image of eruption plume. The black triangles in (a) and (c) and the red dot/triangle in (b) and (d) mark the location of Raikoke. When present, the yellow/blue asterisks indicate the same plume top feature in both satellite images. The blue dot is the shadow terminus on the marine stratocumulus cloud layer in the Hi8 image (Horváth et al., 2021b).

Phase 3:

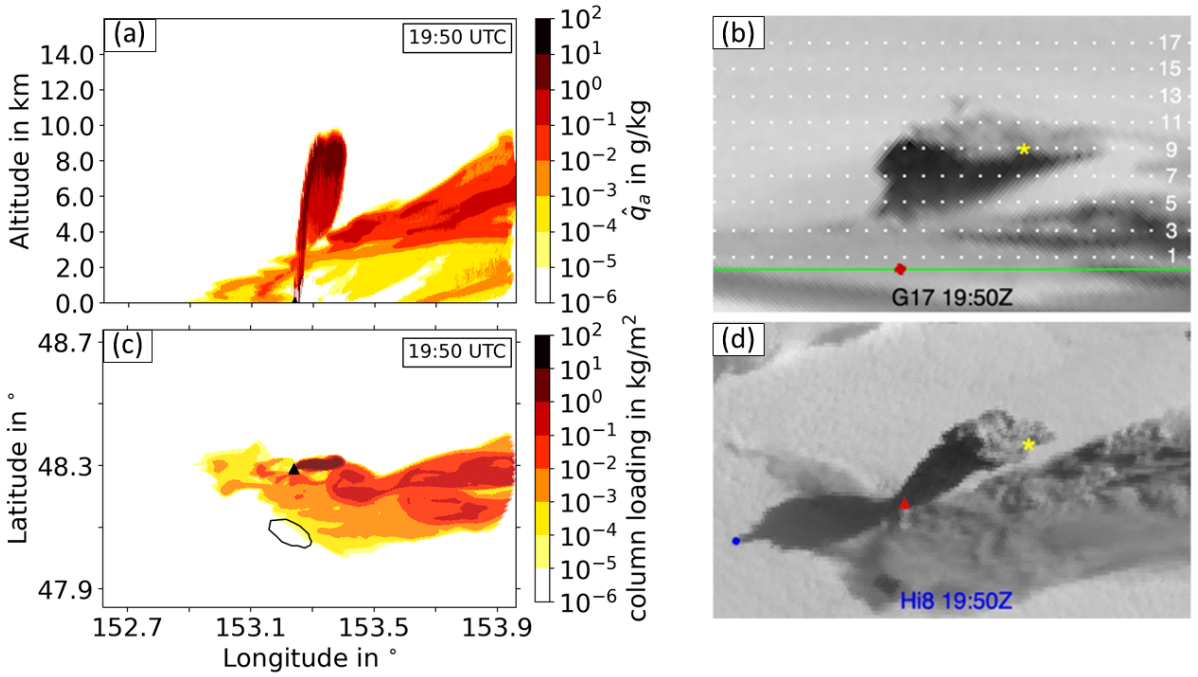

Figure A.2.: Raikoke eruption phase 3. See figure A.1 for description.

Phase 4:

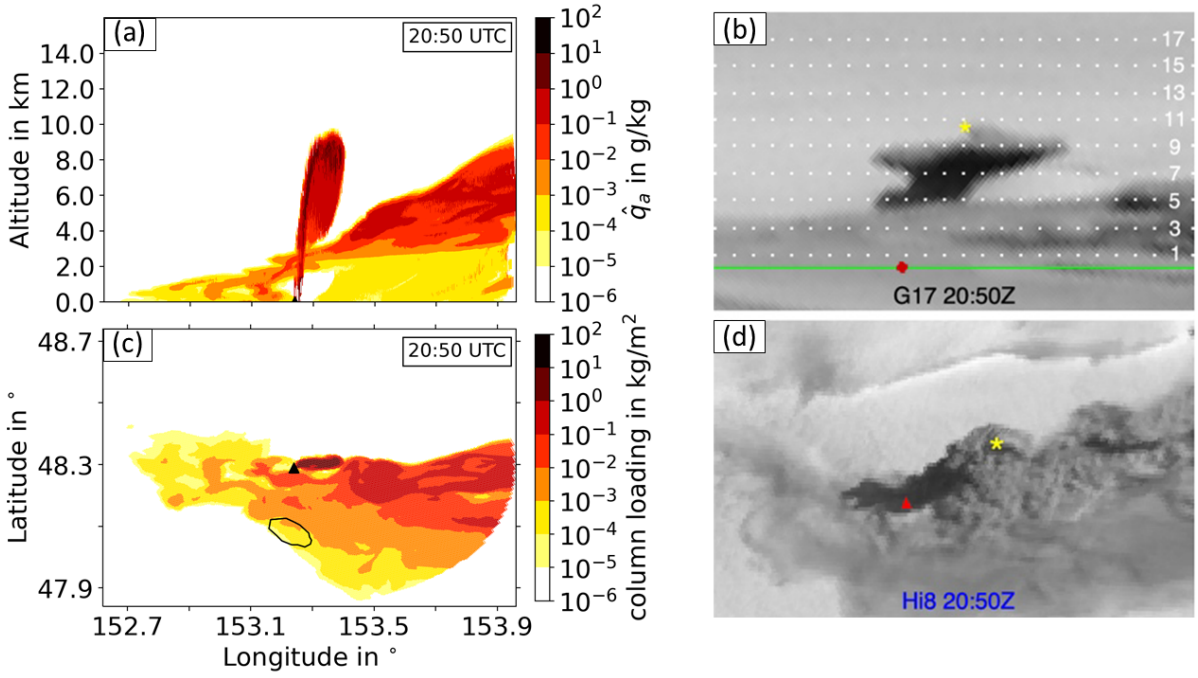

Figure A.3.: Raikoke eruption phase 4. See figure A.1 for description.

Phase 5:

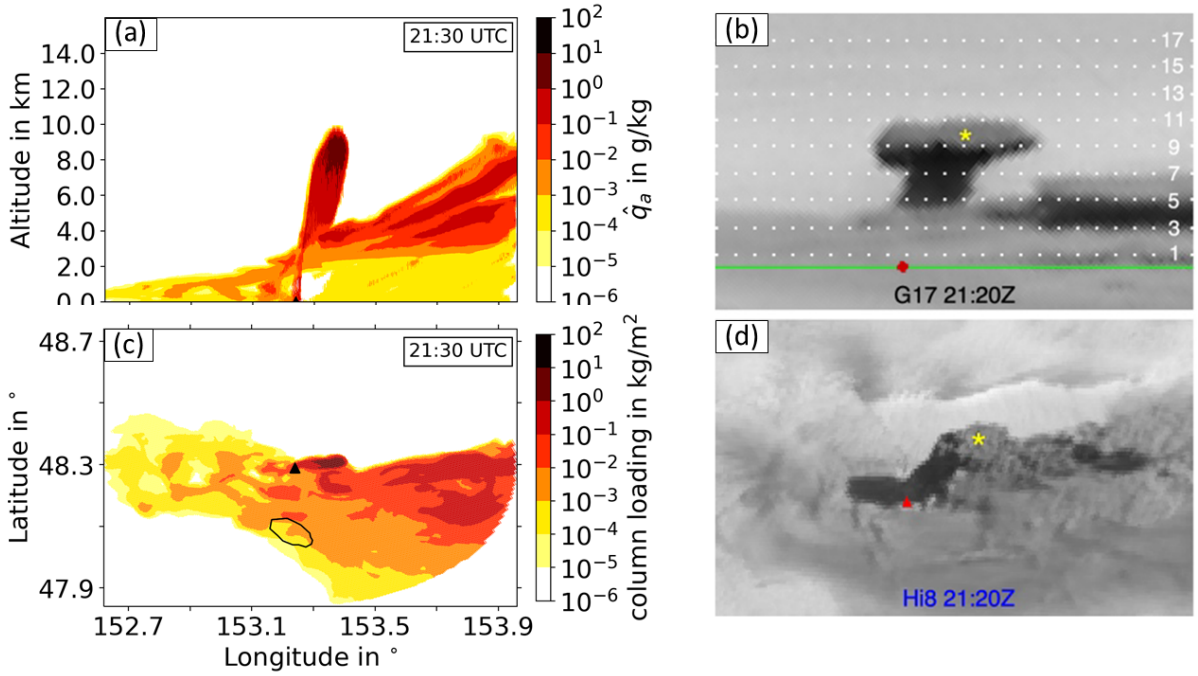

Figure A.4.: Raikoke eruption phase 5. See figure A.1 for description. Note the time shift between model and observation. As for the model result, only the output at 21:30 UTC covers the whole plume, whereas there is no observation available at this time. Hence, the observation at 21:20 UTC is used for the comparison.

Phase 6:

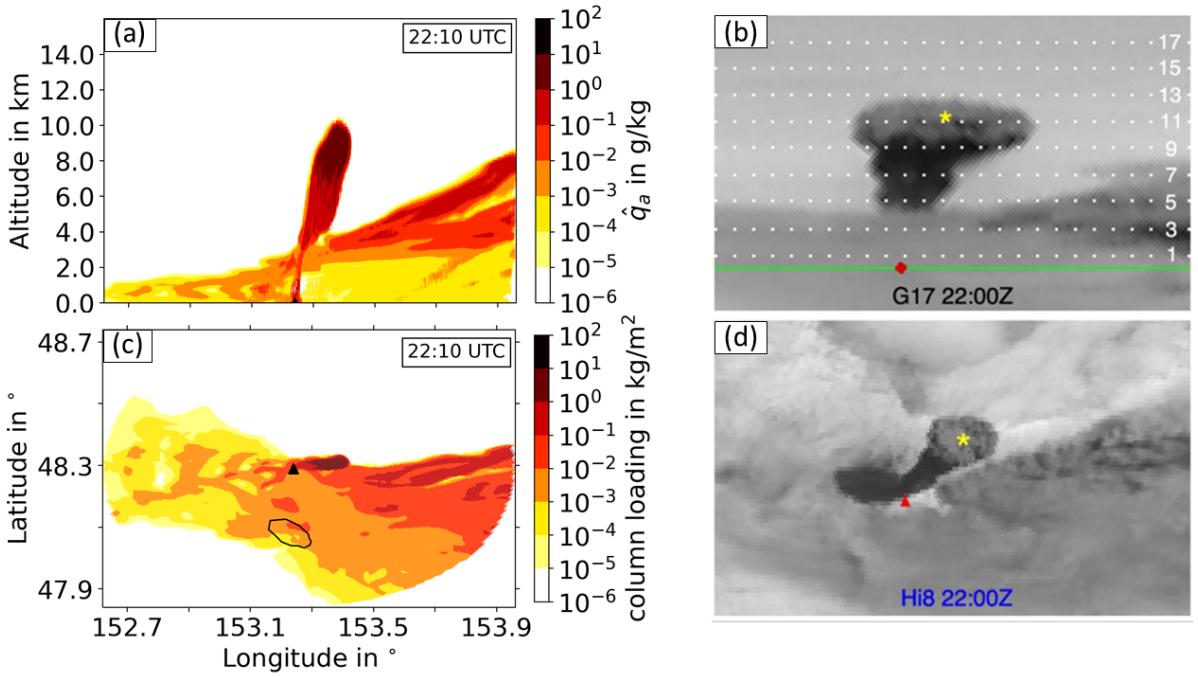

Figure A.5.: Raikoke eruption phase 6. See figure A.1 for description. Note the time shift between model and observation like during phase 5.

Phase 8:

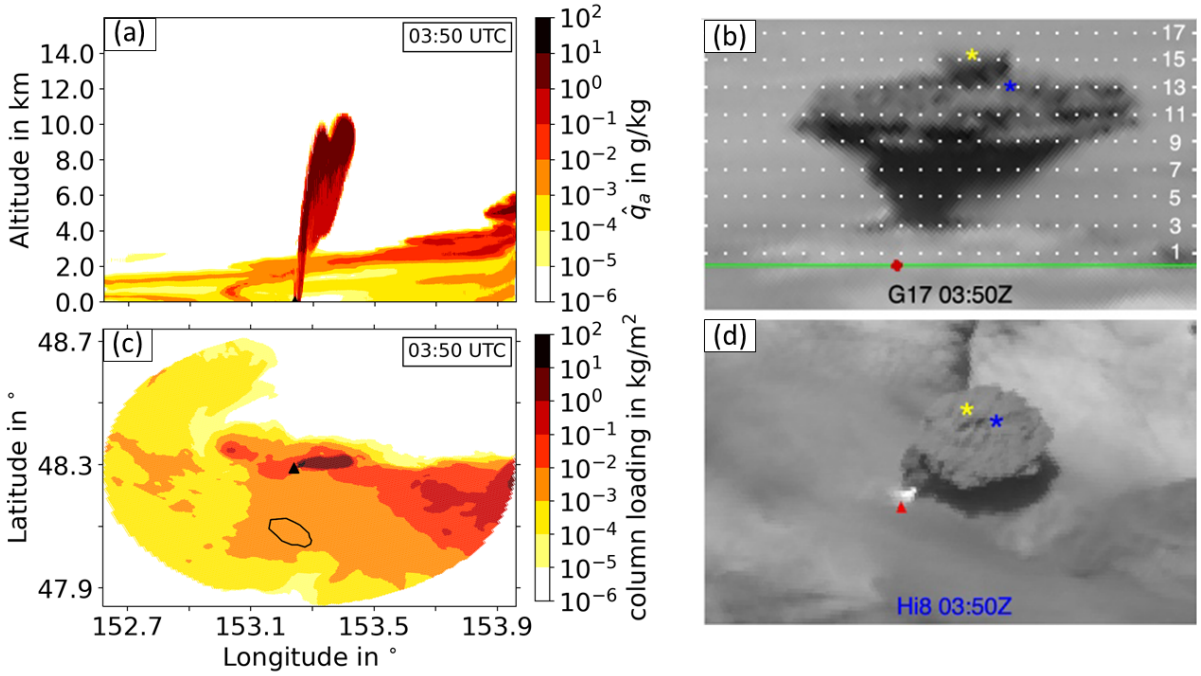

Figure A.6.: Raikoke eruption phase 8. See figure A.1 for description.

Phase 9:

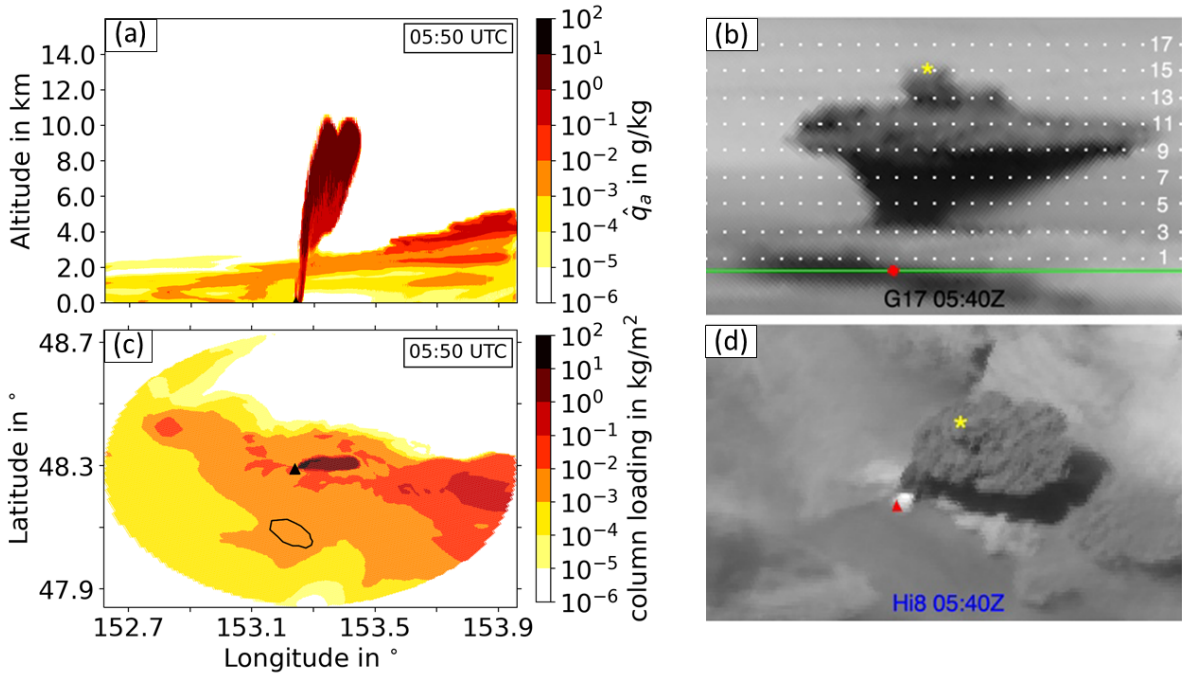

Figure A.7.: Raikoke eruption phase 9. See figure A.1 for description. Note the time shift between model and observation like during phase 5.

A.2. Figures for section 6.2.2

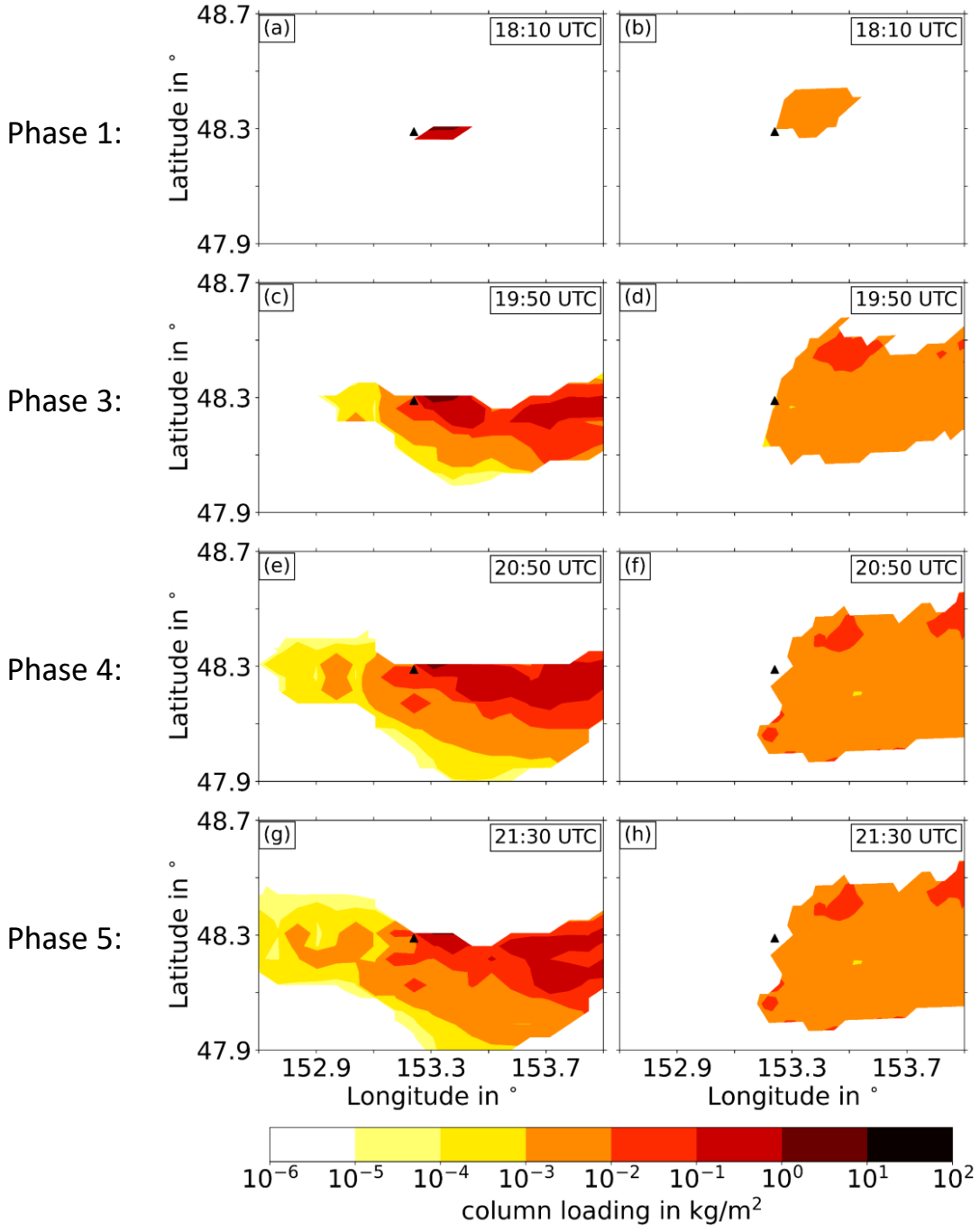

Figure A.8.: Comparison of ash column loading in kg/m^2 between model (a,c,e,g) and VOLCAT retrieval (b,d,f,h) for phases 1, 3, 4, and 5.

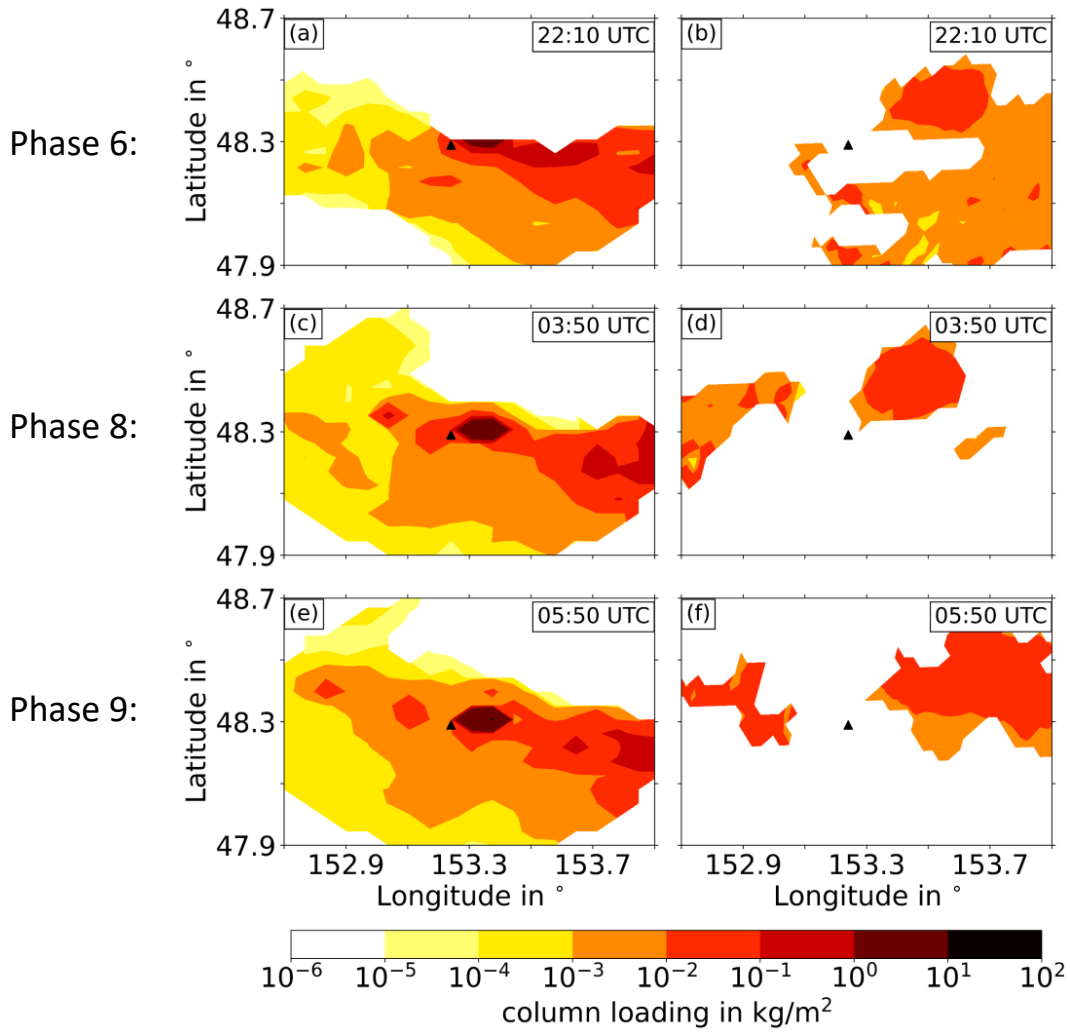

Figure A.9.: Comparison of ash column loading in kg/m^2 between model (a,c,e) and VOLCAT retrieval (b,d,f) for phases 6, 8, and 9.

A.3. Figures for section 6.3.1

Phase 1:

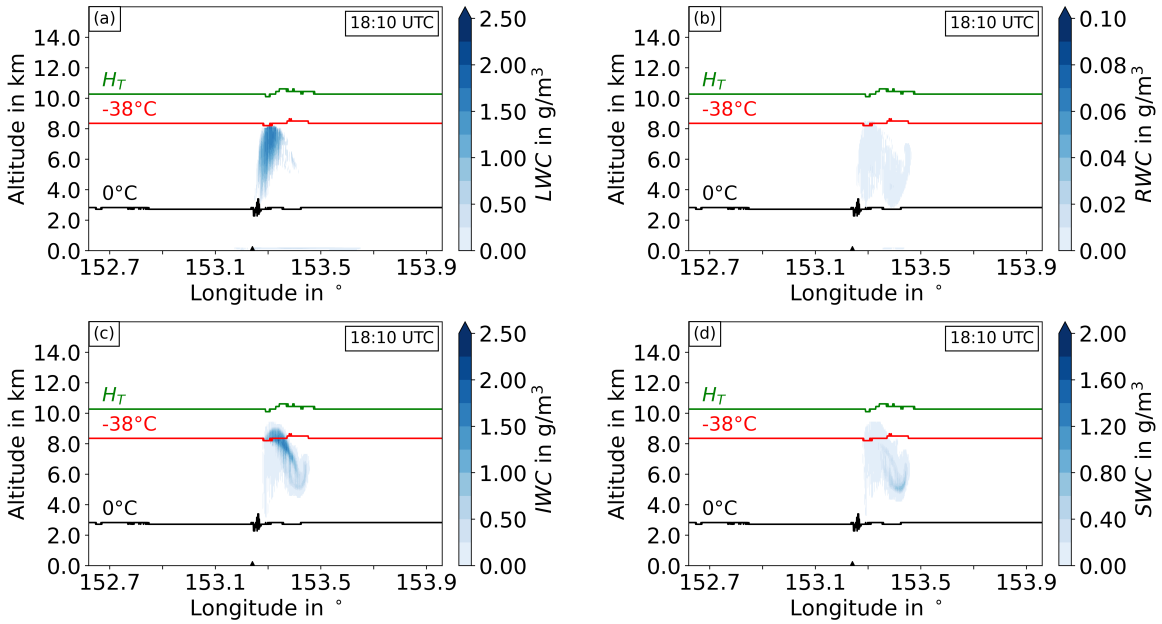

Figure A.10.: Mean water contents in g/m^3 latitudinally averaged from 48.3°N to 48.33°N for phase 1 at 18:10 UTC of (a) liquid clouds (*LWC*), (b) rain (*RWC*), (c) ice clouds (*IWC*) and (d) snow (*SWC*). The black line shows the $T = 0$°C-boundary, red line $T = -38$°C and the green line the tropopause height H_T.

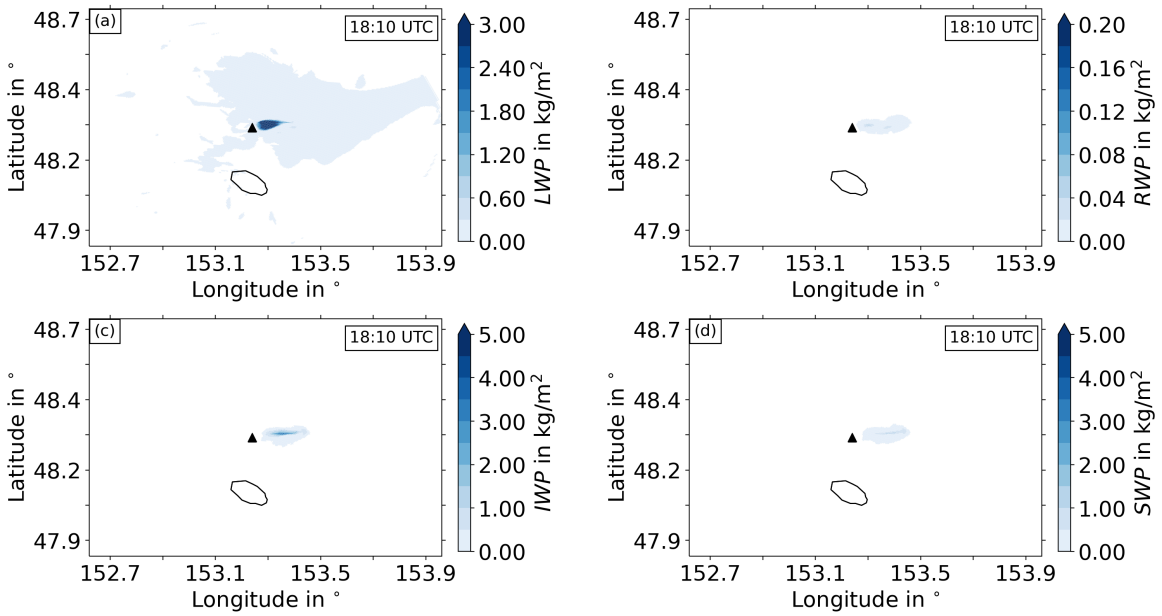

Figure A.11.: Water paths in kg/m^2 for phase 1 at 18:10 UTC of (a) liquid clouds (*LWP*), (b) rain (*RWP*), (c) ice clouds (*IWP*), and (d) snow (*SWP*).

Phase 3:

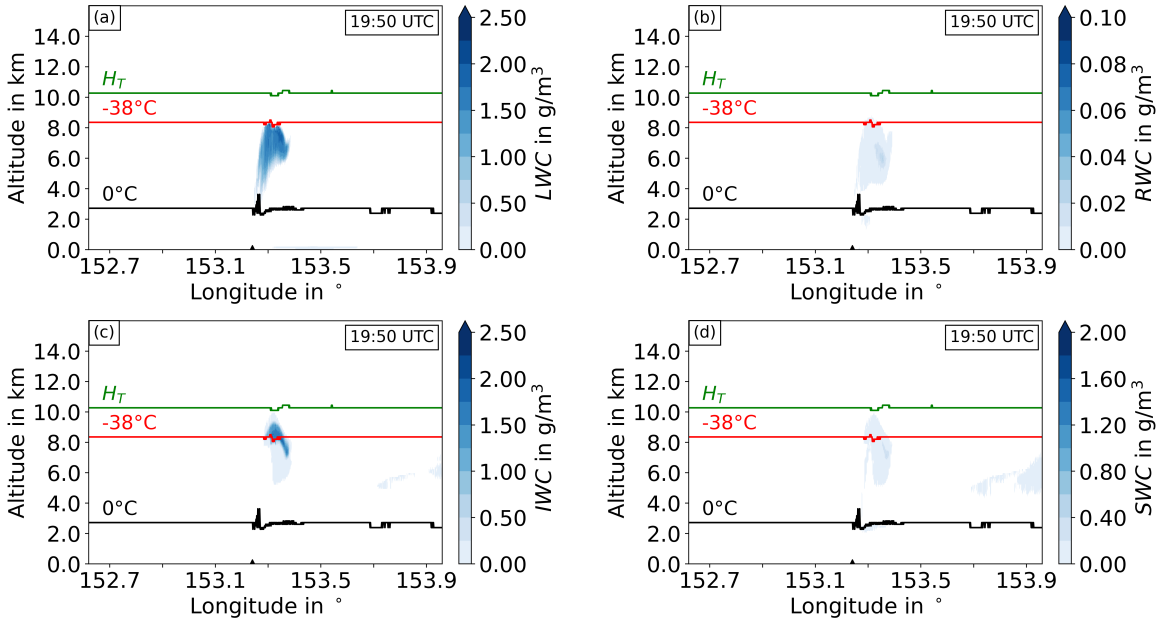

Figure A.12.: Mean water contents in g/m^3 for phase 3 at 19:50 UTC. See figure A.10 for description.

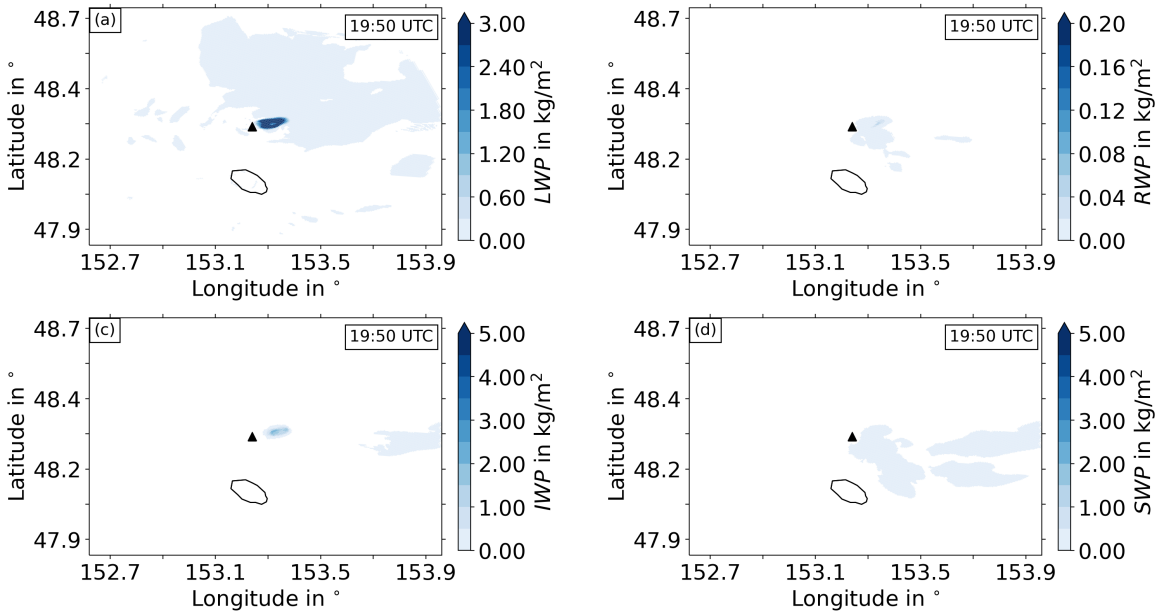

Figure A.13.: Water paths in kg/m^2 for phase 3 at 19:50 UTC. See fig A.11 for description.

Phase 4:

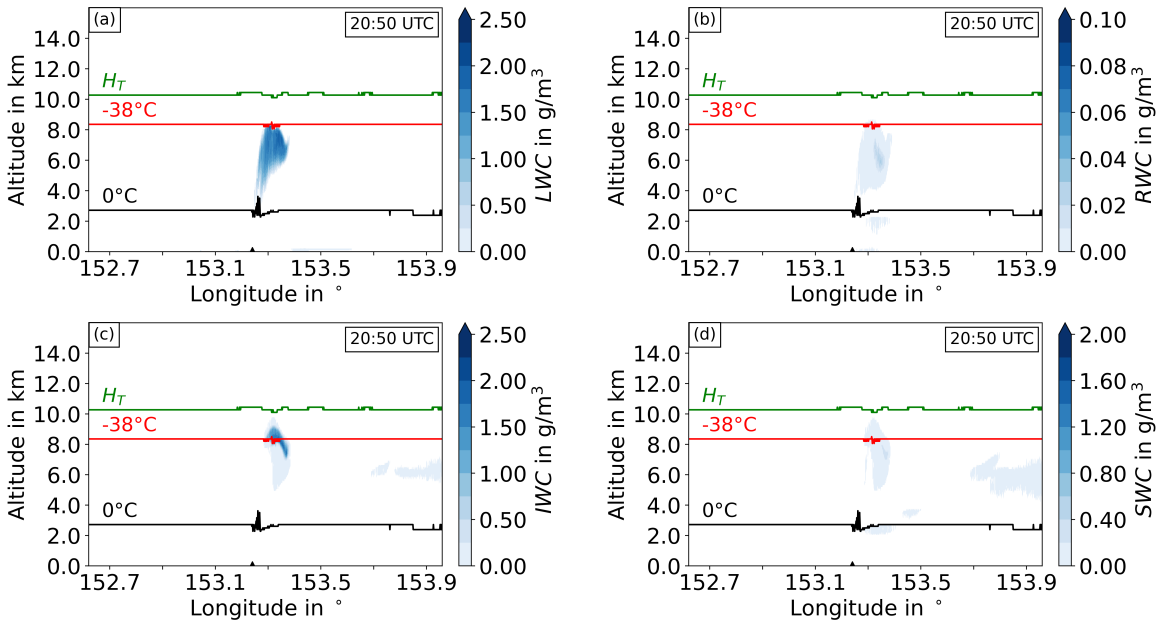

Figure A.14.: Mean water contents in g/m^3 for phase 4 at 20:50 UTC. See figure A.10 for description.

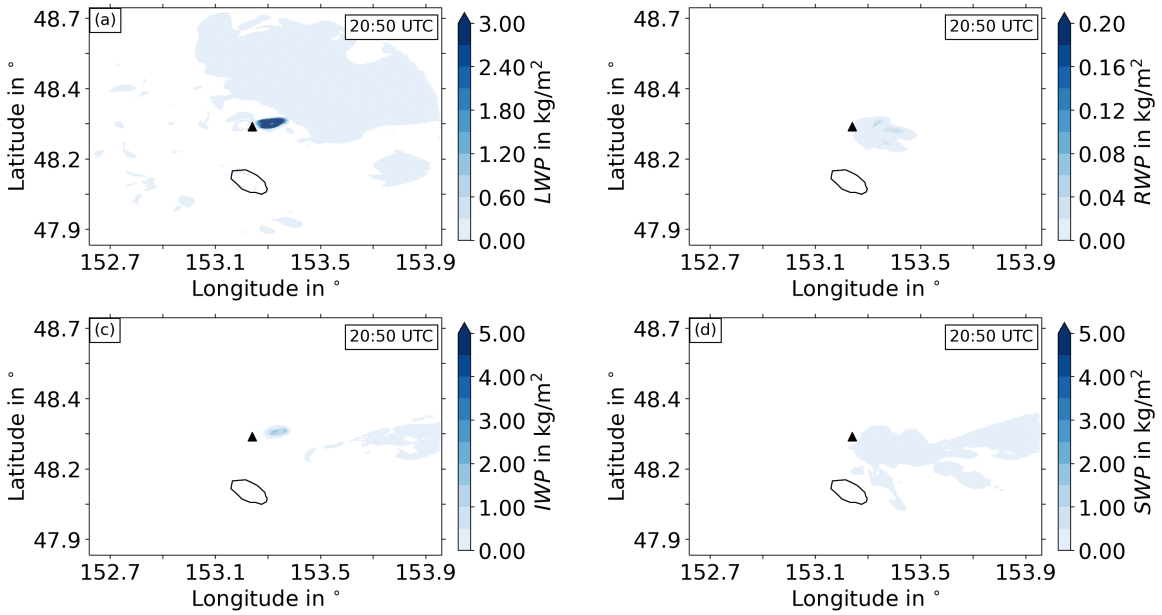

Figure A.15.: Water paths in kg/m^2 for phase 4 at 20:50 UTC. See fig A.11 for description.

Phase 5:

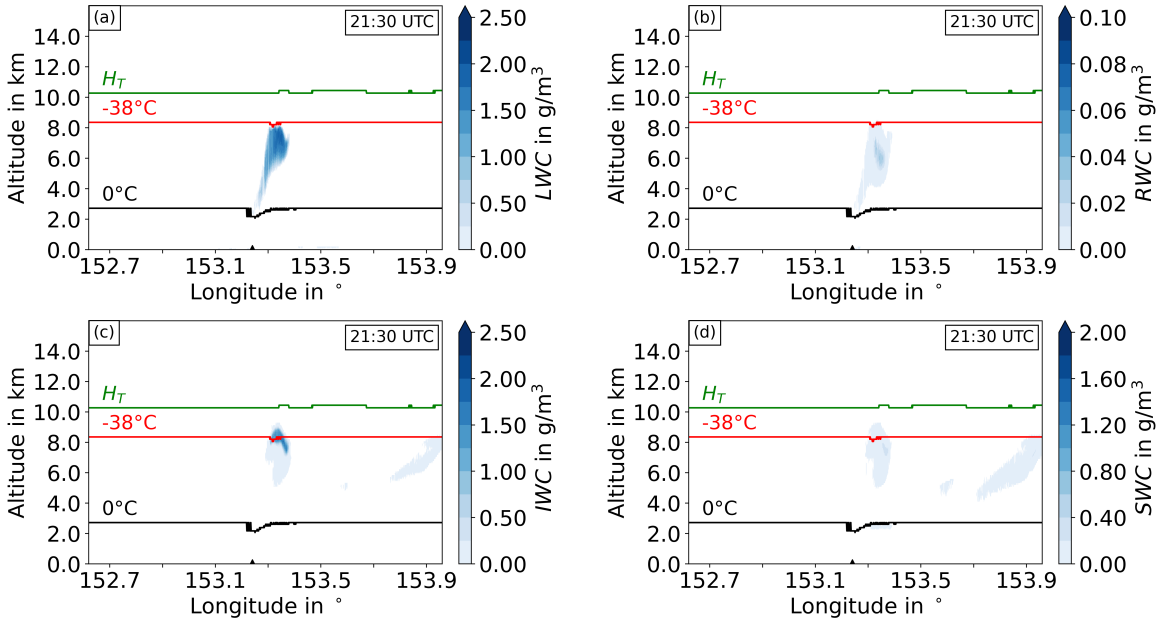

Figure A.16.: Mean water contents in g/m^3 for phase 5 at 21:30 UTC. See figure A.10 for description.

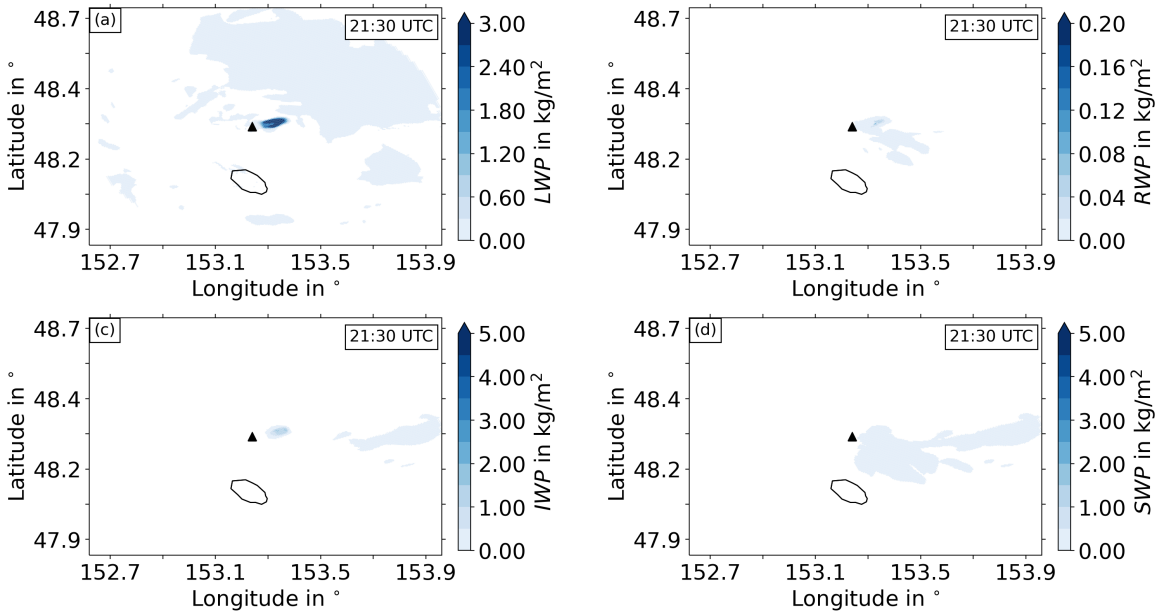

Figure A.17.: Water paths in kg/m^2 for phase 5 at 21:30 UTC. See fig A.11 for description.

Phase 6:

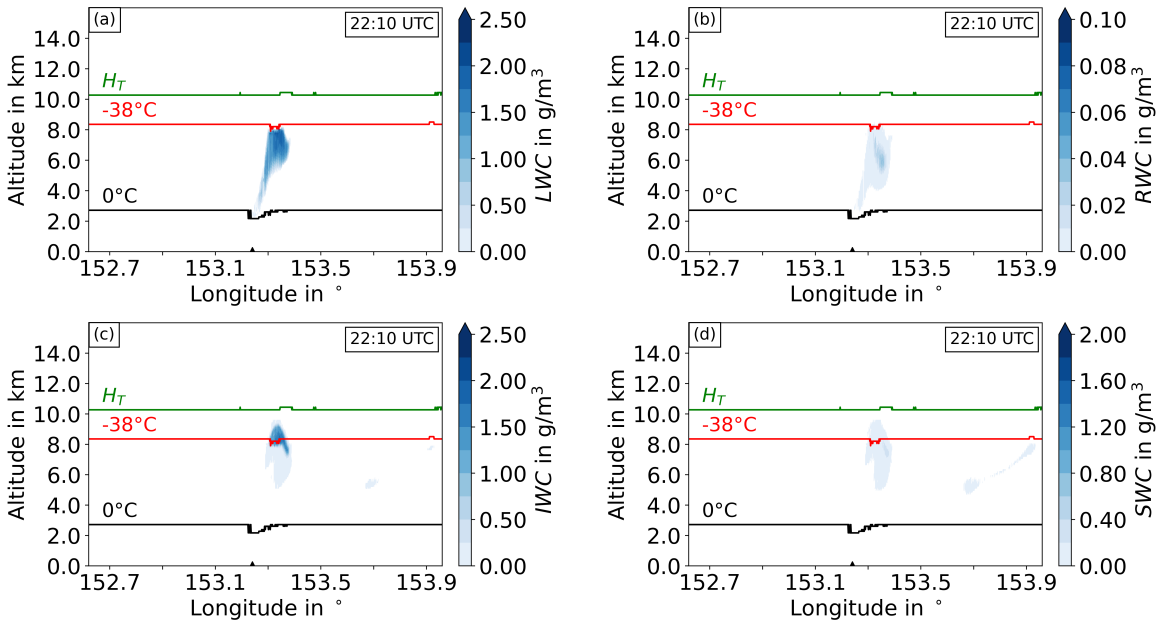

Figure A.18.: Mean water contents in g/m^3 for phase 6 at 22:10 UTC. See figure A.10 for description.

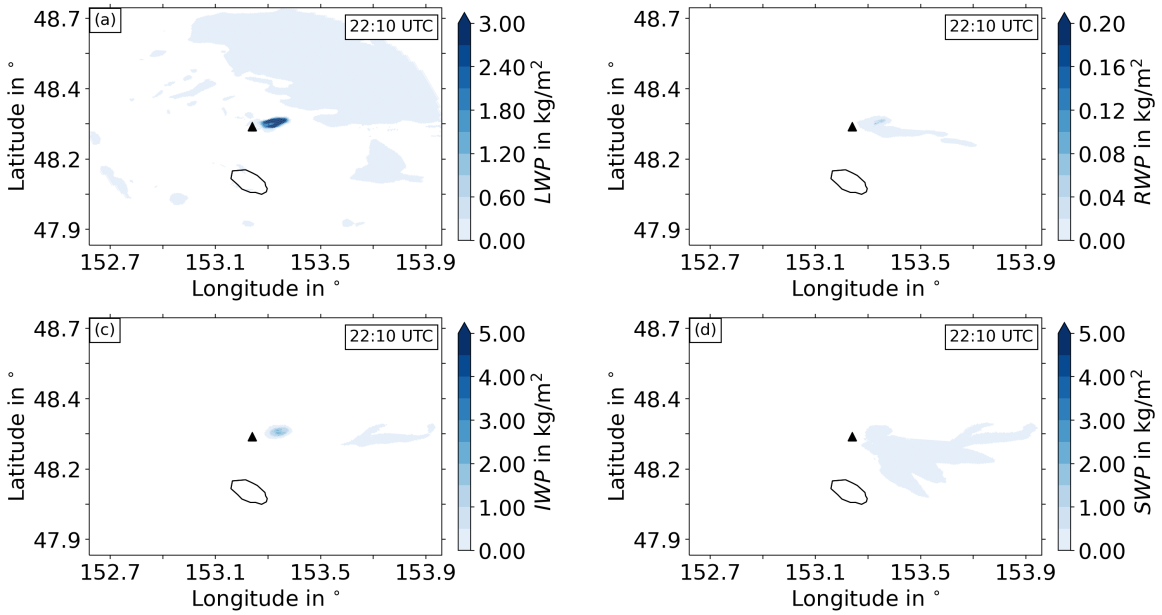

Figure A.19.: Water paths in kg/m^2 for phase 6 at 22:10 UTC. See fig A.11 for description.

Phase 8:

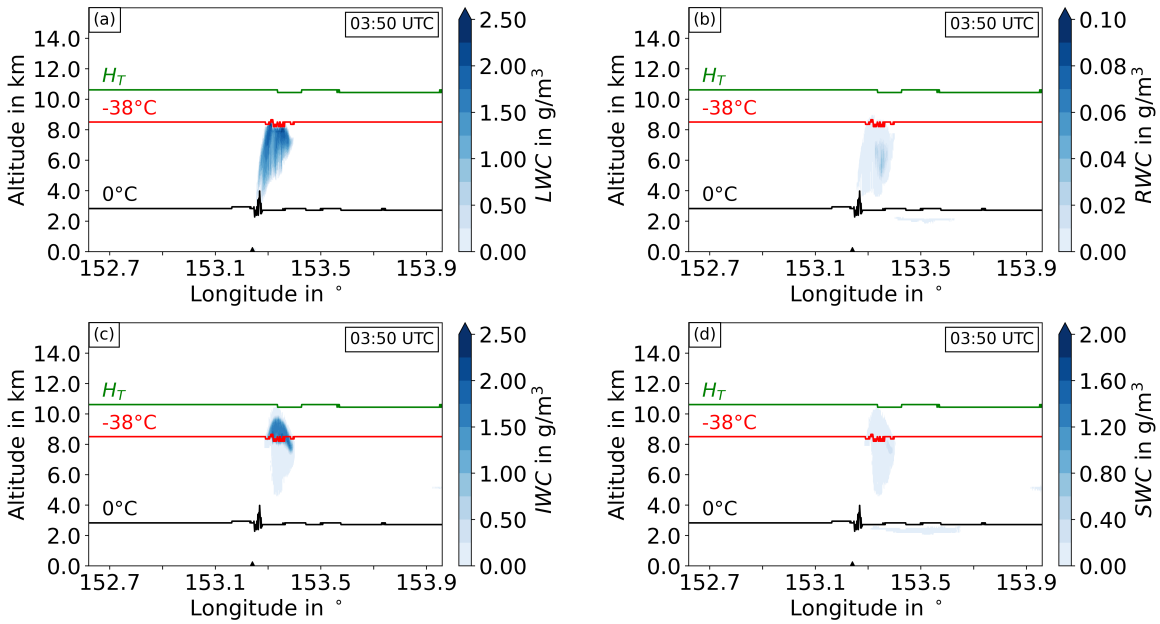

Figure A.20.: Mean water contents in g/m^3 for phase 8 at 03:50 UTC. See figure A.10 for description.

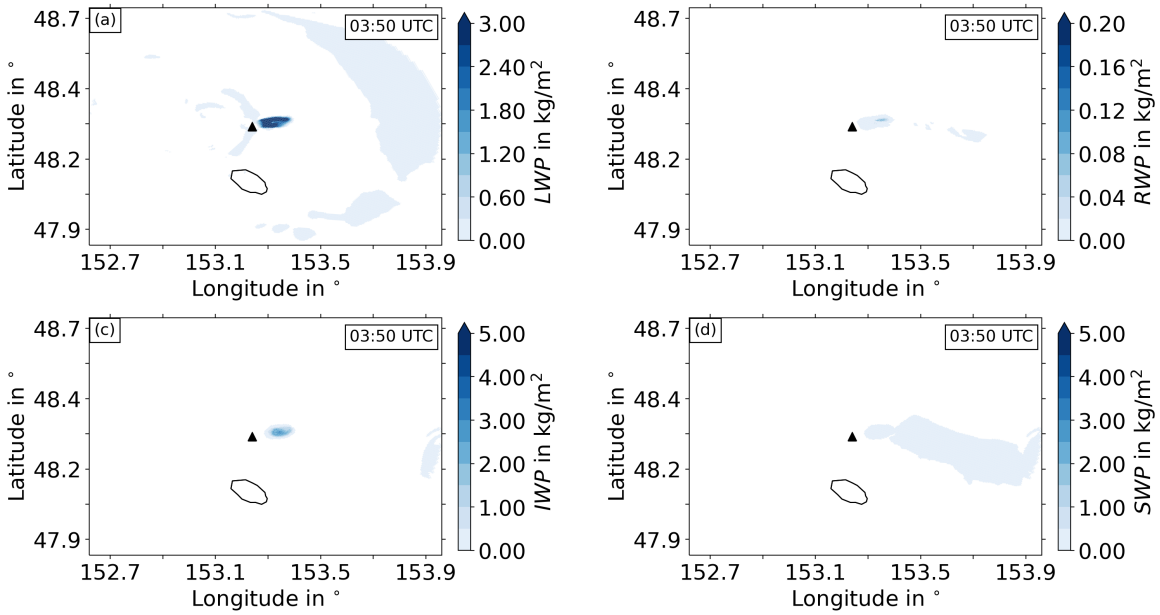

Figure A.21.: Water paths in kg/m^2 for phase 8 at 03:50 UTC. See fig A.11 for description.

Phase 9:

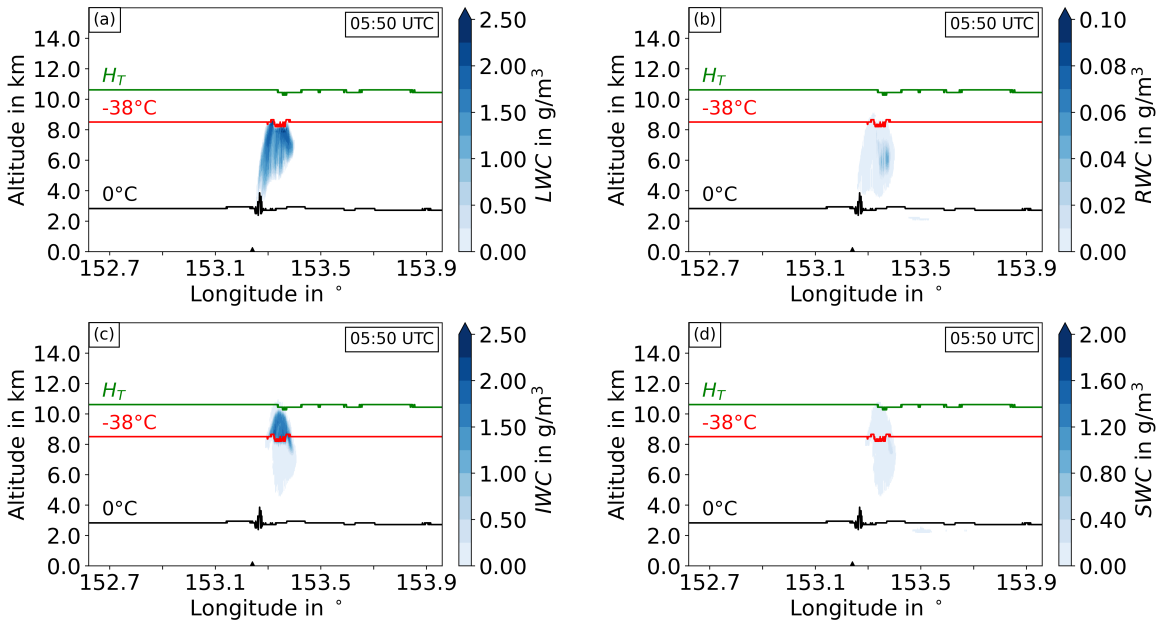

Figure A.22.: Mean water contents in g/m^3 for phase 9 at 05:50 UTC. See figure A.10 for description.

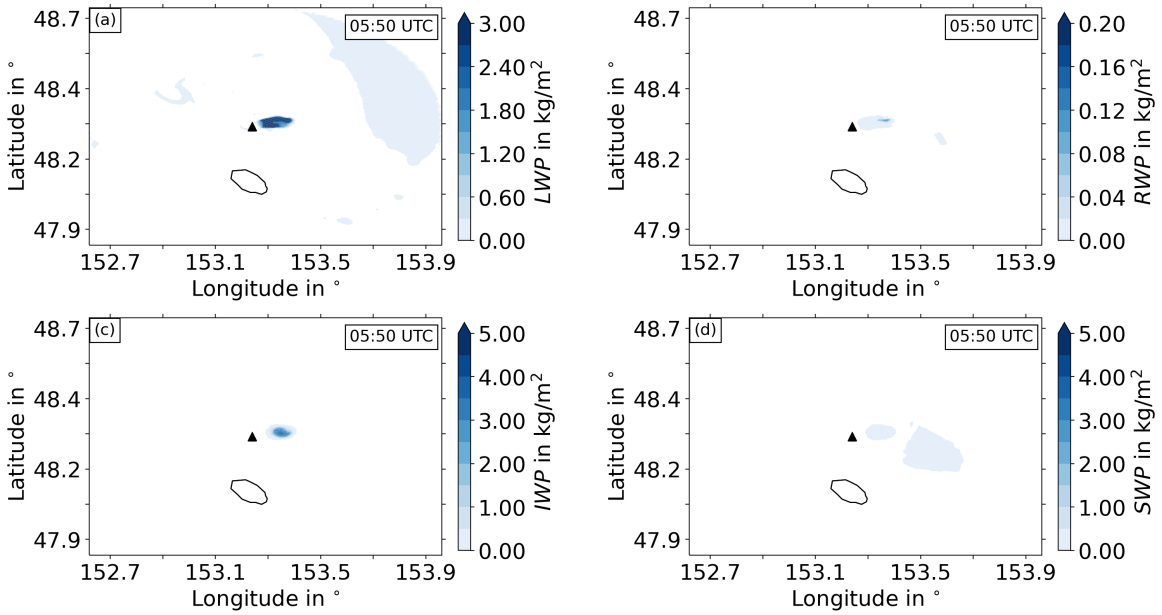

Figure A.23.: Water paths in kg/m^2 for phase 9 at 05:50 UTC. See fig A.11 for description.

A.4. Figures for section 6.3.2

Phase 1:

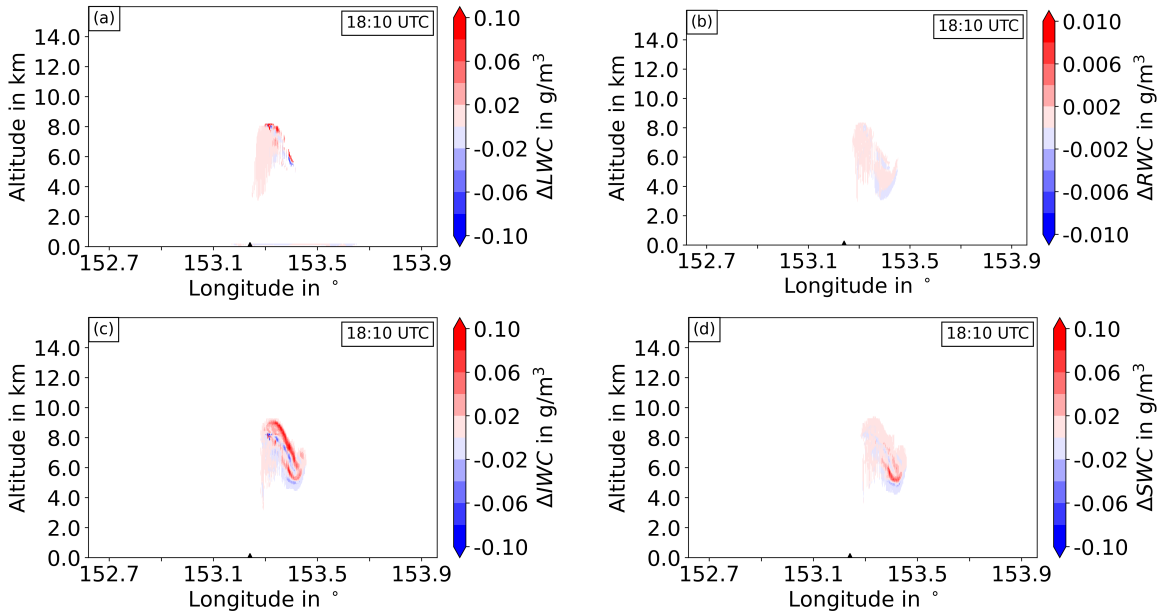

Figure A.24.: Difference of latitudinally averaged (mean) water contents (a) ΔLWC, (b) ΔRWC, (c) ΔIWC, and (d) ΔSWC in g/m^3 between WQ-Exp and NoQ-Exp at 18:10 UTC during phase 1 in the region from 48.3°N to 48.33°N.

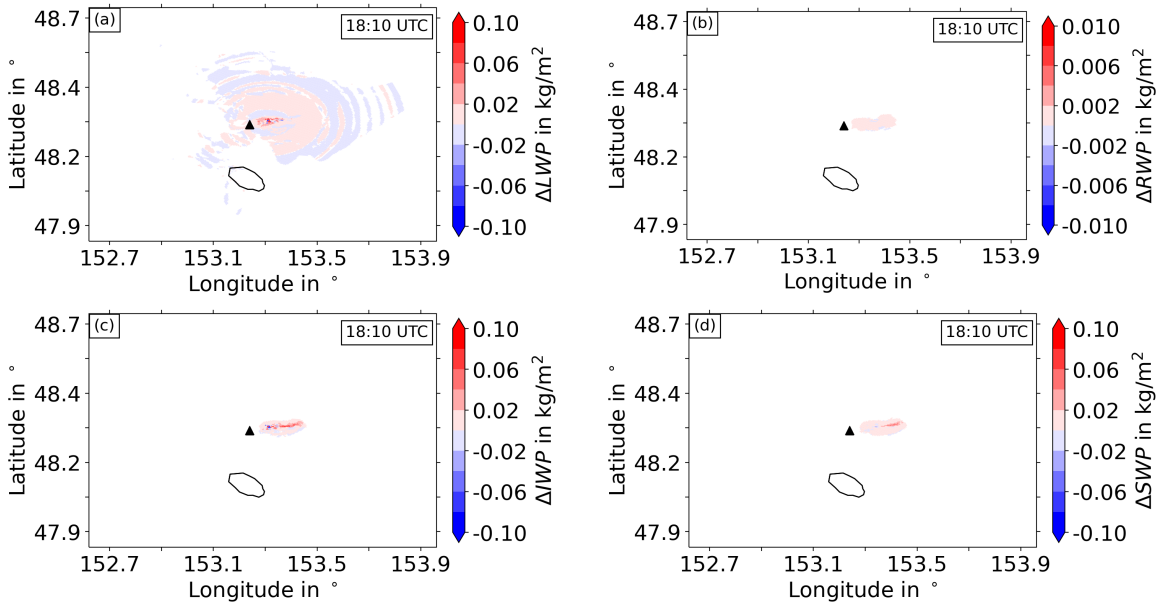

Figure A.25.: Difference of water paths (a) ΔLWP, (b) ΔRWP, (c) ΔIWP, and (d) ΔSWP in kg/m^2 between WQ-Exp and NoQ-Exp at 18:10 UTC during phase 1.

Phase 3:

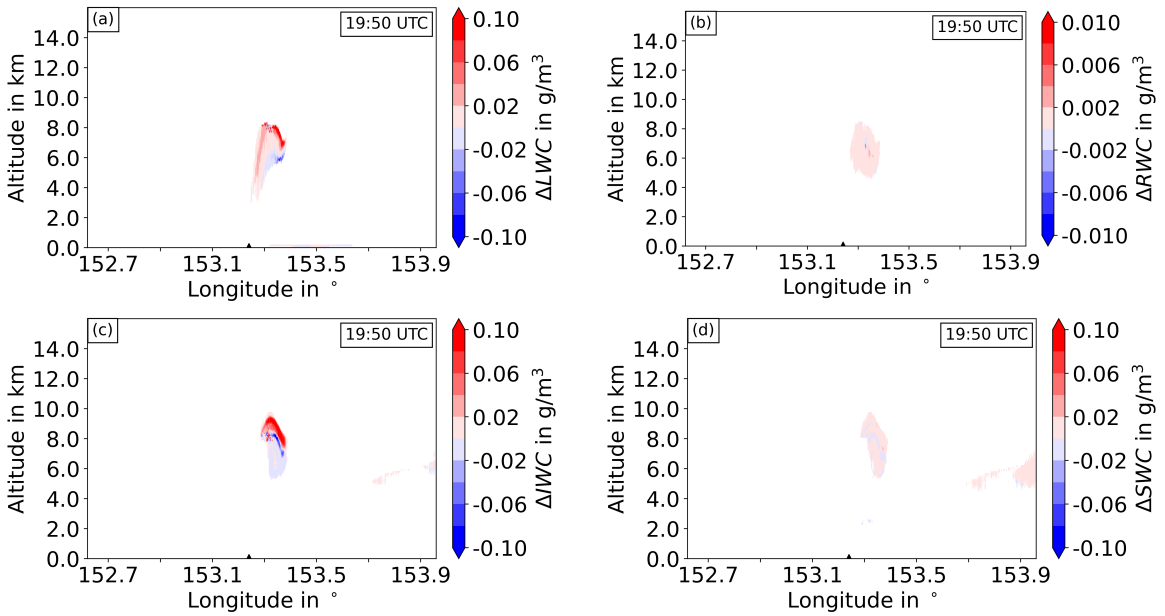

Figure A.26.: Difference of mean water contents between WQ-Exp and NoQ-Exp at 19:50 UTC during phase 3. See figure A.24 for description.

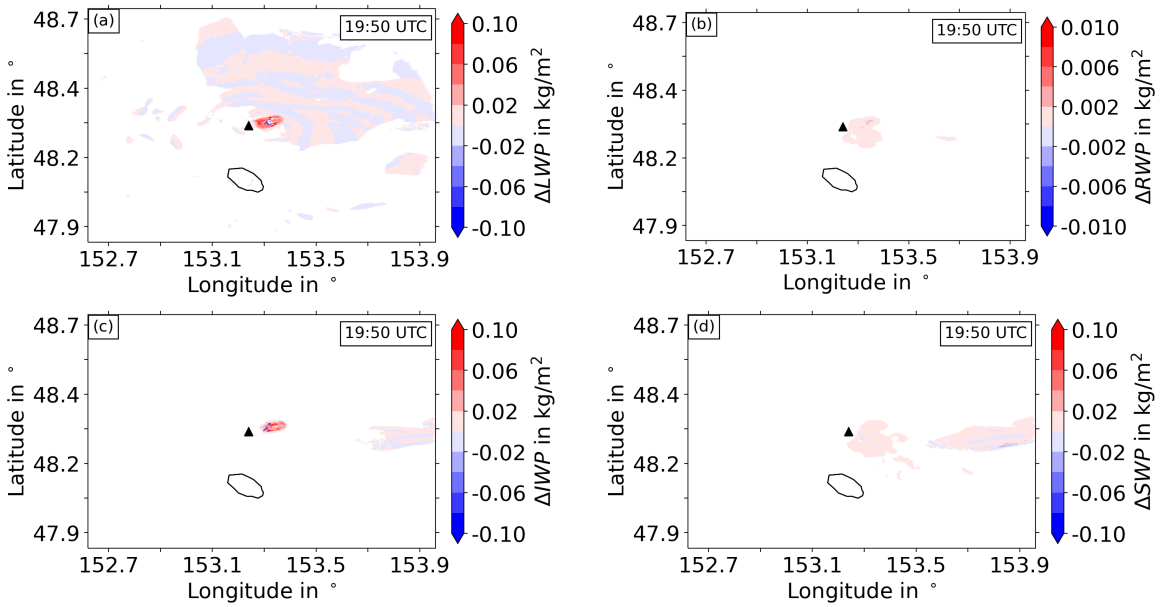

Figure A.27.: Difference of water paths between WQ-Exp and NoQ-Exp at 19:50 UTC during phase 3. See figure A.25 for description.

Phase 4:

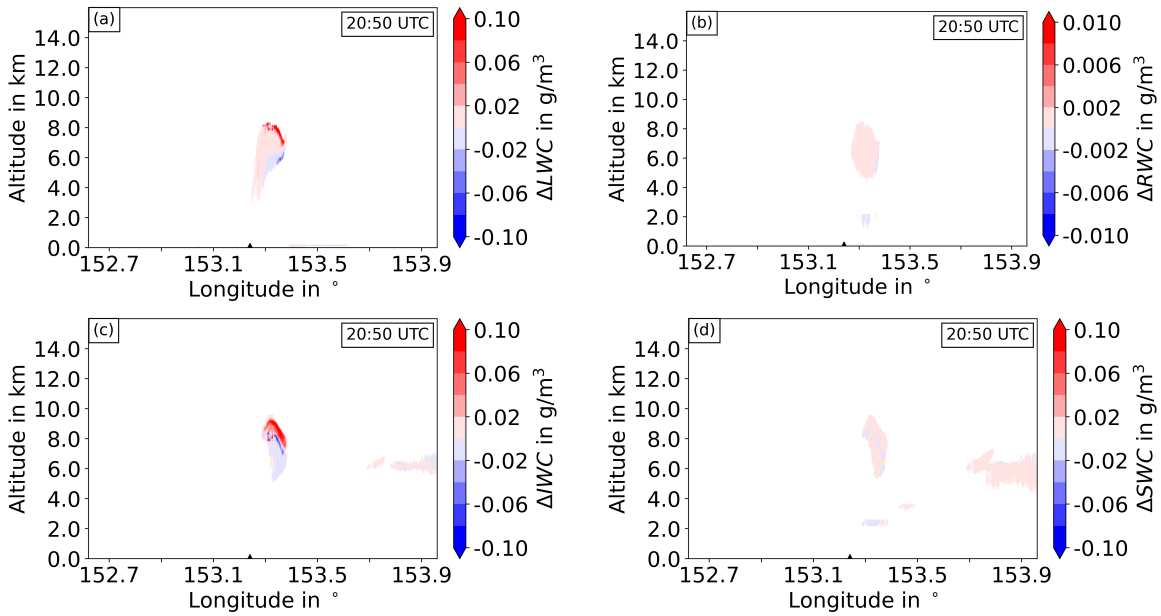

Figure A.28.: Difference of mean water contents between WQ-Exp and NoQ-Exp at 20:50 UTC during phase 4. See figure A.24 for description.

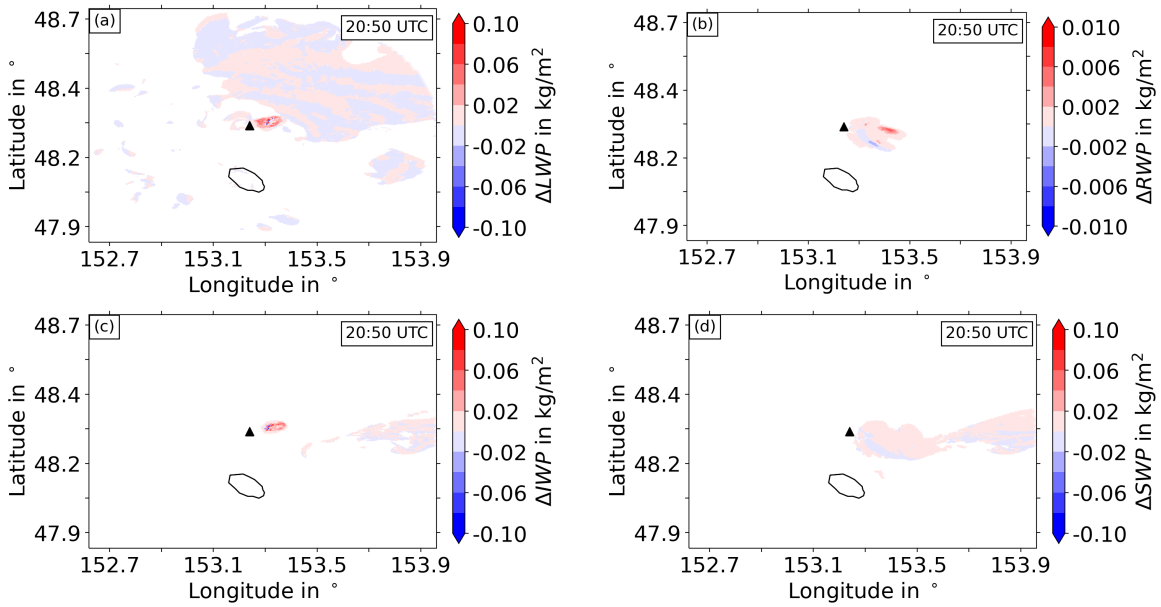

Figure A.29.: Difference of water paths between WQ-Exp and NoQ-Exp at 20:50 UTC during phase 4. See figure A.25 for description.

Phase 5:

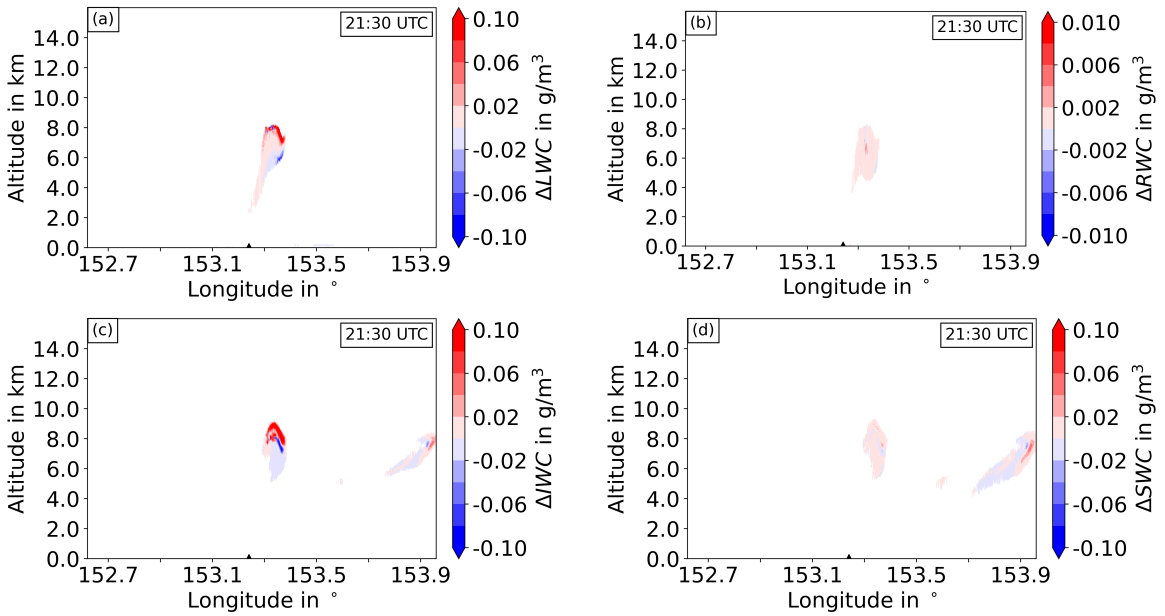

Figure A.30.: Difference of mean water contents between WQ-Exp and NoQ-Exp at 21:30 UTC during phase 5. See figure A.24 for description.

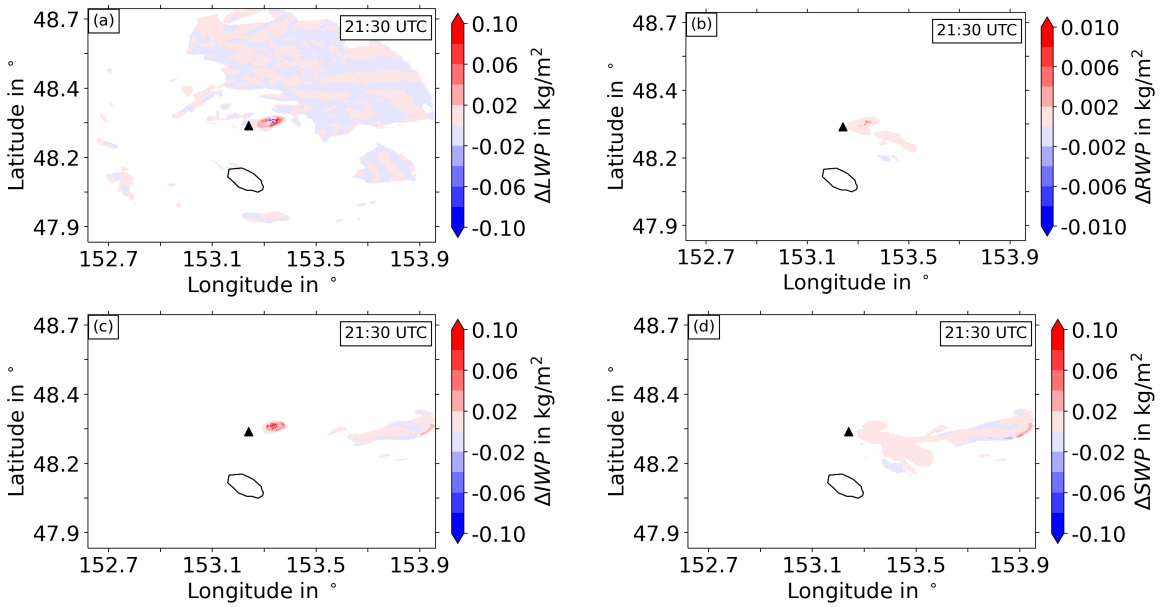

Figure A.31.: Difference of water paths between WQ-Exp and NoQ-Exp at 21:30 UTC during phase 5. See figure A.25 for description.

Phase 6:

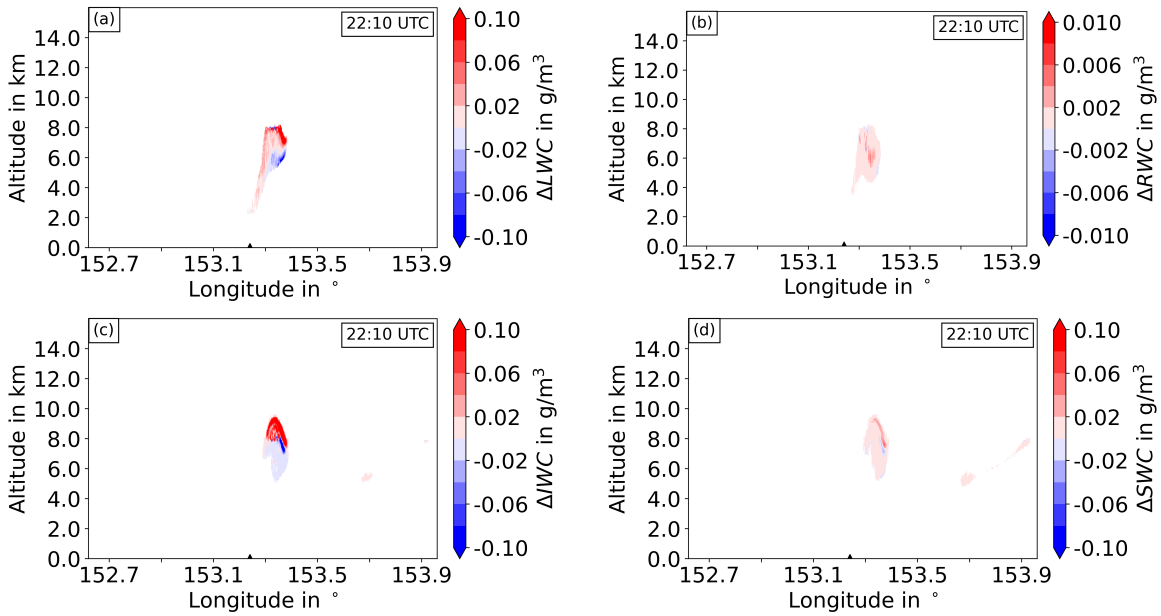

Figure A.32.: Difference of mean water contents between WQ-Exp and NoQ-Exp at 22:10 UTC during phase 6. See figure A.24 for description.

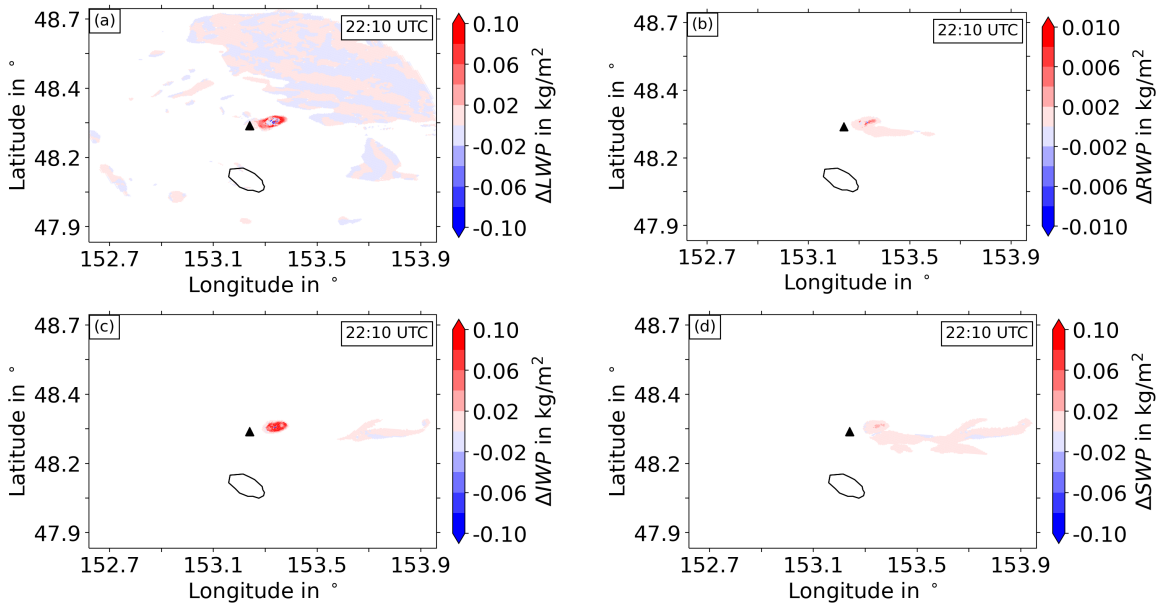

Figure A.33.: Difference of water paths between WQ-Exp and NoQ-Exp at 22:10 UTC during phase 6. See figure A.25 for description.

Phase 8:

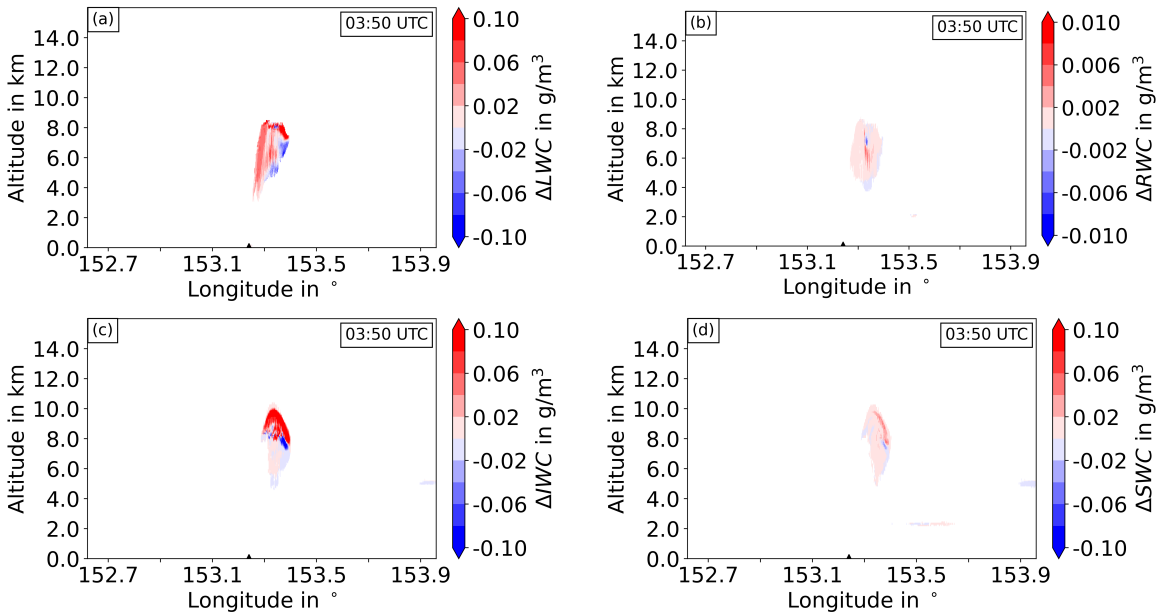

Figure A.34.: Difference of mean water contents between WQ-Exp and NoQ-Exp at 05:50 UTC during phase 8. See figure A.24 for description.

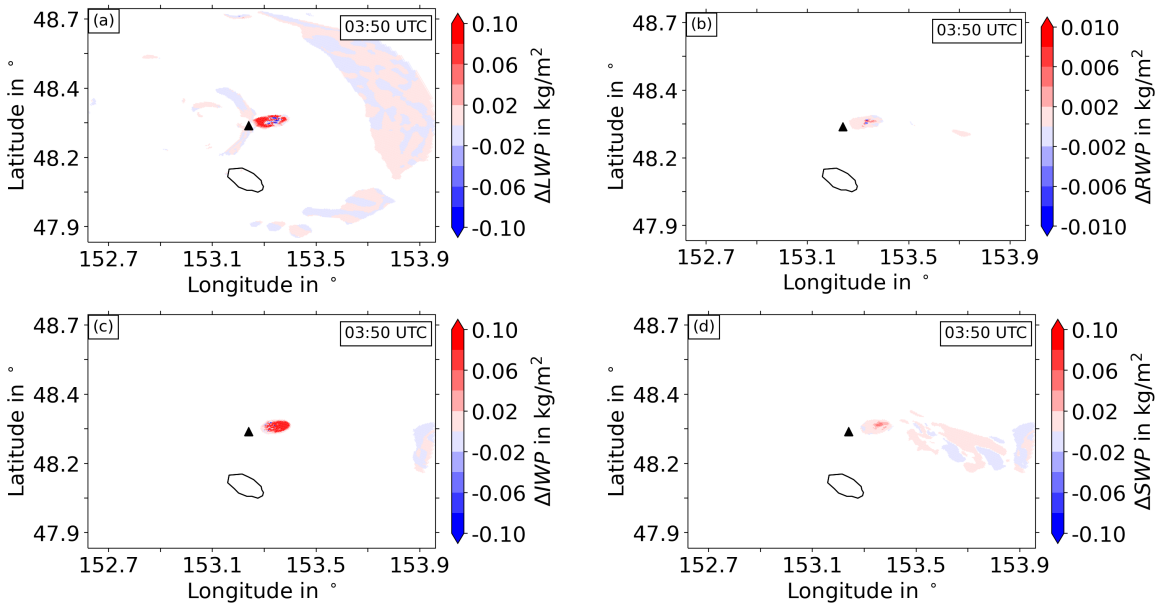

Figure A.35.: Difference of water paths between WQ-Exp and NoQ-Exp at 03:50 UTC during phase 8. See figure A.25 for description.

Phase 9:

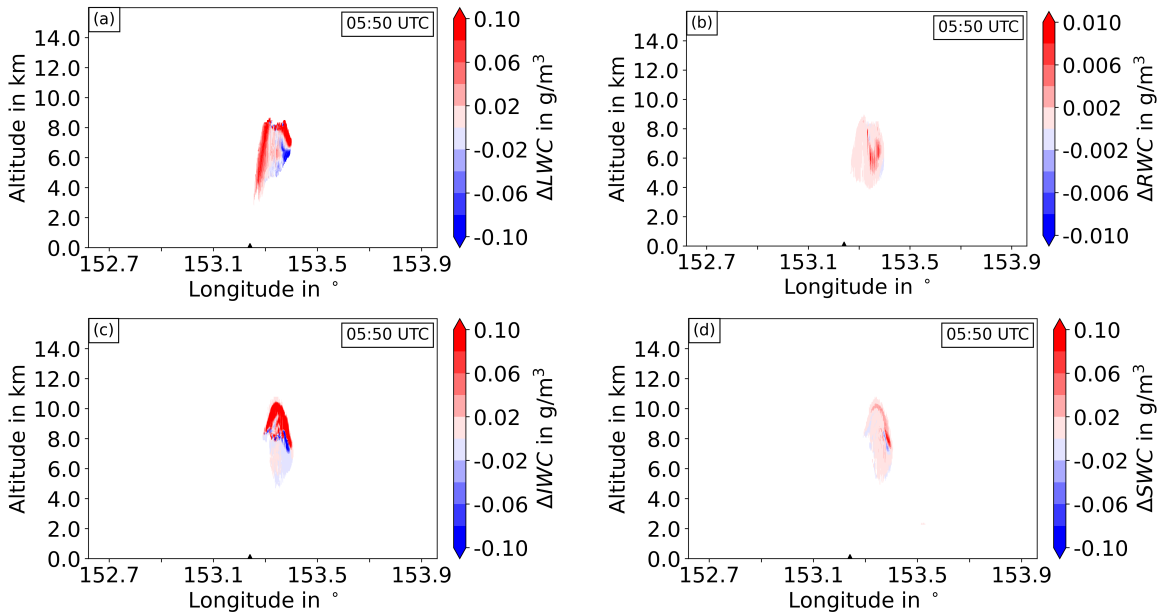

Figure A.36.: Difference of mean water contents between WQ-Exp and NoQ-Exp at 05:50 UTC during phase 9. See figure A.24 for description.

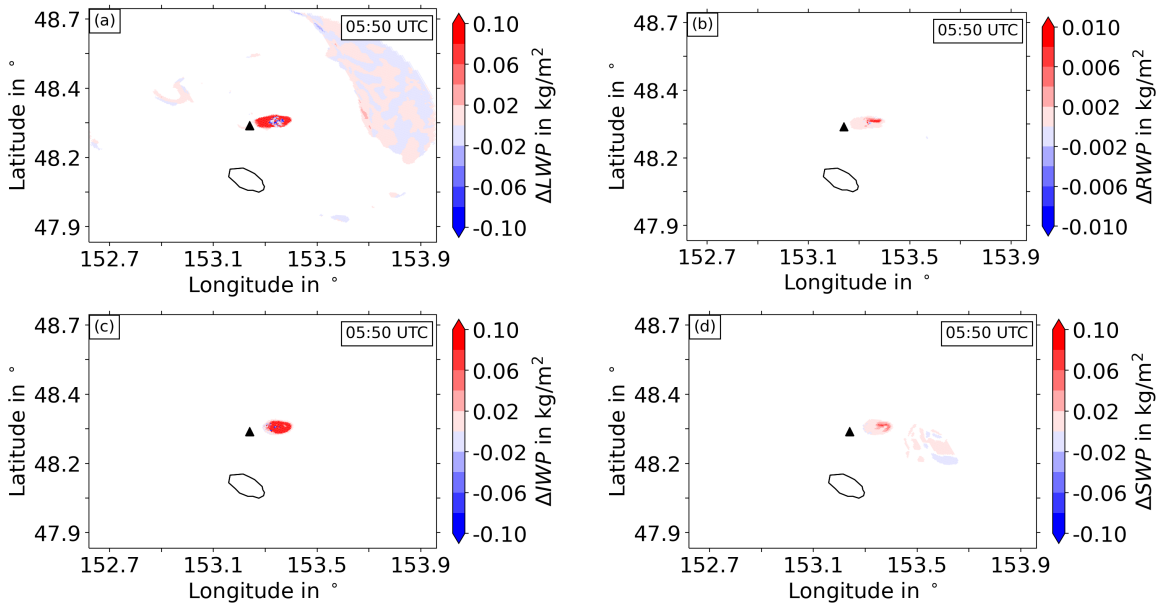

Figure A.37.: Difference of water paths between WQ-Exp and NoQ-Exp at 05:50 UTC during phase 9. See figure A.25 for description.

A.5. Figures for section 6.3.3

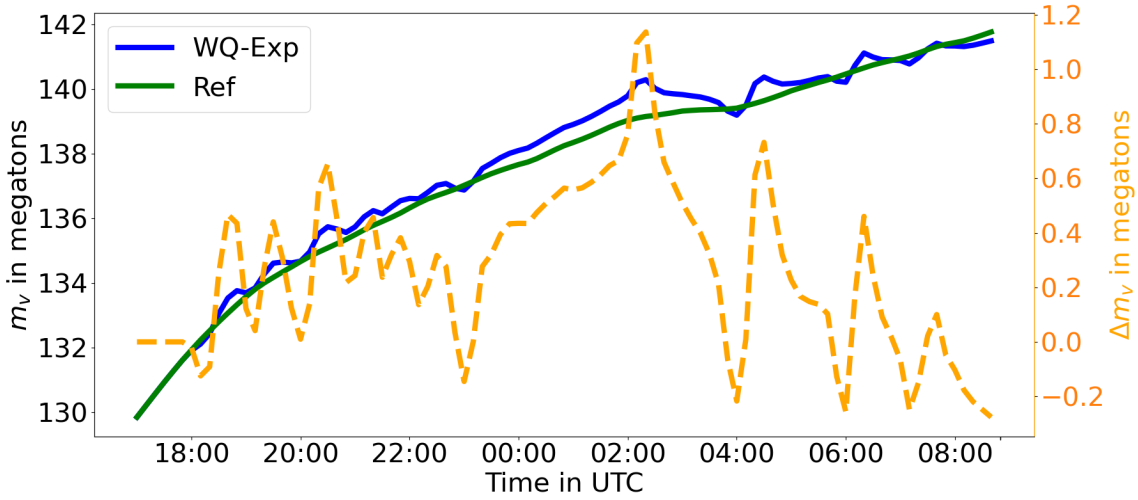

Figure A.38.: Temporal evolution of water vapor mass m_v in megatons in the model domain for WQ-Exp (blue curve), Ref (green curve) and the difference between WQ-Exp and Ref Δm_v (dashed orange curve) in megatons.

B. Acronyms

1-D	one-dimensional
3-D	three-dimensional
AHI	infrared Advanced Himawari Imager
ASHEE	ASH Equilibrium Eulerian
ATHAM	Active Tracer High Resolution Atmospheric Model
B	bisection
BPT	Buoyant Plume Theory
Cb	cumulonimbus
CCN	cloud condensation nuclei
CO_2	carbon dioxide
COSMO	COnsortium for Small-scale MOdeling
DKRZ	German Climate Computing Center
DWD	German Weather Service
G17	GOES-17
GOES	Geostationary Operational Environmental Satellite
Hi8	Himawari-8
HTHH	Hunga Tonga-Hunga Ha'apai
ICON-ART	ICOsahedral Nonhydrostatic - Aerosol and Reactive Trace Gases
IMK	Institute of Meteorology and Cimate Research
IN	ice nuclei
IWC	ice water content
IWP	ice water path
JAXA	Japan Aerospace Exploration Agency
JMA	Japan Meteorological Agency
K-H	Kelvin-Helmholtz

KIT	Karlsruhe Institute of Technology
LBC	lower boundary condition
LAM	Limited Area Mode
LES	large-eddy simulations
LW	longwave
LWC	liquid water content
LWP	liquid water path
Mg	magnesium
MER	mass eruption rate
MPI-M	Max Planck Institute for Meteorology
MCSs	mesoscale convective systems
NBL	neutral buoyancy level
$\mathbf{N_2}$	nitrogen
NMMB-MONARCH-ASH	Nonhydrostatic Multiscale Model on the B-grid – Multiscale Online Nonhydrostatic AtmospheRe CHemistry model – ASH
NOAA	National Oceanic and Atmospheric Administration
NWP	numerical weather prediction model
$\mathbf{O_2}$	oxygen
$\mathbf{O_3}$	ozone
PDAC	Pyroclastic Dispersal Analysis Code
PDC	pyroclastic density current
R	Root Division
RWC	rain water content
RWP	rain water path
Si	silicon
$\mathbf{SiO_2}$	silicon dioxide
$\mathbf{SO_2}$	sulfur dioxide
SW	shortwave
SWC	snow water content
SWP	snow water path

UBC	upper boundary condition
VEI	Volcanic Explosivity Index
VOLCAT	VOLcanic Cloud Analysis Toolkit
VZA	view zenith angle
WRF/ARW	Weather Research and Forecasting Model / Advanced Research WRF

C. Bibliography

Abdelkader, M., S. Metzger, B. Steil, K. Klingmüller, H. Tost, A. Pozzer, G. Stenchikov, L. Barrie, and J. Lelieveld, 2017: Sensitivity of transatlantic dust transport to chemical aging and related atmospheric processes. *Atmospheric Chemistry and Physics*, **17 (6)**, 3799–3821, doi:https://doi.org/10.5194/acp-17-3799-2017.

Adam, D., 2022: Tonga volcano eruption created puzzling ripples in Earth's atmosphere. *Nature*, **601 (7894)**, 497, doi:10.1038/d41586-022-00127-1.

Amores, A., S. Monserrat, M. Marcos, D. Argüeso, J. Villalonga, G. Jordà, and D. Gomis, 2022: Numerical simulation of atmospheric Lamb waves generated by the 2022 Hunga-Tonga volcanic eruption. *Geophysical Research Letters*, **49 (6)**, e2022GL098 240, doi:10.1029/2022GL098240.

Baines, P. G. and S. Sacks, 2017: The generation and propagation of atmospheric internal waves caused by volcanic eruptions. *Atmosphere*, **8 (3)**, 60, doi:10.3390/atmos8030060.

Balachandar, S. and J. K. Eaton, 2010: Turbulent dispersed multiphase flow. *Annual review of fluid mechanics*, **42**, 111–133, doi:10.1146/annurev.fluid.010908.165243.

Bangert, M., C. Kottmeier, B. Vogel, and H. Vogel, 2011: Regional scale effects of the aerosol cloud interaction simulated with an online coupled comprehensive chemistry model. *Atmospheric Chemistry and Physics*, **11 (9)**, 4411–4423, doi:10.5194/acp-11-4411-2011.

Baumgarten, G. and D. C. Fritts, 2014: Quantifying Kelvin-Helmholtz instability dynamics observed in noctilucent clouds: 1. Methods and observations. *Journal of Geophysical Research: Atmospheres*, **119 (15)**, 9324–9337, doi:10.1002/2014JD021832.

Beckett, F. M., C. S. Witham, S. J. Leadbetter, R. Crocker, H. N. Webster, M. C. Hort, A. R. Jones, B. J. Devenish, and D. J. Thomson, 2020: Atmospheric dispersion modelling at the London VAAC: A review of developments since the 2010 eyjafjallajökull volcano ash cloud. *Atmosphere*, **11 (4)**, 352, doi:10.3390/atmos11040352.

Binkowski, F. S. and U. Shankar, 1995: The regional particulate matter model: 1. Model description and preliminary results. *Journal of Geophysical Research: Atmospheres*, **100 (D12)**, 26 191–26 209, doi:10.1029/95JD02093.

Boucher, O., 2015: *Atmospheric aerosols*. Springer.

Brönnimann, S. and D. Krämer, 2016: *Tambora and the" Year Without a Summer" of 1816. A perspective on earth and human systems science*, Vol. 90. Geographica Bernensia.

Bruckert, J., 2023: Impact of eruption dynamics and gas–aerosol interaction on the early stage evolution of volcanic plumes. Ph.D. thesis, Dissertation, Karlsruhe, Karlsruher Institut für Technologie (KIT), 2023.

Bruckert, J., G. A. Hoshyaripour, Á. Horváth, L. O. Muser, F. J. Prata, C. Hoose, and B. Vogel, 2022: Online treatment of eruption dynamics improves the volcanic ash and SO 2 dispersion forecast: case of the 2019 Raikoke eruption. *Atmospheric Chemistry and Physics*, **22 (5)**, 3535–3552, doi:10.5194/acp-22-3535-2022.

Budd, L., S. Griggs, D. Howarth, and S. Ison, 2011: A fiasco of volcanic proportions? eyjafjallajökull and the closure of european airspace. *Mobilities*, **6 (1)**, 31–40, doi:10.1080/17450101.2011.532650.

Bursik, M., 2001: Effect of wind on the rise height of volcanic plumes. *Geophysical Research Letters*, **28 (18)**, 3621–3624, doi:10.1029/2001GL013393.

Carazzo, G., F. Girault, T. Aubry, H. Bouquerel, and E. Kaminski, 2014: Laboratory experiments of forced plumes in a density-stratified crossflow and implications for volcanic plumes. *Geophysical Research Letters*, **41 (24)**, 8759–8766, doi:10.1002/2014GL061887.

Carazzo, G., E. Kaminski, and S. Tait, 2006: The route to self-similarity in turbulent jets and plumes. *Journal of Fluid Mechanics*, **547**, 137–148, doi:10.1017/S002211200500683X.

Carazzo, G., E. Kaminski, and S. Tait, 2008: On the dynamics of volcanic columns: A comparison of field data with a new model of negatively buoyant jets. *Journal of Volcanology and Geothermal Research*, **178 (1)**, 94–103, doi:10.1016/j.jvolgeores.2008.01.002.

Carcano, S., L. Bonaventura, T. Esposti Ongaro, and A. Neri, 2013: A semi-implicit, second-order-accurate numerical model for multiphase underexpanded volcanic jets. *Geoscientific Model Development*, **6 (6)**, 1905–1924, doi:10.5194/gmd-6-1905-2013.

Carr, J. L., Á. Horváth, D. L. Wu, and M. D. Friberg, 2022: Stereo plume height and motion retrievals for the record-setting hunga tonga-hunga ha'apai eruption of 15 january 2022. *Geophysical Research Letters*, **49 (9)**, e2022GL098 131, doi:10.1029/2022GL098131.

Casadevall, T. J., 1994: *Volcanic ash and aviation safety: proceedings of the first international symposium on volcanic ash and aviation safety*. 2047, US Government Printing Office.

Cerminara, M., 2015: The multiphase buoyant plume solution of the dusty gas model. *arXiv preprint arXiv:1506.01638*, doi:10.48550/arXiv.1506.01638.

Cerminara, M., T. Esposti Ongaro, and L. C. Berselli, 2016: ASHEE-1.0: a compressible, equilibrium–Eulerian model for volcanic ash plumes. *Geoscientific Model Development*, **9 (2)**, 697–730, doi:10.5194/gmd-9-697-2016.

Collini, E., M. S. Osores, A. Folch, J. G. Viramonte, G. Villarosa, and G. Salmuni, 2013: Volcanic ash forecast during the June 2011 Cordón Caulle eruption. *Natural hazards*, **66**, 389–412, doi:10.1007/s11069-012-0492-y.

Costa, A., A. Folch, and G. Macedonio, 2013: Density-driven transport in the umbrella region of volcanic clouds: Implications for tephra dispersion models. *Geophysical Research Letters*, **40 (18)**, 4823–4827, doi:10.1002/grl.50942.

Costa, A., Y. J. Suzuki, M. Cerminara, B. J. Devenish, T. E. Ongaro, M. Herzog, A. R. Van Eaton, L. Denby, M. Bursik, M. d. Vitturi, et al., 2016: Results of the eruptive column model inter-comparison study. *Journal of Volcanology and Geothermal Research*, **326**, 2–25, doi:10.1016/j.jvolgeores.2016.01.017.

Dare, R. A., R. J. Potts, and A. G. Wain, 2016: Modelling wet deposition in simulations of volcanic ash dispersion from hypothetical eruptions of Merapi, Indonesia. *Atmospheric Environment*, **143**, 190–201, doi:10.1016/j.atmosenv.2016.08.022.

Dartevelle, S., G. G. Ernst, J. Stix, and A. Bernard, 2002: Origin of the Mount Pinatubo climactic eruption cloud: Implications for volcanic hazards and atmospheric impacts. *Geology*, **30 (7)**, 663–666, doi:10.1130/0091-7613(2002)030<0663:OOTMPC>2.0.CO;2.

de Leeuw, J., A. Schmidt, C. S. Witham, N. Theys, I. A. Taylor, R. G. Grainger, R. J. Pope, J. Haywood, M. Osborne, and N. I. Kristiansen, 2021: The 2019 Raikoke volcanic eruption–Part 1: Dispersion model simulations and satellite retrievals of volcanic sulfur dioxide. *Atmospheric Chemistry and Physics*, **21 (14)**, 10 851–10 879, doi:10.5194/acp-21-10851-2021.

Degruyter, W. and C. Bonadonna, 2012: Improving on mass flow rate estimates of volcanic eruptions. *Geophysical Research Letters*, **39 (16)**, doi:10.1029/2012GL052566.

Degruyter, Wim and Bonadonna, Costanza, 2013: Impact of wind on the condition for column collapse of volcanic plumes. *Earth and Planetary Science Letters*, **377**, 218–226, doi:10.1016/j.epsl.2013.06.041.

Dellino, P., M. Gudmundsson, G. Larsen, D. Mele, J. Stevenson, T. Thordarson, and B. Zimanowski, 2012: Ash from the Eyjafjallajökull eruption (Iceland): Fragmentation processes and aerodynamic behavior. *Journal of Geophysical Research: Solid Earth*, **117 (B9)**, doi:10.1029/2011JB008726.

Doms, G., J. Förstner, E. Heise, H. Herzog, D. Mironov, M. Raschendorfer, T. Reinhardt, B. Ritter, R. Schrodin, J.-P. Schulz, et al., 2011: A description of the nonhydrostatic regional COSMO model.

Part II: Physical parameterization. *Deutscher Wetterdienst, Offenbach, Germany*, URL `http://www.cosmo-model.org`.

Drazin, P., 2015: Dynamical meteorology | Kelvin-Helmholtz Instability.

Druitt, T., 1998: Pyroclastic density currents. *Geological Society, London, Special Publications*, **145 (1)**, 145–182, doi:10.1144/GSL.SP.1996.145.01.0.

Folch, A., A. Costa, and G. Macedonio, 2016: FPLUME-1.0: An integral volcanic plume model accounting for ash aggregation. *Geoscientific Model Development*, **9 (1)**, 431–450, doi:10.5194/gmd-9-431-2016.

Forster, P. M. d. F. and K. Shine, 2002: Assessing the climate impact of trends in stratospheric water vapor. *Geophysical research letters*, **29 (6)**, 10–1, doi:10.1029/2001GL013909.

Gassmann, A. and H.-J. Herzog, 2008: Towards a consistent numerical compressible non-hydrostatic model using generalized Hamiltonian tools. *Quarterly Journal of the Royal Meteorological Society*, **134 (635)**, 1597–1613, doi:https://doi.org/10.1002/qj.297.

Gilbert, J. S. and R. S. J. Sparks, 1998: The physics of explosive volcanic eruptions. Geological Society of London.

Giorgetta, M. A., R. Brokopf, T. Crueger, M. Esch, S. Fiedler, J. Helmert, C. Hohenegger, L. Kornblueh, M. Köhler, E. Manzini, et al., 2018: ICON-A, the atmosphere component of the ICON earth system model: I. Model description. *Journal of Advances in Modeling Earth Systems*, **10 (7)**, 1613–1637, doi:https://doi.org/10.1029/2017MS001242.

Grindle, T. J., 2002: Even minor volcanic ash encounters can cause major damage to aircraft. *ICAO journal*, **2**, 29–30.

Gudmundsson, M. T., T. Thordarson, Á. Höskuldsson, G. Larsen, H. Björnsson, F. J. Prata, B. Oddsson, E. Magnússon, T. Högnadóttir, G. N. Petersen, et al., 2012: Ash generation and distribution from the April-May 2010 eruption of Eyjafjallajökull, Iceland. *Scientific reports*, **2 (1)**, 572, doi:10.1038/srep00572.

Guo, S., G. Bluth, W. Rose, I. Watson, and A. Prata, 2004a: Re-evaluation of SO2 release of the climactic June 15, 1991 Pinatubo eruption using TOMS and TOVS satellite data. *Geochem. Geophys. Geosyst*, **5**, Q04 001.

Guo, S., W. I. Rose, G. J. Bluth, and I. M. Watson, 2004b: Particles in the great Pinatubo volcanic cloud of June 1991: The role of ice. *Geochemistry, Geophysics, Geosystems*, **5 (5)**, doi:10.1029/2003GC000655.

Haghighatnasab, M., J. Kretzschmar, K. Block, and J. Quaas, 2022: Impact of Holuhraun volcano aerosols on clouds in cloud-system-resolving simulations. *Atmospheric Chemistry and Physics*, **22 (13)**, 8457–8472, doi:10.5194/acp-22-8457-2022.

Harvey, N. J., N. Huntley, H. F. Dacre, M. Goldstein, D. Thomson, and H. Webster, 2018: Multi-level emulation of a volcanic ash transport and dispersion model to quantify sensitivity to uncertain parameters. *Natural hazards and earth system sciences*, **18 (1)**, 41–63, doi:10.5194/nhess-18-41-2018.

Heinze, R., A. Dipankar, C. C. Henken, C. Moseley, O. Sourdeval, S. Trömel, X. Xie, P. Adamidis, F. Ament, H. Baars, et al., 2017: Large-eddy simulations over Germany using ICON: A comprehensive evaluation. *Quarterly Journal of the Royal Meteorological Society*, **143 (702)**, 69–100, doi:https://doi.org/10.1002/qj.2947.

Herzog, M. and H.-F. Graf, 2010: Applying the three-dimensional model ATHAM to volcanic plumes: Dynamic of large co-ignimbrite eruptions and associated injection heights for volcanic gases. *Geophysical Research Letters*, **37 (19)**, doi:10.1029/2010GL044986.

Herzog, M., H.-F. Graf, C. Textor, and J. M. Oberhuber, 1998: The effect of phase changes of water on the development of volcanic plumes. *Journal of Volcanology and Geothermal Research*, **87 (1-4)**, 55–74, doi:10.1016/S0377-0273(98)00100-0.

Herzog, M., J. M. Oberhuber, and H.-F. Graf, 2003: A prognostic turbulence scheme for the nonhydrostatic plume model ATHAM. *Journal of the atmospheric sciences*, **60 (22)**, 2783–2796, doi:10.1175/1520-0469(2003)060<2783:APTSFT>2.0.CO;2.

Hesselberg, T., 1926: Die Gesetze der ausgeglichenen atmosphärischen Bewegungen. *Beiträge zur Physik der Atmosphäre*, **12**, 141–160.

Hoose, C. and O. Möhler, 2012: Heterogeneous ice nucleation on atmospheric aerosols: a review of results from laboratory experiments. *Atmospheric Chemistry and Physics*, **12 (20)**, 9817–9854, doi:10.5194/acp-12-9817-2012.

Horváth, Á., J. L. Carr, O. A. Girina, D. L. Wu, A. A. Bril, A. A. Mazurov, D. V. Melnikov, G. A. Hoshyaripour, and S. A. Buehler, 2021a: Geometric estimation of volcanic eruption column height from GOES-R near-limb imagery–Part 1: Methodology. *Atmospheric Chemistry and Physics*, **21 (16)**, 12 189–12 206, doi:10.5194/acp-21-12189-2021.

Horváth, Á., O. A. Girina, J. L. Carr, D. L. Wu, A. A. Bril, A. A. Mazurov, D. V. Melnikov, G. A. Hoshyaripour, and S. A. Buehler, 2021b: Geometric estimation of volcanic eruption column height from GOES-R near-limb imagery–Part 2: Case studies. *Atmospheric Chemistry and Physics*, **21 (16)**, 12 207–12 226, doi:10.5194/acp-21-12207-2021.

Horwell, C. J. and P. J. Baxter, 2006: The respiratory health hazards of volcanic ash: a review for volcanic risk mitigation. *Bulletin of volcanology*, **69**, 1–24, doi:10.1007/s00445-006-0052-y.

Hu, W., T. Zhao, Y. Bai, S. Kong, J. Xiong, X. Sun, Q. Yang, Y. Gu, and H. Lu, 2021: Importance of regional PM2. 5 transport and precipitation washout in heavy air pollution in the Twain-Hu Basin over Central China: Observational analysis and WRF-Chem simulation. *Science of the Total Environment*, **758**, 143 710, doi:10.1016/j.scitotenv.2020.143710.

Jacobs, C. T., G. S. Collins, M. D. Piggott, and S. C. Kramer, 2014: Multiphase flow modelling of explosive volcanic eruptions using an adaptive unstructured mesh-based approach.

Jain, S., 2014: *Fundamentals of physical geology*. Springer.

Jensen, E. J., S. Woods, R. P. Lawson, T. P. Bui, L. Pfister, T. D. Thornberry, A. W. Rollins, J.-P. Vernier, L. L. Pan, S. Honomichl, et al., 2018: Ash particles detected in the tropical lower stratosphere. *Geophysical Research Letters*, **45 (20)**, 11–483, doi:10.1029/2018GL079605.

Kabanov, V., S. Khomenko, G. Khlopov, A. Linkova, T. Tkachova, K. Schuenemann, and O. Voitovych, 2015: Algorithm for the Retrieval of Liquid Water Content Profile of Clouds by Active and Passive Remote Sensing. *Journal of Earth Science Research*, **3 (2)**, 13, doi:10.18005/JESR0302001.

Kawaratani, R. K. and S.-i. Fujita, 1990: Wet deposition of volcanic gases and ash in the vicinity of Mount Sakurajima. *Atmospheric Environment. Part A. General Topics*, **24 (6)**, 1487–1492, doi:10.1016/0960-1686(90)90057-T.

Kerminen, V.-M. and A. S. Wexler, 1995: Growth laws for atmospheric aerosol particles: An examination of the bimodality of the accumulation mode. *Atmospheric Environment*, **29 (22)**, 3263–3275, doi:10.1016/1352-2310(95)00249-X.

Koyaguchi, T. and A. W. Woods, 1996: On the formation of eruption columns following explosive mixing of magma and surface-water. *Journal of Geophysical Research: Solid Earth*, **101 (B3)**, 5561–5574, doi:10.1029/95JB01687.

Kramm, G., K. Beheng, and H. Müller, 1992: Modeling of the vertical transport of polydispersed aerosol particles in the atmospheric surface layer in Precipitation Scavenging and Atmospheric Surface Exchange.

Lacasse, C., S. Karlsdóttir, G. Larsen, H. Soosalu, W. Rose, and G. Ernst, 2004: Weather radar observations of the Hekla 2000 eruption cloud, Iceland. *Bulletin of Volcanology*, **66**, 457–473, doi:10.1007/s00445-003-0329-3.

Lamb, H., 1881: On the vibrations of an elastic sphere. *Proceedings of the London Mathematical Society*, **1 (1)**, 189–212, doi:10.1112/plms/s1-13.1.189.

Luce, H., T. Mega, M. K. Yamamoto, M. Yamamoto, H. Hashiguchi, S. Fukao, N. Nishi, T. Tajiri, and M. Nakazato, 2010: Observations of Kelvin-Helmholtz instability at a cloud base with the middle and upper atmosphere (MU) and weather radars. *Journal of Geophysical Research: Atmospheres*, **115 (D19)**, doi:10.1029/2009JD013519.

Luterbacher, J. and C. Pfister, 2015: The year without a summer. *Nature Geoscience*, **8 (4)**, 246–248, doi:10.1038/ngeo2404.

Macedonio, G., A. Costa, and A. Folch, 2016: Uncertainties in volcanic plume modeling: A parametric study using FPLUME. *Journal of Volcanology and Geothermal Research*, **326**, 92–102, doi:10.1016/j.jvolgeores.2016.03.016.

Malavelle, F. F., J. M. Haywood, A. Jones, A. Gettelman, L. Clarisse, S. Bauduin, R. P. Allan, I. H. H. Karset, J. E. Kristjánsson, L. Oreopoulos, et al., 2017: Strong constraints on aerosol–cloud interactions from volcanic eruptions. *Nature*, **546 (7659)**, 485–491, doi:10.1038/nature22974.

Marshall, L. R., E. C. Maters, A. Schmidt, C. Timmreck, A. Robock, and M. Toohey, 2022: Volcanic effects on climate: recent advances and future avenues. *Bulletin of Volcanology*, **84 (5)**, 54, doi:10.1007/s00445-022-01559-3.

Marti, A., A. Folch, O. Jorba, and Z. Janjic, 2017: Volcanic ash modeling with the online NMMB-MONARCH-ASH v1. 0 model: model description, case simulation, and evaluation. *Atmospheric chemistry and physics*, **17 (6)**, 4005–4030, doi:10.5194/acp-17-4005-2017.

Mastin, L. G., 2007: A user-friendly one-dimensional model for wet volcanic plumes. *Geochemistry, Geophysics, Geosystems*, **8 (3)**, doi:10.1029/2006GC001455.

Mastin, L. G., M. Guffanti, R. Servranckx, P. Webley, S. Barsotti, K. Dean, A. Durant, J. W. Ewert, A. Neri, W. I. Rose, et al., 2009: A multidisciplinary effort to assign realistic source parameters to models of volcanic ash-cloud transport and dispersion during eruptions. *Journal of Volcanology and Geothermal Research*, **186 (1-2)**, 10–21, doi:10.1016/j.jvolgeores.2009.01.008.

Mastin, Larry G, 2014: Testing the accuracy of a 1-D volcanic plume model in estimating mass eruption rate. *Journal of Geophysical Research: Atmospheres*, **119 (5)**, 2474–2495, doi:10.1002/2013JD020604.

Mazzocchi, M., F. Hansstein, and M. Ragona, 2010: The 2010 volcanic ash cloud and its financial impact on the European airline industry. *CESifo Forum*, München: ifo Institut für Wirtschaftsforschung an der Universität München, Vol. 11, 92–100.

McKee, K., C. M. Smith, K. Reath, E. Snee, S. Maher, R. S. Matoza, S. Carn, L. Mastin, K. Anderson, D. Damby, et al., 2021: Evaluating the state-of-the-art in remote volcanic eruption characteriza-

tion Part I: Raikoke volcano, Kuril Islands. *Journal of Volcanology and Geothermal Research*, **419**, 107 354, doi:10.1016/j.jvolgeores.2021.107354.

Medici, E., J. Allen, and G. Waite, 2014: Modeling shock waves generated by explosive volcanic eruptions. *Geophysical Research Letters*, **41 (2)**, 414–421, doi:10.1002/2013GL058340.

Morrisey, M. and L. Mastin, 2000: Vulcanian eruptions in Encyclopedia of Volcanoes, H. Sigurrsson.

Morton, B. R., G. I. Taylor, and J. S. Turner, 1956: Turbulent gravitational convection from maintained and instantaneous sources. *Proceedings of the Royal Society of London. Series A. Mathematical and Physical Sciences*, **234 (1196)**, 1–23, doi:10.1098/rspa.1956.0011.

Murcray, D. G., F. J. Murcray, D. B. Barker, and H. J. Mastenbrook, 1981: Changes in stratospheric water vapor associated with the Mount St. Helens eruption. *Science*, **211 (4484)**, 823–824, doi:10.1126/science.211.4484.823.

Muser, L. O., 2022: Combining Aerosol Aging and Data Assimilation for Improving Volcanic Aerosol Forecast. Ph.D. thesis, Dissertation, Karlsruhe, Karlsruher Institut für Technologie (KIT), 2022.

Muser, L. O., G. A. Hoshyaripour, J. Bruckert, Á. Horváth, E. Malinina, S. Wallis, F. J. Prata, A. Rozanov, C. von Savigny, H. Vogel, et al., 2020: Particle aging and aerosol–radiation interaction affect volcanic plume dispersion: evidence from the Raikoke 2019 eruption. *Atmospheric Chemistry and Physics*, **20 (23)**, 15 015–15 036, doi:10.5194/acp-20-15015-2020.

Neri, A., T. Esposti Ongaro, G. Macedonio, and D. Gidaspow, 2003: Multiparticle simulation of collapsing volcanic columns and pyroclastic flow. *Journal of Geophysical Research: Solid Earth*, **108 (B4)**, doi:10.1029/2001JB000508.

Newhall, C. G. and S. Self, 1982: The volcanic explosivity index (VEI) an estimate of explosive magnitude for historical volcanism. *Journal of Geophysical Research: Oceans*, **87 (C2)**, 1231–1238, doi:10.1029/JC087iC02p01231.

Nguyen, C. M., M. Wolde, and A. Korolev, 2019: Determination of ice water content (IWC) in tropical convective clouds from X-band dual-polarization airborne radar. *Atmospheric Measurement Techniques*, **12 (11)**, 5897–5911, doi:10.5194/amt-12-5897-2019.

Niemeier, U., C. Timmreck, H.-F. Graf, S. Kinne, S. Rast, and S. Self, 2009: Initial fate of fine ash and sulfur from large volcanic eruptions. *Atmospheric Chemistry and Physics*, **9 (22)**, 9043–9057, doi:10.5194/acp-9-9043-2009.

Oberhuber, J. M., M. Herzog, H.-F. Graf, and K. Schwanke, 1998: Volcanic plume simulation on large scales. *Journal of Volcanology and Geothermal Research*, **87 (1-4)**, 29–53, doi:10.1016/S0377-0273(98)00099-7.

Ongaro, T. E., C. Cavazzoni, G. Erbacci, A. Neri, and M.-V. Salvetti, 2007: A parallel multiphase flow code for the 3D simulation of explosive volcanic eruptions. *Parallel Computing*, **33 (7-8)**, 541–560, doi:10.1016/j.parco.2007.04.003.

Otsuka, S., 2022: Visualizing Lamb waves from a volcanic eruption using meteorological satellite Himawari-8. *Geophysical Research Letters*, **49 (8)**, e2022GL098 324, doi:10.1029/2022GL098324.

Pavolonis, M. J., A. K. Heidinger, and J. Sieglaff, 2013: Automated retrievals of volcanic ash and dust cloud properties from upwelling infrared measurements. *Journal of Geophysical Research: Atmospheres*, **118 (3)**, 1436–1458, doi:10.1002/jgrd.50173.

Pavolonis, M. J., J. Sieglaff, and J. Cintineo, 2015: Spectrally Enhanced Cloud Objects—A generalized framework for automated detection of volcanic ash and dust clouds using passive satellite measurements: 1. Multispectral analysis. *Journal of Geophysical Research: Atmospheres*, **120 (15)**, 7813–7841, doi:10.1002/2014JD022968.

Pavolonis, M. J., J. Sieglaff, and J. Cintineo, 2015: Spectrally Enhanced Cloud Objects—A generalized framework for automated detection of volcanic ash and dust clouds using passive satellite measurements: 2. Cloud object analysis and global application. *Journal of Geophysical Research: Atmospheres*, **120 (15)**, 7842–7870, doi:10.1002/2014JD022969.

Pavolonis, M. J., J. Sieglaff, and J. Cintineo, 2018: Automated Detection of Explosive Volcanic Eruptions Using Satellite-Derived Cloud Vertical Growth Rates. *Earth and Space Science*, **5 (12)**, 903–928, doi:10.1029/2018EA000410.

Pinto, J. P., R. P. Turco, and O. B. Toon, 1989: Self-limiting physical and chemical effects in volcanic eruption clouds. *Journal of Geophysical Research: Atmospheres*, **94 (D8)**, 11 165–11 174, doi:10.1029/JD094iD08p11165.

Pruppacher, H. R., J. D. Klett, and P. K. Wang, 1998: Microphysics of clouds and precipitation.

Ragona, M., F. Hannstein, and M. Mazzocchi, 2011: The financial impact of the volcanic ash crisis on the European airline industry. *Governing Disasters: The Challenges of Emergency Risk Regulafion*, 27–50.

Rieger, D., 2017: *Der Einfluss von natürlichem Aerosol auf Wolken über Mitteleuropa*, Vol. 71. KIT Scientific Publishing.

Rieger, D., M. Bangert, I. Bischoff-Gauss, J. Förstner, K. Lundgren, D. Reinert, J. Schröter, H. Vogel, G. Zängl, R. Ruhnke, and B. Vogel, 2015: ICON–ART 1.0 – a new online-coupled model system from the global to regional scale. *Geoscientific Model Development*, **8 (6)**, 1659–1676, doi:10.5194/gmd-8-1659-2015.

Riemer, N., 2002: Numerische Simulationen zur Wirkung des Aerosols auf die tropospharische Chemie und die Sichtweite. Ph.D. thesis, Karlsruhe, Univ., Diss., 2002.

Robock, A., 2000: Volcanic eruptions and climate. *Reviews of geophysics*, **38 (2)**, 191–219, doi:10.1029/1998RG000054.

Robrecht, S., B. Vogel, J.-U. Grooß, K. Rosenlof, T. Thornberry, A. Rollins, M. Krämer, L. Christensen, and R. Müller, 2019: Mechanism of ozone loss under enhanced water vapour conditions in the mid-latitude lower stratosphere in summer. *Atmospheric chemistry and physics*, **19 (9)**, 5805–5833, doi:10.5194/acp-19-5805-2019.

Rose, W. I., G. J. Bluth, and I. M. Watson, 2004: Ice in volcanic clouds: When and where. *Proc. of the 2nd Int. Conf. on Volcanic Ash and Aviation Safety, OFCM, Washington, DC, Session*, Vol. 3, 61.

Rose, W. I., D. Delene, D. Schneider, G. Bluth, A. Krueger, I. Sprod, C. McKee, H. Davies, and G. G. Ernst, 1995: Ice in the 1994 Rabaul eruption cloud: implications for volcano hazard and atmospheric effects. *Nature*, **375 (6531)**, 477–479, doi:10.1038/375477a0.

Rose, W. I. and A. J. Durant, 2009: Fine ash content of explosive eruptions. *Journal of Volcanology and Geothermal Research*, **186 (1-2)**, 32–39, doi:10.1016/j.jvolgeores.2009.01.010.

Schaller, N., T. Griesser, A. Fischer, A. STICK-LER, and S. ONNIMANN, 2009: Climate effects of the 1883 Krakatoa eruption: Historical and present perspectives. *Vjschr. Natf. Ges. Zürich*, **154**, 31–40.

Schmincke, H.-U., 2004: *Volcanism*, Vol. 28. Springer Science & Business Media.

Schoeberl, M. R., Y. Wang, R. Ueyama, G. Taha, E. Jensen, and W. Yu, 2022: Analysis and impact of the Hunga Tonga-Hunga Ha'apai stratospheric water vapor plume. *Geophysical Research Letters*, **49 (20)**, e2022GL100 248, doi:10.1029/2022GL100248.

Schröter, J., D. Rieger, C. Stassen, H. Vogel, M. Weimer, S. Werchner, J. Förstner, F. Prill, D. Reinert, G. Zängl, et al., 2018: ICON-ART 2.1: a flexible tracer framework and its application for composition studies in numerical weather forecasting and climate simulations. *Geoscientific Model Development*, **11 (10)**, 4043–4068, doi:https://doi.org/10.5194/gmd-11-4043-2018.

Schumann, U., B. Weinzierl, O. Reitebuch, H. Schlager, A. Minikin, C. Forster, R. Baumann, T. Sailer, K. Graf, H. Mannstein, et al., 2011: Airborne observations of the eyjafjalla volcano ash cloud over europe during air space closure in april and may 2010. *Atmospheric Chemistry and Physics*, **11 (5)**, 2245–2279, doi:10.5194/acp-11-2245-2011.

Schwartz, M. J., W. G. Read, M. L. Santee, N. J. Livesey, L. Froidevaux, A. Lambert, and G. L. Manney, 2013: Convectively injected water vapor in the North American summer lowermost stratosphere. *Geophysical Research Letters*, **40 (10)**, 2316–2321, doi:10.1002/grl.50421.

Scollo, S., A. Folch, and A. Costa, 2008: A parametric and comparative study of different tephra fallout models. *Journal of Volcanology and Geothermal Research*, **176 (2)**, 199–211, doi:10.1016/j.jvolgeores.2008.04.002.

Seinfeld, J. H. and S. N. Pandis, 2016: *Atmospheric chemistry and physics: from air pollution to climate change*. John Wiley & Sons.

Shindell, D. T., 2001: Climate and ozone response to increased stratospheric water vapor. *Geophysical Research Letters*, **28 (8)**, 1551–1554, doi:10.1029/1999GL011197.

Sioris, C. E., A. Malo, C. A. McLinden, and R. D'Amours, 2016: Direct injection of water vapor into the stratosphere by volcanic eruptions. *Geophysical Research Letters*, **43 (14)**, 7694–7700, doi:10.1002/2016GL069918.

Solomon, S., 1999: Stratospheric ozone depletion: A review of concepts and history. *Reviews of geophysics*, **37 (3)**, 275–316, doi:10.1029/1999RG900008.

Solomon, S., R. Portmann, R. Garcia, L. Thomason, L. Poole, and M. McCormick, 1996: The role of aerosol variations in anthropogenic ozone depletion at northern midlatitudes. *Journal of Geophysical Research: Atmospheres*, **101 (D3)**, 6713–6727, doi:10.1029/95JD03353.

Solomon, S., K. H. Rosenlof, R. W. Portmann, J. S. Daniel, S. M. Davis, T. J. Sanford, and G.-K. Plattner, 2010: Contributions of stratospheric water vapor to decadal changes in the rate of global warming. *Science*, **327 (5970)**, 1219–1223, doi:10.1126/science.1182488.

Sparks, R. S. J., M. Bursik, S. Carey, J. Gilbert, L. Glaze, H. Sigurdsson, and A. Woods, 1997: *Volcanic plumes*. Wiley.

Spence, R., I. Kelman, E. Calogero, G. Toyos, P. Baxter, and J.-C. Komorowski, 2005: Modelling expected physical impacts and human casualties from explosive volcanic eruptions. *Natural hazards and earth system sciences*, **5 (6)**, 1003–1015, doi:10.5194/nhess-5-1003-2005.

Stewart, C., D. Johnston, G. Leonard, C. Horwell, T. Thordarson, and S. Cronin, 2006: Contamination of water supplies by volcanic ashfall: a literature review and simple impact modelling. *Journal of Volcanology and Geothermal Research*, **158 (3-4)**, 296–306, doi:10.1016/j.jvolgeores.2006.07.002.

Stommel, H. and E. Stommel, 1979: The year without a summer. *Scientific American*, **240 (6)**, 176–187.

Stothers, R. B., 1984: The great Tambora eruption in 1815 and its aftermath. *Science*, **224 (4654)**, 1191–1198, doi:10.1126/science.224.4654.1191.

Straka, J. M., R. B. Wilhelmson, L. J. Wicker, J. R. Anderson, and K. K. Droegemeier, 1993: Numerical solutions of a non-linear density current: A benchmark solution and comparisons. *International Journal for Numerical Methods in Fluids*, **17 (1)**, 1–22, doi:10.1002/fld.1650170103.

Stuefer, M., S. Freitas, G. Grell, P. Webley, S. Peckham, S. McKeen, and S. Egan, 2013: Inclusion of ash and SO 2 emissions from volcanic eruptions in WRF-Chem: Development and some applications. *Geoscientific Model Development*, **6 (2)**, 457–468, doi:10.5194/gmd-6-457-2013.

Sulpizio, R., P. Dellino, D. Doronzo, and D. Sarocchi, 2014: Pyroclastic density currents: state of the art and perspectives. *Journal of Volcanology and Geothermal Research*, **283**, 36–65, doi:10.1016/j.jvolgeores.2014.06.014.

Suzuki, Y., A. Costa, M. Cerminara, T. E. Ongaro, M. Herzog, A. R. Van Eaton, and L. Denby, 2016: Inter-comparison of three-dimensional models of volcanic plumes. *Journal of Volcanology and Geothermal Research*, **326**, 26–42, doi:10.1016/j.jvolgeores.2016.06.011.

Tate, P. M. and J. H. Middleton, 2000: Unification of non-dimensional solutions to asymptotic equations for plumes of different shape. *Boundary-layer meteorology*, **94**, 225–251, doi:10.1023/A:1002431928523.

Textor, C., H.-F. Graf, M. Herzog, J. M. Oberhuber, W. I. Rose, and G. Ernst, 2006a: Volcanic particle aggregation in explosive eruption columns. Part II: Numerical experiments. *Journal of volcanology and geothermal research*, **150 (4)**, 378–394, doi:10.1016/j.jvolgeores.2005.09.008.

Textor, C., H.-F. Graf, M. Herzog, J. M. Oberhuber, W. I. Rose, and G. G. Ernst, 2006b: Volcanic particle aggregation in explosive eruption columns. Part I: Parameterization of the microphysics of hydrometeors and ash. *Journal of volcanology and geothermal research*, **150 (4)**, 359–377, doi:10.1016/j.jvolgeores.2005.09.007.

Textor, C., H. F. Graf, A. Longo, A. Neri, T. E. Ongaro, P. Papale, C. Timmreck, and G. Ernst, 2005: Numerical simulation of explosive volcanic eruptions from the conduit flow to global atmospheric scales. *Annals of Geophysics*, **48**, 817–842.

Timmreck, C., 2012: Modeling the climatic effects of large explosive volcanic eruptions. *Wiley Interdisciplinary Reviews: Climate Change*, **3 (6)**, 545–564, doi:10.1002/wcc.192.

Twomey, S., 1974: Pollution and the planetary albedo. *Atmospheric Environment (1967)*, **8 (12)**, 1251–1256, doi:10.1016/0004-6981(74)90004-3.

USGS, 1980: Pyroclastic flow during Aug. 7, 1980 Mount St. Helens eruption. `https://www.usgs.gov/media/images/pyroclastic-flow-during-aug-7-1980-mount-st-helens-eruption`.

Vogel, B., T. Feck, and J.-U. Grooß, 2011: Impact of stratospheric water vapor enhancements caused by CH4 and H2O increase on polar ozone loss. *Journal of Geophysical Research: Atmospheres*, **116 (D5)**, doi:10.1029/2010JD014234.

Vömel, H., S. Evan, and M. Tully, 2022: Water vapor injection into the stratosphere by Hunga Tonga-Hunga Ha'apai. *Science*, **377 (6613)**, 1444–1447, doi:10.1126/science.abq2299.

von Savigny, C., C. Timmreck, S. A. Buehler, J. P. BURROwS, M. A. Giorgetta, G. Hegerl, A. Horvath, G. A. Hoshyaripour, C. Hoose, J. Quaas, et al., 2020: The Research Unit VolImpact: Revisiting the volcanic impact on atmosphere and climate–preparations for the next big volcanic eruption. *Meteorologische Zeitschrift*, 3–18, doi:10.1127/metz/2019/0999.

Wacker, U., T. Frisius, and F. Herbert, 2006: Evaporation and precipitation surface effects in local mass continuity laws of moist air. *Journal of the atmospheric sciences*, **63 (10)**, 2642–2652, doi:10.1175/JAS3754.1.

Wacker, U. and F. Herbert, 2003: Continuity equations as expressions for local balances of masses in cloudy air. *Tellus A: Dynamic Meteorology and Oceanography*, **55 (3)**, 247–254, doi:10.3402/tellusa.v55i3.12097.

Wardman, J., T. Wilson, P. Bodger, J. Cole, and C. Stewart, 2012: Potential impacts from tephra fall to electric power systems: a review and mitigation strategies. *Bulletin of volcanology*, **74**, 2221–2241, doi:10.1007/s00445-012-0664-3.

Weimer, M., J. Schröter, J. Eckstein, K. Deetz, M. Neumaier, G. Fischbeck, L. Hu, D. B. Millet, D. Rieger, H. Vogel, et al., 2017: An emission module for ICON-ART 2.0: implementation and simulations of acetone. *Geoscientific Model Development*, **10 (6)**, 2471–2494, doi:10.5194/gmd-10-2471-2017.

Whitby, K. T., 1978: The physical characteristics of sulfur aerosols. *Sulfur in the Atmosphere*, Elsevier, 135–159.

Wilson, L., R. Sparks, T. Huang, and N. Watkins, 1978: The control of volcanic column heights by eruption energetics and dynamics. *Journal of Geophysical Research: Solid Earth*, **83 (B4)**, 1829–1836, doi:10.1029/JB083iB04p01829.

Wong, G. S., 1986: Speed of sound in standard air. *The Journal of the Acoustical Society of America*, **79 (5)**, 1359–1366, doi:10.1121/1.393664.

Woodhouse, M., A. Hogg, J. Phillips, and R. Sparks, 2013: Interaction between volcanic plumes and wind during the 2010 Eyjafjallajökull eruption, Iceland. *Journal of Geophysical Research: Solid Earth*, **118 (1)**, 92–109, doi:10.1029/2012JB009592.

Woodhouse, M. J., A. J. Hogg, and J. C. Phillips, 2016: A global sensitivity analysis of the PlumeRise model of volcanic plumes. *Journal of Volcanology and Geothermal Research*, **326**, 54–76, doi:10.1016/j.jvolgeores.2016.02.019.

Woods, A., 1988: The fluid dynamics and thermodynamics of eruption columns. *Bulletin of volcanology*, **50**, 169–193, doi:10.1007/BF01079681.

Woods, A. W., 1993: Moist convection and the injection of volcanic ash into the atmosphere. *Journal of Geophysical Research: Solid Earth*, **98 (B10)**, 17 627–17 636, doi:10.1029/93JB00718.

Woods, A. W. and S. M. Bower, 1995: The decompression of volcanic jets in a crater during explosive volcanic eruptions. *Earth and Planetary Science Letters*, **131 (3-4)**, 189–205, doi:10.1016/0012-821X(95)00012-2.

Woods, A. W. and M. I. Bursik, 1991: Particle fallout, thermal disequilibrium and volcanic plumes. *Bulletin of Volcanology*, **53**, 559–570, doi:10.1007/BF00298156.

Xu, J., D. Li, Z. Bai, M. Tao, and J. Bian, 2022: Large amounts of water vapor were injected into the stratosphere by the hunga tonga–hunga ha'apai volcano eruption. *Atmosphere*, **13 (6)**, 912, doi:10.3390/atmos13060912.

Yoo, J.-M., Y.-R. Lee, D. Kim, M.-J. Jeong, W. R. Stockwell, P. K. Kundu, S.-M. Oh, D.-B. Shin, and S.-J. Lee, 2014: New indices for wet scavenging of air pollutants (O3, CO, NO2, SO2, and PM10) by summertime rain. *Atmospheric Environment*, **82**, 226–237, doi:10.1016/j.atmosenv.2013.10.022.

Yu, T. and W. I. Rose, 2000: Retrieval of sulfate and silicate ash masses in young (1 to 4 days old) eruption clouds using multiband infrared HIRS/2 data. *Washington DC American Geophysical Union Geophysical Monograph Series*, **116**, 87–100, doi:10.1029/GM116p0087.

Zängl, G., D. Reinert, P. Rípodas, and M. Baldauf, 2015: The ICON (ICOsahedral Non-hydrostatic) modelling framework of DWD and MPI-M: Description of the non-hydrostatic dynamical core. *Quarterly Journal of the Royal Meteorological Society*, **141 (687)**, 563–579, doi:https://doi.org/10.1002/qj.2378.

D. List of Figures

1.1 Processes and impacts during volcanic eruptions . . . 3

2.1 Schematic of a volcanic eruption plume . . . 13
2.2 Schematic of the dynamical effect of ash on the total mixture . . . 16
2.3 Pyroclastic density current . . . 17

5.1 Straka density current test case simulation . . . 39
5.2 Mass mixing ratio of the mixed-bubble . . . 40
5.3 $\hat{\theta}_v$ and $\Delta\overline{\rho}$ of the mixed-bubble . . . 40
5.4 Temporal evolution of masses for the simulated mixed-bubble . . . 41
5.5 Mass mixing ratio of ash and density difference during an idealized volcanic eruption . . . 43
5.6 Temporal evolution of masses in the idealized simulation of a volcanic eruption . . . 44
5.7 Mass mixing ratio of ash and density difference during an idealized volcanic eruption without considering $\hat{\theta}_{v,e}$ . . . 45

6.1 Simulated model domain for the Raikoke eruption . . . 48
6.2 Raikoke plume dispersion for phase 2 at 19:00 UTC . . . 51
6.3 Raikoke plume dispersion for phase 7 at 01:20 UTC . . . 52
6.4 Raikoke plume dispersion for phase 10 at 07:10 UTC . . . 53
6.5 Simulated horizontal wind conditions at 19:00 UTC . . . 54
6.6 Comparison of ash column loading between model and VOLCAT retrieval for phase 2, 7, and 10 . . . 56
6.7 Estimated and simulated plume heights of the Raikoke eruption . . . 57
6.8 Vertical ash mass distribution for all phases . . . 59
6.9 Difference of vertical ash mass distribution between WQ-Exp and NoQ-Exp for all phases 61
6.10 Vertical and horizontal distribution of liquid clouds for phases 2, 7, and 10 . . . 63
6.11 Vertical distribution of hydrometeors (water contents) for phase 2 at 19:00 UTC . . . 64
6.12 Horizontal distribution of hydrometeors (water paths) for phase 2 at 19:00 UTC . . . 65
6.13 Vertical distribution of hydrometeors (water contents) for phase 7 at 01:20 UTC . . . 66
6.14 Horizontal distribution of hydrometeors (water paths) for phase 7 at 01:20 UTC . . . 66
6.15 Vertical distribution of hydrometeors (water contents) for phase 10 at 07:10 UTC . . . 67
6.16 Horizontal distribution of hydrometeors (water paths) of phase 10 at 07:10 UTC . . . 68

6.17 Temporal evolution of vertical mass distribution of all hydrometeors 69
6.18 Water content differences between WQ-Exp and NoQ-Exp of hydrometeors for phase 2 . 72
6.19 Water path differences between WQ-Exp and NoQ-Exp of hydrometeors for phase 2 . . 72
6.20 Water content differences between WQ-Exp and NoQ-Exp of hydrometeors for phase 7 . 73
6.21 Water path differences between WQ-Exp and NoQ-Exp of hydrometeors for phase 7 . . 73
6.22 Water content differences between WQ-Exp and NoQ-Exp of hydrometeors for phase 10 74
6.23 Water path differences between WQ-Exp and NoQ-Exp of hydrometeors for phase 10 . . 75
6.24 Temporal evolution of the difference of vertical mass distribution between WQ-Exp and NoQ-Exp of all hydrometeors 76
6.25 Temporal evolution of masses of all hydrometeors 77
6.26 Temporal evolution of vertical water vapor mass distribution 80
6.27 Difference of mean water vapor content between WQ-Exp and Ref for phase 7 80
6.28 Temporal evolution of water vapor mass above the tropopause 81
6.29 Captured atmospheric waves by Himawari-8 satellite 83
6.30 Simulated atmospheric waves indicated by pressure 83
6.31 Temporal evolution of pressure and its anomalies compared to Ref 84
6.32 Simulated atmospheric waves indicated by pressure at the beginning of phase 7 85
6.33 Temporal evolution of pressure and its anomalies at the beginning of phase 7 86

A.1 Raikoke plume dispersion for phase 1 at 18:10 UTC 95
A.2 Raikoke plume dispersion for phase 3 at 19:50 UTC 96
A.3 Raikoke plume dispersion for phase 4 at 20:50 UTC 96
A.4 Raikoke plume dispersion for phase 5 at 21:30 UTC 97
A.5 Raikoke plume dispersion for phase 6 at 22:10 UTC 98
A.6 Raikoke plume dispersion for phase 8 at 03:50 UTC 98
A.7 Raikoke plume dispersion for phase 9 at 05:50 UTC 99
A.8 Comparison of ash column loading between model and VOLCAT retrieval for phases 1,3,4,5 100
A.9 Comparison of ash column loading between model and VOLCAT retrieval for phases 6,8,9 101
A.10 Vertical distribution of hydrometeors (water contents) for phase 1 102
A.11 Horizontal distribution of hydrometeors (water paths) for phase 1 102
A.12 Vertical distribution of hydrometeors (water contents) for phase 3 103
A.13 Horizontal distribution of hydrometeors (water paths) for phase 3 103
A.14 Vertical distribution of hydrometeors (water contents) for phase 4 104
A.15 Horizontal distribution of hydrometeors (water paths) for phase 4 104
A.16 Vertical distribution of hydrometeors (water contents) for phase 5 105
A.17 Horizontal distribution of hydrometeors (water paths) for phase 5 105

A.18 Vertical distribution of hydrometeors (water contents) for phase 6 106
A.19 Horizontal distribution of hydrometeors (water paths) for phase 6 106
A.20 Vertical distribution of hydrometeors (water contents) for phase 8 107
A.21 Horizontal distribution of hydrometeors (water paths) for phase 8 107
A.22 Vertical distribution of hydrometeors (water contents) for phase 9 108
A.23 Horizontal distribution of hydrometeors (water paths) for phase 9 108
A.24 Water content differences of hydrometeors between WQ-Exp and NoQ-Exp for phase 1 . 109
A.25 Water path differences of hydrometeors between WQ-Exp and NoQ-Exp for phase 1 . . 109
A.26 Water content differences of hydrometeors between WQ-Exp and NoQ-Exp for phase 3 . 110
A.27 Water path differences of hydrometeors between WQ-Exp and NoQ-Exp for phase 3 . . 110
A.28 Water content differences of hydrometeors between WQ-Exp and NoQ-Exp for phase 4 . 111
A.29 Water path differences of hydrometeors between WQ-Exp and NoQ-Exp for phase 4 . . 111
A.30 Water content differences of hydrometeors between WQ-Exp and NoQ-Exp for phase 5 . 112
A.31 Water path differences of hydrometeors between WQ-Exp and NoQ-Exp for phase 5 . . 112
A.32 Water content differences of hydrometeors between WQ-Exp and NoQ-Exp for phase 6 . 113
A.33 Water path differences of hydrometeors between WQ-Exp and NoQ-Exp for phase 6 . . 113
A.34 Water content differences of hydrometeors between WQ-Exp and NoQ-Exp for phase 8 . 114
A.35 Water path differences of hydrometeors between WQ-Exp and NoQ-Exp for phase 8 . . 114
A.36 Water content differences of hydrometeors between WQ-Exp and NoQ-Exp for phase 9 . 115
A.37 Water path differences of hydrometeors between WQ-Exp and NoQ-Exp for phase 9 . . 115
A.38 Water vapor mass in the model domain for WQ-Exp and Ref 116

E. List of Tables

3.1 Constituents of the air mixture in ICON 24

6.1 Eruption source conditions for all phases of the Raikoke eruption 48

Danksagung

An dieser Stelle möchte ich mich bei all den Menschen bedanken, die diese Arbeit ermöglicht haben, mich betreut und unterstützt haben, ob direkt oder indirekt.
Zuerst gilt mein Dank Prof. Dr. Corinna Hoose für die Betreuung und Begutachtung meiner Arbeit. Vielen Dank für Deine Ratschläge, konstruktive Anmerkungen sowie die Diskussionen über meine Arbeit. Diese haben mir immer sehr geholfen haben. Außerdem bedanke ich mich bei Prof. Dr. Christian von Savigny für die Übernahme als Korreferent.
Ein besonderer Dank geht an Dr. Bernhard Vogel und Dr. Ali Hoshyaripour, die mir diese Arbeit ermöglicht und mir das Vertrauen gegeben haben, in Ihrer Gruppe an diesem Thema zu arbeiten. Ihr habt mir jederzeit sehr wertvolle und wichtige Ratschläge gegeben, mich unterstützt und mir Mut gemacht, wenn es nötig war. Vielen Dank für die regelmäßigen Diskussionen und für Eure Zeit, wann immer ich eine Frage hatte bzw. eine Meinung brauchte.
Außerdem möchte ich mich bei der Arbeitsgruppe Aerosol- und Spurenstoffmodellierung bedanken, für eure Ratschläge, euer Feedback nach Probevorträgen, persönliche Diskussionen außerhalb der Wissenschaft und auch Mittagspausen bedanken. Ein großer Dank geht dabei an Dich, Dr. Heike Vogel, dass Du immer Ratschläge und Ideen gegeben hast, wenn Simulationen mal wieder nicht so ganz liefen und Du bei der Fehlersuche mitgeholfen hast. Aber auch Deine lockere Art und deine Aufmunterungen haben sehr geholfen, um auch mal auf andere Gedanken zu kommen. Als nächstes danke ich Dir, Dr. Anika Rohde, dass ich mit Dir ein Büro teilen durfte und Du immer super hilfsbereit warst und Dir die Zeit genommen hast, wenn ich mal Fragen hatte, ob zu Vorträgen, Python-Skripten, etc. Und, dass Du Dich darum gekümmert hast, dass unser Büro grüner ausgesehen hat. Vielen Dank auch an Dich, Dr. Julia Bruckert, dass ich mit Dir vor allem über die Raikoke Simulationen immer wieder diskutieren konnte, und dass ich deine Daten bekommen habe, damit ich meine Simulationen durchführen konnte. Natürlich auch danke für die Mittagspausen und die Gespräche abseits der Wissenschaft und ganz besonders, dass mich mit zum Hurricane Festival durfte. Vielen Dank auch Dir, Dr. Sven Werchner, dass Du jedes Mal deine Zeit geopfert hast, wenn ich mal wieder irgendwelche Probleme mit ICON-ART hatte oder einfach mal mit Dir über irgendwelchen Quatsch reden konnte. Das war super hilfreich. Vielen Dank natürlich auch an Dich, Dr. Lukas Muser, da Du ebenfalls konstruktives Feedback gerade nach Probevorträgen gegeben hast und Dich mitgefreut hast, wenn Simulationen nach langer Zeit mal funktioniert haben. Ein großes Dankeschön geht hier auch an meine Bürokollegin und gute Freundin Lilly. Wir kennen uns jetzt auch schon ein ganzes Weilchen und reden immer wieder über allen möglichen und lustigen Unsinn, hatten aber auch immer hilfreichen Austausch über unsere Arbeiten, Präsentationen, etc. Vielen Dank

außerdem fürs Probelesen meiner Arbeit.
Ein ganz besonderer Dank gilt auch Dr. Daniel Reinert. Ohne Dich hätte es bestimmt deutlich länger gedauert, diese Arbeit durchzuführen. Vor allem am Anfang hast Du mir so viele wichtige Infos gegeben, aber auch ansonsten warst Du mir eine große Hilfe, wenn ich Fragen zum Modell hatte. Ich habe durch Dich super viel über ICON gelernt.
Diese Arbeit wurde von der Deutschen Forschungsgemeinschaft (DFG) im Rahmen der Forschergruppe VolImpact (FOR2820) gefördert. Danke an das gesamte VolImpact-Team für die super Zusammenarbeit, die Treffen und Summerschools, mitsamt Diskussionen über Ergebnisse. Dadurch habe ich neue Ideen bekommen und habe Einblicke in andere Arbeiten bekommen, wodurch ich viel gelernt habe.
Dabei geht ein besonderes Dankeschön an Dr. Ákos Horváth für das Bereitstellen der Retrievals von Mike Pavolonis und fürs Weiterhelfen bei vielen Fragen vor allem gegen Ende der Arbeit.
Ein großes Dankeschön gilt auch meinen Freunden, angefangen bei meinen Freunden aus der Heimat. Ich bin zwar selten da, für mich ist es trotzdem jedes Mal entspannt und lustig und eine absolut gerngesehene und notwendige Ablenkung. Ich bin froh, dass es sich auch nach langer Zeit nie wirklich geändert hat und mit Euch ist es im positiven Sinne einfach anders.
Weiter geht es mit meinen Freunden, die ich im Studium kennengelernt habe. Mit euch hat das Studium wahnsinnig Spaß gemacht und ohne Euch hätte ich das wahrscheinlich nicht durchgezogen. Vielen Dank für die jedes Mal schöne und witzige Zeit mit Euch und dass Ihr immer ein offenes Ohr hattet, wenn Dinge mal nicht so gut liefen.
A special thanks goes to my good friend and colleague Simran Chopra. You always told me to have faith in myself (which I hadn't many times). You always tried to cheer me up and helped me so much. Thank you very much for proofreading and improving my thesis.
Abschließend bedanke ich mich bei meinen Eltern, meiner Schwester und meinem Schwager. Danke, dass Ihr immer für mich da wart, mich auch während meinem Studium ständig unterstützt habt und mir das alles ermöglicht habt.